Combustor and Turbine Aerothermal Interactions in Gas Turbines with Can Combustors

Ioanna Aslanidou

St Anne's College

This thesis is submitted for the degree of

Doctor of Philosophy

Trinity Term 2015

Acknowledgements

I would like to express my gratitude to my supervisor, Budimir Rosic, for making this possible, for his critical view and his valuable advice, particularly in the last stages of this DPhil. I have learned and grown a lot in the course of the last five years, in ways that would not have been possible had I not been in Oxford.

I thank Mitsubishi Heavy Industries for the financial support of the project and my experimental work. I would specifically like to thank Sumiu Uchida for his technical advice in the first years.

I am grateful to my colleagues in the MHI group for their help with the experimental part of this project and their advice in various times over the last years: Vasudevan Kanjirakkad for the design of the rig and the pressure measurement system, Roderick Lubbock for the design and setup of the inlet pressure control system, Salvador Luque for the setup of the heat transfer measurement and processing system, Cosimo Mazzoni and Simon Jacobi for their always eager presence when required for the conduct of my experiments.

I cannot say enough for the support of the wonderful technicians and personnel of the Osney lab, particularly Gerald Walker for always solving my problems and for being a set of hands, brains and eyes when needed. My gratitude extends to Paul Cox for his help with the health and safety aspect of my experimental work and his support and willingness, particularly for all my heat transfer experiments. Thanks to Trevor Godfrey for the help and encouragement. I also want to thank Bill Godfrey, Hal Surtell, Ollie Smith, Duncan Blake, and Sam Davies for their help with the assembly of the experimental facility, Craig Parsons for the IT support, as well as Kathryn Scott, Laura Hook, and Debbie Andrews for the processing of so many purchase orders.

I wish to thank David Gillespie for the use of the two axis probe calibration rig and Brian Tang for his help with the setup of my numerical studies and his comments and advice on my written work. I also thank Antonio D'Ammaro for his help and advice on certain aspects of this work.

I would like to thank my colleagues in the Osney lab who have helped me in one way or another at different stages of my DPhil. Thank you Holt Wong, Roberto Maffuli, Ben Kirollos, Chris Hambidge, Amir Ibrahim, Amandeep Virdi, Andrew van Paridon, Niharika Gurram, Priyanka Dhopade, Martin Johansson, Pokwang Kwan. I would also like to acknowledge Irene Cresci, Josh Ryley, and Inés Usandizaga for their help in the first years.

I thank St Anne's Boat Club for teaching me to never ever give up and the Linacre Ladies that Lift for keeping me strong, physically and mentally, during the writing up process. Thank you Shez Naqvi, Laura Drössler, and Zoe Reich for pushing me and cheering me up. I also thank Ann Hart for the crucial role she played in the last year in my personal development.

I profoundly thank my friends for the small and big things they have offered me, knowingly or not. I have to single out Victoria Trubody, Sena Serhadlıoğlu, Johanna Rankin, Julian Nowag, Marina Chanidou, Nafsika Stavridou, who kept me sane through the hard times and eagerly shared the happy ones. You have been by my side when I needed it the most and carved wonderful memories into my mind and soul which will stay there forever. I would also like to thank Yasmine El Masri for being there at difficult times.

A special mention goes to my Cranfield family for their support from before I even thought of coming to Oxford and throughout these years, especially Diego Lombetti and Giuseppe Trapani. Yet another goes to my former advisor Pavlos Zachos for his encouragement.

I owe a lot to Anestis Kalfas for always believing in me, for his invaluable advice over the course of the last many years, and for his inspirational talks that got me into research in the first place and also helped me get through this.

And, at last, thank you Lydia, Spyros, and Stella for absolutely everything!

Abstract

As the research into the improvement of gas turbine performance progresses, the combustor-turbine interface becomes of increasing importance. In new engine designs components come closer together and the study of the combustor and turbine interactions can prove to be valuable for the improvement of the aerothermal performance of the vane.

This thesis presents an experimental and numerical investigation of the aerodynamic and heat transfer aspect of the interactions between the combustor and the nozzle guide vane. In the gas turbine studied the trailing edge of the combustor transition duct wall is found upstream of every second vane. In the experimental measurements carried out in a purpose-built high speed experimental facility, the wake of this wall is shown to increase the aerodynamic loss of the vane. On the other hand, the wall alters secondary flow structures and has a protective effect on the heat transfer in the leading edge-endwall junction, a region that has proven to be detrimental to component life. The effect of different clocking positions of the vane relative to the combustor wall are tested experimentally and shown to alter the aerodynamic field and the heat transfer to the vane. The experimental methods and processing techniques adopted in this work are utilized to highlight the differences between the different cases studied.

A new concept of using the combustor wall to shield the nozzle guide vane leading edge is introduced, followed by a proposed design that is numerically analysed, including a new cooling system. This uses continuous cooling slots on the upstream combustor wall to cool the vane leading edge. Coolant to the endwalls is provided from continuous slots on the combustor-turbine interface. The reduction of secondary flow through the removal of the horseshoe vortex in the new design results in improved cooling of the endwalls, with a higher average adiabatic effectiveness than in the original case, using the same coolant mass flow rate. The vane surface and suction side are also successfully cooled using less air than that required for a showerhead.

The new vane is tested in the experimental facility. The improved aerodynamic and thermal performance of the shielded vane is demonstrated under engine-representative inlet conditions. The new design is shown to have a lower average total pressure loss than the original vane for all inlet conditions. The heat transfer on the vane surface is overall reduced for all inlet conditions and the peak heat transfer on the vane leading edge-endwall junction is moved further upstream, to a region that can be effectively cooled from the upstream cooling slots on the combustor wall trailing edge and the endwalls.

Contents

List of Figures

List of Tables

Nomenclature

C	True chord	$[m]$
c_p	Specific heat	$[J/kg \cdot K]$
C_{P_0}	Total pressure loss coefficient $\frac{P_{0,in}-P_{0,local}}{\frac{1}{2}\rho V_{out}^2}$	
C_ω	Non dimensional vorticity $\frac{\omega \cdot C}{V_{CL}}$	
h	Heat transfer coefficient	$[W/m^2K]$
$h(t)$	Impulse response function	
I	Momentum flux ratio $\frac{\rho_c V_c^2}{\rho_\infty V_\infty^2}$	
j^*	Total radiation emitted by the surface of a black body	$[J/s \cdot m^2]$
k	Thermal conductivity	$[W/m \cdot K]$
M	Mach number	
M	Mass flux ratio $\frac{\rho_c V_c}{\rho_\infty V_\infty}$	
Nu	Nusselt number $\frac{h \cdot x}{k}$	
P	Pressure	$[Pa]$
Pr	Prandtl number $\frac{\nu}{\alpha} = \frac{c_p \mu}{k}$	
q	Heat flux	$[W/m^2]$
Re	Reynolds number, based on axial chord	
T	Temperature	$[K]$
Tu	Streamwise turbulence intensity	
V	Velocity	$[m/s]$
V	Voltage	$[V]$
V_{CL}	Mass-averaged velocity at midspan	$[m/s]$
x	Characteristic length	
α	Thermal diffusivity	$[m^2/s]$
γ	Ratio of specific heats	
δ	Thermal penetration depth	$[m]$
η_{ad}	Adiabatic cooling effectiveness $\frac{T_\infty - T_{aw}}{T_\infty - T_c}$	
θ	Normalized temperature $\frac{T_{local}-T_c}{T_\infty - T_c}$	
μ	Dynamic viscosity	$[Pa \cdot s]$
ν	Kinematic viscosity $\frac{\mu}{\rho}$	$[m^2/s]$
ρ	Density	$[kg/m^3]$
σ	Stefan-Boltzmann constant, 5.6704×10^{-8}	$[J/s \cdot m^2 \cdot K^4]$
τ	Time constant	
ω	Vorticity	$[1/s]$

Abbreviations

CAD	Computer Aided Design
CCGT	Combined Cycle Gas Turbine
CFD	Computational Fluid Dynamics
DSA	Digital Sensor Array
EU	European Union
HPT	High Pressure Turbine
HSV	HorseShoe Vortex
IR	InfraRed
LE	Leading Edge
MHI	Mitsubishi Heavy Industries
NGV	Nozzle Guide Vane
NI	National Instruments
PS	Pressure Side
SS	Suction Side
TE	Trailing Edge
TET	Turbine Entry Temperature
TLC	Thermochromic Liquid Crystals

Subscripts

0	Stagnation
aw	Adiabatic wall
ax	Axial
c	Coolant
i	Incompressible constant property
in	Inlet
is	Isentropic
out	Outlet
s	Streamwise
sw	Swirl
tan	Tangential
w	Wall
∞	Free-stream

Chapter 1
Introduction

This thesis presents an experimental and numerical study of the effects of the complex flow field at the exit of the combustor on the nozzle guide vane (NGV) row of the turbine in a gas turbine engine with can combustors. The effect of the combustor wall on the flow field of the nozzle guide vane is investigated in a purpose-built high speed experimental facility. A novel concept of shielding the vanes using the combustor walls is developed numerically and analysed in the experimental facility under both low inlet turbulence and engine-representative inlet conditions. The experimental part of this work was conducted as part of a project sponsored by Mitsubishi Heavy Industries.

This chapter provides a brief discussion on the background for the research presented in this thesis. Section 1.1 discusses the gas turbine engine and the current trends in engine performance, as well as the requirements and challenges that arise for the improvement of engine component designs. These requirements drive the research towards more closely coupled studies of the individual engine components. Sections 1.2, 1.3, and 1.4 present the motivation, the scope, and the aims and objectives of the research. Section 1.5 presents the limitations of this work and section 1.6 provides an outline of the rest of this thesis, which is centred around the aerodynamic and heat transfer measurements for the different geometries and inlet conditions.

1.1 Background

The gas turbine is one of the most important inventions of the 20^{th} century. Its history is linked to that of aircraft. The first gas turbines were mostly developed to power small aircraft, as they could not compete with diesel engines and steam turbines used for power generation. The first major

breakthrough came with their use in military aircraft towards the end of the second World War. In the space of 20 years, gas turbine engines had become more fuel efficient, quiet, and reliable, and were used for civil aircraft propulsion, allowing the development of the high capacity airliners in use today. In the power generation market, it was not until the end of the 20^{th} century that the gas turbine became competitive with diesel engines in terms of thermal efficiency and power output. The first gas turbine for electrical power generation to enter production was introduced in 1937 and had a thermal efficiency of 17% (Walsh and Fletcher, 2004). The unit sizes of those first engines were of the order of 10 MW.

The early engines used for power generation were aero-derivative engines, where the exhaust nozzle of the aircraft engine was replaced by a power turbine, and were commonly used for peak and emergency power requirements; this type of engine is still in use today for power generation. However, high demand led to the development of heavy duty gas turbines, capable of much higher power output and thermal efficiencies, that followed a different development path compared to aircraft engines. Industrial engines do not have the strict size and weight limitations imposed on aircraft engine design. In addition, the kinetic energy of the gas leaving the turbine has to be kept to a minimum, as it represents wasted energy. Engine life and reliability are also very important, as industrial engines are required to have a life of 50000 hours without a major overhaul.

The performance of the gas turbine mainly depends on the compressor pressure ratio, the turbine inlet temperature and the individual component efficiencies. However, limitations on design parameters such as the stress on the blade discs and the operating temperature of the engine are imposed by the thermal and structural properties of the materials.

Modern industrial gas turbines have a power output of up to 300 MW for simple cycle and 500 MW for combined cycle plants. In the latter, the exhaust heat is used to drive a steam turbine, allowing for thermal efficiencies exceeding 60%, compared to 40% which is achieved in simple cycle plants. For example, the Mitsubishi Heavy Industries (MHI) J-type gas turbine has a combined cycle thermal efficiency above 61.5% with a Turbine Entry Temperature (TET) of

1600° C (Mitsubishi Heavy Industries Ltd., 2013). A cross section of a heavy duty industrial gas turbine is shown in Figure 1.1. After the compressor, this engine has a series of can combustors around the annulus, followed by a four stage turbine.

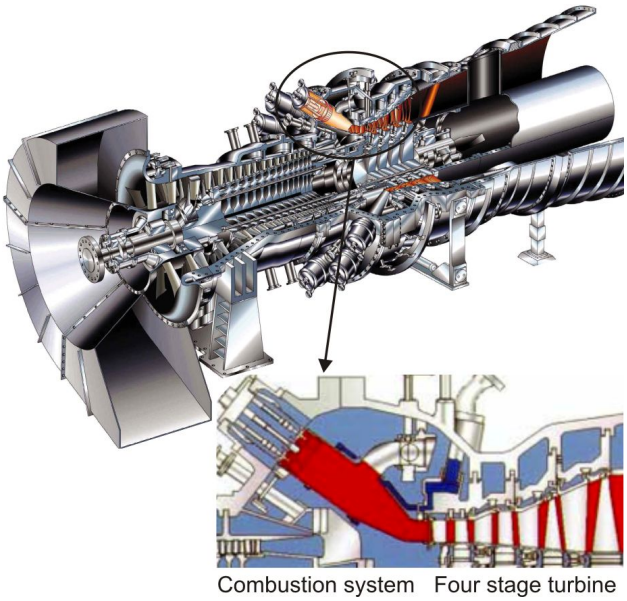

Figure 1.1: Cross section of an industrial gas turbine, Mitsubishi Heavy Industries Ltd.

One of the key requirements to achieve a high efficiency and a high TET is turbine cooling. The turbine blades are exposed to very high heat loads and thermal stresses. High performance cooling schemes are therefore required to maintain the blade temperatures at sufficiently low levels using a small amount of cooling air. New engine designs focus on the increase of TET to 1700° C (Ito et al., 2010) and the development of more advanced cooling systems to maintain engine life and minimize the penalty in thermal efficiency associated with increased cooling requirements.

The row of nozzle guide vanes immediately downstream of the combustor faces the highest heat loads as well as highly non-uniform inlet flow. In modern gas turbines, lean, premixed, swirl-stabilized combustors, a discussion on which can be found in Huang and Yang (2009), are used to lower NO_x emissions and meet the worldwide emissions targets. In order to achieve that, swirlers are used to assist mixing, improve flame stabilization and combustion efficiency; this results in lower peak combustion temperatures and therefore lower NO_x emissions. The addition of swirl results in a non-uniform velocity field at the inlet to the nozzle guide vane row. The employment of

a discrete number of combustors results in localized regions of high temperature flow downstream of the combustor, known as hot streaks. In addition, due to the increased swirl levels and high mixing, the temperature distribution is more homogeneous, resulting in higher temperatures near the endwalls compared to earlier combustor designs. The flow at the exit of the combustor is also highly turbulent, augmenting heat transfer from the hot mainstream flow to the vanes and endwalls.

A small rise in the temperature of the components may significantly reduce their life. Therefore, the cooling system of the nozzle guide vane has to be robust and reliable enough to keep the vane temperatures at acceptable levels under these adverse operating conditions. The cooling system typically comprises a combination of internal and external cooling features, with cold air bled from the compressor used as coolant. The nozzle guide vanes of industrial gas turbines, as shown in Figure 1.2, have a large number of cooling holes on the leading edge and the pressure side, as well as on the suction side.

Figure 1.2: Nozzle guide vane of an industrial gas turbine (Ai et al., 2009)

The interface between the combustor and turbine also features cold leakage flow through gaps between the combustor shell and the main gas path to prevent hot gas ingestion. Although this is not considered part of the cooling design of the vane, it affects the flow field in the leading edge region of the vane and can also be used to assist the endwall cooling.

In the MHI gas turbine the number of vanes is twice the number of combustors and every second vane can be exposed to an upstream combustor transition duct wall. This is another parameter of flow non-uniformity at the inlet of the turbine, as disturbances are shed from the trailing edge

of the combustor wall and can affect the establishment of a stable film of coolant flow on the vane surface.

1.2 Motivation for this Research

The high demand for more efficient ways to generate power is the main motivation for the research focusing on clean energy production. The gas turbine engine is a key component due to its ability to provide reliable, high power output at high thermal efficiencies. New engine designs aim at a higher power output at even higher efficiencies. In order to achieve that, advanced cooling methods are required. Furthermore, as new design trends bring the individual components closer together, the interaction between them becomes even more significant. Therefore, integrated studies of the engine components that were traditionally optimized separately need to be carried out.

The nozzle guide vane row is subjected to non-uniform, highly turbulent, swirling flow at the exit of the combustor, as well as disturbances shed from the upstream combustor wall. These parameters significantly affect the aerothermal field, the cooling of the vanes and endwalls, and can have detrimental effects on the overall engine performance and component life. Numerous researchers have investigated the effects of the combustor exit flow on the nozzle guide vanes, both numerically and experimentally. While numerical studies have the advantage of enabling the variation of flow parameters and the investigation of new geometries and concepts under different operating conditions, a validation against experimental data is needed. In the experimental studies carried out, compromises are always made as to how close the experimental operating conditions are to the real engine conditions. Studies have been carried out on low speed experimental facilities, as will be discussed in Chapter 2, investigating different geometrical parameters, but in order to better understand the flow physics and heat transfer, these effects need to be investigated under more engine-representative conditions.

1.3 Research Scope

The work presented in this thesis investigated the aerothermal field of the nozzle guide vane using experimental and numerical methods. The experimental studies were carried out in a new, high-speed facility, manufactured and commissioned as a part of this project, to investigate the interactions between the combustor and the turbine nozzle guide vanes in an industrial gas turbine with can combustors. The experimental facility enabled the conduct of experimental studies at a high Reynolds number and an engine-realistic Mach number, offering a modular environment where the effect of varying geometric and flow parameters could be investigated.

The main geometric parameter investigated in this study was the effect of the combustor wall on the vane leading edge, including different relative positions to the vane (clocking). The effect of the combustor wall was studied with the aim of developing a novel vane design for the interface of the combustor and the turbine, with improved aerothermal performance under engine-realistic operating conditions. The new vane design was developed through numerical studies and tested in the experimental facility under different inlet swirl and turbulence conditions. A uniform temperature profile was used in these studies. A cooling system for the new vane was developed and investigated numerically. This included leakage flow through the interface of the combustor and the turbine as well as cooling flow to the new vane.

1.4 Aims and Objectives

The main goal of this work was to investigate experimentally and numerically the interactions between the combustor and the nozzle guide vane in gas turbines with can combustors and to propose a design with improved aerothermal performance. The objectives of this work were:

- To assist in the design, manufacture and commissioning of a modular linear cascade with four vane passages and two combustor transition ducts to analyse the aerodynamic flow field and to map the surface heat transfer coefficient.
- To adopt aerodynamic and heat transfer measuring techniques suitable for high speed studies.
- To investigate the influence of the transition duct wall and vane clocking on vane aerodynamics and heat transfer.
- To investigate possible ways of shielding the vane leading edge using the transition duct wall, through numerical studies which are validated against the measurements obtained in the experimental facility.
- To numerically analyse the aerothermal performance and cooling of the shielded vane design.
- To analyse the performance of the shielded vane under engine-representative inlet conditions in the experimental facility.

1.5 Limitations

The work on the design and commissioning of the facility carried out as part of this research aimed at maximizing the experimental flexibility within the limitations set by the project of the industrial sponsor. The experimental facility was a linear cascade, which operated at high speed conditions with an engine-realistic Mach number. The Reynolds number was high enough to ensure turbulent flow, but not matched to the engine operating conditions.

The scope of the experimental work was set by the requirements of the project, due to the costs associated with the commissioning and operation of the facility and the manufacturing of the parts, as well as the operating schedule of the facility. The numerical investigation of cooling was limited

to numerical work on endwall cooling through the leakage slots between the combustor and the turbine and the cooling of the leading edge of the new vane design. No work on vane cooling through film cooling holes could be carried out, as the cooled vane geometry was not available. Experimental work on the cooling of the new shielded vane design could not be carried out before the end of this project, due to the limited availability of the facility. The free-stream turbulence intensity could not be measured due to the lack of a dedicated hot-wire system for use in the facility during the time of this project.

1.6 Thesis Outline

In line with the scope and objectives presented in the previous sections, the following chapters provide a discussion of the general theoretical background, followed by the numerical and experimental methods used in this study. These include the design and commissioning of the experimental facility and the investigation of the effect of the different geometrical and flow parameters on the aerothermal field.

Chapter 2 presents a review of the relevant literature to provide a background understanding of the basic aspects of the flow field in the combustor and turbine interface. This includes both fundamental studies that have established the current knowledge levels, and relevant studies carried out by other researchers, which highlight the need for integrated, high speed studies.

A detailed description of the design of the facility, its capabilities and the measurement techniques used for the investigation of the aerothermal field is presented in Chapter 3. The numerical investigation of the flow field that is required for the definition of the design and operating conditions of the facility is also presented.

Chapter 4 provides a discussion of the experimental measurements obtained in the facility that characterize the aerothermal field in the linear cascade and compares them to numerical studies carried out. Based on this, the modelling methodology followed can then be used for further

numerical studies. The chapter includes a presentation of the methodology for the numerical studies.

Chapter 5 investigates the effect of different clocking positions of the vane relative to the upstream combustor wall in the experimental facility. The upstream combustor wall is shown to have a beneficial effect in protecting the vane leading edge from the hot mainstream flow.

In Chapter 6, a novel concept that takes advantage of the presence of the combustor wall, using it to shield the vane leading edge, is presented and numerically analysed. Effective cooling of the vane can be provided with the new design, and the cooling effectiveness on the endwalls is improved compared to the original design. This new design is found to improve cooling effectiveness on the vane and endwall surfaces.

Chapter 7 investigates the new design in the high speed experimental facility, analysing its aerodynamic and thermal performance in comparison to the original vane, under low inlet turbulence conditions. Chapter 8 investigates the performance of the new shielded vane under engine-representative inlet conditions in the experimental facility and compares them to the original vane. This includes the aerodynamic field, the secondary flow formation, and the heat transfer under high inlet turbulence intensity and inlet swirl.

The last chapter offers a summary of the work presented, draws conclusions from the analyses conducted and discusses the prospective future work. This extends to both numerical and experimental work. In this respect, the modular design of the facility offers a good baseline for validation of computational studies and testing of new concepts. Concluding remarks highlight the contribution of this thesis to academic knowledge.

A journal paper has been published on the development of the vane shielding concept presented in Chapter 6, (Aslanidou et al., 2013), and was also presented at the 2012 ASME Turbo Expo conference by the author. The author was also involved in a second journal paper on the design of the experimental facility (Luque et al., 2015). Further papers based on the results of the experimental work carried out are currently in preparation.

Chapter 2
Literature Review

This chapter provides a review of the literature in the area of combustor and turbine interactions. Relevant studies carried out on the aerothermal field of the nozzle guide vane and the effect of the combustor exit flow are presented in the following sections. Section 2.1 gives a background of the aerodynamic field of a nozzle guide vane that is dictated by secondary flow. Section 2.2 discusses the thermal field of the nozzle guide vane including endwall heat transfer and cooling. Section 2.3 discusses the effect of the flow conditions downstream of the combustor on the aerothermal field of the vane and endwall, including turbulence, swirl, temperature non-uniformities, Mach number, and Reynolds number. Section 2.4 offers a discussion of the fundamentals of experimental studies and cascade design, including a brief mention of commonly used aerodynamic and heat transfer measurement techniques. Section 2.5 gives an introduction to the few integrated combustor and vane studies that have been carried out. Finally, section 2.6 draws some conclusions from the work carried out by other researchers and sets the ground for the work presented in this thesis.

2.1 The Aerodynamic Field of a Nozzle Guide Vane

2.1.1 Secondary Flow

The flow field of a high pressure turbine vane is characterized by secondary flow, which affects both the aerodynamic flow and the heat transfer to the vanes and endwalls. The term secondary flow in a cascade refers to flow features that arise as the difference between the actual flow and an ideal irrotational potential flow. A discussion of the basic theory can be found in Lakshminarayana (1996) and in Longley (2012). The blade-to-blade flow in a cascade establishes a pressure field

that is imposed onto the low momentum flow near the endwalls. A separation saddle point appears upstream of the vane leading edge, a concept first introduced by Langston et al. (1977). As the upstream endwall boundary layer flow approaches the vane leading edge, it is forced to roll into a vortex. This vortex is known as the horseshoe vortex due to its shape around the front part of the vane and starts developing from the saddle point. A reconstruction of the flow field explaining this concept was presented by Langston (1980); Sharma and Butler (1987) and Goldstein and Spores (1988) later proposed more complex models for the endwall flow structures in a turbine cascade. The models were based on the numerous measurements and flow visualization experiments that had been carried out in low speed cascades.

The horseshoe vortex has two legs with opposite senses of rotation. The pressure side leg is deflected toward the adjacent vane suction side by the cross-passage pressure gradient, sweeping the inlet boundary layer fluid and growing into the passage vortex. When this reaches the vane suction side, it is driven up the blade span and away from the endwall. The suction side leg is smaller and stays close to the passage vortex. In order to better define the trajectory of the suction side leg of the horseshoe vortex, which was the main source of disagreement in the previous models, Wang et al. (1997) carried out flow visualization experiments in a linear turbine cascade using multiple smoke wires and a laser light sheet to illuminate various sections of the cascade and visualize the smoke traces. They observed a periodically fluctuating system of vortices near the leading edge. Their model, shown in Figure 2.1, has more vortical structures arising from the leading edge – endwall junction, which gradually collapse into the two main legs of the horseshoe vortex. Comparing the flow visualization results to mass transfer measurements conducted by Goldstein et al. (1995), they suggested that smaller vortices also arise on the vane suction side. A wall vortex, indicated by the local peak of mass transfer, starts near the merging point of the pressure and suction side leg of the horseshoe vortex and is found above the passage vortex. The mass transfer distributions also suggested the presence of a weaker corner vortex in the endwall – suction surface junction below the passage vortex that was not captured by the flow visualization

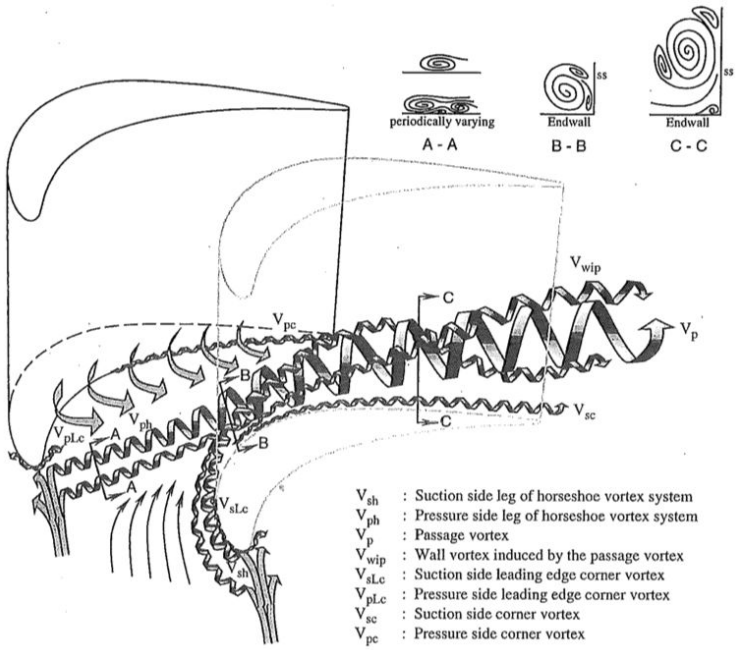

Figure 2.1: Endwall flow model proposed by Wang et al. (1997)

experiments. The unsteadiness of the vortex formation upstream of the leading edge was captured in experimental studies on bluff bodies and cylindrical leading edges by Praisner et al. (1997) and Praisner and Smith (2006a,b), who noted the presence of an unsteady counter-rotating secondary vortex upstream of the horseshoe vortex. Reviews of early research carried out on endwall flows in turbine cascades can be found in Sieverding (1985) and in Langston (2001).

One of the few studies focusing on secondary flow patterns at high speed conditions was carried out by Abo El Ella and Sjolander (2013), who presented results from oil flow visualization measurements in a high speed turbine cascade with an outlet Mach number of 0.8 and an exit Reynolds number of 6×10^5. In the left and central parts of Figure 2.2, the endwall flow visualization is shown, along with the interpretation of the limiting streamlines. Three separation lines are identified in the figure. The first separation line, S_1, marks the separation of the inlet boundary layer from the endwall, from the saddle point A_1 and towards either the pressure side, S_{1P}, or the suction side, S_{1S}. The second line marks the lift-off of the horseshoe vortex and the entrainment of the flow to the pressure side leg, S_{2P}, and the suction side leg, S_{2S}. The separation line associated with the corner vortex is denoted as S_3. The boundary layer formed downstream of the pressure

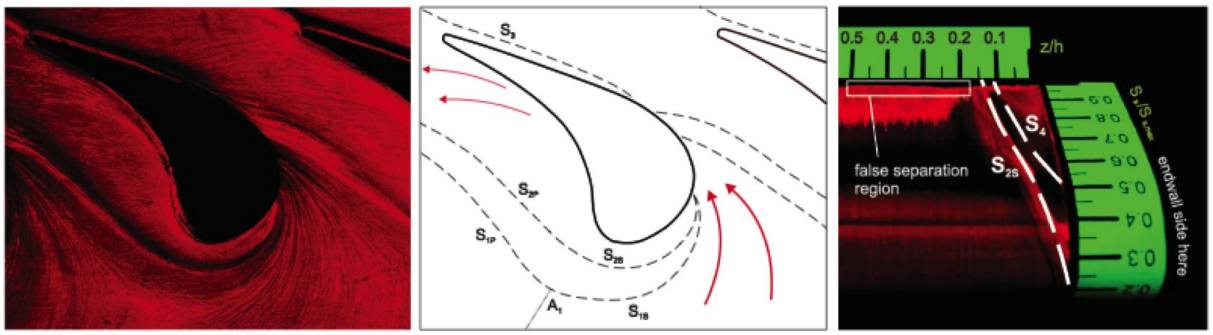

Figure 2.2: Endwall flow visualization and interpreted limiting streamlines (Abo El Ella and Sjolander, 2013)

side leg of the horseshoe vortex (that evolves into the passage vortex) is swept towards the suction side of the adjacent vane due to the pressure gradient across the pitch. In the right part of Figure 2.2, flow visualization results on the vane suction side are shown, along with the dominant separation lines. In that figure, the vane leading edge is at the bottom, the trailing edge at the top, and the endwall at the right. S_{2S} is the suction side leg of the horseshoe vortex that lifts up from the endwall and reaches 15% of the span at the outlet of the passage. S_4 is the passage vortex, that appears on the vane at 50% of the suction side length and penetrates to 10% of the span at the outlet.

2.1.2 Loss Generation

The migration of low energy fluid across the passage results in a non-uniform total pressure loss distribution at the exit of the vane row. The loss near the endwall is low; the peak occurs some way off the endwall, due to these secondary flow structures. Furthermore, the cross-passage flow causes pronounced overturning of the flow near the endwall compared to the mainstream flow, and underturning further away as a consequence of the passage vortex, as shown by Dawes (1990) in a comparison of numerical predictions and experimental measurements of loss in a low pressure linear turbine cascade.

Denton (1993) discussed the physics of secondary flow and analysed the sources of loss in turbomachines, advocating the use of entropy as a measure of loss generation. If entropy is thought

of as ”smoke” that is generated in any process detrimental to the overall efficiency, this enhances the physical understanding of a problem. This smoke cannot be destroyed once created and propagates through the machine; the total penalty in efficiency is then proportional to the concentration of smoke. Entropy is created by viscous friction in boundary layers or free shear layers, by rapid expansions or shock waves and by heat transfer across finite temperature differences. In the boundary layers, entropy generation is concentrated in the inner part of the boundary layer, where the velocity changes more rapidly. In a turbulent boundary layer this occurs mostly in the laminar sublayer. Viscous shear also occurs in wakes, edges of regions of separated flow and in the mixing out of leakage jets, causing large entropy generation.

In turbomachinery flows, the main sources of loss in a blade row are the profile loss, the tip leakage loss and the endwall loss, each amounting to approximately one third of the total loss. In stator vanes, where there is no tip leakage loss, these are reduced to profile loss and endwall loss. The profile loss includes loss due to surface boundary layers, and loss caused by the mixing out of the boundary layers in the wake, known as trailing edge loss. The loss in the boundary layers largely depends on the state of the boundary layer and is therefore affected by boundary layer transition, which depends on free-stream turbulence and Reynolds number. For Reynolds numbers (based on the true chord) above 10^6, the flow is very likely to be turbulent (Miller and Denton, 2012). For lower Reynolds numbers, where the boundary layer may be either laminar or turbulent, pressure loss is significantly higher for a turbulent boundary layer. Regardless of the state of the boundary layer, the majority of loss generation on a blade surface takes place on the suction side, as it is proportional to the surface velocity cubed (Schlichting, 1968). The trailing edge loss depends on the geometry of the trailing edge. Thick trailing edges, such as those of transonic turbine blades, result in significant entropy generation. In these cases, coolant is ejected through the trailing edge to reduce loss.

Endwall loss refers to entropy creation near the endwalls, due to the interaction of secondary flow with the blade surface and the endwalls. Denton and Pullan (2012) numerically investigated

the sources of endwall loss in axial flow turbines and compared their predictions to experimental data obtained in a low speed linear cascade (Harrison, 1990). They found high entropy generation rates in the horseshoe vortex system, which increase where the pressure side leg of the vortex interacts with the suction surface of the vane. This is seen in Figure 2.3 which shows dimensionless entropy generation rates per unit surface area on the vane endwall. They only have a small contri-

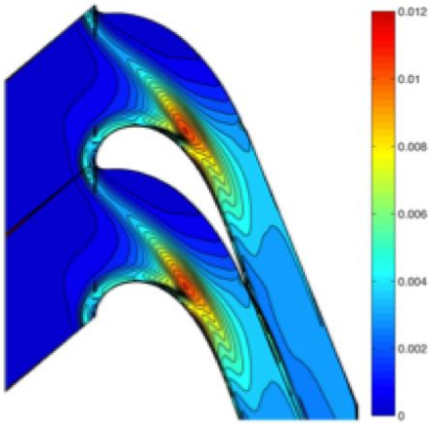

Figure 2.3: Dimensionless entropy generation rates per unit surface area on a vane endwall (Denton and Pullan, 2012)

bution to the overall loss, however, as the surface area is small. In fact, no dominant source of loss was found, as entropy generation is split between the endwall, the blade surfaces, the mainstream and the wake. They concluded that the presence of multiple sources of endwall loss is the reason its accurate prediction and reduction remain a challenge.

2.1.3 Parameters Affecting the Aerodynamic Field

A good understanding of secondary flow formation and behaviour is required in order to predict heat transfer levels to the turbine vane. Some of the more recent experimental and computational studies have focused on an investigation of the parameters that affect secondary flow formation and on the quantification of aerodynamic loss.

Benner et al. (2004) experimentally investigated the effect of the leading edge geometry on two low speed large scale linear cascades with different loading. They concluded that the leading edge geometry itself is of no significant importance, but the increase of the loading of the forward

part of the aerofoil causes a stronger pressure gradient at the leading edge, increases the strength of the passage vortex, and results in higher loss generation.

Hermanson and Thole (2000, 2002) investigated the effects of varying total pressure, velocity, and temperature profiles on the secondary flow in a series of computational studies benchmarked against previously published experimental data on a large scale turbine cascade. They showed that the increase of the inlet boundary layer thickness can strengthen secondary flow, and that different pressure gradients at the inlet can result in different vortex patterns in the passage. They reported that if the stagnation pressure decreases from the endwall to the mid-span a counter-rotating vortex can form within the passage, in addition to the passage vortex. This vortex can drive fluid away from the endwall and towards the mid-span. The dependence of secondary flow development on the pressure profile and the appearance of a counter-rotating vortex was also found in experimental studies of Barringer et al. (2009b,c). They used an inlet profile generator on a true scale, fully annular turbine vane cascade operating at engine-realistic Mach and Reynolds numbers to study the effects of pressure and temperature profiles and measured heat flux on the endwall using thin film gauges. The different secondary flow patterns result in different temperatures and heat transfer rates along the endwall.

2.2 The Thermal Field of a Nozzle Guide Vane

2.2.1 Heat Transfer Parameters

Heat transfer to the vane surface occurs through conduction from the hot mainstream gas and is governed by Fourier's law of heat conduction, which states that the heat flux is proportional to the thermal conductivity of the material and the negative local temperature gradient: $\vec{q} = -k\vec{\nabla}T$. Heat transfer rates are calculated from Newton's law of cooling, $q = h(T_{aw} - T_w)$. This is the solution of the differential equation of Fourier's law, using the heat transfer coefficient, h, as a proportionality coefficient between the heat flux, q, and the driving temperature difference.

The latter is the difference of the temperature of the fluid immediately above the wall and the temperature of the wall, T_{w}. The temperature used for the fluid is the adiabatic wall temperature, T_{aw}, which is the temperature at which the wall would need to be in order to achieve adiabatic conditions. The heat transfer coefficient is usually expressed using the dimensionless Nusselt number based on the thermal conductivity, k, of the fluid and a characteristic length, x, which often is the axial chord for turbomachinery blades.

The heat transfer coefficient for a given geometry depends on the Reynolds number, Prandtl number, free-stream turbulence, surface curvature and roughness, pressure gradients, temperature ratios near the wall, and boundary layer history. Reynolds number, the ratio of the inertial forces to the viscous forces based on a characteristic length x, defines whether turbulent flow, with inertial forces producing large instabilities, prevails over laminar flow, where any disturbances are eliminated by the high viscosity of the fluid. Prandtl number expresses the ratio of the momentum diffusivity to the thermal diffusivity, defining whether heat transfer through convection prevails over heat transfer through conduction, and determining the relative thickness of the momentum to the thermal boundary layer.

The boundary layers that develop on the vane surface act as a buffer between the solid and the fluid. Heat transfer through thin boundary layers is generally higher than through thicker ones; the thinner the boundary layer, the higher the temperature gradient between the vane surface and the mainstream that drives the heat transfer mechanism. Boundary layer state and transition affects not only the aerodynamic loss but also the heat transfer to the vanes. Figure 2.4(a) shows the different heat transfer rates observed around a turbine blade, in laminar, transitional and turbulent boundary layer regions. The local temperature and velocity gradients are very high in the stagnation point, therefore the maximum heat transfer to the vane usually occurs in that region. As the boundary layer that develops on the vane surface gets thicker, the heat transfer rate drops. For high Reynolds numbers, the boundary layer will typically go through transition to turbulent on the vane suction side. Transition on the pressure side may happen later on the vane surface. Boundary layer

transition is associated with high momentum and heat exchange and augments heat transfer rates to the vane. In turbulent boundary layers heat transfer rates are higher than in laminar ones for the same conditions due to the turbulent mixing that is taking place. On the other hand, flow separation results in small velocity and temperature gradients near the wall and therefore low heat transfer. A reattachment point will bring high heat flux to the vane surface. The heat flux distribution around a turbine vane is shown in Figure 2.4(b). Increased heat transfer rates are observed on the vane leading edge; heat transfer drops along the vane pressure side. On the suction side, a sudden increase in heat transfer is again due to flow transition. It is noted that this discussion refers to uncooled parts; addition of cooling to the blades and vanes will alter the heat transfer distribution.

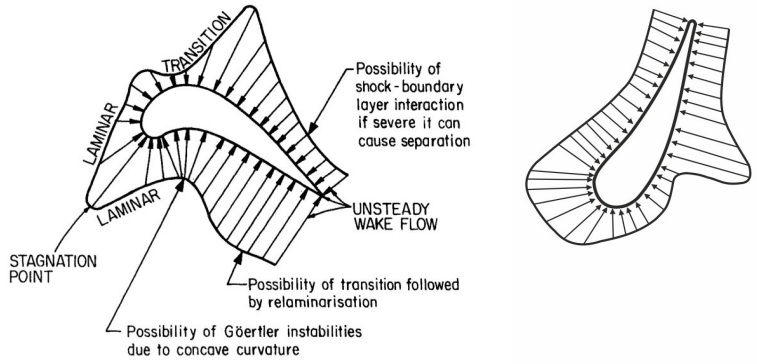

(a) Variation of heat transfer rate around a turbine blade from Daniels and Schultz (1982), collected in Lakshminarayana (1996)

(b) Heat transfer distribution around a turbine vane, adapted from Han and Wright (2006)

Figure 2.4: Heat transfer distribution on turbine blade and vane (uncooled)

2.2.2 The Need for Cooling

Trends in gas turbines in the last 50 years have been towards increased TET combined with increased pressure ratios that offer a significant increase in overall efficiency. As seen in Figure 2.5, which shows the evolution of TET through the years, gas turbines operate at temperatures well above the permissible metal temperatures, marked with the dashed line at the bottom of the chart. The use of blade cooling, introduced on the Conway engine that entered into service in 1960, allowed the operation of gas turbines at higher TET levels, above the melting points of the mate-

rials. Today, a typical commercial heavy duty Combined Cycle Gas Turbine (CCGT) has a TET of 1600°C (Mitsubishi Heavy Industries Ltd., 2013), made possible through the development of more advanced cooling systems and nickel-based superalloys that can withstand temperatures of about 1100°C (Coletti et al., 2011).

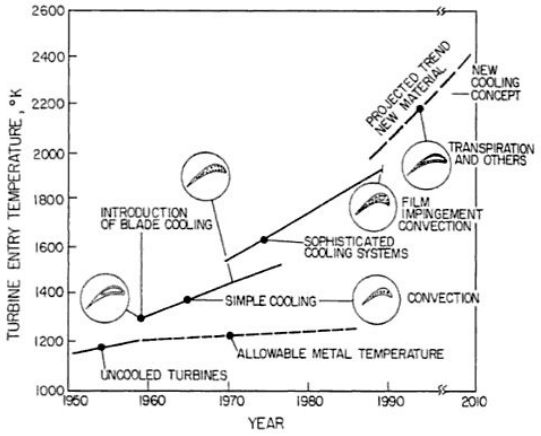

Figure 2.5: Variation of turbine entry temperature over the years (Han et al., 2013)

The NGV is cooled using a combination of internal convective cooling and external film cooling, using air bled from the exit of the compressor as coolant, to maintain the temperature of the blades at an acceptable level. Part of the high pressure coolant is used to cool the hot internal surface of the vane, through jets that impinge perpendicular to the surface (impingement cooling). The coolant then flows towards the trailing edge, and is exhausted through a pedestal bank, an array of cylinders connecting the pressure and suction side of the vane. These are usually staggered and provide structural support, enhance turbulent mixing and increase the surface area, augmenting heat transfer from the internal surfaces of the vane. The other part of the coolant is used for film cooling; it is discharged through holes on the vane surface, forming a film of cold air over the surface and thus protecting the vane from the high temperature mainstream flow. A high and uniform cooling effectiveness reduces thermal stresses, therefore increasing the life of the components.

The increase of TET has been made possible due to advances in materials and cooling technologies. However, as Horlock et al. (2001) discuss, the advantages in efficiency by the further

increase of TET are significantly offset by the required increase in coolant flows, unless there are any further advances in material and coating technologies. The constant aim to improve the overall efficiency therefore requires a reduction in coolant requirements using more efficient cooling methods. To this end, different component cooling configurations have been investigated by various researchers in the past years. An overview can be found in papers by Arts (2001), Bogard and Thole (2006), Bunker (2005), Han (2013), Han et al. (2013), summarizing the progress in cooling methods research.

One of the most demanding regions in terms of cooling is the leading edge of the nozzle guide vanes of the turbine, which is exposed to some of the highest thermal loads. The nozzle guide vane is currently cooled using a showerhead in the leading edge region typically consisting of six to eight spanwise rows of holes for turbine vanes (Bogard and Thole, 2006). Additional film cooling holes in the downstream regions of the vane ensure adequate cooling of the full surface. The nozzle guide vanes of the high pressure turbine (HPT) of industrial gas turbines typically have rows of film cooling holes on both the pressure and the suction surface, whereas those of aircraft engines use impingement cooling for the suction surface. The nozzle guide vanes of the HPT consume the highest amounts of cooling air on current high temperature engines, with values reaching 9% of the compressor inlet flow (Friedrichs, 2012).

The next generation industrial gas turbines aim at a $1700°\mathrm{C}$ class gas turbine, operating in a combined cycle with a target thermal efficiency exceeding 62% (Ito et al., 2010). The higher turbine entry temperature comes with a penalty in overall efficiency due to the required increase of coolant flow, so new, more sophisticated turbine cooling schemes must be employed to achieve even higher cooling efficiencies.

2.2.3 Film Cooling Parameters

The main parameters defining the performance of a film cooling hole can be categorized into coolant to mainstream conditions, hole geometry and configuration and aerofoil geometry. The

factors that have a significant effect on the predictability of the film cooling performance, as identified by Bogard and Thole (2006), are the mass flux or blowing ratio M of the coolant to the mainstream, the momentum flux ratio I of the coolant to the mainstream, and the mainstream turbulence. The shape of the hole, the injection angle of the coolant relative to the mainstream, and the surface curvature of the aerofoil are the main geometric parameters. Cooling performance is most commonly reported in the literature using the adiabatic cooling effectiveness $\eta_{ad} = \frac{T_\infty - T_{aw}}{T_\infty - T_c}$, where T_c is the coolant temperature at the exit of the hole. An equivalent definition is used to present temperature contours of the fluid flow downstream of coolant jets, in the form of the normalized temperature, $\theta = \frac{T_{local} - T_c}{T_\infty - T_c}$.

Numerous experimental studies have been carried out with hole orientations of $30^\circ - 45^\circ$ relative to the surface, that assist the coolant jets to remain attached to the surface, as well as with varying coolant to mainstream conditions to determine the effect of these parameters on the coolant distribution downstream of the cooling holes. Baldauf et al. (2001) found that the location of the maximum cooling effectiveness ranges from 0.5 to 8 hole diameters downstream of the cooling hole, depending on the blowing and momentum flux ratio. A low blowing ratio will result in a jet that remains fully attached to the surface, a moderate blowing ratio will cause the jet to separate from the surface and reattach further downstream, whereas a high blowing ratio will result in a fully detached coolant jet. This was also shown by Thole et al. (1992), who reported that the momentum flux ratio is the best scaling parameter of the thermal field with regard to the separation of coolant jets. This is reasonable, as the dynamics of the interaction of the jet with the crossflow can be expected to depend on the momentum of the two streams. The jets remained attached for $I < 0.4$ and fully detached for $I > 0.8$. For $0.4 < I < 0.8$, the jets were found to initially separate from the surface and then reattach. It is noted that these conclusions generally hold for cylindrical cooling holes.

2.2.4 Endwall Cooling

Upstream of the separation line the endwall boundary layer is thick. After this boundary layer separates and is entrained into the horseshoe vortex, a new, thin, laminar boundary layer is formed, that undergoes transition further downstream. This results in high heat transfer rates to the endwall. In addition, the flatter temperature profiles formed in the modern, low emission combustors noted by Haselbach and Schiffer (2004) result in higher mainstream gas temperatures near the endwalls. Heat transfer rates are becoming higher and therefore more efficient cooling of the endwalls is required. Furthermore, the presence of non-uniform flow at the inlet to the nozzle guide vane will also affect the secondary flow patterns and the heat transfer levels to the endwalls.

The heat transfer on the endwall has been investigated by many researchers. Early studies showed that the horseshoe vortex can increase local heat transfer on the endwall by up to 300% compared to a flat plate (Blair, 1974, Graziani et al., 1980, Kang et al., 1999). Furthermore, a region of very high heat transfer on the endwall on the early suction side of the vane has been noted by Graziani et al. (1980) and can lead to extensive damage. A picture of engine hardware with damage in the high heat transfer region is shown in Figure 2.6. The high heat transfer rates are being dealt with by using series of film cooling holes on the endwalls or modifications to the leading edge of the vane.

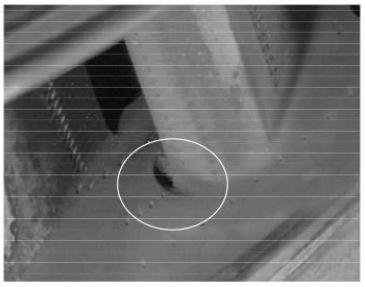

Figure 2.6: Damage on the endwall near the vane suction side (Thole, 2006)

The interaction of the coolant with the three-dimensional flow near the endwalls is a two-way effect; secondary flow can influence coolant trajectories and the ejection of coolant from the endwall surfaces can affect secondary flow. The vane endwalls are cooled using a combination

of film cooling holes located in the vane passage. In the interface between the combustor and the turbine there are gaps between the components resulting from the assembly of the individual parts. Coolant is fed through these continuous slots to prevent hot gas ingestion into the gap. The sealing flow from the gaps between the combustor shell and the main gas path can amount to $1 - 2\%$ of the total core flow for each turbine stage (Bunker, 2007). This is not considered part of the cooling design of the vane but affects the flow field in the leading edge region of the vane and can be used to assist in endwall cooling.

The early studies on cooling flows were carried out on continuous slots that introduce a uniform sheet of coolant and provide ideal cooling performance. Blair (1974) measured the film cooling effectiveness and heat transfer coefficients downstream of a continuous slot in a low speed single vane passage experimental facility at an engine-realistic Reynolds number. Coolant was ejected at three blowing ratios and it was found that as the blowing ratio increased, coolant coverage also increased, which is expected with the low blowing ratios used in the study, $0.5 - 1$. One of the most important findings was the large variation in endwall adiabatic effectiveness across the vane pitch in the trailing edge region, as much of the coolant was swept away by the passage vortex in the corner between the endwall and the vane suction side.

The effects of secondary flow on endwall cooling have been noted in many studies following the one of Blair. Friedrichs et al. (1996, 1997, 1999) studied aerodynamic and heat transfer aspects of film cooling holes on a large scale low speed linear turbine cascade endwall using the ammonia and diazo technique. Their studies revealed the strong interaction between coolant ejection and secondary flow and highlighted that taking into account the secondary flow can significantly improve the design of the endwall film cooling configuration. They also found that coolant ejection downstream of the separation lines on the endwall does not change secondary flow structures and that the placement of film cooling holes in regions of high static pressure reduces the aerodynamic penalties of coolant ejection.

Another experimental study was conducted by Kost and Nicklas (2001) and Nicklas (2001) in a transonic turbine cascade with Reynolds number of 8.5×10^5 with and without coolant ejection on the endwall. They found that the ejection of coolant from both an upstream slot and film cooling holes reduced the endwall crossflow and the passage vortex compared to the case with no coolant ejection, but had a significant strengthening effect on the horseshoe vortex. This was attributed to the location of the slot, which was too close to the vane leading edge and caused an increase in heat transfer coefficient levels in the vane leading edge region. In addition, the ejection of coolant from the film cooling holes augmented turbulence levels and therefore heat transfer to the endwalls.

A computational study on the endwall film cooling was carried out by Knost and Thole (2003), who studied different cooling schemes using combinations of film cooling holes and a continuous slot. It was found that the majority of the coolant from the slot was swept to the vane suction side; the addition of film cooling holes further downstream is required to obtain a better coverage of the endwalls. The cooling system affected the secondary flow pattern, explaining the differences in heat transfer levels between the cases.

Cardwell et al. (2006) investigated the effects of realistic engine features on endwall film cooling in a low speed linear cascade with an exit Reynolds number of 10^6 with upstream slot cooling; vane to vane mid-passage gap, platform misalignment and surface roughness. They concluded that the mid-passage gap limits the coverage of the upstream coolant flow and they also noted ingestion of hot flow from the endwall platform. Misalignment between the platforms had detrimental effects on endwall cooling and surface roughness was shown to decrease adiabatic effectiveness for a high blowing ratio of 2.3, whereas it had no effect for a lower blowing ratio of 1.5. This was attributed to the boundary layer thickness, which has a bigger impact on the coolant jet separation for a high blowing ratio. Cardwell et al. (2007) found that a decrease in the width of the slot resulted in a more uniform coolant distribution exiting the slot, with the mass flow rate kept constant. This was also noted by Lynch and Thole (2008).

Thrift et al. (2012), on a similar configuration to previous studies by Cardwell et al., studied the orientation of the slot, observing a significant increase in cooling effectiveness from a $45°$ forward slot compared to $90°$. Further studies by Thrift et al. (2013) confirmed that a tangential slot ejection results in a more uniform coolant distribution, as seen in Figure 2.7 and noted that the improvement in endwall cooling could outweigh the complexities associated with an angled interface between the combustor and the turbine.

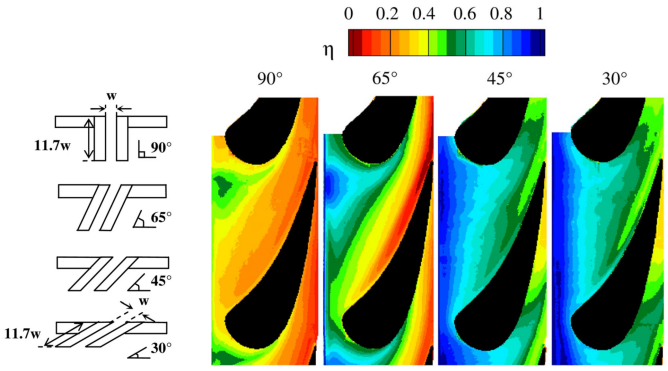

Figure 2.7: Endwall adiabatic effectiveness for different slot orientations (Thrift et al., 2013)

More experimental studies have been carried out using the same experimental facility, investigating the effect of different combinations of parameters, showing the effects of the slot geometry and orientation, the coolant blowing ratio, endwall contouring, as well as swirled leakage flow. The effects of each parameter were shown to vary depending on which other features were kept constant (Hada and Thole, 2011, Lynch and Thole, 2011, Lynch et al., 2013a,b).

Endwall contouring has also been proposed as a means of controlling secondary flow and heat transfer rates to the endwalls. Results from experimental studies by Thrift et al. (2011a,b) showed that it can have a significant effect, reducing heat transfer levels. Endwall contouring improved coolant coverage and adiabatic effectiveness for the slot cooling case, but it reduced coolant coverage from the film cooling holes, due to impingement and turning of the mainstream flow at the contoured endwall surface, showing that there is no universal solution to the endwall cooling problem.

The investigations of the effect of upstream slot cooling on heat transfer to the endwalls have highlighted the effect of secondary flow on the thermal flow field. As the presence of the gaps is inevitable, the leakage flow through them that prevents hot gas ingestion should be used to aid the turbine designer to maximize endwall cooling effectiveness through the optimization of the slot geometry and location.

2.3 Effect of Engine-Representative Inlet Conditions on the Aerothermal Field of a Nozzle Guide Vane

The main types of combustors used in gas turbine engines are the tubular (can) and the annular type, as well as a combination of the two, the cannular or tuboannular combustor. The choice of combustor depends on the particular engine requirements and aims to use the available space as effectively as possible. Therefore, in industrial gas turbines, where accessibility and ease of maintenance are the most important considerations, can combustors are frequently used. A discussion of the fundamentals of combustion can be found in Lefebvre (2010).

In modern gas turbines, lean, premixed combustors are used, where the fuel and air are mixed upstream of the combustor and burnt in an air-rich mixture to reduce flame temperature and reduce NO_x (Huang and Yang, 2009). In order to achieve that, swirl injectors are used to assist mixing and improve flame stabilization and combustion efficiency, resulting in lower peak combustion temperatures and therefore lower NO_x emissions. The flow at the exit of the combustor is therefore characterized by non-uniform distributions of pressure, temperature and velocity, resulting from the design of the combustor. The effect of the highly turbulent, swirling flow with a non-uniform temperature profile on the aerodynamic field and the heat transfer to the vanes is analysed through the review of experimental and numerical studies carried out.

2.3.1 Effect of Turbulence

The flow at the exit of the combustor is highly turbulent; early studies by Goldstein et al. (1983) and Goebel et al. (1993) measured turbulence and velocity profiles at the exit of the combustor. The turbulence intensity levels at the nozzle guide vane leading edge are currently $20 - 25\%$ (Han et al., 2013). It is important, however, to consider the turbulence spectrum at high turbulence intensity values. Turbulence intensity has an effect on the aerothermal field and has been the subject of numerous experimental investigations.

Ames and Plesniak (1997) studied the effect of inlet turbulence on the aerodynamic field in an experimental study conducted in a linear cascade. They found that high free-stream turbulence intensity affects the growth of the boundary layer and results in broader wakes. This was also found in the experimental study of Zhang et al. (2005) in a high speed linear cascade. They noted broader wake profiles on the suction side for increased turbulence intensity due to the earlier transition of the boundary layer, as well as increased aerodynamic loss. This effect of free-stream turbulence on boundary layer transition was reported by Radomsky and Thole (2002) who carried out detailed measurements on the boundary layer development on a large scale turbine vane for turbulence intensity levels of 19.5%.

An early experimental study by Blair (1983) showed the effect of turbulence on heat transfer on a turbulent boundary layer. The study was conducted on a heated flat plate placed in a large scale wind tunnel operating at engine-realistic Mach and Reynolds number. The increase of turbulence intensity from 0.25% to 7% resulted in an increase in heat transfer levels by approximately 20%.

Van Fossen et al. (1995) in an experimental study of inlet turbulence intensity and length scale on an elliptical leading edge found that inlet turbulence intensity generally augments heat transfer levels and this effect becomes stronger with decreasing length scale. Mehendale and Han (1992) experimentally investigated the effect of turbulence on the heat transfer on a film cooled leading edge. For this study, a blunt body with a cylindrical leading edge was placed on a low speed wind tunnel with a Reynolds number of 10^5 and turbulence intensity from $0.75 - 13\%$. The heat load of

the surface was found to increase with increased turbulence intensity. In the leading edge region, turbulence had a detrimental effect on cooling effectiveness for a low blowing ratio of 0.4, whereas the effect for higher blowing ratios of $0.8 - 1.2$ was not as pronounced. In that case, however, turbulence resulted in reduced film effectiveness on the surface downstream of the cooling holes.

Later studies investigated the effect of turbulence on the heat transfer to the vane, verifying the results of the early studies that were carried out on simplistic models. In an experimental study on a large scale, low speed cascade, Ames (1997) found that turbulence length scale has a significant effect on heat transfer on the stagnation region and the pressure surface of the vane. In a later study, Ames et al. (2003) showed that inlet turbulence, particularly with small length scales, shifts the boundary layer transition forward and results in increased heat transfer rates to the vane. The range of values tested was $0.7 - 14\%$ for the turbulence intensity and $0.7 - 8$ cm for the turbulence length scale. Nasir et al. (2009), in an experimental study on a high speed linear cascade at a Mach number of 0.75 and a Reynolds number of 10^6 found that the increase of free-stream turbulence intensity from 2% to 16% resulted in an increase in average heat transfer levels of 50% on the pressure side and 25% on the suction side of the vane.

2.3.2 Effect of Swirl

Although the effect of swirl on combustion and emissions has been thoroughly investigated (a comprehensive review of the literature can be found in Huang and Yang (2009)), its effect on the vane aerodynamics and heat transfer has not. One of the very few studies carried out was by Turrell et al. (2004), who conducted a numerical study of the flow in a high swirl, lean, premixed can combustor and the nozzle guide vane and compared their results against experimental data on nozzle guide vanes with film cooling obtained during development tests of an industrial gas turbine. Temperature sensitive paint on the vanes had indicated the presence of a rotating vortex core emerging from the combustor, that deflected the coolant tracks from the suction side cooling holes towards the hub of the vane. High temperature regions had also been found on the suction

side of the vane and on the hub endwall, close to the vane trailing edge on the suction side. The numerical analysis carried out predicted a swirling vortex core that approaches the vane leading edge at approximately 40% span height, stays close to the vane suction side and migrates towards the hub through the passage.

The presence of swirling flow at the vane leading edge causes a variation in incidence angle along the span. In an experimental study on a high speed linear cascade, Jouini et al. (2001) showed that the variation of incidence angle leads to increased aerodynamic loss and a variation in loading distribution on the leading edge region of the vane. The difference in vane loading also affects the secondary flow and associated loss as discussed in experimental work by Weiss and Fottner (1995) and Benner et al. (2004).

Qureshi et al. (2012a,b) performed experimental studies of aerodynamics and heat transfer on a vane and a rotor blade with highly aggressive swirl at angles up to $\pm 40°$, also supported by a numerical analysis. The experiments were carried out in the Oxford Turbine Research Facility (OTRF), a short duration high speed rotating facility with an engine scale high pressure turbine stage, operating at engine-representative conditions. In these studies, the high incidence angles were shown to have a significant effect on both the aerodynamic performance and the heat transfer to the vane and endwalls. Inlet swirl resulted in significant streamline divergence, particularly on the pressure surface of the vane and on the casing endwall, as shown in Figure 2.8. The loading near the hub and casing was significantly altered, as was the secondary flow structure. The change

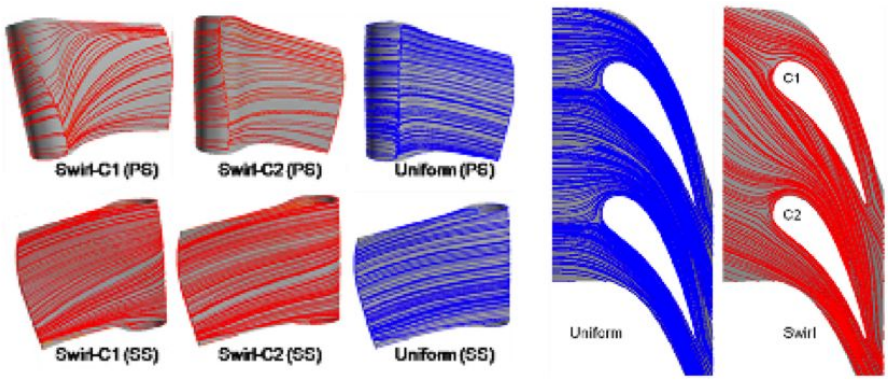

Figure 2.8: Streamlines on the vane surface and casing endwall with high inlet swirl (Qureshi et al., 2012b)

in the streamline pattern on the vane surface caused accumulation of boundary layer fluid, and the change in loading caused a change in surface velocity; these resulted in a significant change in heat transfer and Nusselt number on the vane surface with inlet swirl. The experimentally measured increase in Nusselt number with inlet swirl reached 25% on the vane endwall and was significantly higher for the vane surface near the hub endwall. The heat transfer augmentation reached 200% on the pressure side, and significant increase was seen on the vane suction side, particularly until mid-chord. The numbers varied depending on the relative position of the vane and the swirler. The divergence of the streamlines on both the vane surface and the endwalls has to be taken into account for the design of a cooling system that can perform effectively under these operating conditions. Heat transfer increase in the rotor varied from 7% to 40%, with higher values on the blade pressure side.

2.3.3 Effect of Temperature Non-Uniformities

The employment of discrete combustors results in temperature non-uniformities in the flow at the exit of the combustor. Due to high mixing, the temperature distribution in lean burn combustors has become more homogeneous, resulting in flatter temperature profiles; the temperatures near the endwalls are therefore increased compared to temperature profiles downstream of rich burn combustors. Detailed investigations into the effects of these hot spots on the aerothermal field have been carried out both numerically and experimentally.

One of the first experimental studies in low speed conditions was carried out by Butler et al. (1989), who introduced an inlet temperature distortion upstream of a turbine stage. This did not affect the flow field around the turbine vane, as it did not directly impact onto any of the vanes, but had a significant effect on secondary flow in the rotor, increasing the pressure side temperatures and reducing the suction side temperatures. In their numerical study, Rai and Dring (1990) obtained relatively good agreement with the experimental data by Butler et al. (1989), showing that computational tools can successfully capture the main flow features and provide a valuable tool

for the turbine designer. A review of experimental and numerical studies on migration of these hot streaks from the combustor through the turbine was carried out by Dorney et al. (1999), who highlighted the importance of understanding their impact on secondary flow and heat transfer to the vane surfaces.

Later experimental studies under more engine-representative conditions showed that the hot streaks have a significant impact on heat transfer on the vanes and endwalls. Povey et al. (2007) conducted an experimental study in an annular transonic rotating turbine facility that matches engine operating conditions. When the hot streak was aligned with the vane leading edge it caused a significant increase in heat transfer levels on the mid-span of the vane suction side, whereas when it was aligned with the passage it resulted in a marginal decrease. The pressure side of the vane was not affected by this. Heat transfer to the endwalls was decreased for both temperature profiles compared to the baseline case, due to the lower temperatures near the endwall. Barringer et al. (2009a) studied different pressure and temperature profiles on a full scale, fully annular turbine vane cascade in a high speed experimental facility that matches engine Mach and Reynolds number. They found significant differences in local heat transfer levels to the vanes and endwalls between the different cases. This was attributed to the effect of the inlet pressure profile that influences secondary flow formation which in turn affects the migration of the streamlines through the passage and therefore the local temperature that drives heat transfer.

The migration of hot streaks through the turbine has also been the subject of various numerical studies. Khanal et al. (2013) showed that the combination of a hot streak and inlet swirl had a significant effect on both aerodynamic loss and heat transfer. This effect varies depending on the alignment of the hot streak relative to the vanes, as well as the orientation of the swirl, that results in different migration patterns of the hot streak through the NGV passage, as shown in Figure 2.9.

Numerous studies have also focused on the effects of hot streaks on the rotor blades, as the higher relative momentum of the hot flow causes gradients in relative stagnation pressure, which are a source of additional secondary flow. Hot gases are found to migrate towards the pressure

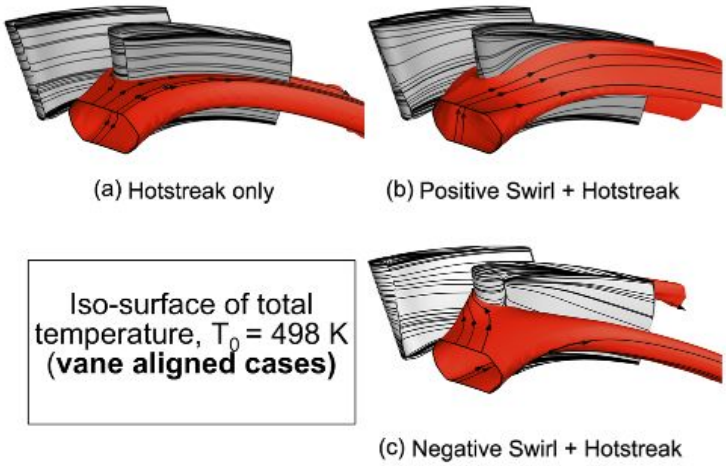

Figure 2.9: Hot streak migration through NGV passage without and with inlet swirl (Khanal et al., 2013)

side and then towards the endwalls, and cold gases towards the suction side. This effect was first observed in experimental studies by Butler et al. (1989) and verified by Roback and Dring (1993). Experimental and computational studies by Ong et al. (2010) and Ong and Miller (2012) showed the detrimental effect of unsteady hot streak migration on the rotor endwall cooling. Further studies showed the effect of the flow field of the stator on the migration of the hot streak (Basol et al., 2012) and the increase of the heat load on the blade tip (Jenny et al., 2012).

The turbine components were typically designed for uniform inlet temperature, which is the peak temperature of the inlet to the vane, causing an overprediction of the cooling requirements. As highlighted by many of the above researchers, a good understanding of hot streak migration patterns, which can be developed from integrated combustor and turbine studies, would greatly benefit the turbine cooling system design, allowing a better utilisation of cooling flow.

2.3.4 Effect of Mach and Reynolds Number

Reynolds number affects the boundary layer state and transition, which in turn has a strong effect on the heat transfer rates to the vane and endwall surfaces. A limited number of studies on the effects of Mach number on heat transfer and film cooling have been carried out, as experimental facilities are designed to operate either at high speed or at low speed conditions. In the majority of

high speed experimental studies carried out, the variation of Mach number also results in variations in Reynolds number, masking any effect of Mach number.

One of the few studies where Mach and Reynolds number were varied independently was an experimental study in a high speed linear cascade by Corriveau and Sjolander (2004) on the effect of loading on the vane performance for different Mach and Reynolds numbers. For all Mach numbers ($0.6 - 1.05$), a lower Reynolds number resulted in higher loss. A small effect of Mach number on loss was noted for subsonic flow (for a constant high Reynolds number), which varied depending on the airfoil geometry. The effect of vane loading on the loss was more pronounced in the transonic region and was small for Mach numbers of 0.6. Perdichizzi (1990) conducted an experimental study on the development of secondary flow with different Mach numbers from 0.32 to 1.38. Reynolds number varied from 0.35×10^6 to 1.6×10^6 respectively, therefore the effects noted in the study are probably caused by the change in Reynolds number and can certainly not be attributed solely to the change in Mach number. The increase in Reynolds (and Mach) number caused the secondary flow structures to be more confined to the endwall region. The passage vortex and the loss core on the wake moved closer to the endwall. Flow angle deviation was also affected, as the increase in flow velocity reduced the maximum underturning and overturning angles. Furthermore, the net secondary loss was found to increase with flow velocity for Mach numbers in the region $0.5 - 0.9$. An experimental study on a turbine vane endwall in a low speed cascade (Kang et al., 1999) investigated the horseshoe vortex in the leading edge region for two different Reynolds numbers. At an exit Reynolds number of 6×10^5 (based on the true chord), the vortex was found to be stronger and more turbulent. The increase of Reynolds number to 1.2×10^6 caused the passage vortex to lift off the endwall, decreasing the static pressure distribution and altering the endwall surface heat transfer patterns.

Kang et al. (1999) also studied the static pressure distribution and heat transfer on the vane endwall and noted the effect of Reynolds number on heat transfer to the vane. The flow field characteristics were found to change with Reynolds number; at the lower Reynolds number ($6 \times$

10^5), the leading edge vortex was shown to be stronger and more turbulent and the separation point upstream of the leading edge moved closer to the vane. At the high Reynolds number (1.2×10^6), the secondary flow was stronger, causing the horseshoe vortex to lift off, decreasing the static pressure on the endwall and enhancing heat transfer near the trailing edge of the vane. A high speed experimental study by Nasir et al. (2009) found that an increased Reynolds number induced earlier boundary layer transition on the vane suction side and increased heat transfer levels throughout the vane. The Mach numbers used in that study were 0.55, 0.75, and 1.01, corresponding to Reynolds numbers of 0.9×10^6, 1.05×10^6 and 1.5×10^6. A numerical study by Wheeler et al. (2011) showed a dependence of heat transfer on Mach number for flow over a blade tip. The Mach number ranged from 0.1 to 0.98 and different vane thickness was used for the different Mach numbers to obtain the same loading. The effect of Mach number was opposite than expected, with higher Mach number resulting in lower heat transfer rates. The variation of the geometry and the particular flow field over the blade tip, however, do not allow direct links to be made to the nozzle guide vane case.

Experimental measurements of the effect of free-stream Mach number on film cooling were carried out by Gritsch et al. (1998) and Liess (1975) on single cooling holes and a row of cooling holes respectively. They both reported no significant effect of Mach number on the film cooling effectiveness for subsonic Mach numbers.

The majority of studies carried out under high speed conditions do not allow conclusions to be made as to whether Mach number has an effect on aerodynamics and heat transfer. Furthermore, the state of the inlet boundary layer is not distinguished from the variations in Reynolds and Mach number in these studies, and this also has a significant effect on the secondary flow development. A strong effect of Reynolds number on the flow field and heat transfer has been shown in numerous studies, and achieving a representative Reynolds number is a priority for experimental studies. The limited data on the effect of Mach number makes it a parameter which should also be considered in experimental studies, as it may depend on the particular geometry. After all, a representative

flow field in a three-dimensional passage can be more easily created using a scaled geometry at the correct Mach number.

2.4 Considerations for Experimental Studies

2.4.1 Design Parameters of an Experimental Facility

Experimental facilities are split into three categories depending on their running time: continuous facilities that run for several hours, intermittent facilities with a running time that ranges from several seconds to a few minutes and transient facilities with a running time of less than 2 seconds. The main criteria for choosing the type of the operating facility, as identified by Sieverding (1993), are the desired level of flow simulation, the financial needs for installation and operation, and the requirements of measurement and data acquisition techniques that will be used.

In academic environments, continuous low speed cascade facilities are commonly used for aerodynamic studies, but their inability to account for Mach number effects makes them unsuitable for the investigation of high speed flows. For such studies, the use of intermittent facilities is widespread, as the operating costs of equivalent high speed continuous facilities are prohibitively large. The longer running times of intermittent facilities compared to transient facilities allow the execution of more detailed studies of the aerodynamic flow field, while still allowing the investigation of heat transfer under engine-representative Mach and Reynolds numbers.

In order for the results of the experimental investigation to be applicable to the real engine performance, similitude between the scaled model and the engine must be achieved. The relevant parameters for cascade aerothermal studies will be discussed here; the theoretical background of dimensional analysis can be found in Dixon (2005). Similitude requires geometric similarity between the vanes of the model and the engine, matching geometric parameters, which can be achieved by applying a single scaling factor to the engine geometry. In order for the operating conditions of the experimental model to be dynamically similar to the engine conditions, the

Reynolds number, turbulence intensity, and Mach number should be matched (Fottner, 1993a). The first two will account for viscous effects, as they influence boundary layer development and transition, which in turn affects both the aerodynamic flow field and the heat transfer mechanisms, and the Mach number will account for compressibility effects. A discussion of cascade flow parameter simulation can be found in Fottner (1993a).

Other similarity parameters that are important for heat transfer studies are the Prandtl number, which is the ratio of the kinematic viscosity of the fluid to its thermal diffusivity, the Eckert number, Ec, which is the ratio of the kinetic energy of the fluid to its enthalpy, and the mainstream-to-wall temperature ratio. The Prandtl number is a property of the fluid that changes with temperature and is a very weak function of pressure. Due to the temperature difference between the engine conditions and the experimental studies which are often carried out at ambient temperatures, the Prandtl number of the working fluid in the experimental studies is approximately 4% lower compared to that at engine conditions. The Eckert number and the mainstream-to-wall temperature ratio are often not matched to the engine; discrepancies in the temperature ratio and the Eckert number, assuming both γ and Mach are matched, can be corrected for using empirical correlations, a summary of which can be found in Abu Talib (2003).

One of the main aims of the design of a linear cascade is the establishment of periodic flow. This depends on the number of passages in the cascade, which has to be such that the flow field in the measurement region will not be affected by the addition of further passages to the cascade. However, the number of passages that can be used is limited by the dimensions of the experimental facility and the mass flow rate requirements in order to achieve the desired operating conditions. The size (scaling) of the blades is therefore also a factor, and the blade chord should not be smaller than 60 mm (Fottner, 1993b), for measurement accuracy.

2.4.2 Aerodynamic Measurement Techniques

The main techniques used for the measurement of the aerodynamic parameters of the flow are thermal anemometry and laser anemometry, that measure instantaneous fluid velocity, and the use of pressure probes that measure the total and static pressure and can also be used to calculate the velocity and the flow angle. Thermal anemometers are relatively inexpensive in comparison to laser anemometry systems but require repair and re-calibration very often and significant time investment to provide high quality results.

Pressure measurements can be obtained using either a steady state system, where any pressure fluctuations are averaged out due to the time response of the transducers and the data acquisition system, or an unsteady system, using fast response transducers to obtain time-resolved data. In a steady state system, the transducers that convert the pressure into voltage are located in a controlled environment, away from vibrations and temperature fluctuations. The tubing between the measurement location and the transducers, usually in the order of a few meters long, dampens any pressure fluctuations. Static pressure tappings are commonly used to obtain static pressure data with minimal disruption to the flow. The important parameters to providing an accurate reading are the diameter of the tapping, which should be significantly smaller than the thickness of the boundary layer above the tapping, the orientation of the hole, which must be perpendicular to the streamlines of the flow at each location, and the geometry of the hole. Angled or rounded edges can lead to underprediction or overprediction of the static pressure, respectively.

Single and multiple hole probes are used to measure static and total pressure and flow angles in a fluid stream. For this, the size of the pressure holes and the design of the probe should be chosen so as to capture the phenomena under investigation, and the effects of frequency response, local Mach and Reynolds numbers, and blockage (more important in transonic flows) should be taken into consideration. In general, smaller probes provide increased accuracy, but this results in reduced mechanical integrity and slower response times. Very small holes can also easily be blocked in dirty environments. Fast response probes where the pressure tapping is replaced

by a miniature pressure transducer for the measurement of aerodynamic loss (Kupferschmied et al., 2000, Pfau et al., 2002) and entropy (Mansour et al., 2008) are used when a high frequency response is required.

2.4.3 Heat Transfer Measurement Techniques

A range of heat transfer measurement techniques have been developed for the determination of surface temperature, heat flux and cooling effectiveness. As with all experimental studies, the method used mainly depends on the individual application, the capabilities and the required type of results.

A very commonly used technique, developed in the Osney Laboratory, employs thin film gauges. A presentation of the theory of thin film gauges can be found in Doorly and Oldfield (1987). This technique was used in early studies by Schultz and Jones (1973) and is very well suited to environments with no optical access to the test surfaces and has therefore been established for tests in rotating facilities (Qureshi et al., 2010). Many researchers use techniques based on the mass/heat transfer analogy to determine the local heat transfer distribution on a surface, which provide higher resolution results. The naphthalene sublimation technique used by Goldstein and Cho (1995) and other researchers can determine wall effectiveness in film cooling tests and has also been used for internal cooling experiments. The ammonia-diazo technique is essentially a flow visualization technique and was first used by Friedrichs et al. (1996) for quantitative cooling effectiveness measurements. The determination of heat transfer coefficient on the surface would require a different technique to be applied. Pressure sensitive paint techniques have been used by Zhang et al. (1999) to measure film cooling effectiveness, and require the use of a gas different than the mainstream for the cooling flow.

Heat transfer measurements are very commonly obtained using optical techniques, which are non-intrusive and therefore require a visualization mode, using a digital camera to record the results of the experimental tests. A full picture of the surface heat transfer can be obtained using

the thermochromic liquid crystal (TLC) technique. A review of the use of TLCs for heat transfer measurements can be found in Ireland et al. (1999) and in Gillespie et al. (1998) and a detailed description of this technique is provided by Ireland and Jones (2000). One of their main limitations is that the crystals typically used in experiments can capture a change in temperature of up to 20 K; for wider temperature differences a combination of more types of crystals is required. Another disadvantage is that they cannot be used for high heat fluxes, above $2000\,\mathrm{W/m^2}$. The liquid crystal method is very commonly used to measure heat transfer in internal cooling passages.

Another method that can provide detailed heat transfer distributions is the infrared (IR) thermography technique, that has grown in popularity with the development of high resolution digital cameras. This technique is capable of providing full surface temperature maps and can be used in both low speed and high speed experiments. Ekkad et al. (2004) advocated the use of the IR thermography, as it only requires a single transient test for the determination of the heat transfer parameters and it can capture the initial temperature distribution. The accurate definition of the initial temperature distribution with the use of IR thermography reduces experimental uncertainty in comparison to the TLC for film cooling studies, and can account for non-uniform initial model temperatures. The infrared thermography method has been widely used in many recent studies (Lynch and Thole, 2011, O'Dowd et al., 2010) and can also be used to determine the film cooling effectiveness. The methodology followed to obtain the surface heat transfer coefficient distributions through infrared thermography is presented in detail in Chapter 3.

2.5 Integrated Combustor and Vane Studies

The effects of inlet flow distortion and disturbances from the combustor on the interface with the turbine have been investigated by various researchers. However, very few studies have been carried out to analyse their combined effects on vane and endwall aerothermal performance.

The cooling and aerodynamics of the nozzle guide vane are affected by the complex flow interactions between the hot gas and the cold coolant flow. In industrial gas turbines with can

combustors, the vane leading edge is also exposed to wake disturbances from the upstream combustor wall. The leading edges of the nozzle guide vanes after the combustor are currently cooled using a showerhead arrangement of film cooling holes. The effect of the combustor wall on the vane leading edge film cooling was numerically investigated by Rosic and Klostermeier (2009) and Rosic et al. (2011). In both cases, the interface was modelled using a flat plate for the combustor wall and a cylindrical leading edge downstream, as shown in the top left of Figure 2.10.

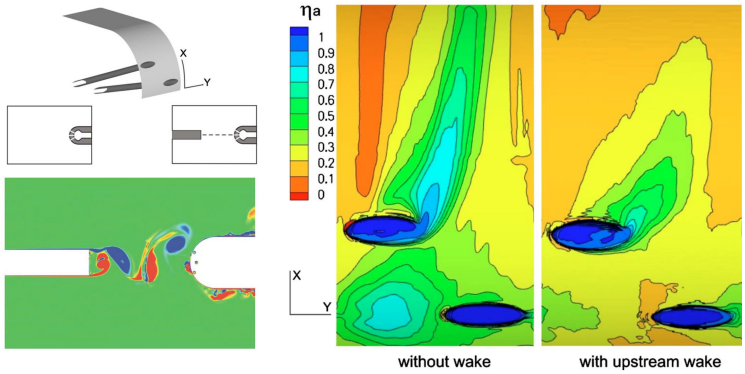

Figure 2.10: Computational flow domain of the cylindrical leading edge with upstream plate (top left), y-vorticity contours at the cylindrical leading edge (bottom left) and cooling effectiveness on the vane surface without (centre) and with upstream wake (right), from Rosic et al. (2011)

Contours of y-vorticity at the cylindrical leading edge are shown in the bottom left of the figure and contours of adiabatic cooling effectiveness on the the vane surface are shown in the right part of the figure. It can be seen that the combustor wall can have a significant effect on the vane surface cooling, as vortices shed by the wall destroy the coolant film that forms on the vane surface. This results in significantly reduced cooling effectiveness in the case with upstream wake (right) compared to the case without wake (centre). The effect of the wakes from the upstream combustor wall on the vane leading edge film cooling was further analysed in numerical studies by Mazzoni et al. (2014). Rosic et al. (2011) suggested that with the minimization of axial distance between the combustor and the vane, a continuous slot could be used at the interface to provide uniform cooling to the vane.

After highlighting the detrimental effect of disturbances shed from the combustor wall trailing edge on the vane leading edge cooling, Rosic et al. (2011) introduced a radical concept of inte-

grating the combustor trailing edge with the nozzle guide vane row to eliminate this effect and improve the overall performance of the components. Figure 2.11 shows the total pressure distribution downstream of the vane trailing edge for the original case with separated combustor wall and vane and for the shielded case with the integrated combustor wall and vane. The total pressure distribution was almost identical between the two cases, with a marginally smaller loss core in the case of the shielded vane.

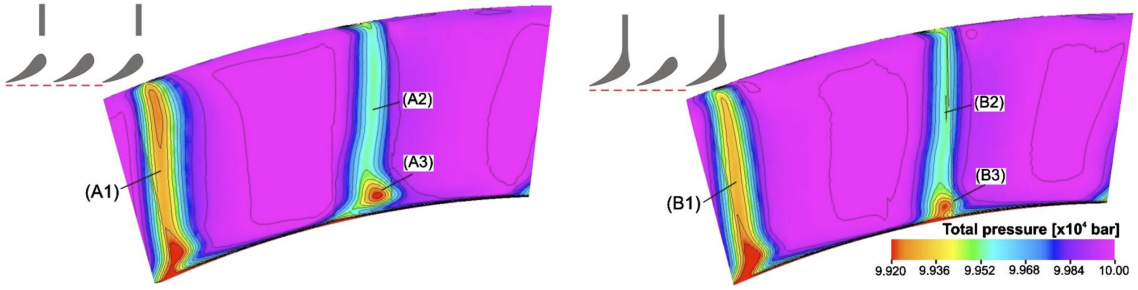

(a) Separated combustor wall and vane (b) Integrated combustor wall and vane

Figure 2.11: Total pressure distribution downstream of the vane TE, Rosic et al. (2011)

It was then argued that the integration of the two parts could allow the removal of the vanes and the use of the combustor wall to provide the required turning for the downstream rotor, without detrimental effects on the aerodynamic performance. The work by Rosic et al. (2011) focused on describing the new concept and did not address issues related to the high aerodynamic loads of the integrated design or the cooling requirements for the extended combustor wall.

2.6 Conclusions

The flow field in a nozzle guide vane passage is characterized by secondary flow. As the incoming endwall boundary layer meets the vane leading edge, vortical structures arise and migrate through the passage, affecting heat transfer to the vanes and endwalls. A good understanding of this behaviour is required to design a good and efficient cooling system for the vane.

The flow field of the vane passage is further complicated by the combustor exit flow, which is characterized by increased turbulence intensity and swirl levels, and non-uniform temperature

distributions. The flow field downstream of the combustor affects the development of secondary flow and the heat transfer to the endwalls, highlighting the need for integrated studies that will enable the researcher to develop a good understanding of the governing physical phenomena. Reynolds number has been shown to have a significant effect on the state of the boundary layer and heat transfer rates to the vanes and endwalls, as does the inlet boundary layer itself, whereas the effect of Mach number is unclear.

Numerous researchers have investigated the effects of the combustor exit flow on the nozzle guide vane aerothermal flow field, both numerically and experimentally. While numerical studies have the advantages of enabling the variation of flow parameters, producing quick results, and the investigation of new geometries and concepts, they always need to be validated against experimental data. In experimental studies, compromises are always required as to how close the experimental operating conditions are to the real engine conditions. Furthermore, the study of the interface between the combustor and the turbine can lead to the development of novel concepts and the optimization of the geometric features that are present there, resulting in improved engine performance.

Heat transfer levels are still not easily and accurately predicted by numerical studies, therefore detailed experimental data is required in order to investigate the effect of the various parameters of interest on heat transfer. Matching Reynolds number and the non-dimensional pressure field is very hard to achieve at low speed; engine-representative data can more easily be obtained under high speed conditions. A new experimental facility presented in the next chapter enables the conduct of high speed experimental studies on the combustor-turbine interface, offering a modular environment where the effect of varying geometric and flow parameters can be investigated and novel concepts can be validated under engine-representative operating conditions.

Chapter 3
Methods for High Speed Experimental Studies

The MHI Cascade is a high speed experimental facility designed and built to investigate combustor and turbine aerothermal interactions under engine-representative conditions. The facility is described in this section; an overview of the design and its capabilities is given, as well as details about the instrumentation setup.

Preliminary research and the definition of the concept of the facility were carried out by Dr Budimir Rosic. A conceptual design of the high pressure parts of the facility and the test section was done by Dr Vasudevan Kanjirakkad. The design of the high pressure parts of the facility was done by A J Metal Products Ltd. The design of the parts of the test section inside the test plenum was done by the author and the components were manufactured by the technicians in the Southwell Laboratory. The inlet pressure control system was designed by Dr Roderick Lubbock. The LabVIEW program for the operation of the probe traverse system was written by Wes Ramm. The DSA system was assembled by Dr Kanjirakkad and the pressure transducer boxes by Dr Salvador Luque. The LabVIEW program for the heat transfer measurements and the post-processing routine was written by Dr Luque. The commissioning of the experimental facility after its installation was carried out by the author and Dr Luque.

The features of the facility described in this work were designed to provide the maximum possible flexibility for experimental studies; not all capabilities of the facility are used in this thesis but they are presented here for completeness and to assist future users, as this is the first thesis in the laboratory using this facility.

The configuration of the heavy duty gas turbine studied, with 20 can combustors and 40 vanes, results in the presence of a combustor transition duct upstream of every pair of vanes, as discussed

in previous chapters. The experimental facility is a high subsonic, blow-down linear cascade with two combustor transition ducts modelling the transition between the combustor and the turbine and four vane passages and is presented in the following sections.

3.1 Description of the Experimental Facility

A schematic view of the facility is presented in Figure 3.1 and the facility itself is shown in Figure 3.2. The facility comprised an inlet pressure control and safety system, followed by an

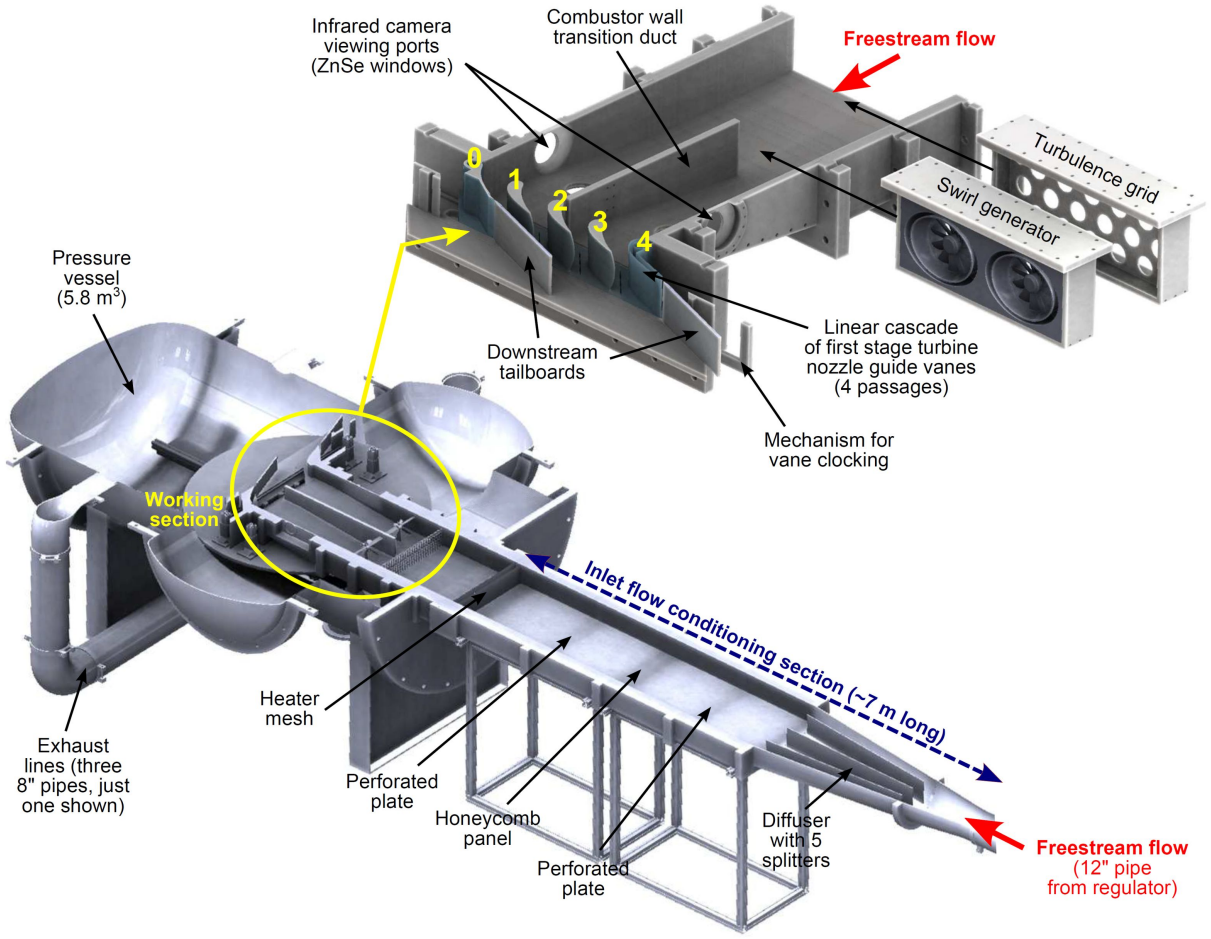

Figure 3.1: Schematic view of experimental facility including details of the working section (Luque et al., 2015)

inlet flow conditioning section to ensure uniform distribution of the flow at the inlet to the cascade. The working section was enclosed in a cylindrical test plenum with a diameter of 1.6 m. The

test plenum had a main door at the back and two side doors that allowed access to the working section. A combustor simulator unit followed the flow conditioning section, consisting of a heater mesh upstream of the test plenum and turbulence and swirl generators within the plenum. The two transition ducts and four vane passages completed the working section. The parts of the experimental facility are described in detail in the following sections.

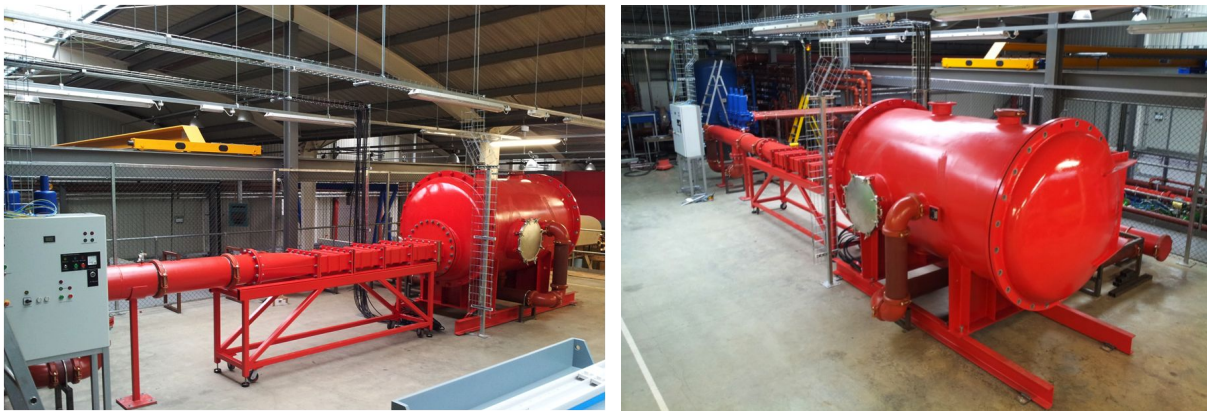

(a) Front view (b) Back view

Figure 3.2: View of experimental facility

3.1.1 Pressure Control System

Compressed air at 400 psi (27.6 bar) and ambient temperature was supplied to the experimental facility from two $30\,\mathrm{m}^3$ storage tanks, located outside the laboratory building. A series of valves in the inlet line were used for pressure control and to ensure safe operation: a 4" mechanical gate valve and two 4" ball valves. The first two were used to shut off the air supply between runs; the last ball valve was fitted with a pneumatic actuator that could open and close the valve slowly (with an opening time of up to 20 s) at the beginning and end of each run. A pressure regulator was used to maintain the inlet pressure at a constant level of 14 barg for the duration of the run, while the air supply pressure was decreasing from 27.6 barg. An orifice with a diameter of 45 mm was installed downstream of the regulator. This was constantly choked during operation and fixed the mass flow rate through the facility at 4.8 kg/s. The upstream pressure control system is shown in Figure 3.3.

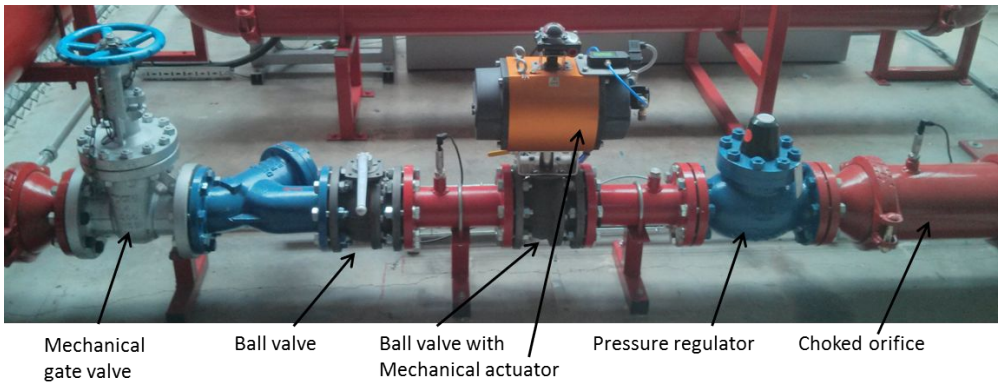

Figure 3.3: View of pressure control system of the experimental facility

In the event of failure of the pressure control system or blockage of the exhaust system which would cause pressure to build up in the facility, a number of safety features were installed to ensure safe operation, and the facility was designed and tested in accordance with the European Union (EU) safety requirements for pressure vessel design (Pressure Equipment Directive 97/23/EC).

3.1.2 Inlet Flow Conditioning System

A divergent duct allowed for a transition from the circular duct coming from the control system to a rectangular duct that would model the combustor ducts upstream of the working section. After the control system, the flow went through a series of conditioning units, in a 7 m long section, as shown in Figure 3.4. This consisted of five diffuser plates in the diverging duct, a perforated plate, a honeycomb flow straightener, and a second perforated plate. The rectangular ducts were significantly reinforced to prevent their deformation during operation and were supported by a trolley placed underneath them.

3.1.3 Heater Mesh

A fast response heater mesh, based on the concept introduced by Gillespie (1996) and shown in Figure 3.5, was installed to provide the required step change in inlet temperature for heat transfer studies (discussed in section 3.5.2). It consisted of a woven steel wire mesh, placed in crossflow, and soldered to brass bus-bars, through which electrical power could be dissipated to the mesh

Figure 3.4: Flow conditioning unit

and provide a step change in the temperature of the incoming air flow. Tufnol plates were used to provide insulation and support for the mesh and the upstream filters, which ensured no dust particles in the air flow would impact upon the mesh. The details of the heater mesh are shown in Figure 3.5(a).

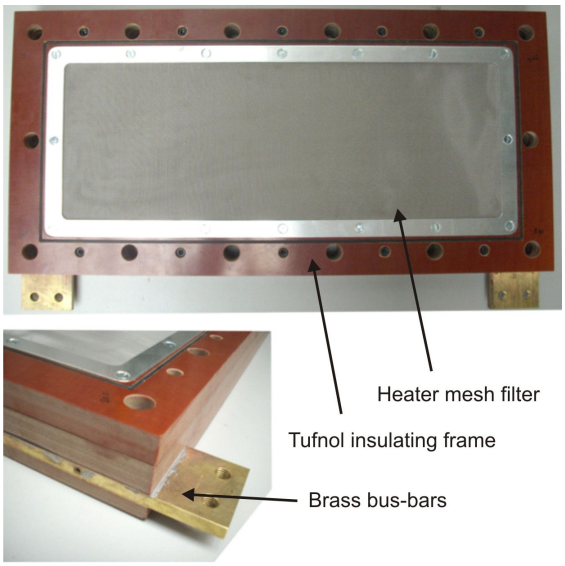

(a) Heater mesh details

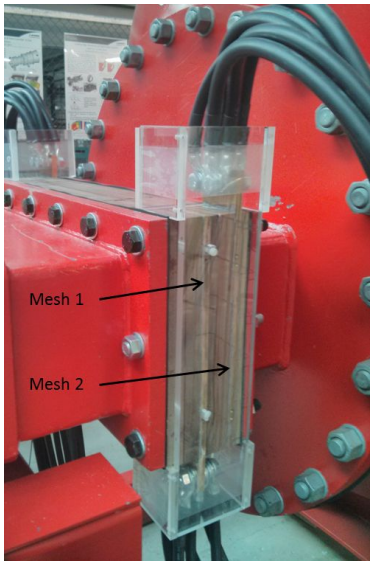

(b) Two stage heater mesh installed in the experimental facility

Figure 3.5: Fast response heater mesh

The main design parameter of the heater mesh is the diameter of the steel wires. This defines the electrical resistance and therefore the electrical current through the wires which in turn governs the temperature rise achieved. The temperature rise through the mesh is a function of the mass flow rate and the power dissipated through the mesh (equation 3.1). The maximum voltage applied by

the power supply unit is 115 V, resulting in currents of the order of 1300 A. However, due to losses in the power supply system, the voltage measured in the facility was reduced by approximately 25%. This reduced the maximum possible temperature rise in the facility from 30 K to 25 K (for $\dot{m} = 5$ kg/s, $c_p = 1005$ J/kgK). The design of the heater mesh was done by the author. A later heater mesh design, realized by Dr S Luque, had the voltage split between two meshes with $280\,\mu$m wires installed in series, as shown in Figure 3.5(b), to reduce the electrical current through the wires, while providing a temperature rise of $25°$C. The open area fraction of the mesh was 36%.

$$P = V \cdot I = \dot{m} \cdot c_p \cdot \Delta T \tag{3.1}$$

The time constant, τ, of the temperature rise of the wires as electric current is driven through them can be calculated using the experimental correlation derived by Gillespie (1996), equation 3.2, where V is the flow velocity. This resulted in a time constant of 2 ms with a flow velocity of 81.09 m/s through the throat of the mesh (for $P_0 = 1.6$ bar, $T_0 = 280$ K and a corrected flow area taking into account the open area fraction of the mesh).

$$\tau = 0.111 \cdot V^{0.914} \tag{3.2}$$

The correct design of the heater mesh is very important, as any manufacturing imperfections or dust particles impacting upon the mesh will inevitably lead to its failure. Round holes were cut around the edges of the mesh to relieve the electrical stress on the mesh; mesh failure was often due to a hot spot that originated at one of the round cuts propagating across in a straight line, cutting the mesh in two. A detailed discussion on heater mesh design and performance can be found in Gillespie (1996) and in Luque (2012).

3.2 Determination of Design Parameters of the Experimental Facility

As described in Chapter 2, some of the main considerations regarding linear cascade design involve the scaling of the cascade and the setup of flow periodicity. This section presents the numerical studies carried out to determine the basic parameters of the cascade during the preliminary design process. Initial studies were done on the datum cascade geometry, focusing on the definition of the vane profile to be used, the size of the vanes and the test section, and the establishment of flow periodicity. Further studies on flow periodicity were done for different vane clocking positions. These studies ensure that the design parameters chosen allow the establishment of periodic flow in the facility and that the design operating conditions are representative of those of the engine.

Preliminary numerical studies for the selection of the vane profile to be used in the experimental facility and the scale of the vanes were conducted using the structured flow solver TBLOCK, developed by Prof J. Denton. A structured, multi-block mesh was generated by the flow solver using user-specified parameters for the mesh density and spacing. The turbulence modelling in TBLOCK is a simple mixing length model; the mixing length is proportional to the distance from the nearest solid wall, and the wall shear stress is obtained from wall functions. A single vane passage was modelled in these studies. Subsequent numerical studies were carried out using ICEM CFD for the generation of the mesh, to allow the representation of more complex geometries and the flow through the cascade was modelled numerically using commercial software Ansys FLUENT v13, as will be discussed in section 4.3. These studies were carried out using uniform total pressure and total temperature at the inlet and uniform static pressure at the outlet.

3.2.1 Definition of Vane Profile

The flow through a single vane passage with periodic boundaries was modelled using TBLOCK. A simple structured H-mesh was created in TBLOCK, as shown in Figure 3.6. The profile of the vane in study is seen in Figure 3.6(a). The inlet stagnation pressure and temperature and the outlet static pressure were specified. In linear cascades, a two-dimensional blade profile is often used, typically the mid-span profile as this is the region of interest in most studies, extruded to the blade span. For the purpose of this study, three cases were compared:

- Flow through an annular cascade (with a 3D vane profile) simulating the engine geometry
- Flow through an infinite linear cascade with a 3D vane profile
- Flow through an infinite linear cascade with a 2D vane profile

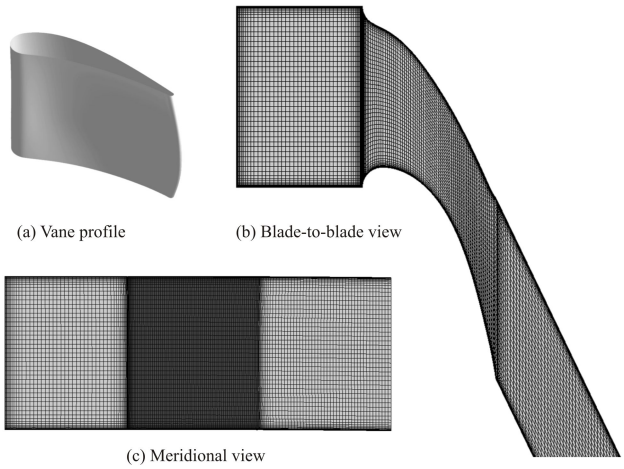

Figure 3.6: 3D Vane profile and computational mesh

In the second case, the vane profile was created in two ways; by unwrapping the cylindrical endwalls to linear planes and by projecting the hub and tip sections to the linear endwalls. The comparison of the results from these two profiles showed no difference; this is thought to be due to the very high hub radius of the vane. It is noted that in all cases the vane profile had a thick trailing edge, as in the engine, but was used without trailing edge cooling (and without a slot).

The surface Mach number distribution for the three cases at 10%, 50% and 90% span is compared in Figure 3.7. The 3D profile in a linear cascade matched the engine 3D geometry better than the 2D profile in a linear cascade. Mach number was matched at the mid-span between the annular engine geometry and the rig 3D profile geometry. At the hub it was reduced by 10% and at the tip increased by 10%. This was caused by the radial pressure gradient in an annular cascade and the different vane pitch from hub to tip.

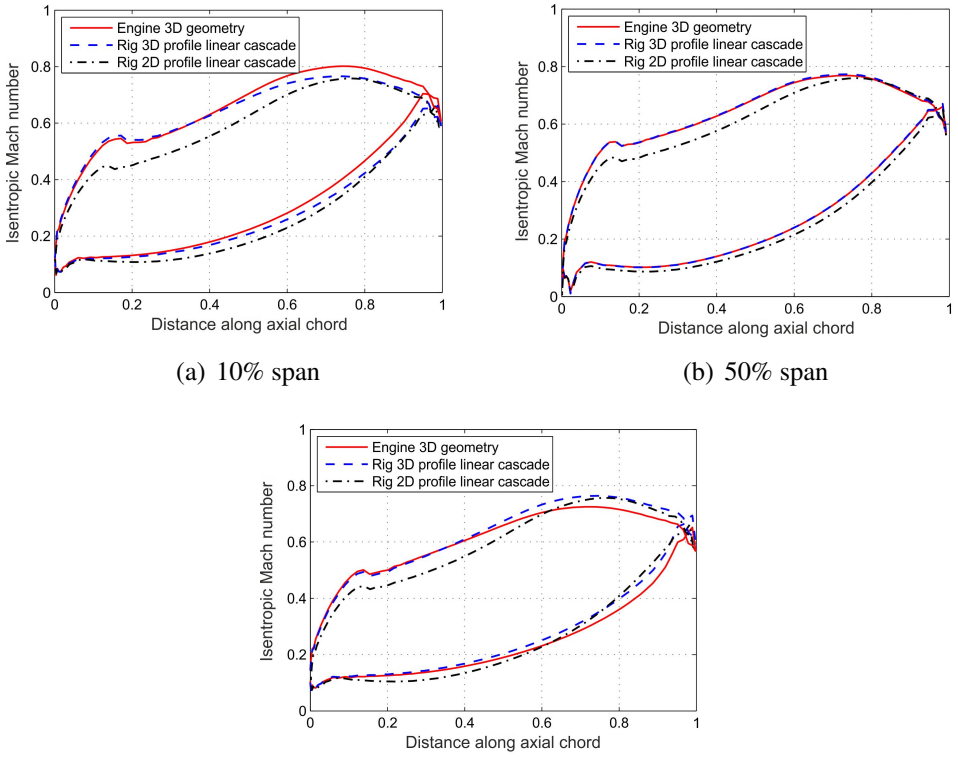

(a) 10% span

(b) 50% span

(c) 90% span

Figure 3.7: Isentropic Mach number distribution on the vane surface

The yaw angle and total pressure loss coefficient 17% of the axial chord downstream of the vane trailing edge are presented in Figures 3.8(a) and 3.8(b). The comparison of the results from the three cases showed that the use of a 3D vane in the linear cascade provided the best agreement to the real engine annular geometry. In addition, it gave better matching of the yaw angle and the downstream total pressure profile than the 2D vane with the mid-span profile. Since the vane is not highly three-dimensional, the use of a 3D profile is more feasible in a linear cascade, and it can give a better representation of the spanwise distribution of the turning of the flow and of the

secondary flow structures developing in the passage. In addition, it allows the testing of cooled vane designs with minimal modifications; a different vane can be tested without the need to modify the geometry of the internal cooling system and reposition the cooling holes.

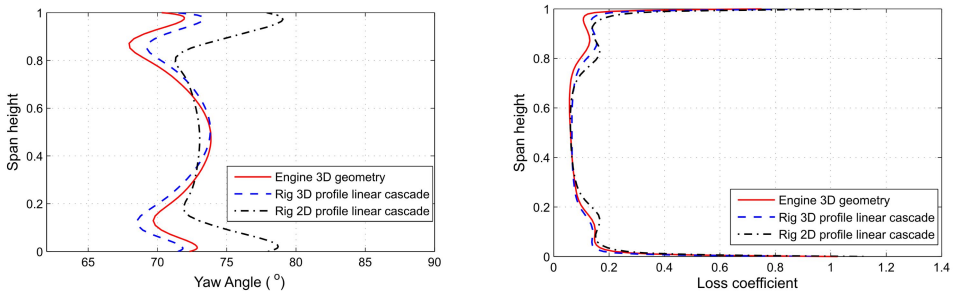

(a) Yaw angle (b) Total pressure loss coefficient

Figure 3.8: Spanwise distributions downstream of the vane trailing edge

3.2.2 Vane Scaling

In order to achieve flow similarity in an experimental test, the non-dimensional numbers characterising the flow (Reynolds, Mach, turbulence intensity and length scale) should be matched between the engine and the test case (Fottner, 1993a). Reynolds number has been found to affect secondary flow development, boundary layer transition, and surface heat transfer distribution (section 2.3.4), whereas the effect of Mach number is unclear. It is often not easy to match the Reynolds number and the non-dimensional pressure field to the engine with experiments run at low speed conditions. However, conducting experiments at high speed conditions allows the recreation of a more representative flow field through the achievement of a high Reynolds number.

The air supply in the laboratory limits the running time, which depends on the mass flow rate through the facility. With matched exit Mach number and set exhaust pressure, the mass flow rate depends on the cross-sectional area of the cascade, which in turn is defined by the scaling factor of the cascade and the number of vane passages. The vane downstream of the combustor wall was at the centre of the cascade and an even number of vane passages was required to allow the transition

duct to be modelled. In addition, the available power supply to the heater mesh imposes a limit to the mass flow rate through the heater mesh in order to achieve a sufficient temperature rise.

Initial calculations were undertaken using the isentropic flow equations that relate the total and static pressures, temperatures, and densities to the Mach number and the ratio of specific heats, γ. These were used in conjunction with the known geometric parameters of the blades to determine the operating conditions of the engine and the facility, including the pressure ratio, the mass flow rate and the Reynolds number, for a range of Mach numbers and vane sizes. The calculations for the engine conditions predicted a Reynolds number (based on the true chord) of 5.9×10^6 and an exit Mach number of 0.62. A mass flow rate of approximately 5 kg/s in the cascade resulted in a running time of the facility between 90 and 120 seconds. Calculations for the cascade showed that the use of four vane passages allowed for a Reynolds number above 10^6, where the flow is most likely to be turbulent (Miller and Denton, 2012), and an exit Mach number that could be matched to that of the engine, while maintaining a large enough vane size. Studies in low speed cascades (Kang et al., 1999, Thrift et al., 2011a) suggested that a representative flow field is achieved at Reynolds numbers (based on true chord) of 1.2×10^6. Taking into account the limitations set above, the vane was scaled down to approximately two thirds of its original size. CFD calculations were undertaken to determine the exact vane size to be used in the cascade. A scale of 62.023% was chosen, to meet the capacity requirement and match the exit Mach number, resulting in a vane span of 104 mm. For this case, the Reynolds number based on the true chord was 2.51×10^6. The geometric and inlet conditions for the cascade are compared to engine-representative values in section 3.4.

A comparison of the hot (engine) operating conditions for 100% scale vane and cold (rig) conditions for the 62% scale vane with the 3D profile is presented here. Figure 3.9 shows the isentropic Mach number distribution on the vane surface for these cases at 10%, 50% and 90% span. Mach number was matched at mid-span, was decreased at the hub and increased at the tip, due to spanwise Mach number variations in the annular case, providing good agreement overall.

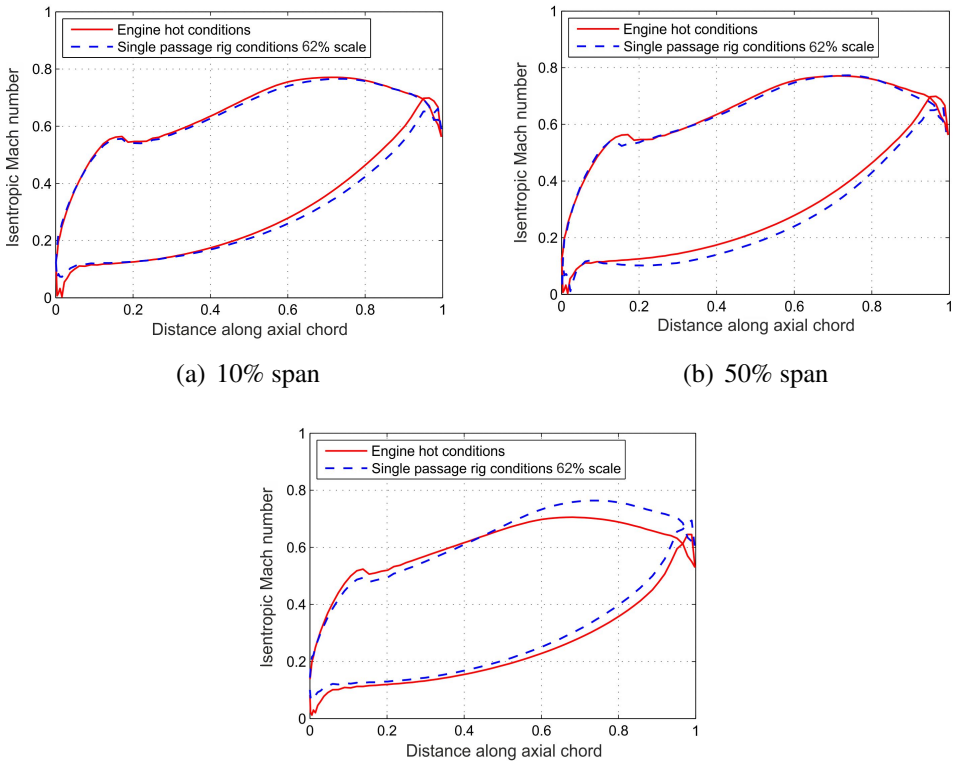

(a) 10% span

(b) 50% span

(c) 90% span

Figure 3.9: Isentropic Mach number distribution on the vane surface

3.2.3 Periodicity

Flow periodicity was achieved with a suitable design of the sidewalls and tailboards of the cascade to provide a good representation of the actual flow field using a finite number of vanes and could be verified by a pitchwise pressure traverse downstream of the vane trailing edge. The essential condition for good flow periodicity is that the stagnation streamlines of the outer vanes of the cascade are identical (Fottner, 1993b).

A parametric computational study of the flow in a cascade with two transition ducts and four vane passages was carried out to optimize the design of the sidewalls and the angle of the tailboards. This study was carried out in Ansys FLUENT and the mesh was created in ICEM CFD (further details are presented in section 4.3). The length of the transition ducts and the area ratio between the inlet and the outlet of the duct were representative of those in the engine. Figure 3.10 shows a schematic of the passages including the sidewalls and tailboards. The sidewalls for the

datum case were based on the relevant side of the vane. The pressure side sidewall was the pressure side of the vane from the leading edge to the trailing edge. This was extended upstream towards the combustor transition duct side and downstream towards the tailboard. The suction side sidewall was respectively the suction side of the vane. The angle of the tailboards for the datum case, where the vane leading edge was aligned with the combustor wall trailing edge, was at 71.5° relative to axial.

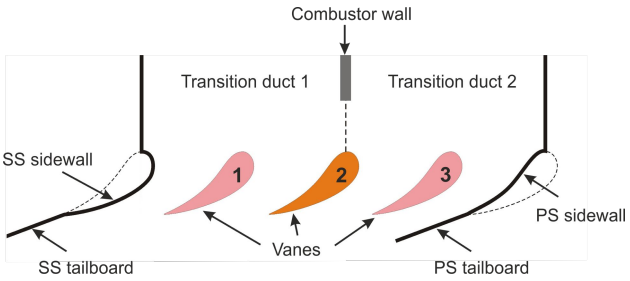

Figure 3.10: Naming of cascade parts, datum case

Figure 3.11 shows the total pressure 17% of the axial chord downstream of the vane trailing edge relative to the inlet value. The three wakes of the vanes could be clearly identified and the total pressure of the flow through each passage was the same, showing that flow periodicity could be achieved with this setup. The wake of the central vane was different from the other two due to the presence of the combustor wall upstream, which introduced loss into the flow, and it was asymmetric, with greater loss on the vane suction side.

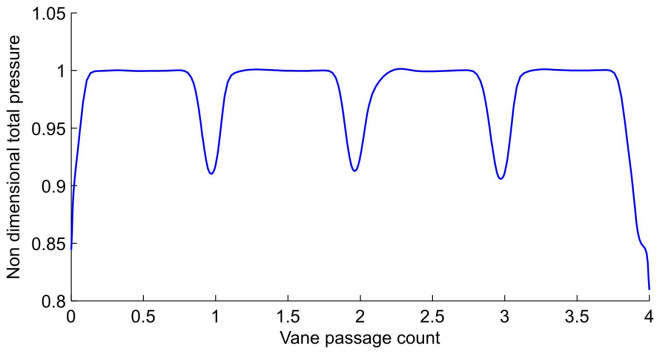

Figure 3.11: Non-dimensional total pressure 17% C_{ax} downstream of vane trailing edge, datum case

3.2.4 Vane Clocking Studies

One of the aimed functionalities of the cascade was the study of the effect of different clocking positions (relative positions of the combustor wall and the vane leading edge) on the nozzle guide vane flow field and heat transfer. The relative position of the wall and the vane significantly alters the flow field and the heat transfer, especially in the vane leading edge region, as disturbances shed from the upstream wall interact with the flow and can affect the coolant distribution on the vane surface. The design of the cascade enabled different relative positions between the vane leading edge and the combustor wall to be tested, including 50% pitch and 10% pitch towards both the pressure and suction sides, as shown in Figure 3.12. The pressure side sidewall is at the top of the cascade and the suction side sidewall is at the bottom of the cascade in the schematic.

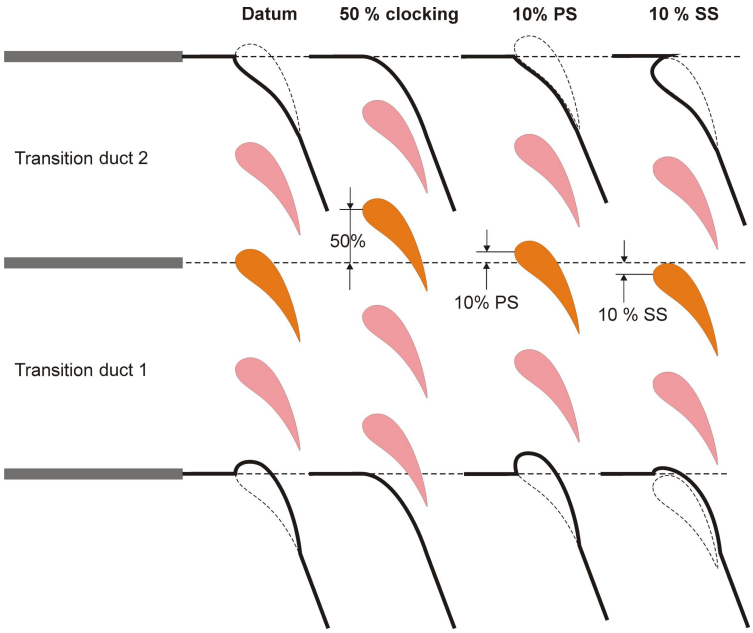

Figure 3.12: Different clocking positions of wall and vane

The sidewalls were optimized for each clocking position to ensure periodic flow. The sidewalls for the 10% clocking cases were the same as for the datum case. The sidewalls for the 50% clocking case were based on a streamline through the middle of the passage at mid-span, obtained from CFD studies, which was then extended to a 2D profile. The optimum angle of the tailboards

was at 71.5° relative to axial for the 10% pressure side clocking and the 10% suction side clocking cases and at 70.4° for the 50% clocking case.

Figure 3.13 shows a comparison of the non-dimensional total pressure for the datum and the 10% PS and 10% SS clocking cases, where the circumferential distance has been suitably modified to allow the three curves to collapse at the wakes of the three vanes. The total pressure loss downstream of the suction side of the central vane was similar in the datum and 10% SS clocking cases and was reduced in the 10% PS clocking case.

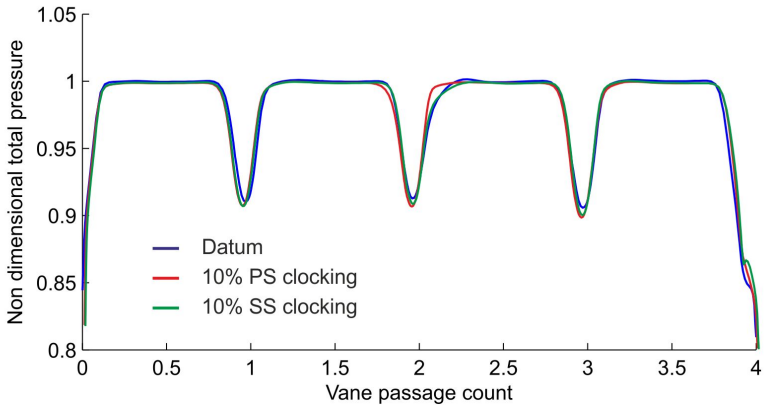

Figure 3.13: Comparison of non-dimensional total pressure 17% C_{ax} downstream of vane trailing edge

3.3 Working Section

Inside the test plenum, the flow went through two sections which contained a turbulence grid and a swirl generator. These were designed as cassettes that could be easily removed in order to investigate the effects of inlet swirl and turbulence. A converging transition duct followed, and the next section had inserts for two boxes that replicated the hub and casing coolant plena. The following section contained the three vanes and two sidewalls that had been optimized to have minimal disturbance to the flow in the four vane passages, as well as the two tailboards that were adjustable in order to set flow periodicity. Figure 3.14 shows the manufactured working section

inside the test plenum. Inside the test plenum the working section was designed to withstand pressures of up to 3 bar; the operating pressure did not exceed 1.6 bar.

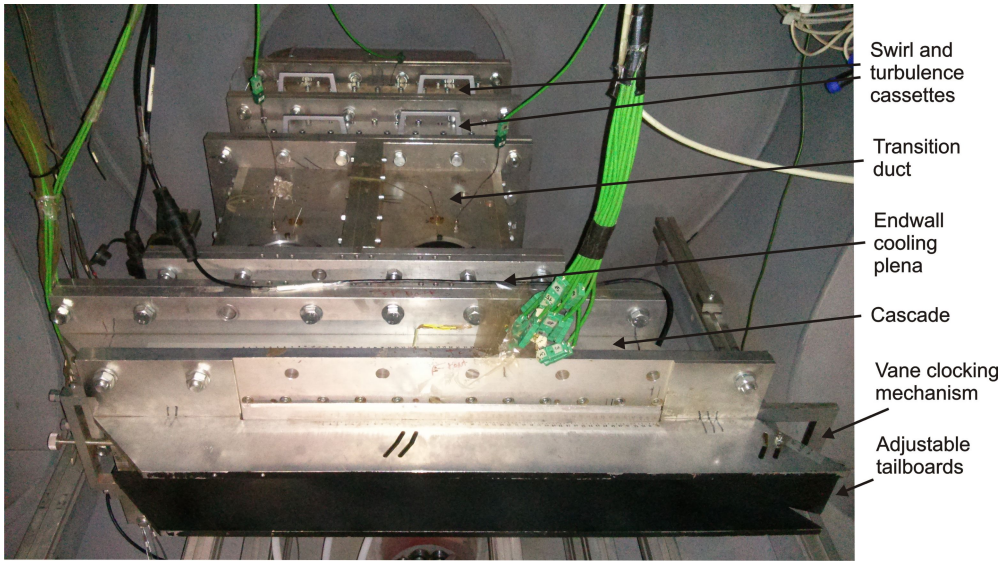

Figure 3.14: Manufactured working section inside the test plenum

3.3.1 Vane Cascade

The profile of the vane used in the cascade was the actual three-dimensional profile, as discussed in section 3.2.1, with linearised endwalls. This gave a better representation of the spanwise distribution of the turning of the flow, and allowed the study of complex features which could be translated to the real engine geometry more easily.

The vanes, the sidewalls, and the endwall cavities were manufactured as separate components to enable the interchangeability of parts and allow the modelling of complex internal geometries. The vanes and endwall cavities were manufactured by stereolithography (SLA) using the clear Huntsman Renshape SL 7870 resin. The building layer thickness was 0.1 mm and the manufacturing accuracy ± 0.15 mm per 100 mm. The sidewalls and tailboards were manufactured by selective laser sintering (SLS) using the white colour Polyamide PA2200, with a building layer thickness of 0.12 mm and a manufacturing accuracy of ± 0.25 mm per 100 mm to reduce manufacturing costs. All parts were made by *Ogle Models and Prototypes UK*.

The sections that hold these components are shown in Figure 3.15. The hub and casing endwall cavities can be seen in the front view, along with the vanes and sidewalls. The boxes were airtight and were designed as a single item each, so that different geometries of the cavity seals could easily be tested by manufacturing and replacing a single item, to ensure sealing and provide maximum flexibility. The middle vane in these pictures was instrumented for surface pressure measurements. The two adjustable tailboards are shown in the back view.

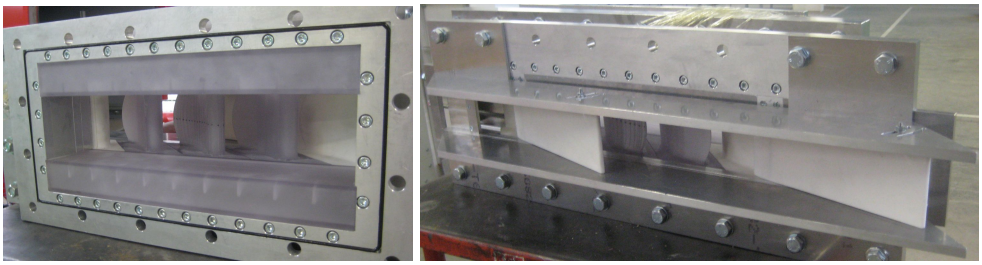

(a) Front view (b) Back view

Figure 3.15: Endwall cavities and vanes with sidewalls in the working section

The Huntsman Renshape SL resin was deemed appropriate for the conduct of this study, especially due to ease of manufacture of the prototypes. The focus of this work is to determine the differences between the different vane geometries, which are not affected by the material itself. Furthermore, the use of the laser sintering process allows the manufacture of complex geometries at a relatively low cost, increasing experimental flexibility.

3.3.2 Modular Design

Particular emphasis was given on the modularity of the design of the experimental facility, to enable the interchangeability of parts of the working section and easy testing of different geometric and flow features. In order to achieve that, various design innovations were implemented:

- A cassette system was designed for the turbulence grid and the swirl generator, where they could slide in and out of the combustor simulator unit to provide inlet turbulence, swirl, or clean inflow

- The vanes slided into the working section and were fixed in place from the two sides, enabling variations of clocking position of the vane leading edge relative to the combustor wall trailing edge

- The working section was placed on a trolley that allowed it to slide in and out of the test plenum and ensured the parts are always aligned when assembled

- The endwall cooling geometry and coolant supply system could easily be changed by manufacturing and placing a new part, without any modification to the working section

The conceptual design of the above features was done before the author started working on the project; the realisation of the sliding system for the vanes and endwall cavities and the design and setup of the cooling supply feed system was carried out by the author. The cooling system is discussed in the Appendix.

3.3.3 Periodicity and Clocking

Different clocking positions of the vane leading edge relative to the combustor wall were tested and the sidewalls of the working section were optimized to achieve periodic flow for each clocking position. The sidewalls used for the datum case, where the vane leading edge was aligned to the combustor wall, and the 10% clocking cases, with the vane leading edge at 10% of the vane pitch towards the pressure or suction side, are shown in Figure 3.16(a). The sidewalls for the 50% clocking case are shown in Figure 3.16(b). For this case, the sidewalls were manufactured as a single unit that includes the adjacent vane.

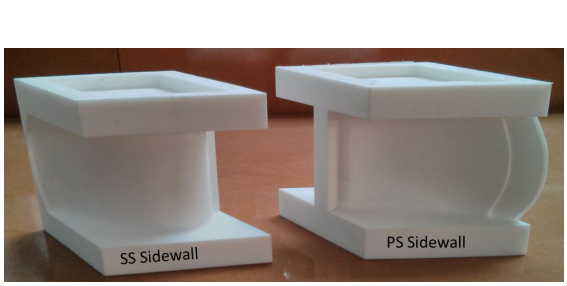

(a) Datum and 10% clocking

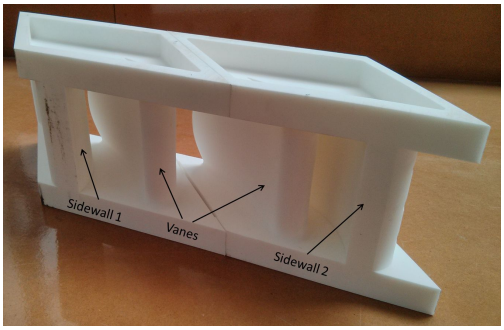

(b) 50% clocking

Figure 3.16: Sidewalls used for the different cases

3.3.4 Turbulence Grid and Swirl Generator

In order to generate the desired turbulence intensity levels, a turbulence grid designed by Dr S. Luque according to the guidelines given by Roach (1987), was used to achieve an inlet turbulence intensity of over 10%. A 5 mm thick aluminium plate was manufactured with 17 holes of 45 mm diameter and fitted inside a cassette, as shown in Figure 3.17(a). The wetted surfaces of the cassette were painted black to minimize any reflections that might affect the heat transfer measurements.

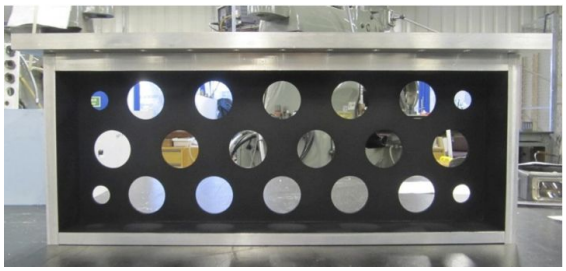

(a) Turbulence grid, painted black to minimize reflections

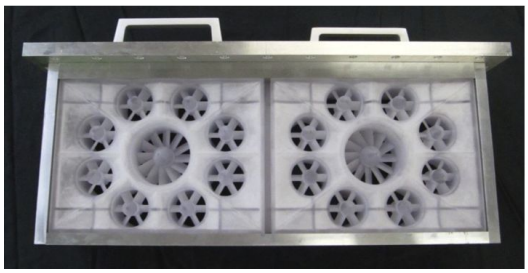

(b) Swirl generator, details in Jacobi (2013)

Figure 3.17: Turbulence grid and swirl generator

A swirl generator consisting of one pilot swirler in the centre and eight main swirlers around the pilot was designed by Jacobi (2013) and manufactured using stereolithography. As the cascade models two combustor transition ducts, two swirl generators were manufactured and fitted in the cassette, shown in Figure 3.17(b). A second swirl generator geometry was also manufactured, to

increase the average swirl angles achieved. Details on the design of the swirl generators can be found in Jacobi (2013).

3.4 Inlet Conditions and Geometric Parameters

The high mass flow pressure regulator of the inlet pressure control system maintained a constant inlet pressure while the supply pressure was decreasing. Typical inlet total and static pressure traces during a run of the facility are shown in Figure 3.18(a). Flow to the test section started at the

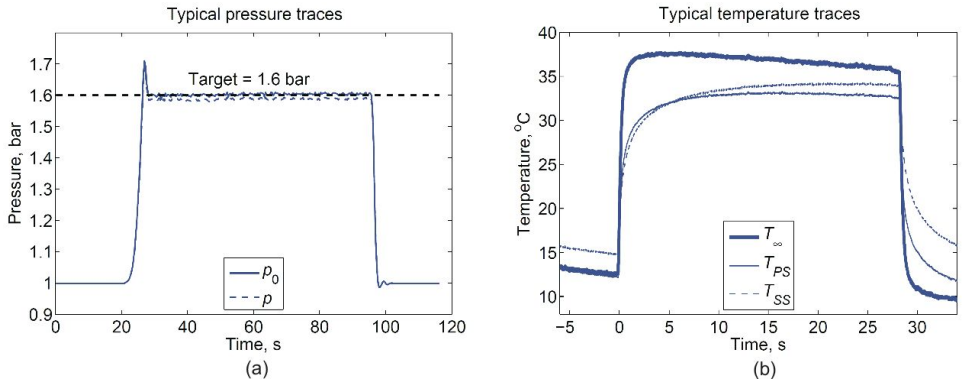

Figure 3.18: Pressure (a) and temperature (b) traces during a run of the facility

20 s mark with the operation of the pneumatically actuated ball valve which was shut just before the 100 s mark. Temperature traces of the free-stream flow and the vane pressure and suction side during a run of the facility with the operation of the heater mesh are shown in Figure 3.18(b). During the run of the facility, the heater mesh was turned on at the 0 s mark and turned off shortly before the 30 s mark. It is noted that no correction was made for the temperature drop during the run of the heater mesh, which was $0.5 - 1$ K per 10 s of mesh operation. The mesh was switched on after the inlet flow had stabilized (15 s after the valve is turned on) and the air flow through the facility was continued for 20 s after the mesh was switched off, to allow it to cool down. The geometric parameters of the scaled vane and the flow conditions at the inlet to the test section are summarized in table 3.1 and compared to typical engine values.

Table 3.1: Inlet conditions

Parameter	**Experimental Facility**	**Engine (approximate)**
Vane true chord [mm]	150	242
Vane axial chord [mm]	89	143
Vane pitch [mm]	120	193
Vane span [mm]	104	168
Combustor wall thickness [mm]	15.3	25
Inlet total pressure [Pa]	1.55×10^5	16×10^5
Typical inlet total temperature [K]	310	1600
Mainstream mass flow rate per vane passage [kg/s]	1.2	13
Exit Mach number	0.625	0.625
Exit Reynolds number (based on true chord)	2.51×10^6	5.1×10^6
Prandtl number	0.69	0.72
Inlet turbulent intensity	$0.2 - 13\%$	13% (guess)
Scaling factor	62.023%	-
Typical inlet temperature rise [K]	25	-
Exit static pressure [Pa]	1.19×10^5	-
Running time [s]	120	-
Duration of heater mesh operation [s]	$20 - 30$	-

3.5 Measurement Capabilities

3.5.1 Aerodynamic Measurements

A *Scanivalve* Digital Sensor Array (DSA) 3217 pressure scanner with 16 channels was used for high accuracy pressure measurements. The DSA scanner had 16 temperature compensated piezoresistive pressure sensors with a pneumatic calibration valve and a microprocessor. The latter compensated for temperature changes and controlled an internal calibration valve to perform on-line calibrations before each experimental test. This provided a long-term accuracy of $\pm 0.05\%$ of the full scale. The measurement range of the DSA pressure scanner is 1 bar, resulting in a measurement uncertainty of ± 50 Pa. The DSA pressure scanner was used for measurements obtained with the pressure probes, as well as measurements of the mainstream flow in three locations upstream of the cascade. 48 high accuracy pressure transducers from *Sensortechnics*, with a

measurement range of 1 bar and a maximum combined non-linearity, hysteresis and repeatability uncertainty of ± 500 Pa, were used for surface pressure measurements on the endwalls. Temperature measurements were obtained using K-type thermocouples, connected to a 32-channel unit, which had an uncertainty of ± 1.5 K. Temperature measurements included the mainstream flow as well as the surface temperature of the vane and endwalls.

Mainstream flow measurements of inlet total and static pressure and temperature were obtained at three locations: upstream of the swirl and turbulence cassettes and at both combustor transition ducts. Measurements of stagnation pressure were obtained with fixed Pitot probes and measurements of static pressure with pressure tappings on the endwall. Coolant flow measurements of total pressure and temperature could also be obtained in the coolant plena. A cross-section through the working section at mid-span with the measurement locations is shown in Figure 3.19.

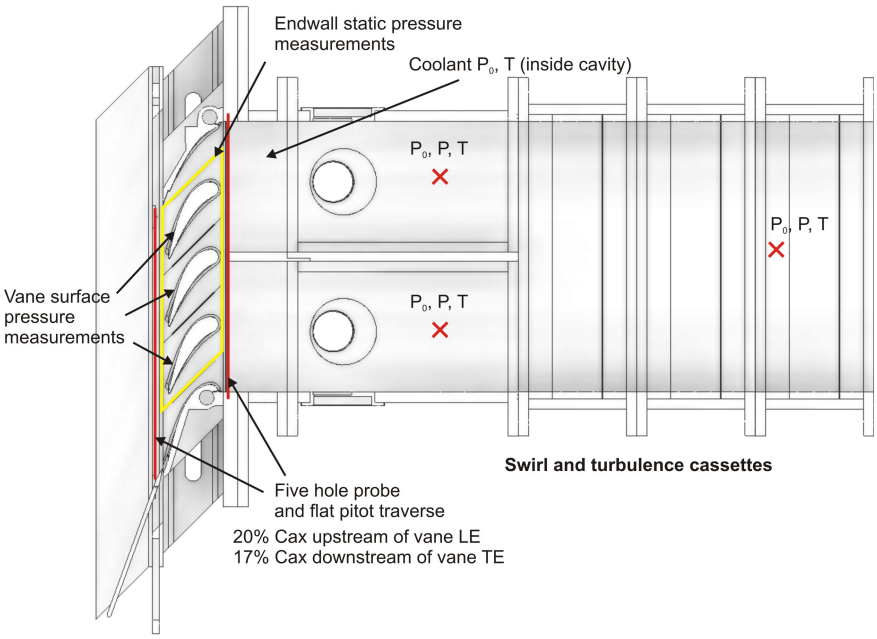

Figure 3.19: Schematic of the measurement locations upstream and downstream of the working section

Endwall pressure measurements were obtained at 20%, 40%, 60%, and 80% pitch, with 12 pressure tappings at each pitchwise location. Vane surface measurements were obtained at 10%, 50% and 90% span, using 32 pressure tappings at each spanwise location. Due to the limited space available on the vanes and to increase measurement resolution, the tappings shared a single chan-

nel for each axial location. Measurements for each spanwise location were obtained by externally masking the tappings on the other two locations. The instrumented vanes for endwall and surface pressure measurements are shown in Figure 3.20. The modular design of the facility enabled the conduct of measurements on the vane surfaces and the vane endwalls by moving the instrumented vanes to the desired position in the cascade.

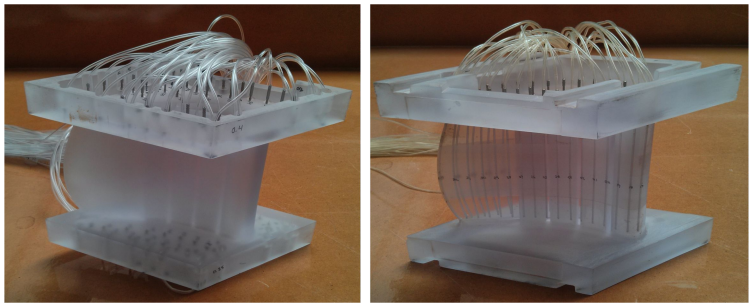

Figure 3.20: Instrumented vanes for endwall (left) and surface (right) pressure measurements

Measurements on the vane surface were obtained using 0.076 mm thick thermocouple wires on the vane surface to minimize disruption of the boundary layer. The instrumented vane for temperature measurements, which was used to calibrate the high resolution infrared camera, is shown in Figure 3.21. Four thermocouples were placed on each surface (hub endwall, casing endwall, pressure side, suction side).

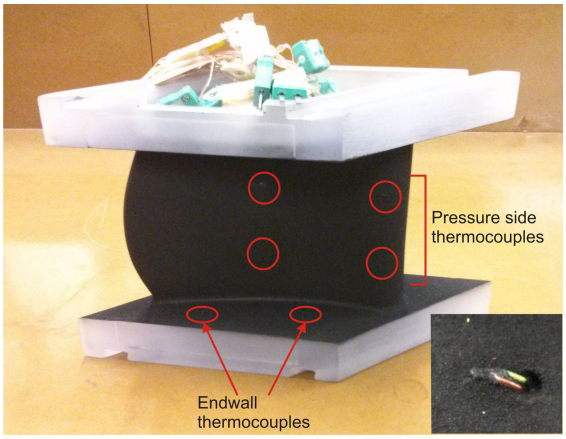

Figure 3.21: Instrumented vane for surface temperature measurements

The DSA pressure scanner and the 32-channel temperature measurement unit were connected to a *National Instruments* (NI) PXI system, a PC-based platform for measurement and automation

systems. All the pressure and temperature data obtained during the experimental tests were logged into the NI PXI workstation. NI LabVIEW 2013 was employed for pressure, temperature, and video data acquisition programming, as well as for the control of the automated traverse system for pressure probe measurements.

3.5.1.1 Pressure Probes for Flow Measurements

A five-hole probe was used in this study for flow traverse measurements to determine the yaw and pitch angles of the flow in addition to the total and static pressure. The probe head, designed by Dr V. Kanjirakkad, was conical, as shown in Figure 3.22(a), with an included angle of $90°$, a diameter of 2.4 mm, and holes with a diameter of 0.4 mm. It is noted that lower included angles result in better accuracy for static pressure measurements but reduced sensitivity and therefore lower accuracy for flow angle measurements. An angle of $90°$ offers a good compromise between

(a) Probe head

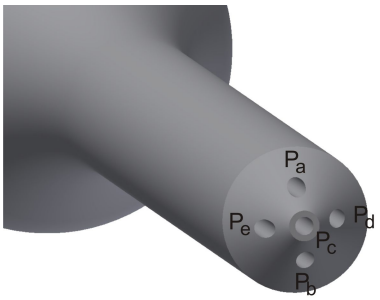

(b) CAD drawing

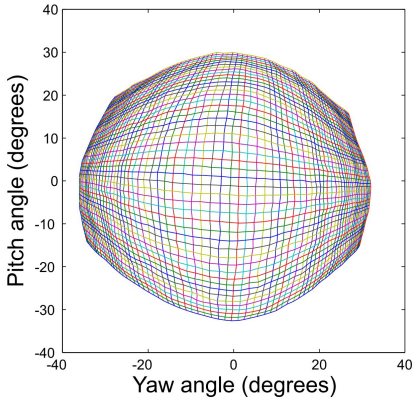

(c) Calibration map

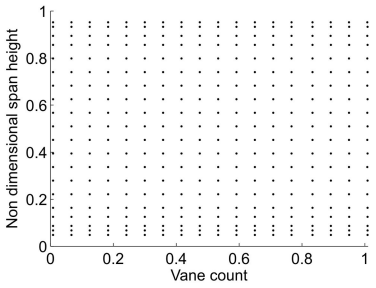

(d) Typical measurement resolution of a single vane passage

Figure 3.22: Five hole probe

the two. The cylindrical part of the probe extended for 16.5 mm with a diameter of 2.4 mm before widening to a diameter of 6 mm to allow space for the plastic pressure tubes. The probe head was manufactured using laser sintering and assembled into an 8 mm stem.

For its calibration, the five hole probe was placed in uniform axial flow and a two axis traverse mechanism was used to allow variations of both pitch and yaw angle. During the calibration, the probe obtained pressure measurements for different yaw and pitch angles; these were used to calculate the pitch and yaw coefficients from equations 3.3, 3.4, 3.5. The numbering of the holes is shown in Figure 3.22(b). The value of the pitch and yaw coefficient was matched to the known pitch and yaw angle for each measurement point and stored in the form of a calibration map, shown in Figure 3.22(c). A look-up table was then used to obtain the yaw and pitch angle, which results in lower uncertainty compared to the use of a polynomial fit, as has also been noted in the literature (Behr et al., 2006).

$$C_{\text{yaw}} = \frac{P_{\text{d}} - P_{\text{e}}}{P_{\text{c}} - P_{\text{avg}}} \tag{3.3}$$

$$C_{\text{pitch}} = \frac{P_{\text{a}} - P_{\text{b}}}{P_{\text{c}} - P_{\text{avg}}} \tag{3.4}$$

$$P_{\text{avg}} = \frac{P_{\text{a}} + P_{\text{b}} + P_{\text{d}} + P_{\text{e}}}{4} \tag{3.5}$$

The measurement range of the five-hole probe, as determined by the calibration, was $\pm 30^{\circ}$ for the yaw angle and -24° to $+30^{\circ}$ for the pitch angle. The uncertainty of the measurements with the five-hole probe was determined through a statistical analysis of the results from the 1517 (41×37) experimental data points obtained in the calibration facility and confirmed with an analysis of 400 data points obtained from a separate test. The calibration coefficients calculated from the measurements were substituted into the look-up table to provide the total pressure, yaw angle, and pitch angle. The uncertainty magnitude of the measurements followed a normal distribution, with a maximum error of $\pm 0.32^{\circ}$ to within 95% confidence for the yaw angle and $\pm 0.3^{\circ}$ to within 95%

confidence for the pitch angle. The uncertainty of the total pressure measurement was ± 130 Pa to within 95% confidence for the probe measurement range.

The measurement uncertainty for the yaw angle and the total pressure were verified in situ under uniform axial flow conditions. The uncertainty in pressure measurements for small flow angle variations ($\pm 10^{\circ}$) was within the measurement accuracy of the DSA system (± 50 Pa). Re-calibration of the probe after the conduct of the experimental studies showed differences within the measurement accuracy of the system.

The five hole probe was used to obtain area traverse measurements, driven by a remotely operated, three-axis automated motion control system supplied by *LG Motion*. This could drive the probe in the pitchwise and spanwise direction, as well as rotate it in the yaw angle direction. The motors used were PK264-03B and PK266-03B for the linear directions and PK243-01B for the rotational direction. The lead screws in both linear directions had a pitch of 4 mm to provide a high traversing speed for the probe. Limit switches were enabled to ensure the system is not driven past the traversing distance in the lead screw, and encoders provided live feedback to the system to verify the location of the probe at each instant. The mounting assembly ensured that the probe rotated around its tip so that the measurement location was the same when traversing in the rotational direction. The total distance covered by the probe in the pitchwise direction is 430 mm, which was typically the central part of the cascade, apart from the quarter of the passage near each sidewall.

The measurement resolution for the experimental studies presented in this work included 360 points per passage, 20 along the span and 18 along the pitch. A typical map is shown in Figure 3.22(d). Measurement points were clustered together close to the endwalls. A typical experimental run covered 80 points during 90 s. An overlap between the runs was maintained to verify the repeatability of the data between the sequential runs. A full map from the measurements was obtained through interpolation between the data points in MATLAB.

Total pressure measurements near the endwalls were conducted with flat Pitot probes, that could measure as close as 1 mm from the wall. 1.6 mm metal tubes were flattened at the tip to reduce Reynolds number sensitivity for near-wall measurements, and fitted into 8 mm stems, similar to the one used for the five-hole probe. The distance from the centre of the stem to the tip of the probe was the same as in the five-hole probe, to ensure measurements are obtained at the same axial location in both cases. The typical measurement steps for the flat Pitot probes were 0.5 mm. The flat Pitot probes used for the hub and casing endwalls and for the upstream sidewalls are shown in Figure 3.23.

The measurement of stagnation pressure is generally sensitive to the direction of the flow, with different probe designs having different tolerance to the yaw angle of the flow. Straight Pitot probes are insensitive to yaw angle variations of $\pm 10^{\circ}$ (Hodson and Miller, 2012). The verification of the measurements obtained by the flat Pitot was done by comparison to the total pressure measured in the same location with the five-hole probe. When measurements are obtained near the wall, the presence of the probe causes a deflection of the streamlines, that can affect the accuracy of the readings. This effect, which is more pronounced in static pressure and velocity measurements, is reduced with the use of flattened probe tips, that minimize probe interference. For endwall measurements, the height of the probe tip was less than 1 mm, resulting in small deflections in pitch angle, and variations in pressure measurements that ware within the measurement accuracy of the system. Upstream temperature measurements near the endwalls were carried out with a thermocouple glued to the flat Pitot probe.

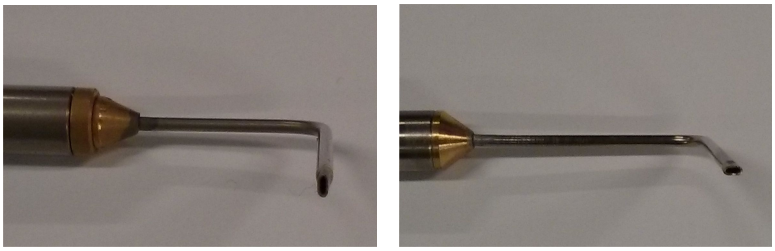

(a) Hub/casing endwall (b) Upstream sidewall

Figure 3.23: Flat Pitot probes for near wall measurements

The pressure loss downstream of a nozzle guide vane was quantified using the total pressure loss coefficient. For turbines, this is typically defined as the total pressure loss relative to the outlet dynamic head, as shown in equation 3.6.

$$C_{P_0} = \frac{P_{0,in} - P_{0,local}}{{}^1\!/_2 \rho V_{out}^2} \tag{3.6}$$

3.5.2 Heat Transfer Measurements

Heat transfer measurements on the vane and endwall surfaces were conducted with the use of infrared thermography. This technique was used as it can obtain detailed surface heat flux distributions and it can capture the initial temperature distribution which is required for film cooling studies, allowing greater experimental flexibility. In addition, IR thermography can be used over a wider temperature range compared to the liquid crystal technique, which makes it more suitable for the particular application.

The fundamentals behind the use of infrared thermography lie in Planck's law that states that the electromagnetic radiation of a black body is a function of its temperature for a certain wavelength. Integrating over all wavelengths, the total radiation emitted by the surface of a black body, j^*, is only a function of its temperature to the fourth power (Stefan-Boltzmann law, $j^* = \sigma \cdot T^4$, where σ is a constant). Any surface with a temperature greater than absolute zero radiates energy. This energy is a fraction of the maximum radiation emitted from a black body. The surface temperatures in the facility during operation ranged from $280 - 320\,\mathrm{K}$; the peak emission would therefore be between $9 - 10.4\,\mu$m, derived using Wien's displacement law which refers to emission from a black body. In order to increase the emissivity of the surfaces, the vanes and endwalls were painted with *Nextel Velvet Coating 811-21*, which had an emissivity of at least 0.96 at wavelengths of $8 - 12\,\mu$m. The use of this matt black paint ensured that the surfaces measured are as close as possible to an ideal black body. The increase in surface roughness would increase the heat transfer levels, as shown by Blair (1994), as the boundary layers were expected to be fully turbulent.

During an experimental run, a step rise in the inlet temperature was provided by the heater mesh. The temperature rise was nearly instantaneous, with a time constant of $0.15\,\mathrm{s}$. A high resolution (640×480 pixels) thermal imaging camera (*FLIR* A655sc) recording over a spectral range of $7.5 - 14\,\mu$m a frame rate of $50\,\mathrm{Hz}$ was used to record the response of the vanes and the endwalls to this temperature rise as a function of time. An infrared camera detects emitted radiation intensity in the infrared spectrum, at wavelengths just above those of the colour red ($700\,\mathrm{nm}$), and assigns a greyscale value to the signal within the temperature range the camera operates in. For a 16-bit camera, this is a value between $0 - 65535$. The temperature resolution therefore depends on the temperature range of the camera.

The IR camera was used to obtain greyscale intensity measurements on the vane surface and the endwalls through a number of different view ports, as shown in Figure 3.24. The hub and casing endwalls and the vane suction side were viewed from downstream of the working section, whereas the leading edge and the vane pressure side could only be accessed from upstream of the working section. A Zinc-Selenide window with an anti-reflective coating (at 8-12 μm) was installed in the required location upstream of the cascade for each experimental test. The window was transparent to infrared radiation and had a transmissivity of 98% between 8 and 11.5 μm. From 11.5 to 14 μm the transmissivity of the window was between 98% and 90%. The reflectance of the window was 0.6% from $7.2 - 13$ μm and outside this range it was under 1.2%.

The viewing angle on the vane surfaces, as seen in Figure 3.24, was between 60° and 90°; the lower angles were due to the curvature of the vane. The viewing angle on the endwall was lower, in the order of 35°, resulting in higher measurement uncertainty. This was addressed by O'Dowd (2010), who argued that the error induced by the variation in viewing angle results in a maximum temperature difference of the order of $1\,\mathrm{K}$. The effect of distance between the test surface and the camera was not found to be significant by O'Dowd (2010).

Schematics of the different views of the cascade are shown in Figure 3.25. The images on the left hand side are from the CAD drawings and the images on the right hand side are sketches

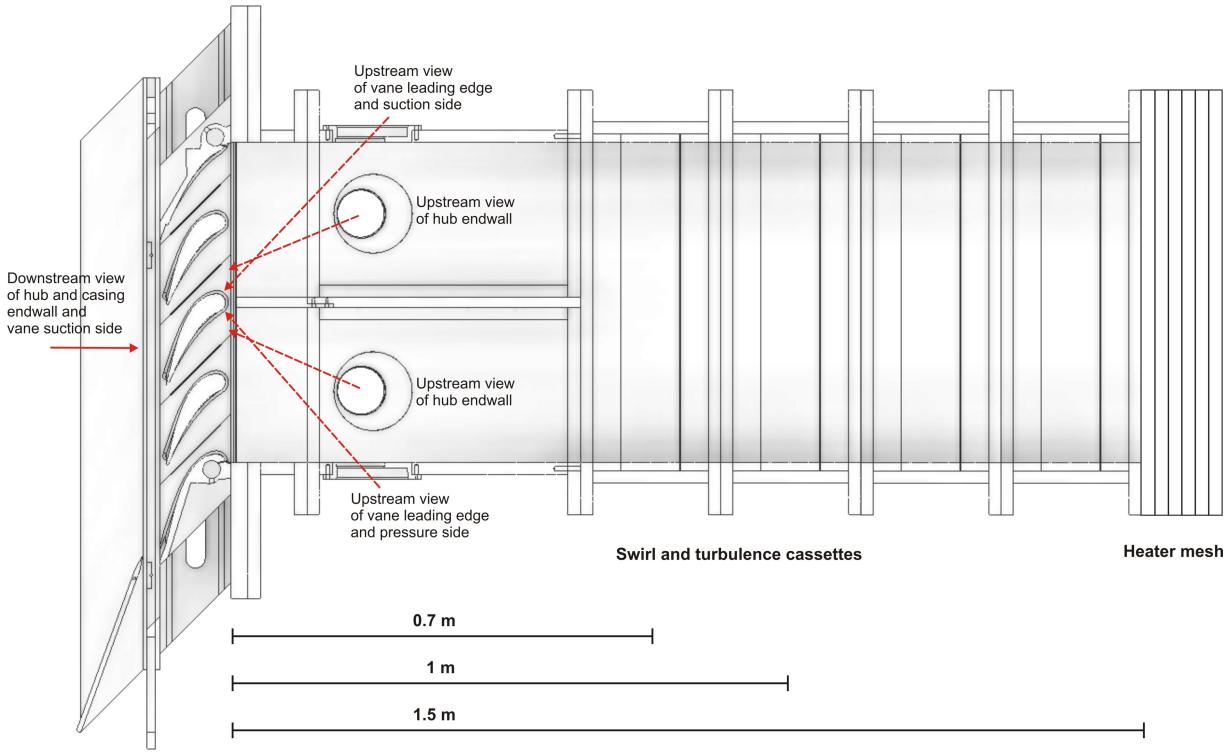

Figure 3.24: View ports for IR measurements

obtained from the camera views. The areas of interest that were accurately seen from the camera in each view are shaded grey in these sketches. Figure 3.25(a) focuses on the pressure side of vane 2, which is immediately downstream of the combustor wall, from 0 to 50% of the axial chord. Figure 3.25(b) shows the leading edge and early suction side of vane 2, from 0 to 10% of the axial chord. Part of the pressure side of vane 1 near the trailing edge (from $90 - 95\%$ of the axial chord) could also be seen from this view. The hub and casing endwalls in both views were at a very shallow viewing angle, therefore no useful data could be obtained. Figure 3.25(c) presents part of the suction side of vane 2, from $50 - 100\%$ of the axial chord, viewed from downstream of the cascade. Figure 3.25(d) is a view of the hub endwall between vanes 1 and 2 and the leading edge of vane 2 as seen from upstream of the cascade. Figure 3.25(e) is a view of the hub endwall

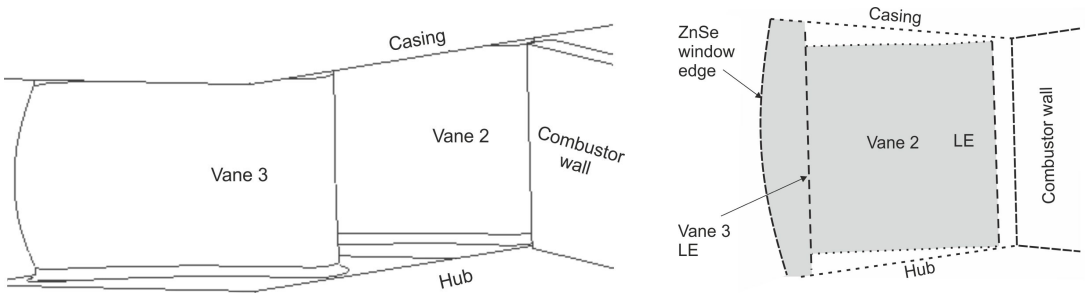

(a) Vane pressure side (view 1)

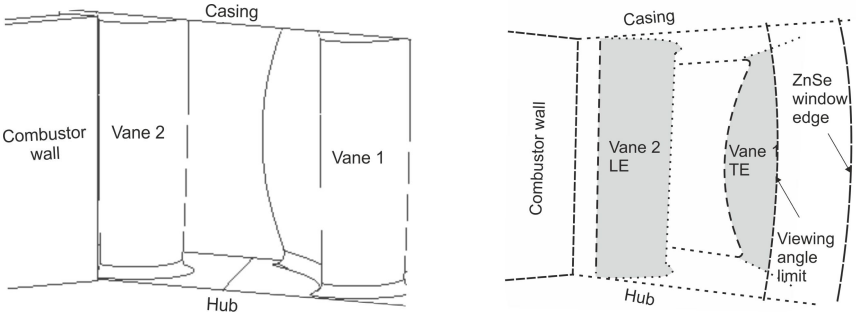

(b) Vane leading edge (view 2)

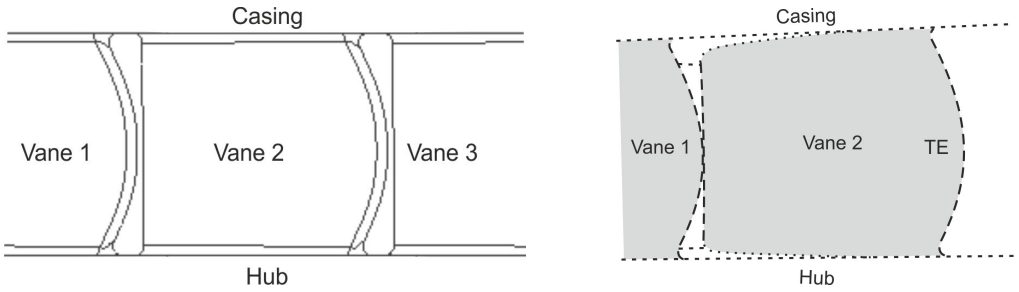

(c) Vane suction side (view 3)

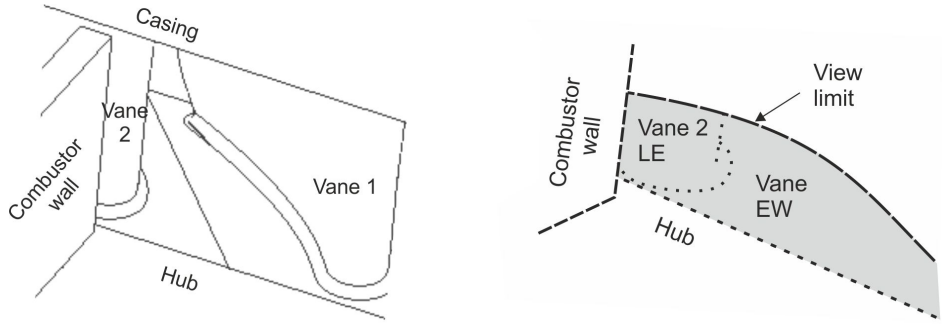

(d) Hub endwall, viewed from upstream (view 4)

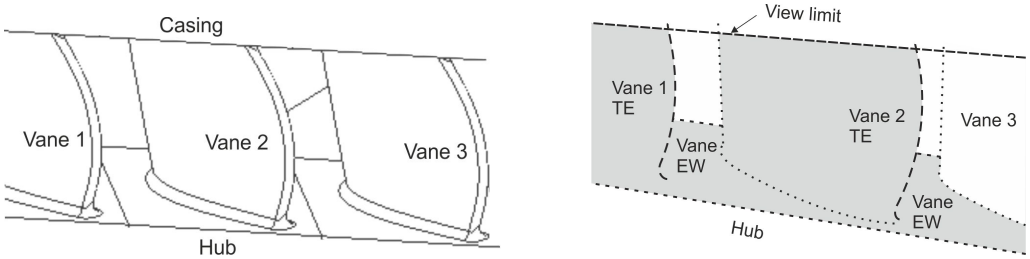

(e) Hub endwall, viewed from downstream (view 5)

Figure 3.25: Views of the cascade for IR measurements - CAD image (left) and measurement region (right)

from downstream of the cascade. Parts of the suction side of vanes 1 and 2 near the endwall were also seen in this view, whereas vane 3 was at a shallow viewing angle.

3.5.2.1 Heat Transfer Measurement Processing

The greyscale intensity of the test surfaces acquired during the experimental tests was converted to temperature using the linear relationship between the two obtained from the calibration of the camera. In order to determine the temperature of the test surface, the knowledge of a number of parameters of the surroundings of the object was required. These included the emissivity of the object, the transmissivities of the lens of the camera and the ZnSe window, the relative humidity, and the temperature of the surroundings, including the lens of the camera, the window, and the air between the camera and the object. The calibration of the camera was performed in situ to ensure the calibration is valid in the test environment. In-situ calibration reduced the uncertainty that would be introduced by estimating the temperatures of the surroundings; values for the other parameters that were still required for the setup of the camera were provided by the manufacturers.

For the calibration, the test vane with the thermocouples on the surface was set up in the experimental facility. This was heated with a heat gun and its response was recorded by the camera. The greyscale intensity signal of the camera at the reference thermocouple locations was then plotted against the temperature measured by the thermocouples; the linear relationship between the two parameters was used in the processing of the data. Due to the limited availability of the facility, the calibration data used was provided by Dr Salvador Luque. The thermal effusivity ($\rho C_p k$) of the resin used for the manufacturing of the test vanes was experimentally determined by Luque et al. (2015). The value obtained was $562.7 \pm 19.9\, J/m^2 K s^{\frac{1}{2}}$ to within 95% confidence.

The temperature traces acquired were processed into heat fluxes using the impulse-response method developed by Oldfield (2008). Other techniques for the determination of the heat transfer coefficient using IR thermography were investigated by O'Dowd et al. (2011), who found this method to be the most accurate and computationally efficient.

As discussed in section 2.2.1, the heat flux to the surface is given by Newton's law of cooling, equation 3.7. The heat transfer parameters determined from the experimental measurements were the heat transfer coefficient, h, and the adiabatic wall temperature, T_{aw}. The analysis was based on Fourier's law of heat conduction on a one-dimensional, semi-infinite solid body. A penetration depth analysis was carried out to assess the validity of this assumption for the technique used in this study, using the criterion of Schultz and Jones (1973), equation 3.8. In this equation, δ is the thermal penetration depth, α is the thermal diffusivity and t is the time. The maximum penetration depth was 5.1 mm, therefore the assumption was valid for 11.4 s; data acquired in the first 10 s of heater mesh operation only was used for the transient IR thermography technique. It should be noted that the semi-infinite assumption is not valid for the vane trailing edge, the corner regions, and regions of high curvature.

$$q = h(T_{aw} - T_w) \tag{3.7}$$

$$\delta = \sqrt{4\alpha t} \tag{3.8}$$

The post-processing routine used to obtain the heat transfer coefficient from the experimental data was written by Dr S. Luque, based on the MATLAB program and technique by Prof Martin Oldfield. As explained in Oldfield (2008), the response of a system such as the surface temperature $T(t)$ and surface heat transfer rate $q(t)$ can be calculated from the impulse response $h(t)$ of the system by the convolution integral (equation 3.9). The continuous signal of temperature was sampled at a chosen period to give discrete signals. The impulse response function required for the transient processing technique was derived using a pair of non-singular analytical solutions $q_1(t)$ and $T_1(t)$ for heat transfer on a semi-infinite surface with a given thermal effusivity. With this known solution, the impulse response function was found by deconvolution, using the function *filter* in MATLAB. This impulse response function was then used to process sampled temperature data into heat flux, using the function *fftfilt*.

$$q(t) = h(t) \cdot T(t) = \int_{-\infty}^{\infty} h(\tau)\, T(t-\tau)\, \mathrm{d}\tau \tag{3.9}$$

A least squares line was fitted to the measurement points of heat flux against surface temperature to obtain the heat transfer coefficient (the slope of the line) and extrapolated to find the adiabatic wall temperature (the temperature where the heat flux would be zero). This is shown in Figure 3.26 for a sample pixel. The full heat transfer coefficient and adiabatic wall temperature maps were obtained with this method for each pixel of the frame.

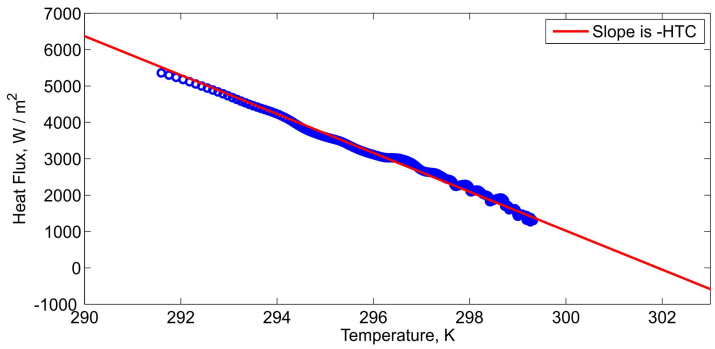

Figure 3.26: Heat flux versus surface temperature for a sample pixel

Heat transfer data is commonly presented in the non-dimensional form of the Nusselt number, $Nu = \frac{h \cdot x}{k}$. The Nusselt number can be corrected for discrepancies in the mainstream-to-wall temperature ratio, using the correlation by Fitt et al. (1986), equation 3.10. The temperature ratio in the experimental facility was 1.035, whereas a typical value in an engine is 1.5 (Harasgama et al., 1992). As the Mach number was matched to the engine conditions, the Nusselt number can be scaled up by 9.7% to achieve engine-representative values. It is noted that this has not been done in the experimental results presented in the following chapters.

$$Nu = Nu_i(\frac{T_w}{T_\infty})^{0.25} \tag{3.10}$$

3.5.2.2 Heat Transfer Measurement Uncertainty

A measurement uncertainty analysis was conducted for the Nusselt number distributions based on the work by Moffat (1988) for experimental studies. The main parameters of uncertainty arose from the uncertainty in the values of the material properties, the mainstream temperature, and the

wall temperature. These include errors in the calibration process, as well as the least squares fit of the heat flux versus temperature curve obtained from the measurements.

The overall uncertainty in Nusselt number due to the uncertainties in the above variables was determined using the partial derivatives method described by Kline and McClintock (1953). The partial derivatives were estimated using finite difference approximations to determine the overall uncertainty in Nusselt number, as described by Moffat (1988). The contributions of the uncertainties of the various parameters to the overall uncertainty were estimated based on a baseline set of data for which the Nusselt number was determined. The standard error of estimate for the determination of the calibration curve and for the heat flux versus temperature curve was calculated from equation 3.11 as described by Coleman and Steele (2009).

$$SEE = \left\{ \frac{\Sigma_{i=1}^{N} (Y_i - (a \cdot X_i + b))^2}{N - 2} \right\}^{\frac{1}{2}} \tag{3.11}$$

The contribution of the uncertainty in the thermal effusivity of the material to the uncertainty in Nusselt number was calculated by comparing the value of the Nusselt number for the baseline and the maximum thermal effusivity. In this case, the baseline effusivity was $562.7 J/m^2 K s^{\frac{1}{2}}$ and the maximum was $572.6 J/m^2 K s^{\frac{1}{2}}$, resulting in an uncertainty of $\pm 3.54\%$ in the Nusselt number. The uncertainty in the value of the wall temperature arose from the calibration process and the error in greyscale reading of the camera during the experiment. The uncertainty in wall temperature during the experiment was calculated at 0.5%, contributing to an uncertainty of 5.9% in Nusselt number. An uncertainty in the value of the mainstream temperature of 1.6 K arose from the measurement uncertainty of the inlet temperature thermocouples and the drop in temperature during the experiment. This resulted in a 0.42% uncertainty in Nusselt number. The uncertainty in the evaluation of the different parameters is summarized in Table 3.2 and results in an overall uncertainty of $\pm 6.9\%$ in Nusselt number.

An additional source of error is the lower performance of the ZnSe window (in terms of reflectance and transmissivity) in the part of the measurement range of the camera which is outside

Table 3.2: Effect of Measurement Uncertainty on Nusselt Number

Source	**Uncertainty**
Mainstream Temperature	0.42%
Wall Temperature	5.9%
Material Properties	3.54%
Overall	**6.9%**

the nominal range of the window ($7-8\mu$m and $12-14\mu$m). Another source of error is the lateral conduction that may invalidate the one-dimensional heat conduction assumptions in some regions of the vane. These however do not affect the results presented in this work.

3.5.3 Measurement Repeatability

The repeatability of the aerodynamic measurements with the five hole probe was assessed by conducting two different traverses downstream of the central vane for the same configuration. The pitchwise averaged total pressure loss coefficient and yaw angle distribution for the two tests are shown in Figure 3.27. The results matched very well, proving the repeatability of the measurements with the five-hole probe. These tests were carried out on the geometry discussed in Chapter 4.

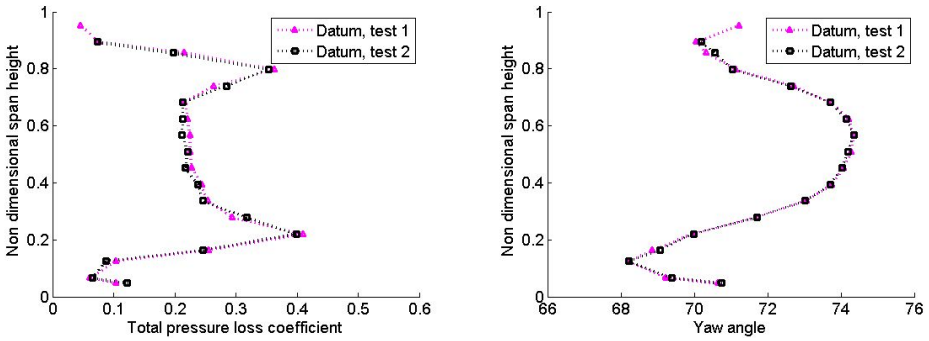

(a) Total pressure loss coefficient (b) Yaw angle

Figure 3.27: Repeatability of aerodynamic measurements

The repeatability of the heat transfer measurements was verified in the facility comparing different experiments carried out on the same configuration. The measurements with the IR camera showed good repeatability, as shown in Figure 3.28. These tests were on a geometry which will be

discussed in Chapters 7 and 8. The difference between the two tests is plotted in Figure 3.28(c). All figures show Nusselt number data. The data shown in Figure 3.28 was further analysed to calculate the measurement repeatability error. The difference between the two tests was seen to follow a normal distribution with a mean value for the percentile difference between the two tests of 0% (absolute value of Nu=-1) and a standard deviation of 3% (corresponding to Nu=34), therefore more than 95% of the data points were within $\pm 6\%$ (absolute value of Nu ± 70).

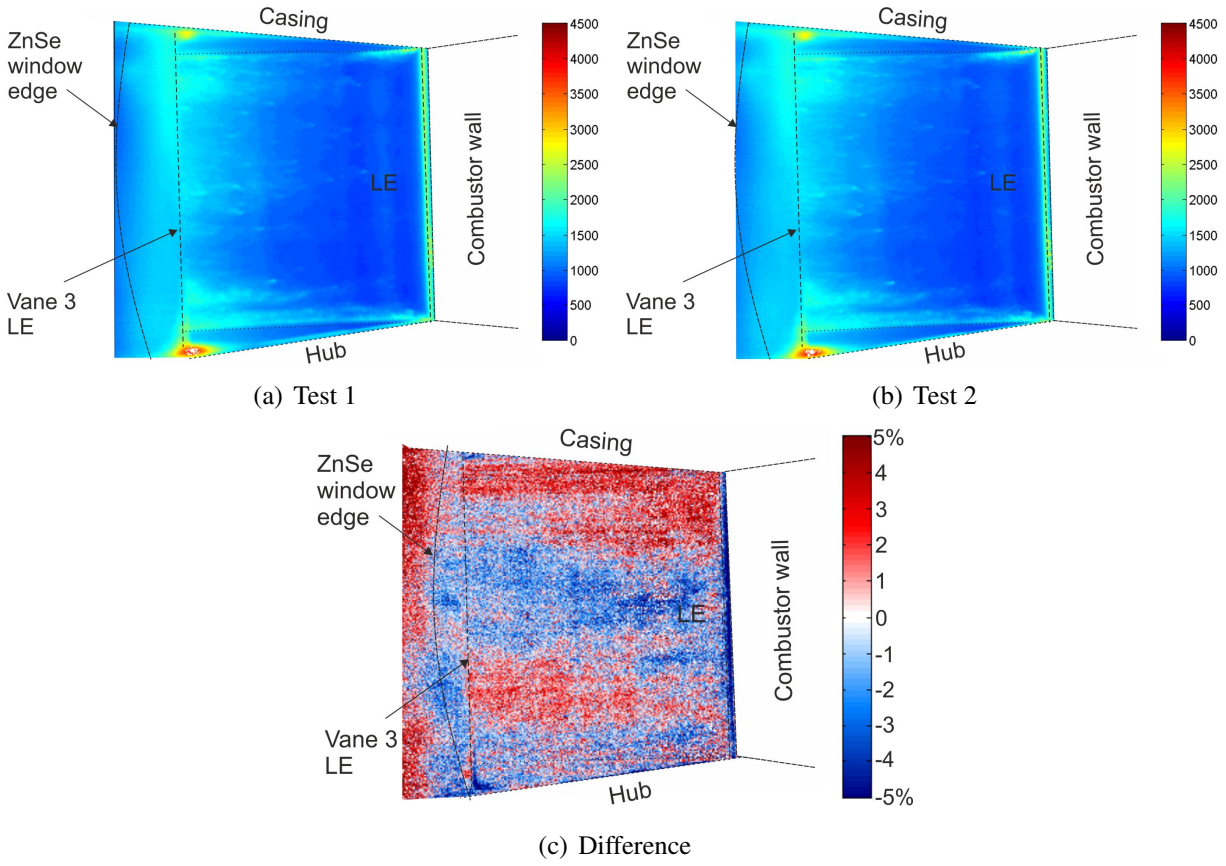

(a) Test 1

(b) Test 2

(c) Difference

Figure 3.28: Repeatability of heat transfer measurements

3.6 Summary

The design of the high speed experimental cascade was presented in this chapter, following the results of the preliminary numerical studies carried out. The experimental facility was presented in detail, including the inlet pressure control system, the flow conditioning unit, the heater mesh, and the working section. The main functionalities and modularity of the facility were highlighted,

including the inlet turbulence and swirl generators, and the vane clocking mechanism. The experimental facility provided a modular environment with the flexibility of a low speed facility for high speed studies. An overview of the measurement techniques used for aerodynamic and heat transfer studies was given, including a discussion on the processing of heat transfer measurements and measurement uncertainty and repeatability.

The effect of parameters such as the thermal conductivity of the material, the transmissivity of the ZnSe window, the non-reflective paint on the vanes, and the accuracy of the calibration of the probe and the camera are expected to affect in the same way all measurements obtained in the facility. This provides high confidence in the comparison of the aerodynamic and heat transfer performance of the different geometries.

Chapter 4
The Aerothermal Field in the Linear Cascade for the Datum Case

A detailed experimental investigation of the aerothermal interactions between the can combustor and the nozzle guide vane was carried out in the facility. This chapter presents the high speed aerodynamic and heat transfer measurements obtained for the datum cascade geometry. Measurements were obtained to characterize the inlet flow and to verify flow periodicity. Detailed aerodynamic measurements of the static pressure distribution on the vanes and endwalls, measurements of the flow downstream of the cascade, as well as measurements of the heat transfer were conducted and compared to the data obtained from numerical studies.

4.1 Upstream Traverse Measurements

One of the key aspects in achieving periodic flow in a linear cascade is the uniformity of the inlet flow. For this reason, two-dimensional traverse measurements of the flow at the exit of the combustor transition duct were conducted using the five-hole probe for the mainstream and the flat Pitot probes for the near wall regions. Both the total and the static pressure readings were the same between the two transition ducts, showing that the flow is well conditioned, with a uniform distribution of pressure and mass flow rate between the two ducts.

Figure 4.1 shows a total pressure loss coefficient map at 20% of the axial chord upstream of the vane leading edge. The mainstream flow had a uniform pressure distribution and the boundary layers on the duct were also captured. The variation in the boundary layer thickness, observed mainly at the hub endwall, was due to the design of the woven mesh that provides the temperature

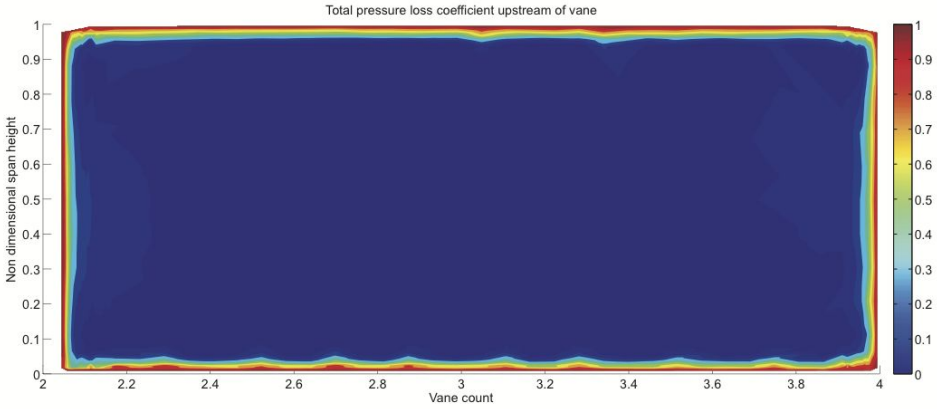

Figure 4.1: Total pressure loss coefficient upstream of the cascade

rise; the small cuts on the perimeter of the mesh may extend into the wetted surface of the mesh. The measured boundary layer thickness, defined here as the point where the total pressure loss is 1% of the inlet dynamic head, was 9.1 mm. The average pitch and yaw angles of the mainstream flow measured with the five-hole probe were zero, with variations within the measurement accuracy of the system. The mass-weighted pitchwise average total pressure loss coefficient is shown in Figure 4.2(a) and the spanwise averaged profile in Figure 4.2(b). Loss of the order of one inlet dynamic head was observed in the near wall regions, while a relatively constant pressure level was maintained in the mainstream flow.

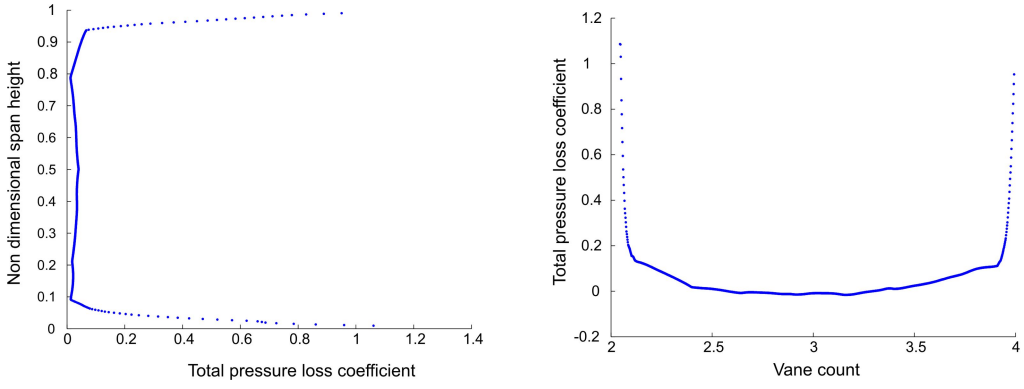

(a) Pitchwise averaged (b) Spanwise averaged

Figure 4.2: Mass-weighted average total pressure loss coefficient upstream of the cascade

A temperature profile was obtained at the same measurement plane. This was done over several runs in order to limit the operating time of the heater mesh. The non-dimensional temperature

relative to the upstream value is plotted against the non-dimensional span height in Figure 4.3. The temperature of the mainstream flow, from 20% to 50% span, was very close to the upstream value. The temperature near the wall was lower than the mainstream, reached a maximum at 15% span and then dropped again to the mainstream value.

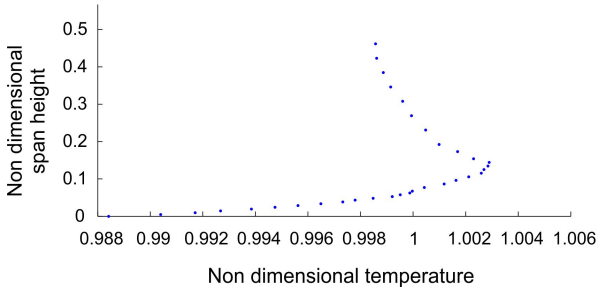

Figure 4.3: Inlet temperature profile

This temperature profile was the result of viscous dissipation that causes the temperature rise of the fluid as the kinetic energy of the flow is converted to internal energy in the boundary layer. As the surface was not insulated, the temperature near the wall was lower than the mainstream by $3\,\mathrm{K}$. This temperature profile causes a difference in the driving temperature profile between the vane and the endwall surfaces. In order to cancel out this effect and allow comparisons between the different experimental tests, the operating procedure was kept the same, with a set time of air flow before the heater mesh is turned on, followed by a set time of heater mesh operation and a set time of cool down. The time between each experimental test was also set, and the tests were carried out at the same ambient temperature. The effect of the inlet temperature profile was therefore the same for all experimental runs, allowing an accurate comparison between the different geometries for all operating conditions, which is the aim of this thesis.

4.2 Flow Periodicity

A series of experimental tests measuring the surface pressure distribution were carried out to assess the periodicity of the flow in the cascade. Different angles of the two tailboards were tested

and the surface pressure distributions were obtained for the three vanes in all cases. The different cases tested are presented in Table 4.1.

Table 4.1: Tailboard setup

PS tailboard	**SS tailboard**
70°	70°
71.5°	71.5°
73°	73°
Removed	71.5°

Figure 4.4 shows isentropic Mach number distributions on the three vanes at 10%, 50% and 90% span with the tailboard on the pressure side sidewall removed and the tailboard on the suction side sidewall at 71.5°. The vane numbering is shown in Figure 4.4(d). The flow periodicity achieved can be verified by the matching isentropic Mach number distributions of the three vanes

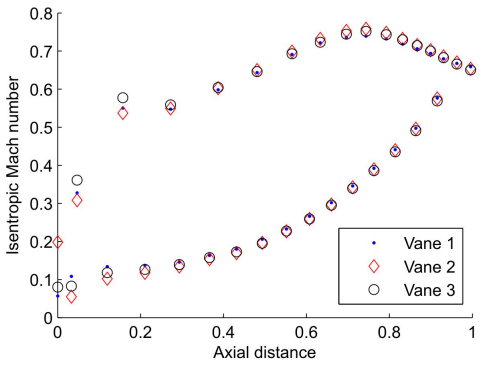

(a) 10% span

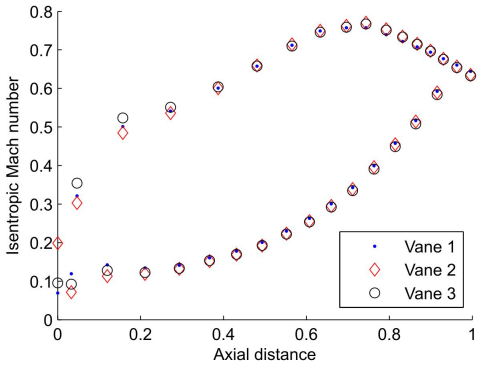

(b) 50% span

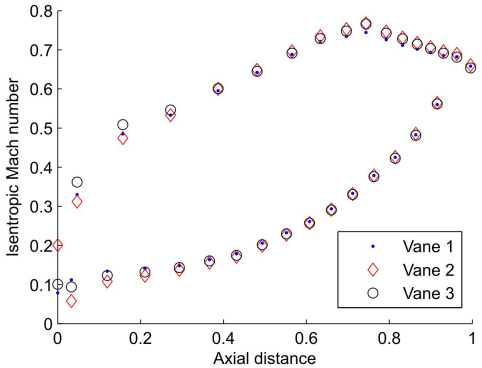

(c) 90% span

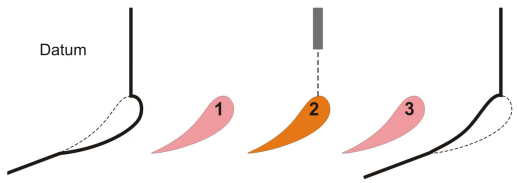

(d) Vane numbering

Figure 4.4: Isentropic Mach number distribution on the three vanes at three spanwise locations with the tailboard on the pressure side sidewall removed

at all spanwise locations. The removal of the tailboards has been reported to have beneficial effects on flow periodicity in high speed flows in an annular sector by Wiers and Fransson (2000). The removal of the tailboard on the pressure side sidewall also allowed significantly improved optical access for the IR camera from the downstream viewing locations.

The effect of the combustor wall on the isentropic Mach number distribution in the leading edge region was also captured in these measurements. The lower total and static pressure in the region downstream of the combustor wall resulted in a lower isentropic Mach number on the early suction side ($0-25\%$ axial chord) of vane 2 compared to the adjacent vanes. The same effect was observed on the vane pressure side, where the isentropic Mach number on vane 2 was also lower than the adjacent vanes in the region of $0-25\%$ of the axial chord.

4.3 Numerical Methods

The high speed cascade was designed in Autodesk Inventor and the flow domain was meshed using a hexahedral structured multi-block mesh in ICEM CFD. The flow through the cascade was modelled numerically using the pressure-based solver in commercial software Ansys FLUENT v13. At convergence, second-order discretization was used for all parameters.

4.3.1 Single Passage Studies

The flow through a single vane passage was studied using Ansys FLUENT to determine the most appropriate turbulence model and solver setup for the numerical studies. The different turbulence models tested for the single passage numerical studies are shown in Table 4.2. The numerical results obtained were compared to the experimental measurements to determine the most suitable model for both the aerodynamic and the heat transfer field. All models provided good agreement with the experimental data on the aerodynamic field, therefore the analysis focused on the heat transfer. The Spalart-Allmaras model captured the general trends on heat transfer on the vanes and endwalls but did not capture the particular effects on the vane surface seen in the experiment,

which is presented in section 4.4.2, and captured by the $k-\epsilon$ model. The $k-\omega$ model did not capture the general trends as well as the $k-\epsilon$ model did. The Reynolds Stress Model provided similar results to the $k-\epsilon$ model, but at a higher computational cost. Overall, the most suitable turbulence models were found to be the $k-\epsilon$ realizable model with standard wall functions and the Reynolds Stress Model with standard wall functions.

Table 4.2: Turbulence models tested for single passage numerical studies

Turbulence model	**Options**
Spalart-Allmaras	-
$k-\epsilon$	Standard, standard wall functions
$k-\epsilon$	RNG, standard wall functions
$k-\epsilon$	Realizable, standard wall functions
$k-\epsilon$	Realizable, enhanced wall treatment
$k-\omega$	Standard
$k-\omega$	SST
Reynolds Stress Model	Standard wall functions
Reynolds Stress Model	Non-equilibrium wall functions

4.3.2 Two Passage Studies

A grid independence study was carried out to determine the minimum meshing requirements for both the aerodynamic and the thermal flow field. The domain modelled was a rectangular duct with two vane passages, as shown in Figure 4.5. These studies used the total pressure profile obtained from experimental studies in the facility for the inlet boundary conditions. Periodic boundary conditions were set on the sides, in an infinite cascade setup, to allow comparison with experimental measurements with half the mesh size compared to that required for a four passage cascade.

The different grid sizes tested are shown in Table 4.3. Both the $k-\epsilon$ realizable model with standard wall functions and the Reynolds stress model with standard wall functions were tested.

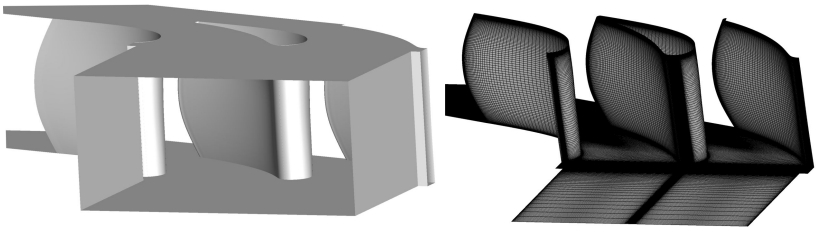

(a) Computational domain (b) Computational mesh

Figure 4.5: Domain and mesh for two passage studies

Good agreement with the aerodynamic experimental data was achieved with both models, but the $k - \epsilon$ model was found to be more time-efficient and robust for the range of numerical studies carried out and agree better with the experimental studies for the heat transfer field. The solution was found to be grid independent for 10.5 million cells. It should be noted that grid independence for the aerodynamic flow field was achieved with the coarse grid.

Table 4.3: Grid sizes tested for two passage numerical studies

Grid	**Cell number**
Coarse	3×10^6
Medium	6×10^6
Fine	10.5×10^6
Extra fine	17×10^6

The convergence criteria used for these simulations were that the residuals were flat and had dropped by at least three orders of magnitude, and six in the case of the energy variable. The overall mass imbalance for the domain was checked to ensure it was below 0.1% of the inlet mass flow rate, and the integral of the heat transfer coefficient was checked to ensure it was not changing with successive iterations. Figure 4.6 shows a typical convergence history.

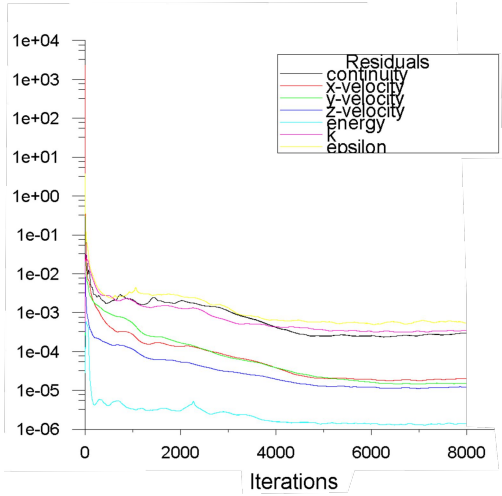

Figure 4.6: Scaled residuals showing a typical convergence history

4.3.3 Four Passage Studies

For the study of the aerodynamic flow field, where a smaller mesh size is required to achieve grid independence, numerical studies of the flow in the linear cascade were carried out using a computational domain consisting of two transition ducts and four vane passages, with the same model setup and mesh structure as the domain for the two passage studies. This domain was used to optimize the flow periodicity setup and the design of the sidewalls presented in section 3.2. The grid size for this study was coarser than for the heat transfer studies, with 6 million cells, enough to provide grid independence for the aerodynamic field.

4.4 Experimental and Numerical Results for the Datum Case

The aerodynamic and heat transfer measurements for the datum configuration are presented in this section. For the heat transfer numerical studies presented in this chapter, the domain modelled was a single rectangular transition duct and two vane passages, with periodic boundary conditions on the sides, to allow comparison with experimental measurements with a smaller mesh size compared to that required for a four passage cascade. The mesh size for these studies was 10.5 million

cells and the results presented here were obtained with the use of the k-ϵ turbulence model. The inlet total pressure boundary conditions were those obtained from the experimental measurements.

4.4.1 Aerodynamic Results

4.4.1.1 Static Pressure Measurements

Static pressure measurements at mid-span on the central vane are compared to CFD data in Figure 4.7(a) in the form of isentropic Mach number. The stagnation point was located on the early pressure side, at approximately 5% of the axial chord. After an initial high acceleration until 15% of C_{ax} the flow accelerated slowly over the pressure surface until 60% of C_{ax}. At that point the acceleration became significantly higher all the way to the trailing edge of the vane. On the vane suction side, the flow was accelerated highly around the leading edge, from the stagnation region until 15% of C_{ax}, when the acceleration became more gradual until the peak velocity occured at 75% of C_{ax}; the flow was then decelerated smoothly until the trailing edge. Overall good agreement was observed between the experimental measurements and the numerical result, though CFD underpredicted the flow acceleration and isentropic Mach number on the late pressure side.

The wake of the combustor wall was directed toward the vane suction side, as seen in Figure 4.7(b), and carried total pressure loss. The static pressure field was also affected by the combustor wall, as discussed before, resulting in lower isentropic Mach number in the leading edge region: static pressure contours at midspan around the central and the adjacent vane are shown in Figure 4.7(c).

Surface pressure measurements were also obtained for the hub and casing endwalls at four pitchwise locations for each vane passage. The data was interpolated to provide maps of surface static pressure, non-dimensionalized by the inlet total pressure, which are shown in Figure 4.8(a) for the hub and Figure 4.8(b) for the casing endwall. In both figures the experimental measurements are shown on the left hand side and numerical results on the right hand side. The black lines mark the area where the measurement points (noted with black dots) are located. The comparison

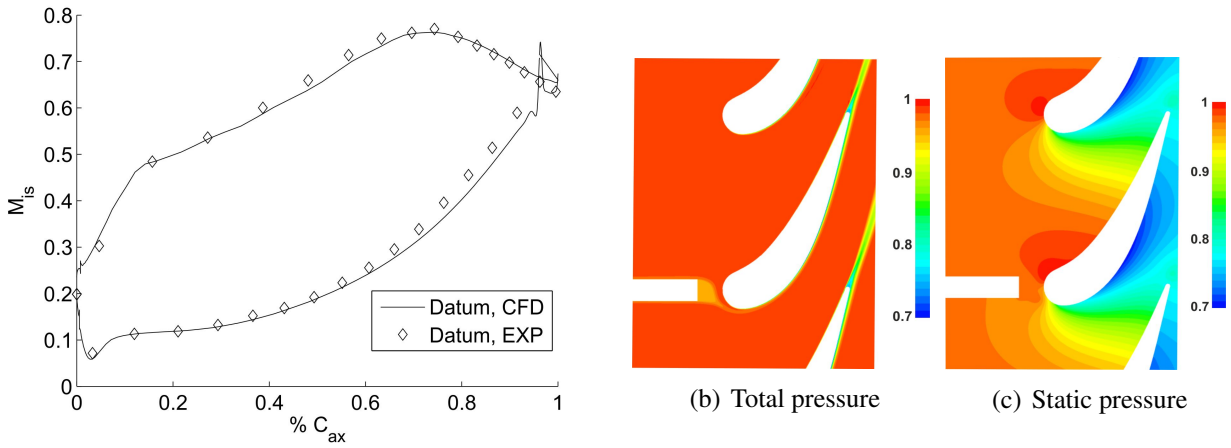

(a) Isentropic Mach number for the central vane

(b) Total pressure

(c) Static pressure

Figure 4.7: Isentropic Mach number (experimental result) and pressure field (numerical result) at mid-span

of the experimental to the numerical data shows good agreement in the measured region (from 20% to 80% pitch); the flow periodicity achieved in the cascade extended to the low momentum endwall flow.

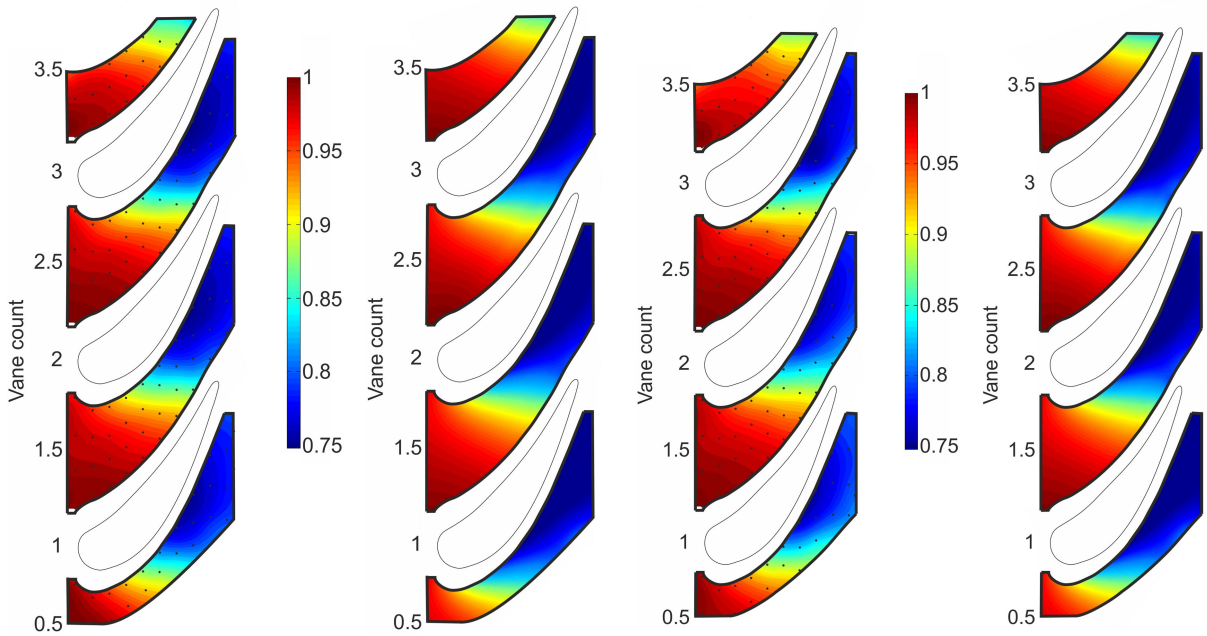

(a) Hub endwall

(b) Casing endwall

Figure 4.8: Non-dimensional static pressure on the endwalls, experimental measurement (left) and numerical prediction (right)

4.4.1.2 Flow Field Measurements Downstream of the Cascade

Flow periodicity was verified with a traverse with the five-hole probe at 20% of the axial chord downstream of the cascade at mid-span. The total pressure loss coefficient (relative to the outlet dynamic head) obtained for the cascade is shown in Figure 4.9. The total pressure in all passages was the same, and so was the loss in the wakes of vanes 1 and 3. The maximum total pressure loss coefficient for the central vane was 10% higher than vanes 1 and 3 and the wake of the vane was wider.

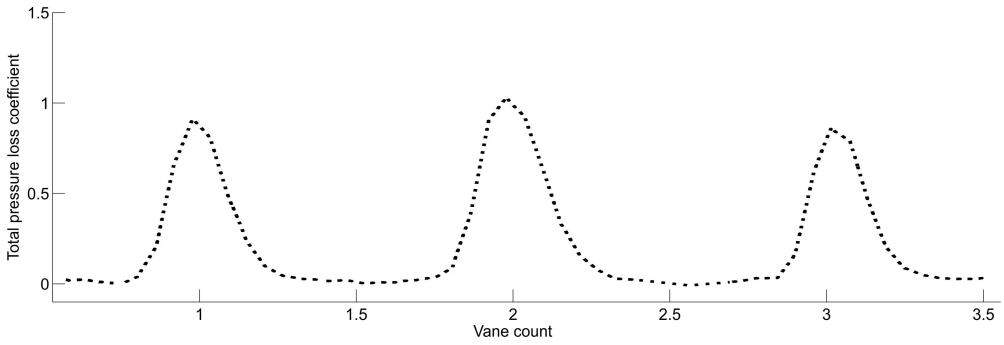

Figure 4.9: Total pressure loss coefficient at mid-span

A spatially resolved map of the total pressure downstream of the cascade was obtained with the five-hole probe. The total pressure loss coefficient is shown in Figure 4.10. The wakes of the three vanes followed the curvature of the vane trailing edge, due to the three-dimensional vane profile used. The wake of the central vane was significantly wider than the wakes of the adjacent vanes, in agreement with the observation at mid-span, due to the presence of the combustor transition duct wall upstream of the vane, which introduced additional loss. It is noted that the total pressure loss coefficient for all vanes was based on clean flow and did not include the total pressure deficit in the wake of the wall.

The total pressure loss showed two peaks at 20% and at 80% span, which coincided with the locations of the passage vortex. The loss arose from the pressure side leg of the passage vortex, which has high aerodynamic loss associated with it (Langston et al., 1977, Sharma and Butler, 1987). Moderate loss was observed further away from the endwalls, as seen in the mass-

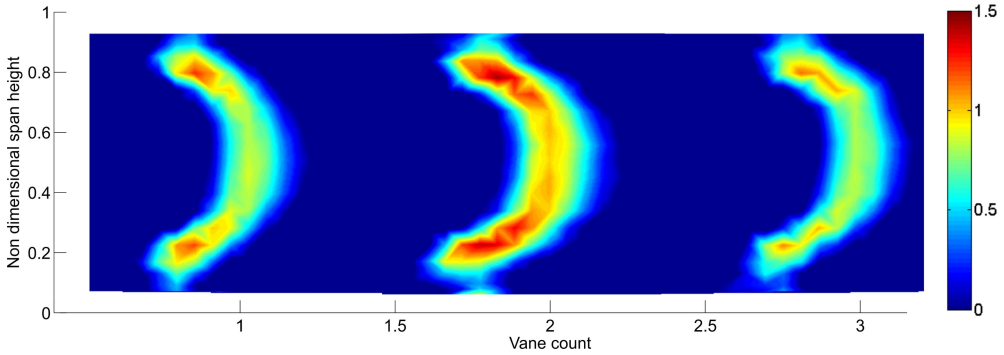

Figure 4.10: Spatially resolved total pressure loss coefficient map downstream of the cascade

weighted pitchwise average data for the three vanes in Figure 4.11. The mass-weighted average total pressure loss coefficient downstream of the central vane was 9.2% of the outlet dynamic head higher than the adjacent vanes. Dotted lines have been used to connect the experimental data points in the mass-weighted pitchwise average plots to assist the reader in identifying the differences between the parameters measured.

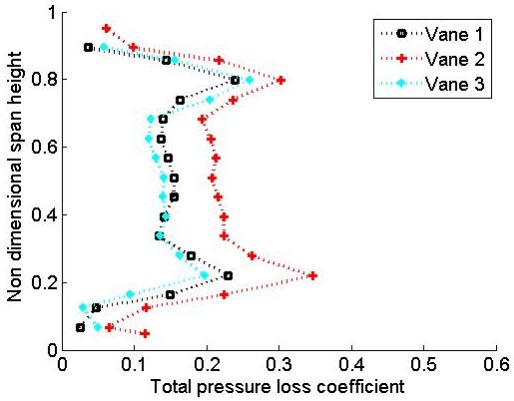

Figure 4.11: Mass-weighted pitchwise average total pressure loss coefficient downstream of the cascade

The distribution of yaw angle downstream of the cascade, as obtained by the five-hole probe measurements, is shown in Figure 4.12 for the central vane passage. The region of the wake showed overturning of the flow downstream of the vane trailing edge from 20% to 80% span that followed the curvature of the vanes. Near the endwalls, the secondary flow that develops through the passages leads to underturning of the flow. The range of yaw angle from hub to casing is within 5° in the passage and 15° in the wakes of the vanes. The five-hole probe could not

capture the endwall boundary layers, as the minimum measurement distance from the wall was 5 mm. However, some overturning of the flow between the wakes was captured near the endwalls

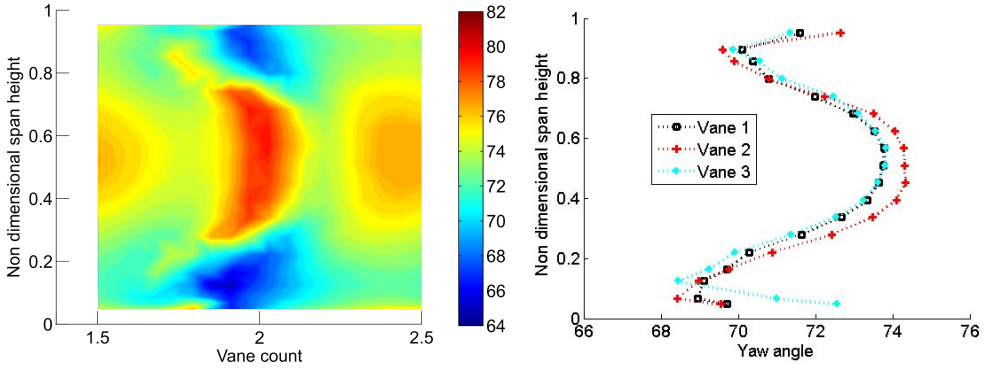

(a) Spatially resolved (b) Mass-weighted pitchwise average

Figure 4.12: Yaw angle downstream of the cascade

and is clearly seen in the mass-weighted pitchwise average data in Figure 4.12(b). The yaw angle distribution for the three vanes was similar, with the central vane showing marginally higher overturning at mid-span and higher underturning near the endwalls. The maximum difference in yaw angle was less than 1°, in the mid-span region.

Evidence of secondary flow in the cascade was also seen in the pitch angle distribution downstream of the cascade, Figure 4.13. Regions of highly rotating flow were observed near the hub and casing endwalls downstream of the vane trailing edge. The flow was rotating clockwise near the hub and anticlockwise near the casing. The locations of the counter-rotating flow on the endwalls were downstream of the suction side of the vanes. The sense of rotation of the flow was as expected by the passage vortex that develops through the passage and was in agreement with the simple model of endwall flow phenomena described by Langston (1980). The extent of the passage vortex was significant, covering 20% of the vane span on both the hub and the casing, in agreement with experimental studies in the literature presented in Chapter 2.

4.4.1.3 Effect of Non-Reflective Paint on the Aerodynamic Flow Field

As discussed in Chapter 3, the vanes and endwalls were painted with a special black coating to minimize reflections that could affect the heat transfer measurements; aerodynamic and heat

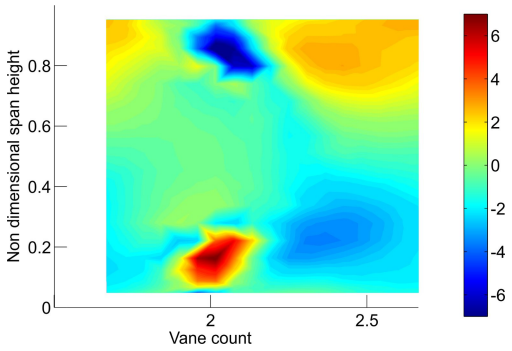

Figure 4.13: Spatially resolved pitch angle downstream of the cascade

transfer measurements were obtained on the painted vanes. The effect of the increased surface roughness due to the layer of matt black paint on the aerodynamic loss of the vanes was analysed through a comparison of data collected on a painted and on an unpainted vane. The mass-weighted pitchwise average total pressure loss coefficient downstream of the central vane is shown in Figure 4.14(a). The mass-weighted pitchwise average yaw angle is shown in Figure 4.14(b). CFD data is also shown in both figures.

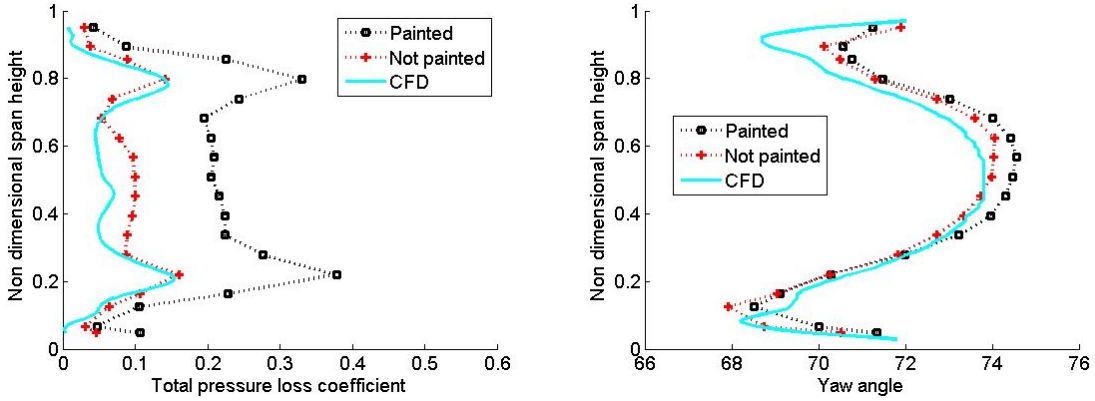

(a) Total pressure loss coefficient

(b) Yaw angle

Figure 4.14: Mass-weighted pitchwise averaged data downstream of unpainted and painted vane

The effect of paint on the aerodynamic loss was significant, with an increase in the average loss of 10.5% of the outlet dynamic head compared to the unpainted vane. This effect was uniform on the entire vane surface aside from the area from $5 - 15\%$ and from $85 - 95\%$ span, which was outside the wake of the vane and was not affected by the endwall loss. The loss cores were also stronger but their location was not altered; the paint was not seen to affect secondary flow

structures. CFD captured the location of the loss cores and the magnitude of total pressure loss downstream of the vane and was seen to underpredict total pressure loss in the region from $30 - 70\%$ span. The flow turning downstream of the central vane was not significantly affected by the surface roughness due to the non-reflective paint. The difference in yaw angle between the two cases was less than 0.5° at mid-span. CFD was seen to agree with the experimental data for the bottom half of the vane. In the region from $50 - 100\%$ span, the flow was affected by the continuous slot at the casing for the five-hole probe traverse, which caused an asymmetry in the yaw angle distribution between the hub and the casing in the experimental results.

4.4.1.4 Secondary Flow

The strength and characteristics of the secondary flow field in the linear cascade are further analysed with the help of the numerical studies carried out. The aerodynamic results presented showed higher loss for the central vane, which was due to the upstream combustor wall, but did not capture the effect of the wall on the secondary flow that affects heat transfer to the vanes and endwalls. Non-dimensional streamwise vorticity coefficient contours on the leading edge of vanes 1 and 2 are shown in Figures 4.15(a) and 4.15(b) respectively. The presence of the combustor wall altered

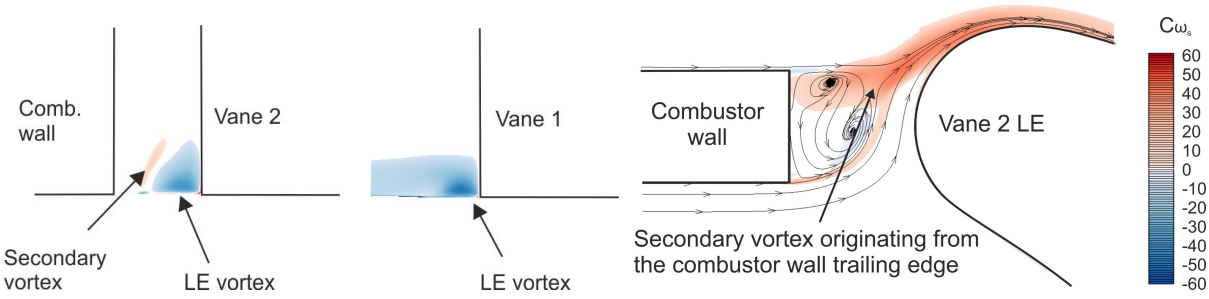

(a) Central vane LE (b) Adjacent vane LE (c) Leading edge of the central vane at 8% span

Figure 4.15: Non-dimensional streamwise vorticity contours on the vane leading edge

the horseshoe vortex development upstream of the vanes. The shape of the horseshoe vortex on vane 2 (central vane) was different from the adjacent vanes; the vortex was larger and the maximum vorticity at its core was lower. The horseshoe vortex on the leading edge of vane 1 was flat and elliptical in shape, whereas the vortex on the central vane had a triangular shape and extended

to a greater percentage of the vane span. A second vortex, with opposite sense of rotation, formed immediately upstream and above the horseshoe vortex on the leading edge of the central vane. This vortex, which was only present on the central vane, went around the leading edge towards the suction side of the vane and stayed above the suction side leg of the horseshoe vortex. Its size and strength were significantly smaller than the horseshoe vortex. The difference in the horseshoe vortex geometry and the appearance of the secondary vortex were caused by the combustor transition duct wall. As the flow approached the leading edge of the vane from the pressure side, it could not deflect towards the suction side as early as in the case of the adjacent vane, due to the presence of the wall. As it went around the wall, the flow near the endwall was forced to roll away from the endwall due to the presence of the horseshoe vortex. This resulted in a vortex with an opposite sense of rotation to the horseshoe vortex forming on the wall and moving towards the vane suction side with the bulk flow. Figure 4.15(c) shows non-dimensional streamwise vorticity contours around the central vane. This plot is on the blade-to-blade plane at 8% span. The secondary vortex is seen between the combustor wall and the suction side of the central vane. In the adjacent vane no other vortex was present apart from the horseshoe vortex.

4.4.2 Heat Transfer Results

The heat transfer distribution on the vanes and endwalls was measured using IR thermography as described in sections 3.5.2 and 3.5.2.1. Experimental data was obtained for the vane leading edge and the early pressure side, viewed from upstream, as well as the vane suction side and the hub endwall viewed from downstream. The view from all locations was limited by the lens of the camera, the edges of the window, and the viewing angle. The data outside the viewing limit is either at a very shallow viewing angle, resulting in high measurement uncertainty, or is a view of the supporting structure for the working section, that is facing no flow. It is also noted that data at the trailing edge of the vane is not accurate due to the reduced material thickness in the region which results in a violation of the semi-infinite assumption, as discussed in section 3.5.2.1. The

viewing limits are marked in the following figures with a black dotted line. The hub and casing endwalls are at a shallow viewing angle in all views apart from the explicitly stated hub endwall views. The endwalls and combustor wall upstream of the cascade have been removed altogether from the figure, as the semi-infinite assumption is not valid for the heat transfer to those surfaces. The heat transfer data obtained from this method is presented in the non-dimensional form of the Nusselt number. Numerical data for the heat transfer on the vanes and endwalls was obtained from the solution of two otherwise identical cases with different isothermal boundary conditions on the vane and endwall surfaces, which allowed the determination of the heat transfer coefficient and the adiabatic wall temperature.

The Nusselt number on the pressure side of the central vane is shown in Figure 4.16(a). The experimental measurements showed Nusselt numbers of 1300 immediately downstream of the combustor. These dropped to half as the flow started accelerating downstream of the stagnation point, and increased to 1500 at the mid-span of the vane. An overprediction of heat transfer levels near the stagnation region was observed in CFD studies, Figure 4.16(b), with a Nusselt number above 2000. Further downstream on the vane surface, the Nusselt number dropped to 1000 and gradually increased again towards the mid-chord. Higher heat transfer was also observed on the vane surface close to the endwalls at 10% and 90% span. The agreement between the experimental and the numerical studies was not very good on Nusselt number levels, but the CFD captured the trends observed in the experiments. The high Nusselt number spots on the vane surface seen in the experimental studies were due to imperfections in the paint applied to the vane, resulting in locally increased surface roughness.

Figure 4.17(a) presents the Nusselt number distribution on the leading edge of the central vane. The combustor wall can be identified on the left hand side of the figure, and the late pressure side of vane 1 on the right hand side. The Nusselt number on the vane surface immediately downstream of the combustor wall was 1200 and corresponded to the part of the vane that was protected and faced the wake of the combustor wall trailing edge. Further downstream, as the flow accelerated

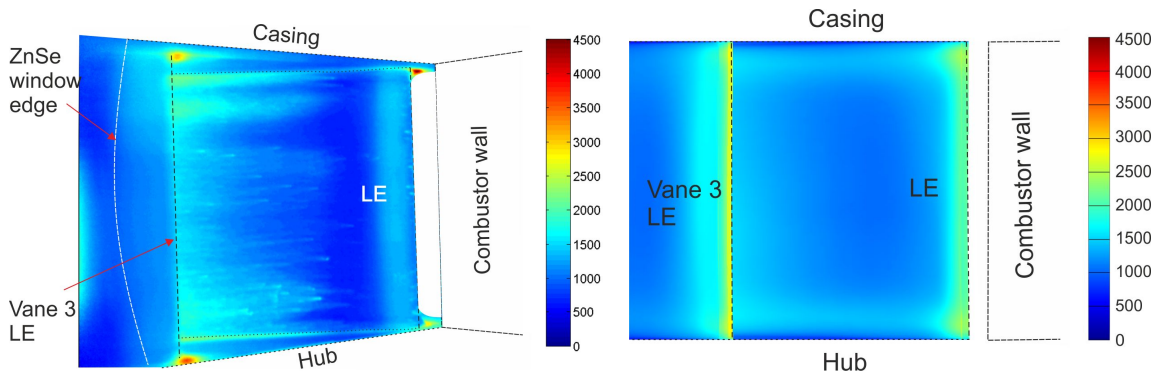

(a) Experimental measurement (b) Numerical result

Figure 4.16: Nusselt number distribution on the vane pressure side (view 1, Figure 3.25(a))

around the vane leading edge, the heat transfer was significantly increased, and the Nusselt number rose to 3000. An even higher Nusselt number was observed near the hub and casing, 3500. This was where the horseshoe vortex that formed ahead of the vane leading edge reached the vane surface. As the vortex wrapped around the vane leading edge, it caused the flow to roll into the vortex, increasing the local heat transfer to the vane immediately above the location of the vortex on the suction side. This feature was in agreement with observations in the literature (Goldstein et al., 1995). The particular shape of the horseshoe vortex on the leading edge of the central vane, which extended further away from the endwall on the vane surface compared to the adjacent vane, and the presence of the secondary vortex resulted in a peak in heat transfer near the hub and casing at 6% span, immediately above the low heat transfer trail of the vortex on the vane surface.

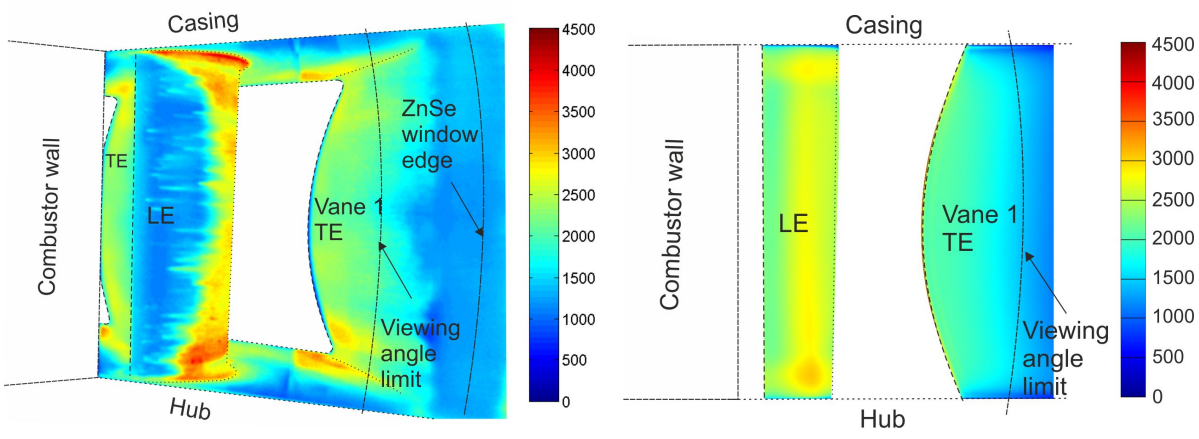

(a) Experimental measurement (b) Numerical result

Figure 4.17: Nusselt number distribution on the vane leading edge (view 2, Figure 3.25(b))

Figure 4.17(b) presents numerical predictions of the Nusselt number in the same location. The Nusselt number immediately downstream of the combustor wall was higher in the CFD, as discussed for the vane pressure side. The Nusselt number increased to 2800 in the transition region and locally to 3000 and 3200 on the casing and hub respectively, in the region just above the leg of the horseshoe vortex on the vane suction side. With the exception of the vane leading edge, CFD marginally underpredicted heat transfer levels on the vane surface, and predicted flow transition earlier on the vane suction side compared to the experimental studies. This is thought to be caused by the errors in the estimation of the turbulence properties in the numerical studies.

On the late pressure side of vane 1, CFD predicted a Nusselt number of 2000 in comparison to 2300 in the experiment. The hot spot on the vane surface close to the hub and near the trailing edge in Figure 4.17(a) was not seen in the numerical results and did not seem to be caused by a flow feature that is captured by the CFD. This is attributed to a local imperfection on the vane surface.

The heat transfer patterns on the suction side of the central vane, Figure 4.18, were in agreement with the characteristics seen on the early suction side from the upstream viewing port. The leading edges of the vanes were not seen in this figure, due to the curvature of the vanes and the viewing angle. The first point of the central vane on the left hand side of each figure corresponds to 50% of the axial chord, and the leading edge of the vane is behind this. The trailing edge of the central vane is seen on the right hand side. The trailing edge of vane 1 is also seen on the left hand side of the figure and part of the suction side of vane 3 is seen on the right hand side.

In the central region of the vane span, from $30 - 70\%$, the maximum Nusselt number was observed on the early suction side, in agreement with the increased Nusselt number in the transition region. The heat transfer on the vane surface then decreased gradually until the trailing edge of the vane. The Nusselt number in the experimental studies ranged from 2500 at mid-chord to 1900 at the trailing edge region. In the numerical studies, the Nusselt number was seen to drop faster

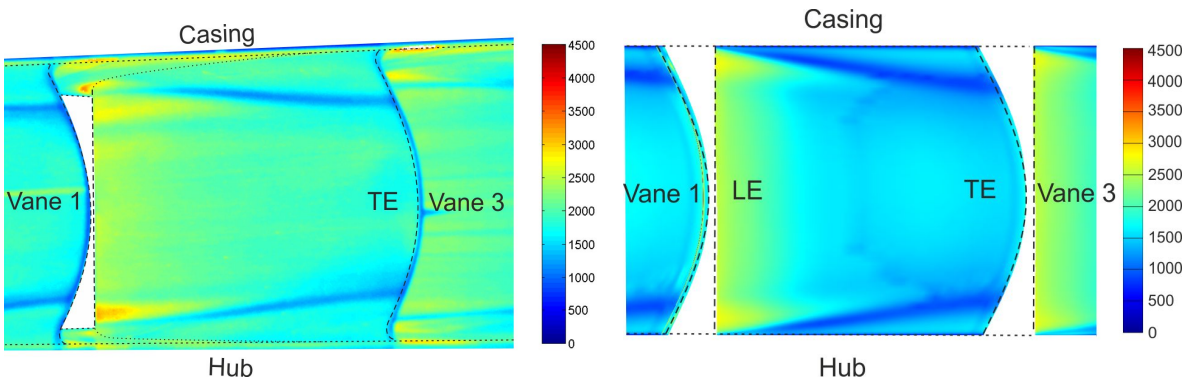

(a) Experimental measurement (b) Numerical result

Figure 4.18: Nusselt number distribution on the vane suction side (view 3, Figure 3.25(c))

after the transition region, from 2500 at mid-chord to 1700 at 70% of C_{ax} and down to 1500 at the trailing edge.

Closer to the endwalls, the heat transfer distribution is more interesting, with more features due to secondary flow structures. The main feature was the low Nusselt number trails near the hub and casing. These were linked to the passage vortex on the vane suction side and were seen to penetrate to $15-20\%$ of the vane span at the trailing edge of the vane, which was in agreement with the observations from the aerodynamic measurements presented in the previous section. A region of higher heat transfer was observed closer to the endwalls, below the vortex on the hub and above the vortex on the casing. Another higher heat transfer region was observed on the other sides of the vortices near the mid-chord of the vane. Those higher Nusselt number trails which continued from the peaks observed in the leading edge region, were immediately above the suction side leg of the horseshoe vortex, which begins to lift off the endwall when the passage vortex reaches the vane suction side. The higher heat transfer then dissipated after 70% of C_{ax}. The peak Nusselt number in the region near the endwalls was 3000 in the experimental measurements and 2800 in the numerical calculations. Further downstream, the Nusselt number near the endwalls was 1800, and 1200 in the passage vortex trails. The numerical results captured the same trends, underpredicting the Nusselt number by 200.

The features depicted in the heat transfer measurements are better understood when looking at the secondary flow structures around the vane. The origin of the high heat transfer region on the vane surface near the leading edge, occurring at approximately 20% and 80% span, is the pair of counter-rotating vortices from the leading edge of the central vane seen in the numerical studies in Figure 4.15(a). The secondary vortex sits above the suction side leg of the passage vortex as seen in Figure 4.19(a), which shows non-dimensional axial vorticity contours at 0%, 5% and 10% of the axial chord. This results in mainstream flow impacting the vane surface between the vortices, increasing the heat transfer in that region. The lower heat transfer region on the side of the mid-span of the vane corresponds to the trail of the secondary vortex on the vane surface. On the adjacent vane, the absence of the secondary vortex, Figure 4.19(b), results in an extended region of high heat transfer above the suction side leg of the horseshoe vortex.

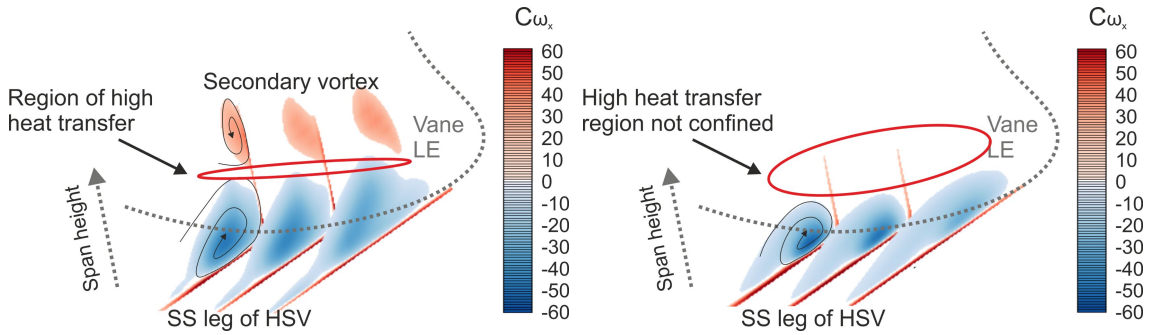

(a) Central vane (b) Adjacent vane

Figure 4.19: Origin of the high heat transfer region on the vane leading edge (view from upstream)

As a result of this secondary flow structure, the heat transfer in the leading edge region of the central and the adjacent vane, obtained from numerical studies, is shown in Figure 4.20. The high heat transfer region on the central vane is limited, Figure 4.20(a), and confined by the pair of counter-rotating vortices. On the adjacent vane the heat transfer on the vane leading edge is higher and the peak near the endwall is not confined, Figure 4.20(b).

Further downstream on the vane surface the region of low heat transfer starts when the passage vortex reaches the vane suction side. In that region a counter-rotating tertiary vortex is induced by the passage vortex as noted in the secondary flow model of Wang et al. (1997). This results

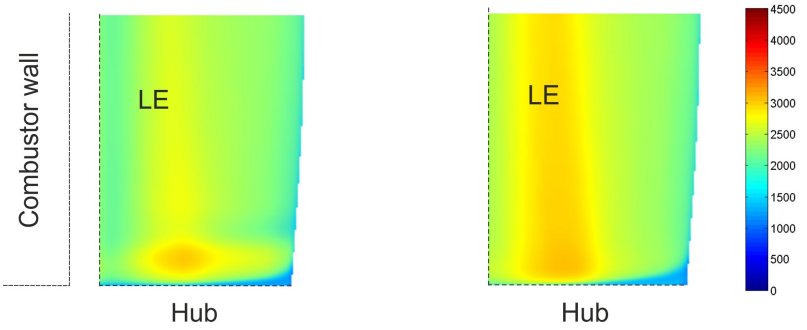

(a) Central vane (b) Adjacent vane

Figure 4.20: Heat transfer on the vane leading edge (view from upstream), numerical result

in low heat transfer which corresponds to the trails of this tertiary vortex on the vane surface, Figure 4.21. This figure shows circumferential vorticity contours at 85%, 90%, and 95% of the axial chord. On the side of the tertiary vortex which is closer to the endwall, the passage vortex lifts off the boundary layer from the vane surface, bringing mainstream flow closer to the vane and resulting in increased heat transfer, at levels similar to those observed away from the endwalls.

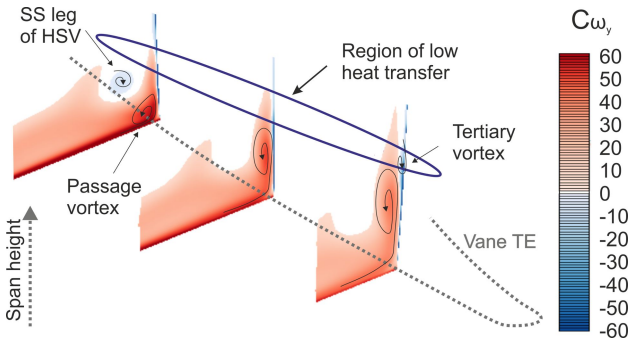

Figure 4.21: Origin of the low heat transfer regions on the suction side of the vane near the trailing edge (view from downstream)

Figure 4.22 presents the Nusselt number distribution on the hub endwall. This view includes part of vanes 1, 2, and 3, as well as the endwall in the passages between them. The same features discussed in Figure 4.18 were observed here on the vane surface and the Nusselt number values were in agreement with those measured on the vane suction side, indicating the repeatability of the results. The Nusselt number levels in the early parts of the endwall were lower than the vanes, due to the presence of the boundary layer in the incoming flow. The endwall boundary layer then separated as it reached the vane leading edge and was entrained into the horseshoe vortex. Further

downstream on the vane passage, as the pressure side leg of the vortex was swept towards the suction side of the vane, the fluid was accelerated into the vortex, increasing the heat transfer in the region downstream of the separation line. The flow separation allowed a new boundary layer to form on the endwall downstream of the separation lines, thus increasing Nusselt number levels from 1000 upstream of the separation lines to 2200 downstream. This was also captured by CFD, with good agreement on Nusselt number levels on the endwall. The smoother Nusselt number distribution in Figure 4.22(b) was due to the absence of misalignments in the numerical model compared to the experimental case.

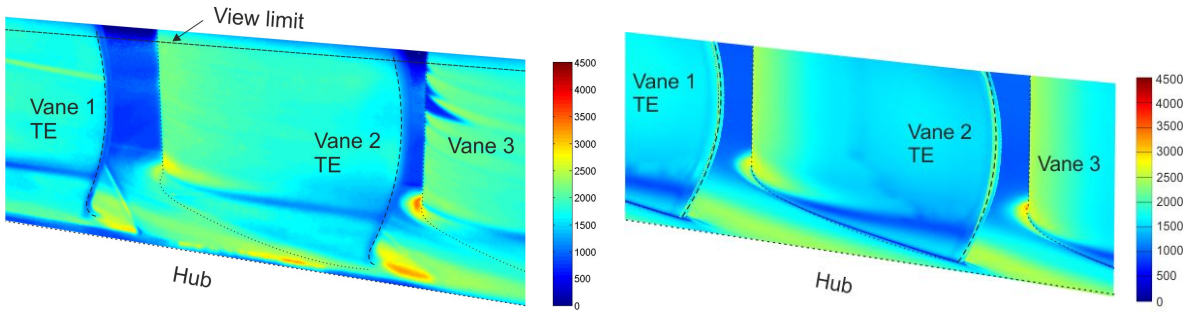

(a) Experimental measurement (b) Numerical result

Figure 4.22: Nusselt number distribution on the hub endwall viewed from downstream (view 5, Figure 3.25(e))

Another significant feature on the endwall was the peak Nusselt number on the endwall on the early suction side, which has been identified in studies by Graziani et al. (1980) and Goldstein et al. (1995). For vane 3 the peak Nusselt number was 3500, whereas for vane 2 it was 2700. This difference was observed in both the experimental and the numerical result and was due to the difference in the suction side leg of the horseshoe vortex between vane 3 and the central vane. Figure 4.23 shows non-dimensional vorticity contours at the leading edge and at 15% of the axial chord on the suction side of the vane for the central and the adjacent vane viewed from upstream. The flat elliptical shape of the vortex upstream of vane 3, Figure 4.23(b), resulted in a greater unprotected area in the junction of the vane suction side and the endwall, with high heat transfer rates. On the other hand, the triangular vortex upstream of the central vane stayed closer to the vane surface, providing better protection from the mainstream flow and moderate heat transfer

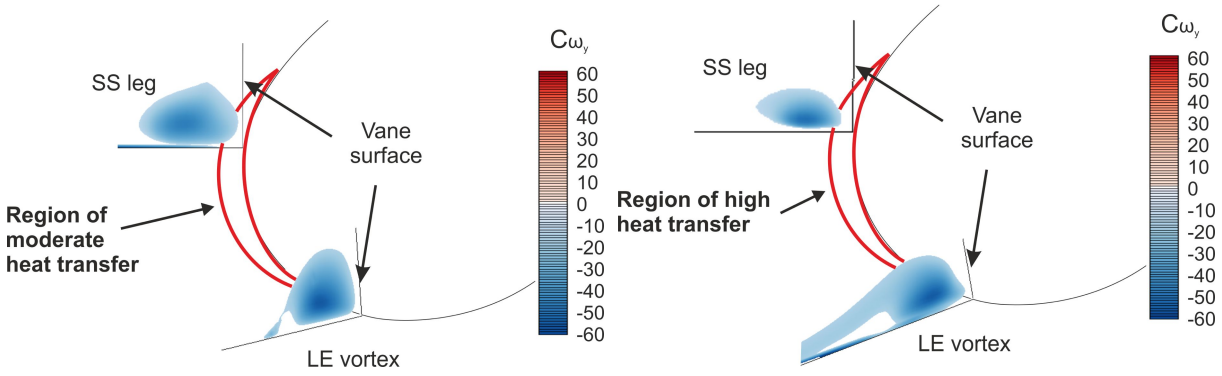

(a) Central vane (b) Adjacent vane

Figure 4.23: Origins of the high heat transfer regions on the suction side-endwall junction near the vane leading edge (view from upstream)

rates in comparison to the adjacent vane. The alteration of secondary flow structures on the central vane due to the presence of the combustor wall has therefore resulted in a significant reduction of the peak heat transfer to the endwall. The difference in Nusselt number on the endwall between the central and the adjacent vane is seen in Figure 4.24. This figure shows the numerical result on the endwall region of the two vanes around the leading edge. The CFD does not agree with the magnitude of the reduction, which is higher in the experiment, but captures the trend and the cause of the phenomenon.

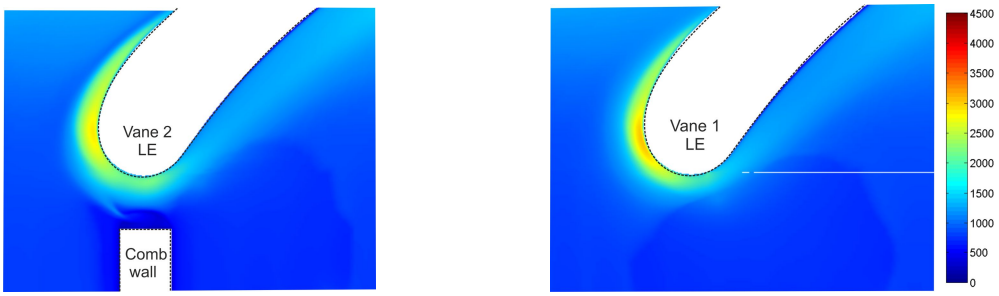

(a) Central vane (b) Adjacent vane

Figure 4.24: Heat transfer on the vane endwall, numerical result

4.5 Conclusions

The aerodynamic and heat transfer measurements for the linear cascade in the datum configuration were presented in this chapter. Measurements of the upstream flow showed the flow uniformity that, along with the design of the sidewalls, allowed the setting of periodic flow in the cascade. Static pressure measurements were obtained on the three vane locations for different tailboard angles and it was found that the optimum angle with the use of two tailboards is 71.5°. The removal of the tailboard on the pressure side sidewall showed a beneficial effect on flow periodicity, therefore the experiments were carried out with the tailboard on the suction side sidewall only. The aerodynamic measurements were compared to numerical studies that were carried out on a computational domain of one combustor transition duct and two vane passages. This included static pressure measurements on the surface of the vane and the endwalls. The measurements on the hub and casing endwall verified that flow periodicity extends to the endwall regions.

Flow measurements downstream of the cascade conducted with a five-hole probe provided a detailed map of the total pressure loss coefficient with good resolution of the vane wakes. The loss downstream of the central vane was found to be significantly higher than the adjacent vanes due to the additional total pressure loss from the upstream combustor wall trailing edge. The wake of the central vane was wider and the loss cores were greater in size and magnitude, resulting in a mass-weighted average value that was 9.2% of the outlet dynamic head higher. The passage vortex was seen to cover 20% of the vane span near the hub and the casing, agreeing with the findings of experimental studies in the literature.

A comparison of the total pressure loss coefficient distribution downstream of a painted and an unpainted central vane showed the effect of the added roughness of the non-reflective paint on the aerodynamic loss. The mass-weighted pitchwise average total pressure loss coefficient downstream of the vane was increased by 50% in the region of $15 - 85\%$ span for the painted vane, whereas the region outside this, between the end of the wake of the vanes and the endwalls,

was not significantly affected. CFD captured the effects of secondary flow on the aerodynamic loss and underpredicted total pressure loss coefficient in the region of $30 - 70\%$ span. The effect on the flow turning downstream of the vane was small, with a maximum difference of 0.5° in the yaw angle, with higher turning for the painted vane.

The secondary flow in the cascade was analysed with a comparison of the streamwise vorticity on the leading edge of the vanes, obtained through CFD to provide better understanding of the flow that affects heat transfer to the vanes and endwalls. The central vane showed a larger vortex on the leading edge compared to the adjacent vanes, with lower vorticity at the core. A secondary vortex with an opposite sense of rotation was found to arise immediately upstream and above the horseshoe vortex on the central vane and follow the suction side leg of the horseshoe vortex on the early suction side.

Detailed heat transfer measurements were obtained on the vanes and endwalls using IR thermography. This technique allows full coverage of optically accessible areas (directly or with a use of a special window) and collection of detailed data. Experimental results were obtained at four locations. The stagnation region was at an axial location of $5\%C_{ax}$ on the vane pressure side, where the Nusselt number was 1300. Further downstream on the pressure side, the Nusselt number dropped to 650 at 20% of C_{ax} and then gradually increased until the trailing edge of the vane. This agreed with the very slow flow until 40% of C_{ax} on the vane pressure side, that was followed by rapid acceleration to the trailing edge, seen from the isentropic Mach number distribution on the vane surface. On the other side of the stagnation region, the flow was highly accelerated around the leading edge of the vane, resulting in low Nusselt number until 15% of C_{ax}. The Nusselt number then increased rapidly on the suction side of the vane after 15% of C_{ax}, due to transition from laminar to turbulent flow occurring in that region. Two regions of high Nusselt number were identified close to the endwalls, above the suction side leg of the horseshoe vortex on the vane suction side, until 70% of C_{ax}. These were caused by the combination of the suction side leg of

the horseshoe vortex and the secondary vortex causing the flow impacting the vane surface, locally increasing heat transfer rates.

Extensive secondary flow structures with low heat transfer were observed on the vane suction side, as the air from the endwall boundary layer was entrained into the passage vortex, leaving low Nusselt number trails near the vane hub and casing. These were caused by a tertiary vortex induced by the passage vortex on the vane suction side. Closer to the endwalls, the passage vortex lifts off the boundary layer, resulting in high heat transfer rates to the vane. Away from the endwalls, the heat transfer was seen to gradually increase toward the vane leading edge. The heat transfer patterns on the vane pressure and suction side were in agreement with those found in the literature (Dunn et al., 1986, Han et al., 2013). The main difference with the patterns in the literature is the relatively low heat transfer in the stagnation region, an effect of the combustor wall upstream of the vane.

On the endwall the peak Nusselt number occurs around the vane leading edge on the suction side below the horseshoe vortex (Goldstein et al., 1995, Graziani et al., 1980), and can lead to extensive damage to the vanes (Thole, 2006). The peak Nusselt number was found to be 23% lower for the central vane compared to the adjacent one, due to effect of the combustor wall on the shape of the horseshoe vortex. On the rest of the endwall the heat transfer patterns for the vane passages were similar. The Nusselt number was low in the beginning of the endwall and increased downstream of the separation point of the passage vortex on the endwall, reaching a maximum of 2200 near the vane trailing edge.

The comparison of the experimental and numerical studies showed that CFD generally underpredicted Nusselt number on the vane surfaces. However, the Nusselt number levels on the stagnation region on the vane downstream of the combustor wall and the early pressure side were significantly overpredicted, showing that CFD should be used with caution. The magnitude and location of the low Nusselt number trails of the passage vortex on the vane suction side were cap-

tured by the numerical studies, increasing the confidence in numerical predictions for the analysis of secondary flow development.

Although the imperfections of the vane geometry, alignment, and model setup may result in a mismatch between the experimental and numerical results, they do not limit the purpose of the use of the numerical models in this work. They are used to explain flow features that are captured in the experiment with the more detailed results from the numerical studies, as well as to investigate different concepts, with greater confidence in the numerical prediction. Furthermore, any features on the vane that are caused by a geometry imperfection do not limit the purpose of this series of experimental work, which is the comparison of the effect of different geometric configurations and inlet conditions on the aerodynamic and heat transfer field.

Chapter 5
The Effect of Vane Clocking on the Aerothermal Field

As discussed in Chapter 3, the experimental facility has been designed and built to allow the investigation of the aerothermal field under varying geometric and inlet conditions. The modular design of the facility enables the variation of the clocking position of the vane leading edge relative to the combustor wall. Experimental measurements for 10% pressure side clocking and for 10% suction side clocking, where the combustor wall is closer to the vane pressure or suction side respectively by 10% of the vane pitch, are presented in this section. They are compared to the datum case, where the vane leading edge is aligned with the combustor wall trailing edge. Results from numerical studies are employed to enhance the physical understanding of the flow phenomena captured in the experimental studies. It should be noted that as in the experimental facility the combustor wall is fixed, the experiments were carried out by moving the vane cascade within the working section. The different clocking positions are shown in Figure 5.1.

5.1 Aerodynamic Field

Computational studies for 10% PS and for 10% SS clocking presented in Chapter 3.2 showed that flow periodicity can be achieved with an optimum angle for the tailboards at $71.5°$, as in the datum case. The periodicity of the flow was verified experimentally for both cases without the tailboard on the pressure side sidewall by a downstream traverse of the five-hole probe as well as by surface pressure measurements on the three vanes.

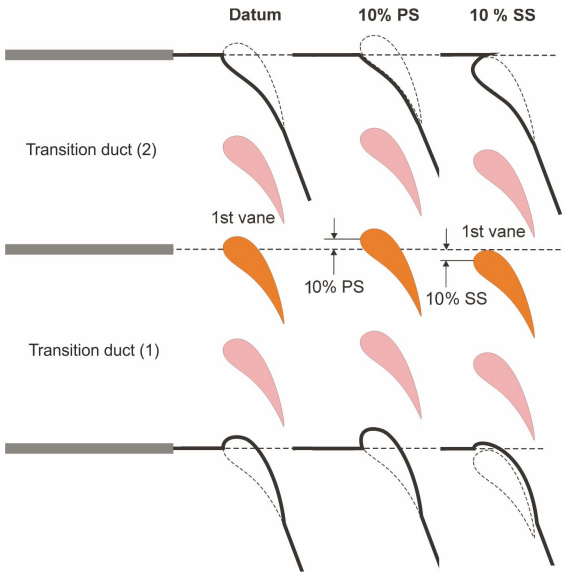

Figure 5.1: Different clocking positions investigated

The effect of the combustor wall on the aerodynamic field is highlighted in the following figures. Total and static pressure contours in the vane leading edge region for the three cases obtained from CFD studies are shown in Figures 5.2(a) and 5.2(b). The pressure is non-dimensionalized with respect to the inlet value. Figure 5.2(c) shows the experimentally measured isentropic Mach number on the central vane for the datum, 10% PS, and 10% SS clocking cases, along with the numerical solution for the datum case. The effect of the combustor wall can be seen in the leading edge region, with variations in the isentropic Mach number distribution between the three cases. Figure 5.3 focuses on the flow near the vane leading edge using the more detailed data obtained from numerical studies, showing the isentropic Mach number along with flow streamlines.

In the datum case the wake of the combustor wall was directed towards the suction side of the vane (Figure 5.2(a)) and the stagnation point was located at a distance of two percent of the axial chord downstream of the starting point of the vane (Figures 5.2(c) and 5.3). Total and static pressure contours and flow streamlines for 10% SS clocking showed a very similar flow field to that observed in the datum case. The location of the stagnation region was marginally shifted upstream, as the combustor wall was now further away from the vane leading edge in the circumferential direction. The wake of the combustor wall reached the vane suction side further

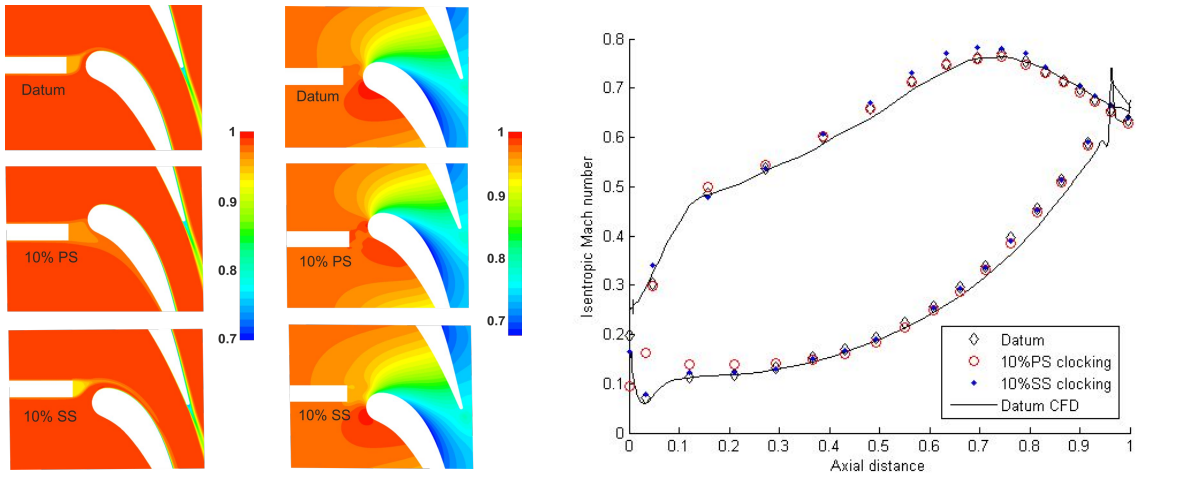

(a) Total pressure (b) Static pressure (c) Isentropic Mach number at 50% span

Figure 5.2: Pressure field (numerical result) and isentropic Mach number for datum, 10% PS, and 10% SS clocking

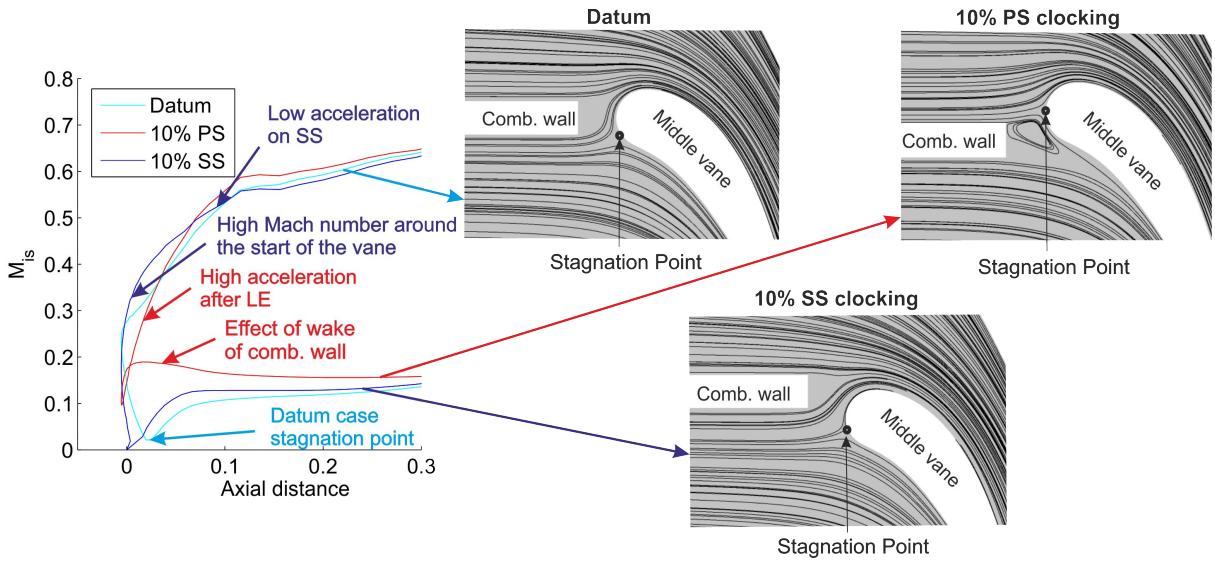

Figure 5.3: Isentropic Mach number and surface streamlines (numerical result)

downstream of the leading edge for 10% SS clocking. This caused the difference in the isentropic Mach number distribution seen in Figures 5.2(c) and 5.3, with a higher Mach number around the start of the vane and reduced acceleration of the flow over the vane suction side in comparison to the datum case. On the vane pressure side, the difference between the datum and 10% SS clocking was caused by the marginal shift in the location of the stagnation point further upstream.

For vane clocking the effect of the combustor wall trailing edge wake on the vane isentropic Mach number distribution was found to be more pronounced for clocking towards the pressure

side of the vane. With this change in the relative position of the two components the wake of the combustor wall was impacting upon the pressure side of the vane (Figure 5.2(a)), resulting in a shift in the location of the stagnation point which was outside the wake and coincided with the start of the vane. This is seen in the flow streamlines for the two cases (Figure 5.3) and resulted in higher acceleration of the flow near the vane leading edge on the suction side of the vane. The high Mach number on the early pressure side was followed by a marginal deceleration where the low momentum wake impacted the vane. In this case the vane had reduced loading in the leading edge region and until 10% of C_{ax}, as seen in Figures 5.2(c) and 5.3. The flow acceleration on the vane suction side was highest for 10% PS clocking, as the low momentum wake impacted the other side of the vane compared to the datum and 10% SS clocking.

The wake of the combustor wall was affected by the potential field (and relative location) of the vane and was seen to diffuse for 10% PS clocking compared to the datum case, where it was significantly smaller in width. The total pressure downstream of the leading edge region, at 30% of the axial chord, Figure 5.4(a), shows that the wake of the combustor wall had merged with the boundary layer on the vane suction side for the datum case. For 10% PS and 10% SS clocking, the wake was distinctly seen on the pressure side and near the suction side of the vane respectively. This effect was observed throughout the passage, with lower total pressure levels on the side of the vane that faced the wake of the combustor wall until the trailing edge of the vane, Figure 5.4(b). For 10% SS clocking the relative contribution of the suction side to the total loss was higher than for the 10% PS clocking and vice versa for the pressure side. Downstream of the trailing edge the effect of the wake of the combustor wall was reduced, and no significant differences are seen in Figure 5.4(c).

A comparison of the total pressure loss coefficient relative to the outlet dynamic head obtained in the experimental facility for the datum case and for 10% PS and 10% SS clocking at 20% of the axial chord downstream of the vane is shown in Figure 5.5. The loss cores at 20% and 80% span, arising from the passage vortices on the hub and casing endwall as discussed in Chapter 4, were

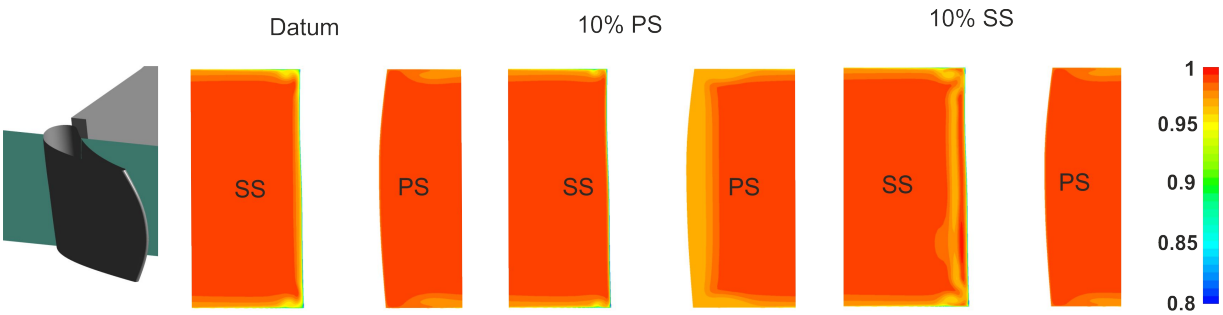

(a) 30% C_{ax} downstream of vane LE

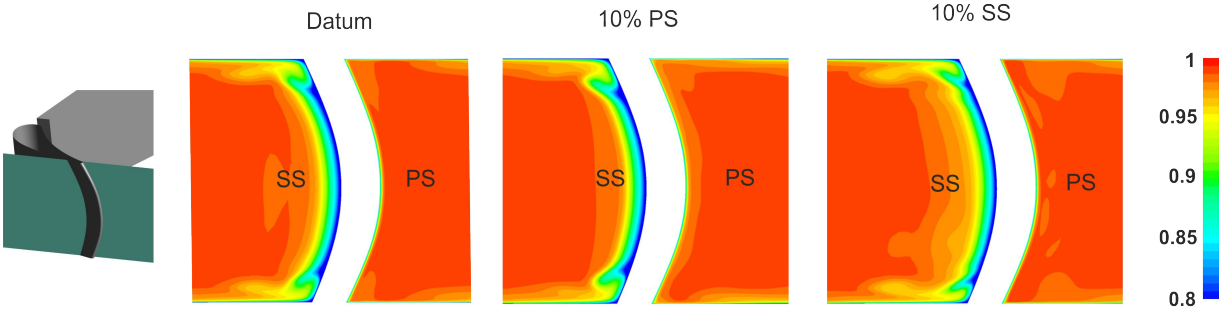

(b) 95% C_{ax} downstream of vane LE

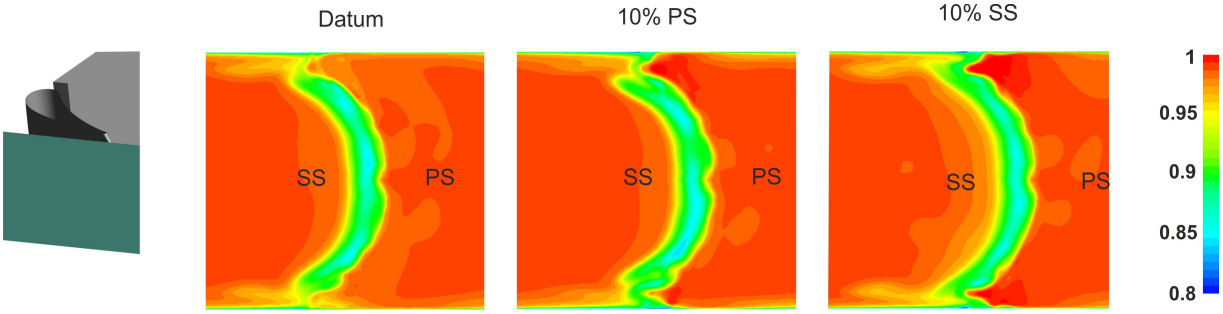

(c) 10% C_{ax} downstream of vane TE

Figure 5.4: Total pressure contours on vane pressure and suction side at different axial locations

well captured with the five-hole probe, enabling the identification of the differences between the cases. Although differences had been observed in the pressure field near the vane leading edge between the datum and the 10% PS clocking, the total pressure distribution downstream of the vane was similar. For 10% SS clocking, the thickness of the wake at mid-span was 12% higher compared to the other two cases, and the area of low loss $(0.5 - 0.8)$ was highest. This was due to the diffusion over the vane suction side. The loss cores were noticeably weaker and the overall loss distribution was affected.

The mass-weighted average loss in the downstream measurement plane is shown in Figure 5.6(a). The lower loss of the cores for the 10% SS clocking is also seen in this figure; the

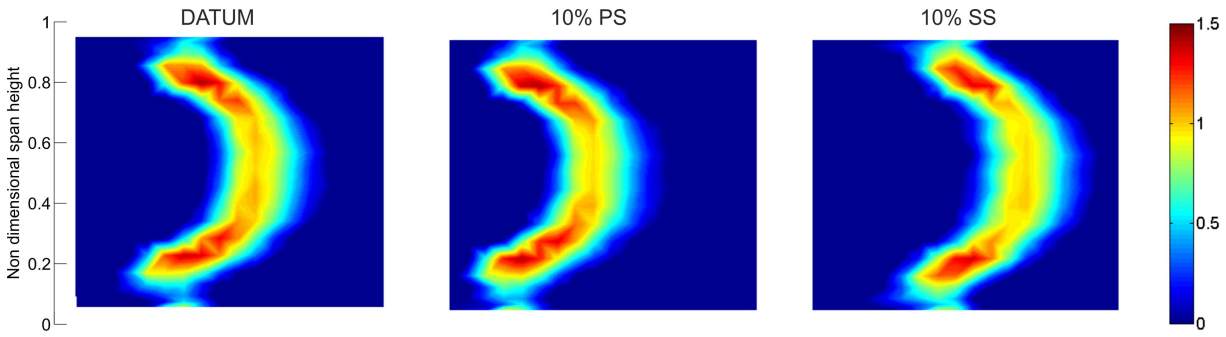

Figure 5.5: Spatially resolved total pressure loss coefficient downstream of the central vane

mass-weighted average total pressure loss coefficient was 0.5% of the outlet dynamic head lower than the datum case at 20% and at 80% span. Overall, the average loss downstream of the vanes was 1.1% of the outlet dynamic head higher than the datum for 10% SS clocking and 0.2% of the outlet dynamic head higher than the datum for 10% PS clocking.

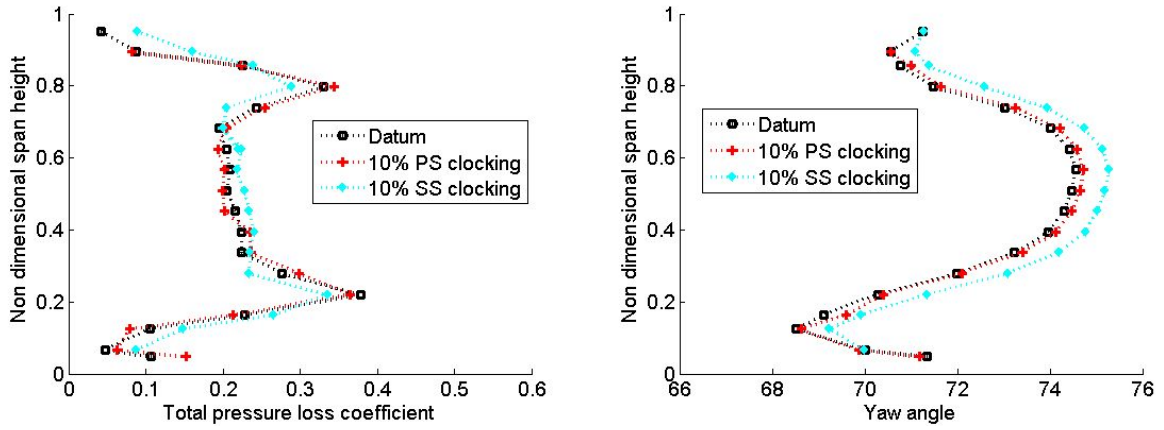

(a) Mass-weighted average total pressure loss coefficient (b) Mass-weighted pitchwise average yaw angle

Figure 5.6: Effect of clocking position on the aerodynamic field

The mass-weighted average yaw angle distribution was compared between the three cases in Figure 5.6(b). The yaw angle was the same for the datum and the 10% PS clocking cases, and was increased by $0.5°$ for the 10% SS clocking case, showing that clocking does not significantly affect the flow turning downstream of the passage.

The effect of vane clocking on the secondary flow formation is shown in Figure 5.7, which shows non-dimensional vorticity magnitude contours at the leading edge and early pressure and suction side of the central vane (at 20% of the axial chord) for the three clocking positions, as well

as for the adjacent vane in the datum case. The differences between the central and the adjacent vane were discussed in Chapter 4. The vorticity of the leading edge vortex was in the circumferential direction, whereas the pressure and suction side legs had opposite senses of rotation in the direction of the streamlines. This figure uses vorticity magnitude to facilitate the comparison between the different cases and the two legs of the vortex.

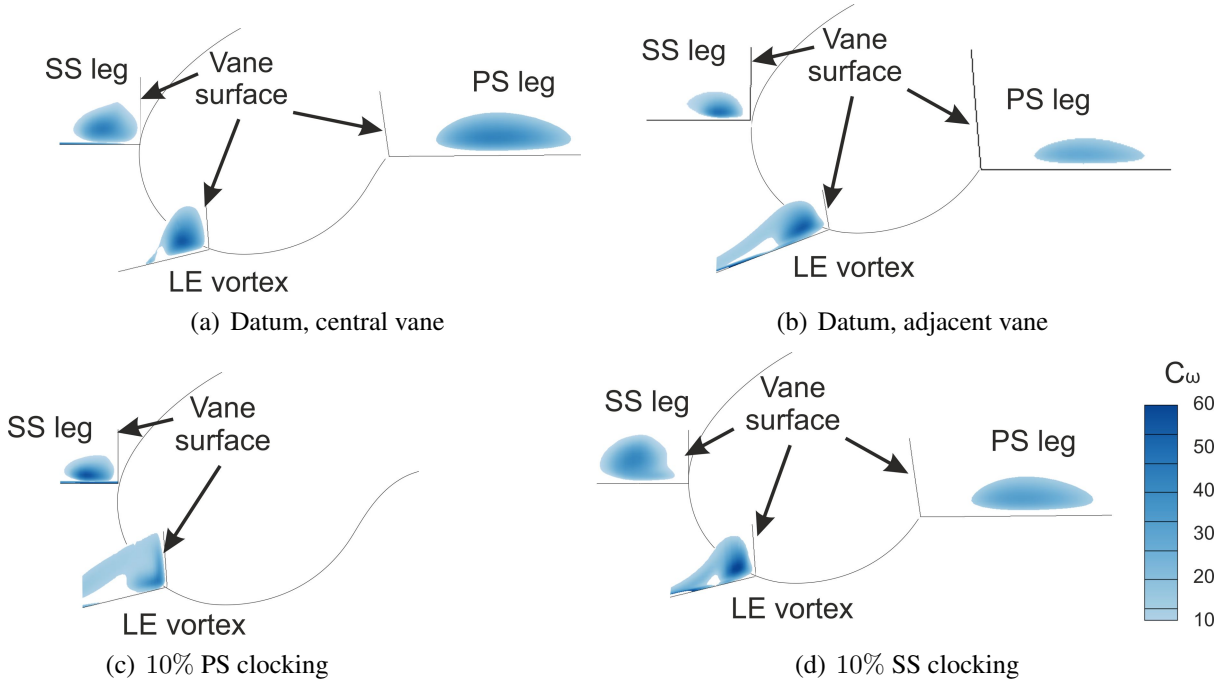

(a) Datum, central vane

(b) Datum, adjacent vane

(c) 10% PS clocking

(d) 10% SS clocking

Figure 5.7: Effect of clocking position on the horseshoe vortex

The stronger pressure gradient upstream of the vane leading edge for 10% SS clocking resulted in a stronger horseshoe vortex, with a maximum vorticity which was 10% higher than in the datum case. The shape of the vortex was similar to the one observed in the adjacent vane. As the vortex went around the vane leading edge, the suction side leg was larger for 10% SS clocking compared to the datum and had a marginally lower maximum vorticity. The suction side leg of the vortex was similar in size to the one seen in the datum case, but was further away from the vane surface. The pressure side leg was smaller compared to the datum case and was similar to the one seen in the adjacent vane which was not facing the wake of the combustor wall. On the other hand, the lower stagnation pressure for 10% PS clocking resulted in 15% lower maximum vorticity upstream of the leading edge and a different vortex shape. This vortex was then directed to the suction side of

the vane, and there were no traces of a vortex on the pressure side. The maximum vorticity of the suction side leg was 24% higher for 10% PS clocking. The vortex was similar to that observed in the adjacent vane in strength and size, as the suction side of the vane was further away from the wall in this case.

5.2 Thermal Field

The effect of vane clocking on the heat transfer on the central vane and the endwall is presented in this section, which compares experimental measurements for the three cases in the non-dimensional form of Nusselt number based on the axial chord. Numerical studies are again employed to enhance the understanding of the physical background behind the effects observed in the experiments. It is noted that the cases presented in the next figure were run with isothermal walls.

For a vane facing uniform hot inlet flow, a thermal boundary layer starts developing from the vane leading edge. As the wake of the combustor wall is directed to different sides of the vane with the change in clocking position, the driving temperature difference for the heat transfer to the vane surfaces changes. Non-dimensional temperature contours (relative to the inlet value) and flow streamlines are presented for the three cases in Figure 5.8. In the datum case where the wake of the combustor wall was directed to the suction side of the vane, a thin layer of mainstream fluid originating from the opposite side of the combustor wall was seen between the vane leading edge and the wake of the combustor wall, directed towards the vane suction side. This diffused quickly and the wake merged with the boundary layer further downstream. For 10% PS clocking, the wake of the combustor wall was directed to the vane pressure side instead. A small part of the wake was directed to the suction side of the vane, resulting in marginally higher thickness of the thermal boundary layer compared to a vane facing uniform inlet flow. For 10% SS clocking there was a thick layer of mainstream fluid on the suction side between the vane and the wake of the combustor wall which stayed detached from the boundary layer on the vane. The effect of

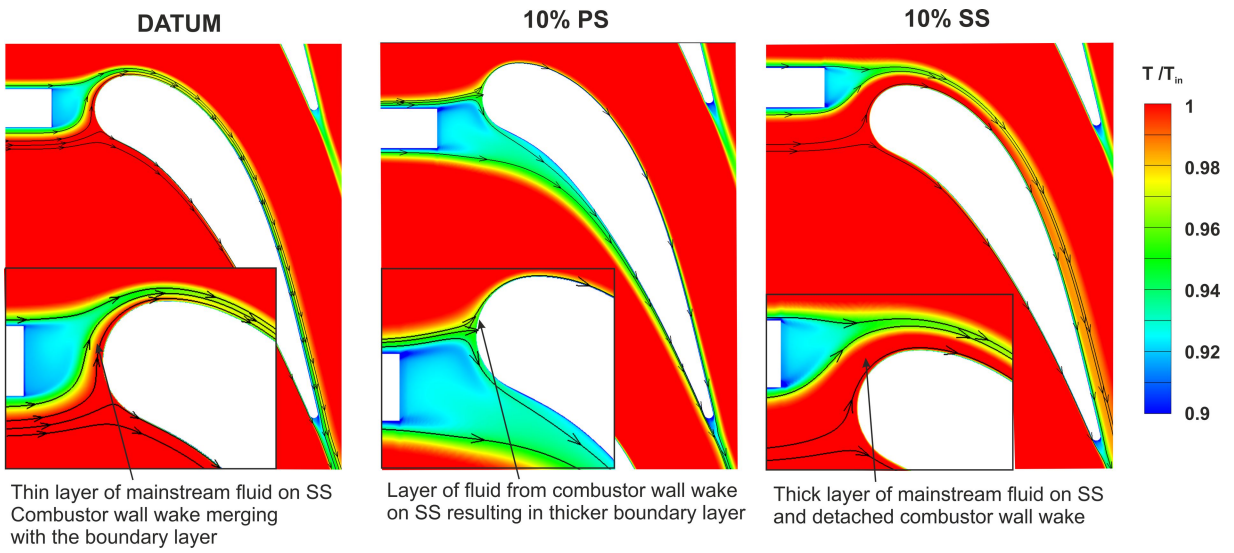

Figure 5.8: Temperature contours and flow streamlines for datum, 10% PS and 10% SS clocking (numerical result)

the thermal boundary layer development is depicted in the heat transfer results presented in the following figures.

Figure 5.9 shows the Nusselt number distribution on the vane pressure side for the three cases. In the 10% PS clocking case, Figure 5.9(b), the start of the vane was partially hidden by the combustor wall. The region immediately downstream (left in this view) of the combustor wall had a higher Nusselt number compared to the datum case, Figure 5.9(a). The flow initially accelerated on the pressure side downstream of the axial starting point of the vane, and then maintained a constant isentropic Mach number until 30% of the axial chord, as noted in Figure 5.3. As seen from the figure, the isentropic Mach number was up to 5 times higher for 10% PS clocking compared to the datum case, resulting in higher heat transfer for the clocked case in that region. Further downstream on the vane pressure side, the thick boundary layer due to the wake of the combustor wall led to lower heat transfer levels.

The data obtained from the heat transfer measurements was also plotted in terms of difference between the respective runs, to highlight the effect of vane clocking on the heat transfer to the vanes and endwalls. These figures were generated by overlapping the respective plots in MATLAB, aligning the edges of the vanes and endwalls, and extracting the difference between

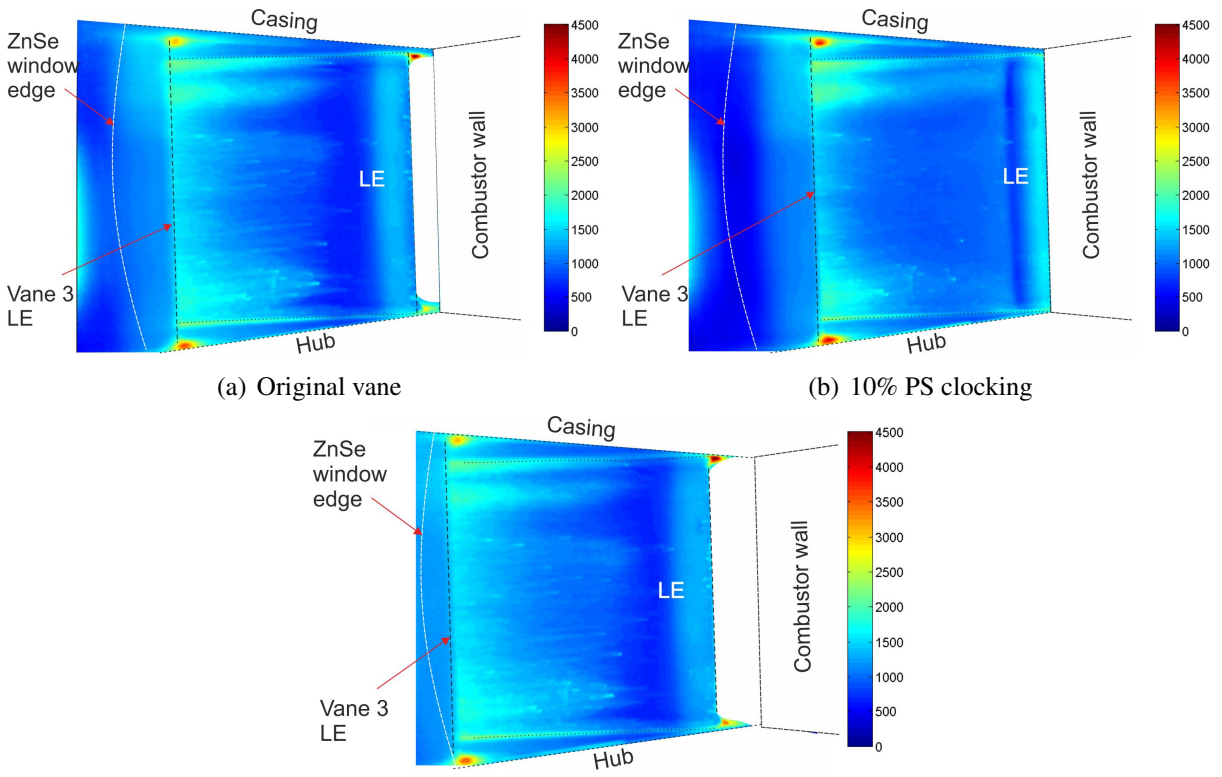

(a) Original vane

(b) 10% PS clocking

(c) 10% SS clocking

Figure 5.9: Nusselt number distribution on the vane pressure side for the three clocking positions (view 1, Figure 3.25(a))

them. They did not take into account the small difference in view angle and perspective due to the difference in the location of the test area relative to the camera, which may result in small misalignments outside the region of interest.

The differences between the datum and the 10% PS clocking cases can be seen more clearly in Figure 5.10(a), with an increase in Nusselt number of 15% at the start of the vane, followed by a small reduction of $5 - 10\%$ and then a larger increase that reached 60%. Further downstream, from 30% to 50% of the axial chord, the Nusselt number was reduced by 20% for the clocked case compared to the datum.

A comparison of the 10% SS clocking case, Figure 5.9(c), to the datum, Figure 5.9(a), showed similar levels for the two cases as the flow field was not significantly altered, with lower Nusselt numbers on average for the clocked case. The difference between the cases, plotted in Figure 5.10(b), showed a small increase immediately downstream of the combustor wall due to the

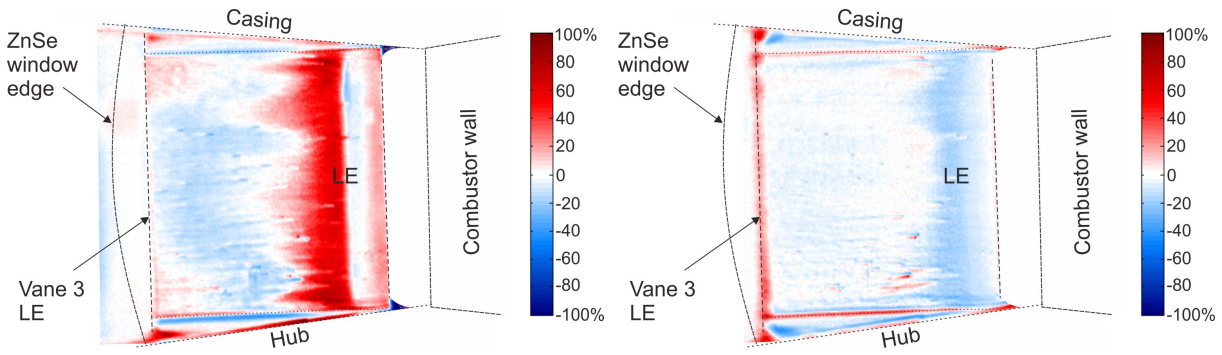

(a) 10% PS clocking (b) 10% SS clocking

Figure 5.10: Effect of the clocking position on the Nusselt number on the vane pressure side (view 1, Figure 3.25(a))

greater distance between the two components in the circumferential direction, which allowed a thicker layer of mainstream flow to be directed towards the vane suction side compared to the datum case. Further downstream a reduction of 25% in Nusselt number was observed due to the lower Mach number for 10% SS clocking, followed by a marginal reduction of 5% which was comparable to the measurement uncertainty.

The Nusselt number distribution on the vane leading edge, the region most affected by the combustor wall, is shown in Figure 5.11 for the three cases. The displacement of the combustor wall towards the pressure side, Figure 5.11(b), resulted in a higher Nusselt number in the vane leading edge region in comparison to the datum case. For 10% PS clocking the wake of the combustor wall impacted upon the vane pressure side and the stagnation region moved towards the vane suction side. Furthermore, the thickness of the boundary layer was smaller due to the higher acceleration of the flow around the vane leading edge, increasing the heat transfer to the vane. This was in agreement with the trends observed on the vane pressure side, Figure 5.9. The maximum Nusselt number on the vane surface, in the turbulent region after the transition region, was also higher for 10% PS clocking. Figure 5.12(a) shows the difference in Nusselt number on the vane leading edge between the two cases. 10% PS clocking resulted in an increase in Nusselt number of 60% in the vane leading edge region, which was left unprotected by the combustor wall, and smaller differences further downstream, where the flow was not as affected.

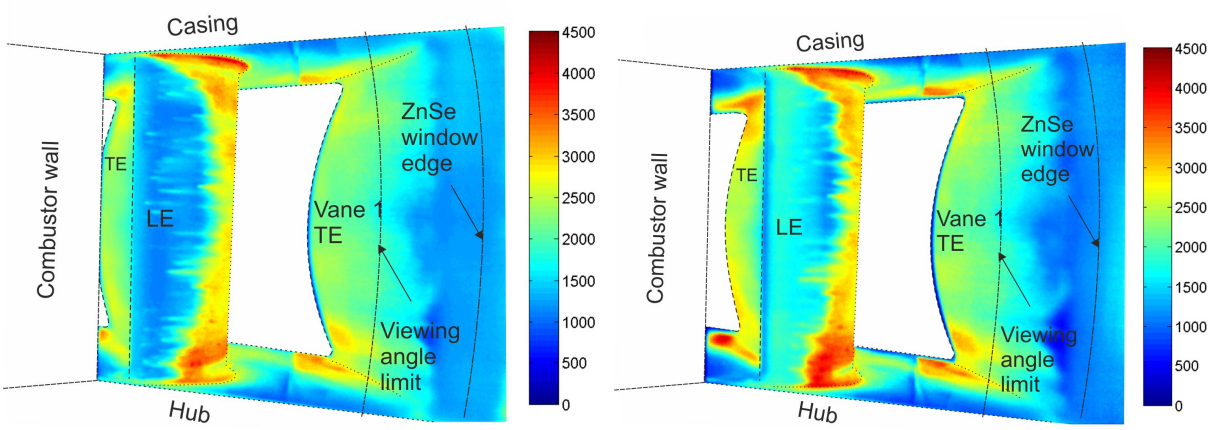

(a) Original vane

(b) 10% PS clocking

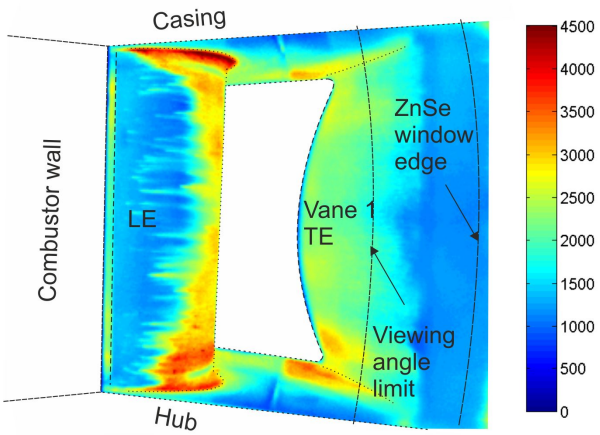

(c) 10% SS clocking

Figure 5.11: Nusselt number distribution on the leading edge for the three clocking positions (view 2, Figure 3.25(b))

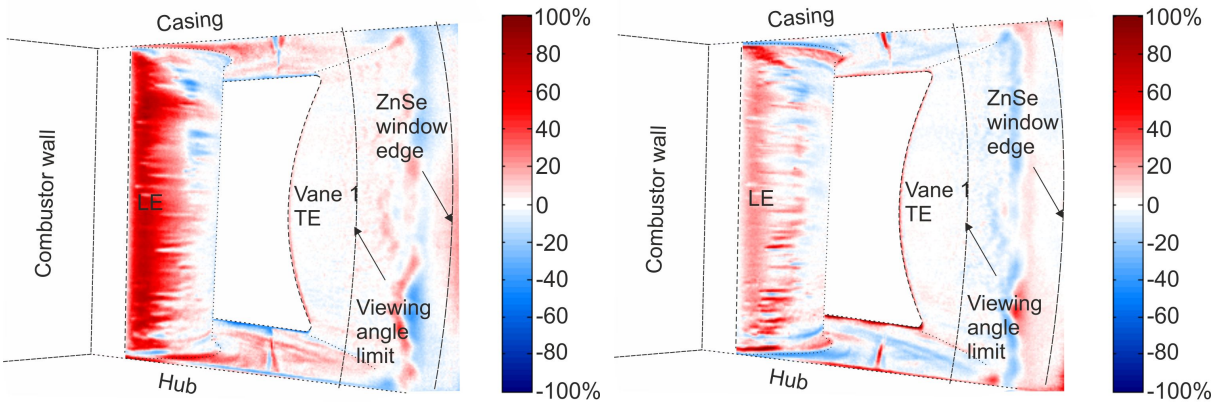

(a) 10% PS clocking

(b) 10% SS clocking

Figure 5.12: Effect of the clocking position on the Nusselt number on the vane leading edge (view 2, Figure 3.25(b))

The heat transfer patterns for 10% SS clocking, Figure 5.11(c), were similar to those observed in the datum case, as the wake of the combustor wall was directed to the vane suction side in both cases. Clocking towards the suction side caused an increase of 25% in Nusselt number on the leading edge compared to the datum case, in the high Mach number region around the start of the vane. This was due to the thicker layer of mainstream flow between the wake of the combustor wall and the vane compared to the datum case. In the downstream region patches of higher and lower Nusselt number (compared to the datum case) were observed owing to the lower acceleration of the flow in the clocked case and the non-uniform unsteady flow downstream of the combustor wall. The heat transfer on the pressure side of vane 1 which is also seen from this view was similar in all cases, as expected.

The suction side of the vane is shown in Figure 5.13. The patterns observed on the vane surface were similar in all cases. The Nusselt number on the vane suction side was lower in the 10% PS clocking case, Figure 5.13(b), on the majority of the vane surface. The reduction ranged from 1% at mid-chord (first view point of the vane suction side) to 10% closer to the trailing edge, Figure 5.14(a). This drop in heat transfer did not agree with the CFD results, which predicted a marginal rise in Nusselt number. The discrepancy between the experiments and the CFD could be caused by a small misalignment of the wall and the vane, with the vane clocked towards the SS in the experiment. This would result in a thicker layer of mainstream fluid between the combustor wall wake and the vane, which would increase heat transfer to the vane in the datum case and a thicker boundary layer in the 10% PS clocking case, reducing heat transfer to the vane surface. This would not affect the results observed on the pressure side and on the vane leading edge, where the differences between the two cases are significantly larger and are due to the difference in Mach number in the former and boundary layer thickness due to highly accelerating flow in the latter.

Another feature observed was that the traces of the horseshoe vortex near the hub and casing had moved further away from the endwalls in the clocked case. This resulted in a local drop

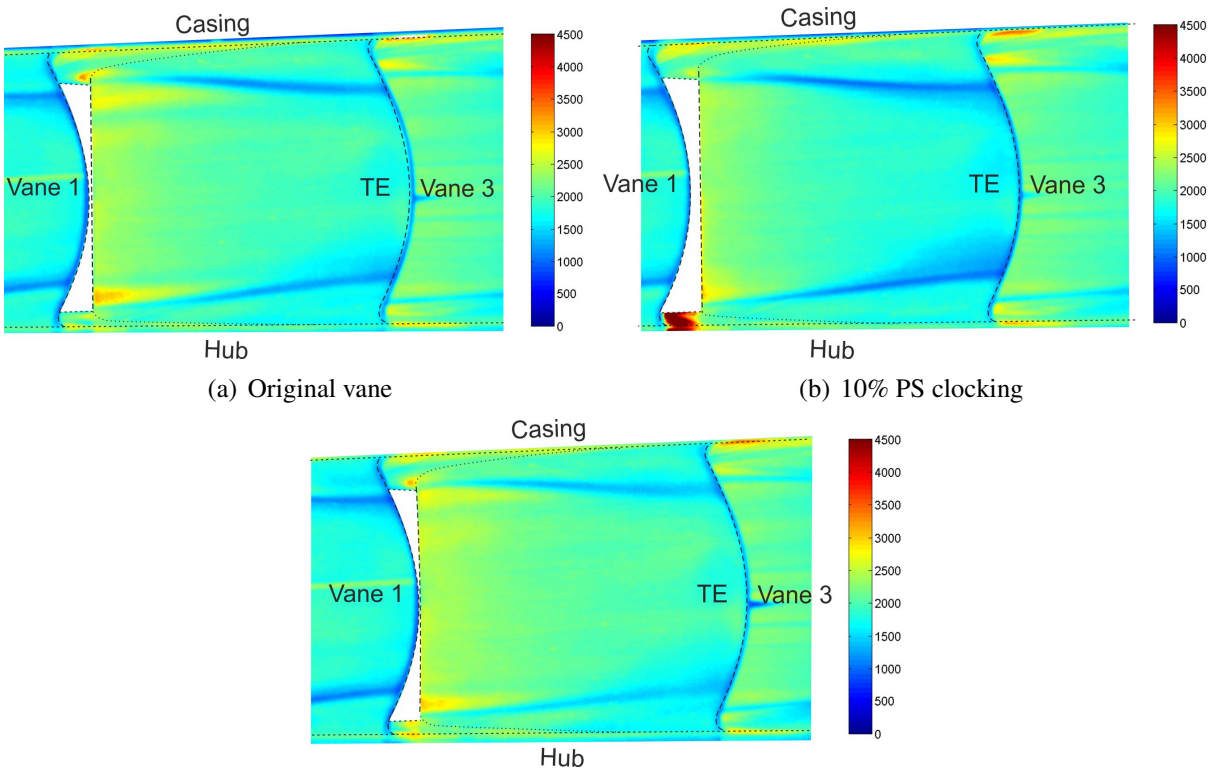

(a) Original vane

(b) 10% PS clocking

(c) 10% SS clocking

Figure 5.13: Nusselt number distribution on the vane suction side for the three clocking positions (view 3, Figure 3.25(c))

in Nusselt number of 40% near the casing and 25% near the hub. The asymmetry between the two was due to the different trajectory and magnitude of the passage vortex trails. The vortex moved further away from the endwall for 10% PS clocking, resulting in the significant reduction in Nusselt near the endwall at mid-chord and an increase in Nusselt further downstream which locally reached 40% near the casing. The difference in Nusselt number near the endwalls was less than 5% between the two cases.

The effect of clocking towards the suction side (Figure 5.13(c)) was the opposite, as seen in Figure 5.14(b). The majority of the vane suction side had a higher Nusselt number in the clocked case, with an increase of up to 10% closer to the trailing edge, as it was exposed to a thicker layer of mainstream fluid between the boundary layer and the wake of the combustor wall compared to the datum case, as seen in Figure 5.8. The horseshoe vortex trails on the vane surface had a higher Nusselt number, by 35% near the casing and 25% near the hub. Regions of lower Nusselt number

than in the datum case were observed on the sides of the passage vortex trails, with a difference of less than 5%.

The isentropic Mach number near the endwalls at at 5% and 95% span was similar between the three cases for the late suction side (from $60 - 100\%$ axial chord). For 10% PS clocking the value was 1.5% higher than in the datum case and for 10% SS clocking it was 1.5% lower at 70% of the axial chord. This difference is not enough to significantly affect the heat transfer to the vane, but in combination with the fact that the vane suction side is more or less exposed to the mainstream flow for 10% PS and 10% SS clocking respectively relative to the datum, it explains the small differences between the three cases. For 10% PS clocking, the vane is more exposed to the mainstream flow. However, the isentropic Mach number is marginally lower at 70% of the axial chord, resulting in a marginal reduction in Nusselt number in that region. Further downstream, on the other hand, the isentropic Mach number is the same as in the datum case, and the Nusselt number near the endwall is higher. The opposite is the case for 10% SS clocking.

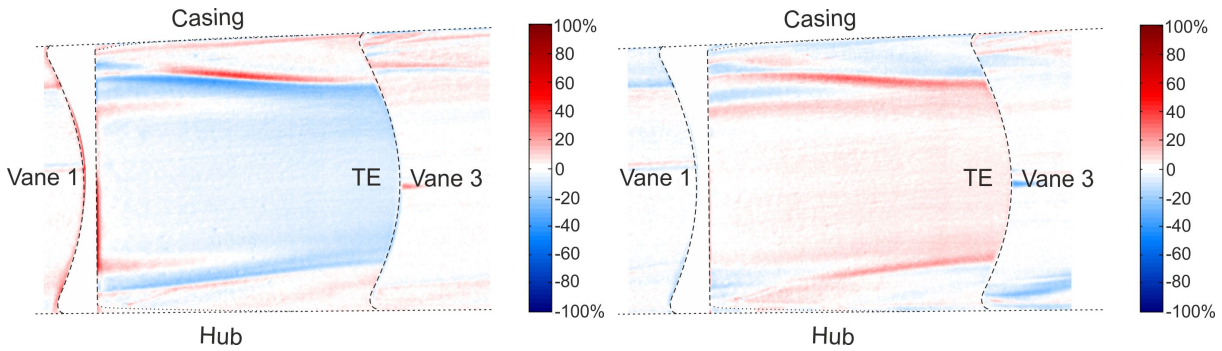

(a) 10% PS clocking

(b) 10% SS clocking

Figure 5.14: Effect of the clocking position on the Nusselt number on the vane suction side (view 3, Figure 3.25(c))

The small differences in Nusselt number on the vane suction side between the different cases are better understood when looking at the secondary flow structures around the vane for each clocking position. The pressure and suction side legs of the vortex are shown in Figure 5.15 which focuses on the leading edge of the vane, showing non-dimensional axial vorticity contours at 0%, 5% and 10% of the axial chord. In the 10% SS clocking case the flow directed to the vane suction

side was again sandwiched between the combustor wall trailing edge and the horseshoe vortex, resulting in the formation of the secondary vortex as in the datum case. For 10% PS clocking the flow did not go toward the vane suction side and therefore did not have to face the added obstacle of the combustor wall but only the horseshoe vortex, similar to the case of the adjacent vane.

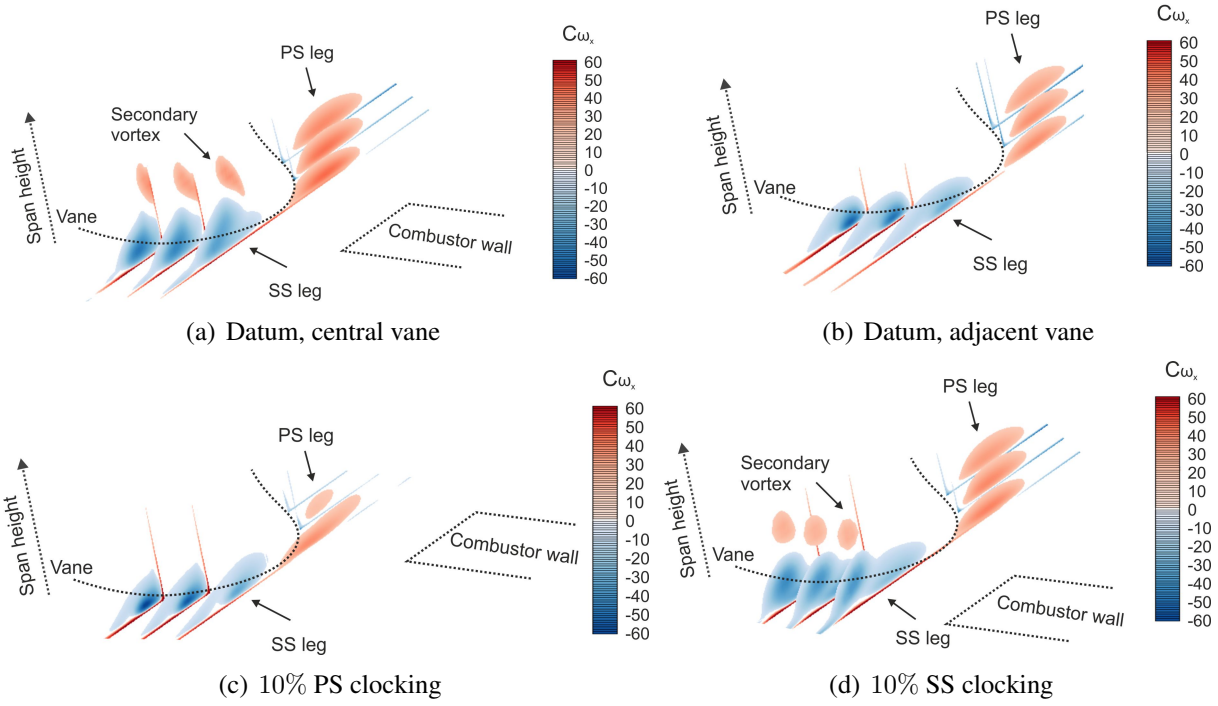

(a) Datum, central vane

(b) Datum, adjacent vane

(c) 10% PS clocking

(d) 10% SS clocking

Figure 5.15: Effect of clocking position on the pressure and suction side legs of the horseshoe vortex

This pair of counter-rotating vortices was the source of high heat transfer on the vane surface near the leading edge at approximately 20% and 80% span in the datum and the 10% SS clocking cases, as was discussed in Figure 4.19 for the datum case. The absence of the secondary vortex in the 10% PS clocking case resulted in lower heat transfer to the vane surface in that region. The higher heat transfer region on the mid-span side of the secondary vortex in the 10% SS case compared to the datum was due to the different shape of the secondary vortex, which was more detached from the vane, allowing more mainstream fluid to impinge on the vane surface.

Figure 5.16 shows non-dimensional circumferential vorticity contours on the vane suction side near the trailing edge at 85%, 90% and 95% span for the three different clocking positions, as well as for the adjacent vane. As seen in Figures 5.16(a) and 5.16(b), there was no difference between

the central and the adjacent vane in the datum case. For 10% PS clocking the suction side leg of the

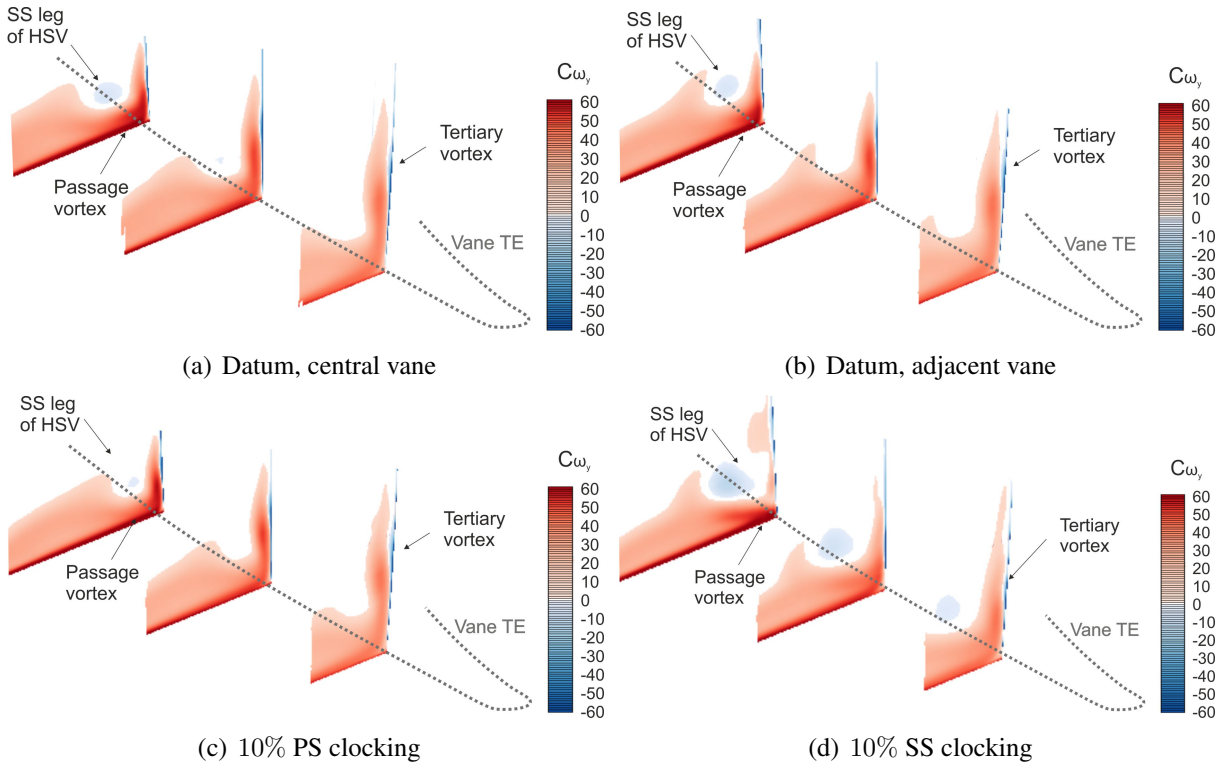

(a) Datum, central vane

(b) Datum, adjacent vane

(c) 10% PS clocking

(d) 10% SS clocking

Figure 5.16: Effect of clocking position on the vortex structure near the trailing edge

vortex was weaker than in the datum case whereas the passage vortex was not affected. Clocking towards the suction side resulted in the the suction side leg of the horseshoe vortex being larger than in the datum case with higher vorticity and the passage vortex being more confined to the endwall. The tertiary vortex in this case was then also closer to the endwall, which was depicted in the difference in the location of the low heat transfer trails.

A comparison of the heat transfer on the hub endwall viewed from upstream is shown in Figures 5.17 and 5.18. This view includes the early suction side of the central vane near the hub endwall and the endwall region as well as the leading edge fillet. The Nusselt number was higher for both clocked cases on both the vane and the endwall, in agreement with the observations on the vane leading edge. The peak heat transfer region on the hub endwall near the vane surface was also worse for the two clocked cases. An increase in Nusselt number of 15% was observed for 10% PS clocking. For 10% SS clocking the effect was stronger, with an increase of 25% and the high heat transfer region covering a greater part of the endwall surface.

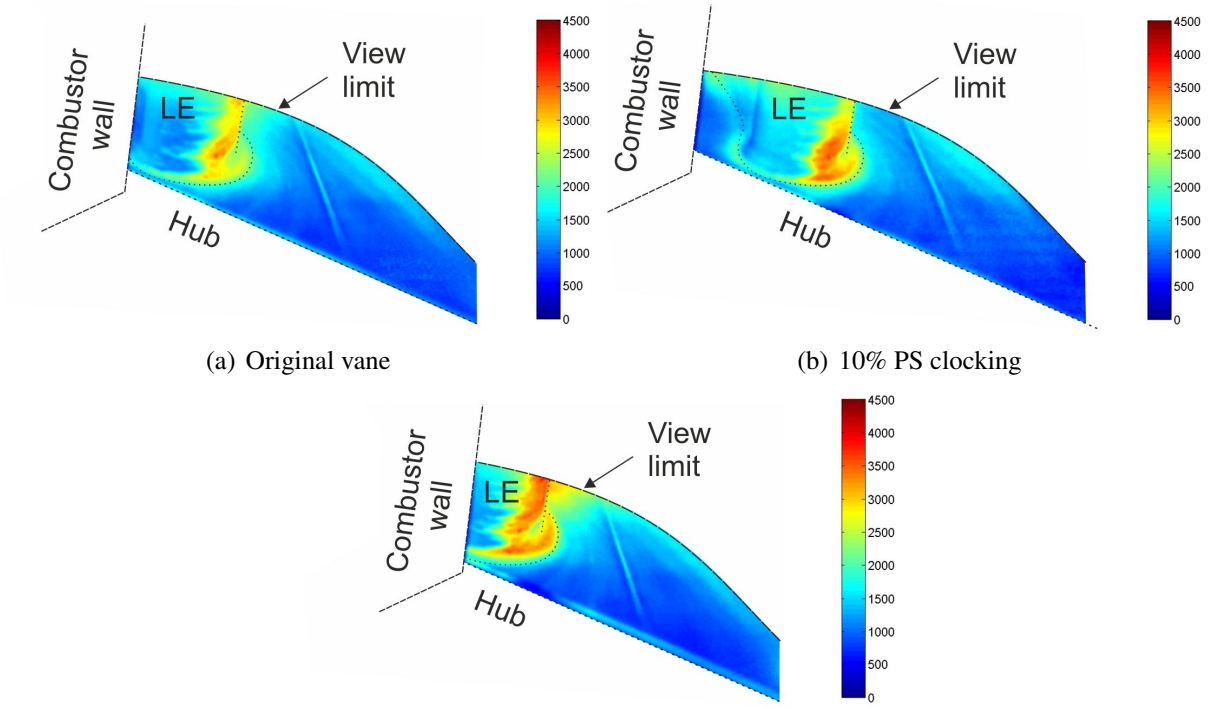

(a) Original vane

(b) 10% PS clocking

(c) 10% SS clocking

Figure 5.17: Nusselt number distribution on the vane endwall viewed from upstream for the three clocking positions (view 4, Figure 3.25(d))

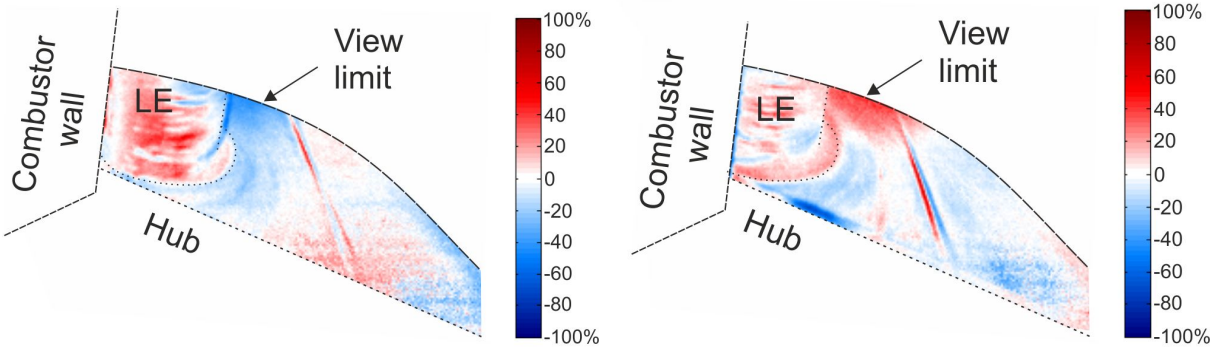

(a) 10% PS clocking

(b) 10% SS clocking

Figure 5.18: Effect of the clocking position on the Nusselt number on the vane endwall viewed from upstream (view 4, Figure 3.25(d))

The downstream view of the hub endwall is shown in Figures 5.19 and the differences between the cases are plotted in Figure 5.20. The trends observed on the vane surfaces had already been discussed in this section and this data was in agreement with the measurements on the vane suction side. The heat transfer on the endwall was increased in both clocked cases. In the 10% PS clocking case the Nusselt number was the same as in the datum case on the early parts of the endwall

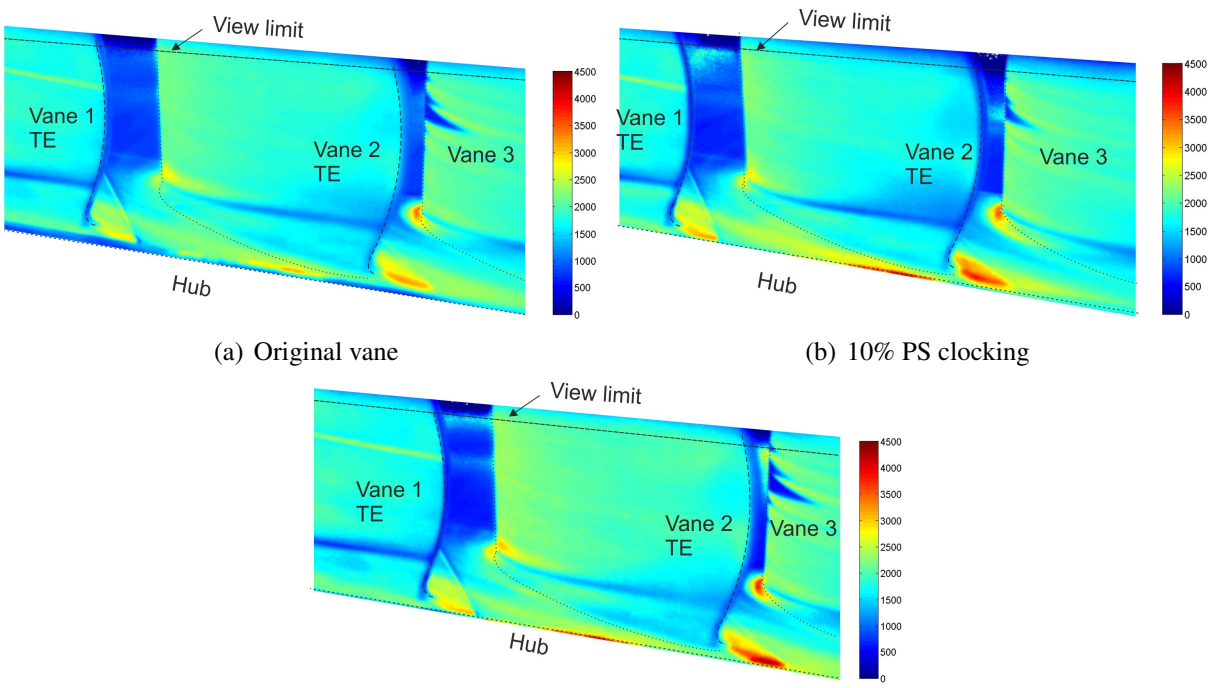

(a) Original vane

(b) 10% PS clocking

(c) 10% SS clocking

Figure 5.19: Nusselt number distribution on the vane endwall viewed from downstream for the three clocking positions (view 5, Figure 3.25(e))

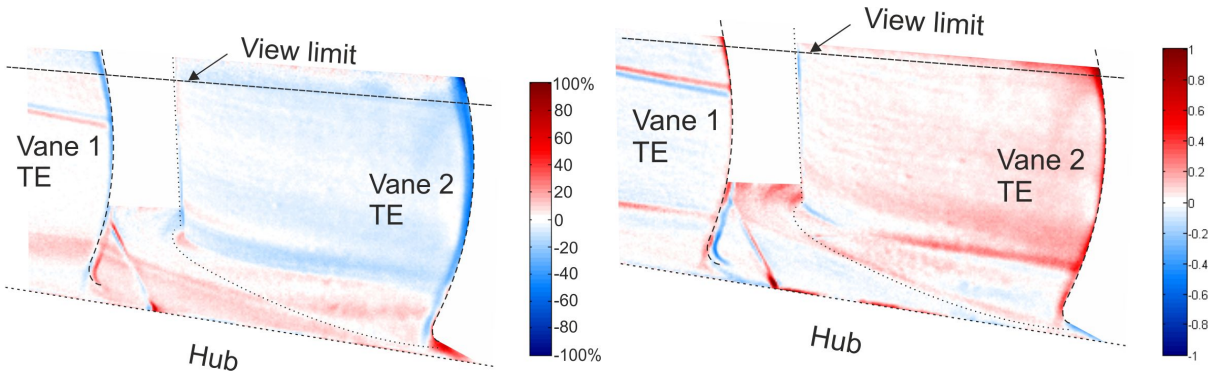

(a) 10% PS clocking

(b) 10% SS clocking

Figure 5.20: Effect of the clocking position on the Nusselt number on the vane endwall viewed from downstream (view 5, Figure 3.25(e))

and was increased by 10% relative to the datum case downstream of the separation line of the horseshoe vortex on the endwall. In the 10% SS clocking case the heat transfer was higher in the peak region on the vane suction side relative to the datum, as seen in the upstream view, and the higher Nusselt number extended to a greater region. The Nusselt number was also higher near the trailing edge of vane 1. The rest of the endwall did not show significant differences and the

Nusselt number around the region of the separation of the horseshoe vortex on the endwall was similar for the two cases.

5.3 Conclusions

A study of the effect of the relative position of the combustor wall trailing edge to the leading edge of the downstream vane on the aerothermal performance of the vane was presented in this chapter. Two different cases were studied in the experimental facility with a circumferential misalignment of 10% pitch; the combustor wall was upstream of the vane pressure side in one case and upstream of the vane suction side in the second case.

A clocking position of 10% pitch towards the pressure side resulted in a small increase in total pressure loss in the wake of the vane by 0.2% of the outlet dynamic head. The total pressure loss distribution and the yaw angle downstream of the vane were similar to the datum case. Clocking of the wall towards the vane SS was shown to increase the total pressure loss in the wake of the vane by 1.1% of the outlet dynamic head. The loss cores of the passage vortex exhibited a loss reduction relative to the datum but the total pressure loss at mid-span was higher, and higher diffusion was observed on the vane suction side, resulting in an average loss that was higher than the datum case.

The effect of vane clocking on the heat transfer distribution was particularly pronounced on the vane leading edge, where the heat load was significantly increased for 10% PS clocking compared to the datum, as the wake of the combustor wall was directed to the pressure side of the vane, leaving the leading edge and early suction side exposed. Further downstream the heat transfer on the majority of the vane suction side was reduced by $10 - 15\%$ with the exception of small regions of higher Nusselt number on either side of the passage vortex trails. In those regions the wake of the combustor wall had no effect on the heat transfer, which was increased as the vane was more exposed to the mainstream flow. On the vane pressure side the heat transfer was also increased downstream of the leading edge, although the Nusselt number did not exceed 1500 for

the majority of the vane surface. A small reduction was observed further downstream, a result of the thick boundary layer due to the wake of the combustor wall. The heat transfer on the endwall was also increased with 10% PS clocking, and a significant increase was observed in the peak heat transfer region on the endwall near the vane suction side, negating the protective effect of the wall on the vane that was discussed in Chapter 4.

Clocking towards the vane suction side resulted in marginally higher heat transfer on the vane leading edge, as the combustor wall was further away compared to the datum case, allowing a thicker layer of mainstream flow between the wake of the wall and the vane surface. Nusselt number on the early suction side was not significantly affected. The Nusselt number on the vane suction side was higher than the datum by $5 - 10\%$ on the majority of the vane surface, except for two regions of lower heat transfer on either side of the passage vortex trails on both the hub and the casing, a trend that was reversed from that observed in the 10% PS clocking case. In the 10% SS clocking case, the vane suction side was less exposed to the mainstream flow compared to the datum case, leading to marginally lower heat transfer near the endwalls where there was no effect of the wake of the combustor wall. A small reduction was observed on the majority of the vane pressure side, with the exception of a patch downstream of the leading edge, where the reduction in Nusselt number was 25% due to the lower Mach number in the region. The heat transfer on the endwall was increased, particularly near the leading edge, with a bigger region of high Nusselt number on the vane endwall in the peak heat transfer region of the leading edge fillet.

The differences in the endwall region and the vane suction side between the three cases were caused by the difference in the vortex formation between the combustor wall and the vane. A secondary vortex similar to the one observed in the datum case on the central vane was seen for the 10% SS clocking case, which was however more detached from the vane surface, allowing mainstream flow to locally increase heat transfer rates in the region of the vortex. The vortical structures for the central vane in the 10% PS clocking case were similar to those observed on the adjacent vane in the datum case. This resulted in the absence of the hot spots observed in the

central vane for the datum case. The different trails of the passage and tertiary vortices further downstream of the vane suction side, and their difference in size resulted in small differences between the three cases near the endwalls.

As seen in the studies presented, a change in the circumferential location of the combustor wall relative to the vane leading edge has an impact on the performance of the vane. The aerodynamic field in the leading edge region was affected but this had no detrimental effect on the flow downstream of the vane. The alteration of the pressure distribution and the flow field resulted in reduced or increased heat load to the vane surface, highlighting the effect of the combustor wall, which can be either protective or detrimental to the heat transfer to the vane.

Chapter 6
Development of the Vane Leading Edge Shielding Concept

In the experimental studies presented in Chapters 4 and 5 the effect of the combustor wall on the vane aerodynamics and heat transfer was analysed and it was shown that it can have a beneficial effect on the local heat transfer. The wake of the wall, however, and its mixing with the vane boundary layer has a negative effect on aerodynamic loss. In the numerical studies in the literature discussed in Chapter 2, the reduction of the axial distance between the two parts was seen to protect the leading edge of the vane from the hot inlet flow. With the addition of conventional film cooling, this beneficial effect was cancelled out and the wall was seen to have a detrimental effect on the cooling of the nozzle guide vane. Vortices shed by the wall periodically removed the coolant from the leading edge surface, leaving large uncooled regions between cooling holes which resulted in increased thermal stresses and reduced component life.

This detrimental effect can be overcome with the use of the combustor transition duct walls to shield the nozzle guide vane leading edge from the high heat loads, as proposed by Rosic et al. (2011). The axial distance between the parts can be minimized and the wall upstream of the vane can be exploited to provide coolant for the vane leading edge.

In this chapter the concept was numerically investigated in an engine-realistic geometry to determine the effect of the vane shielding on the aerodynamic field and the vane and endwall heat transfer and cooling and a new, improved vane design was proposed, along with a new cooling system for the vane.

6.1 Development of Conceptual Design

6.1.1 Model of Original Cascade

The original geometry with an annular sector comprising one cylindrical combustor transition duct and two vane passages was modelled with periodic boundaries. The computational domain is shown in Figure 6.1. Continuous circumferential slots on the hub and casing were used to model the gaps that result from the assembly of the individual components. The geometry of the hub and the casing leakage cavities is shown schematically in the top and bottom left of the figure. The trailing edge of the upstream combustor wall is cooled through a continuous slot which was also modelled in this study, as shown in the central diagram on the bottom part of the figure. The details of the geometric and flow parameters used in this study are presented in Table 6.1.

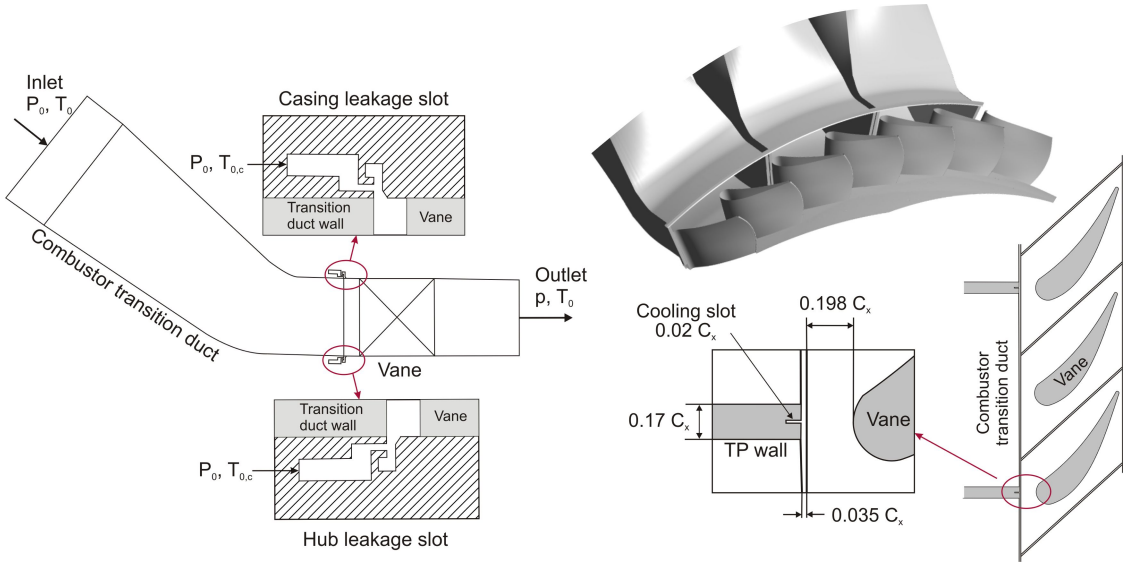

Figure 6.1: Computational domain geometry (duplicated for clarity) with details of the cooling slots for the original vane

The methodology followed for the numerical studies was as described in section 3.2. For this preliminary study, the k-ϵ turbulence model was used, as it was more robust than the other models tested for all the cases investigated. Furthermore, the effects of the modifications presented here

are mainly pressure driven and therefore are expected to be well captured using most turbulence models used today.

Table 6.1: Geometric and flow parameters

Geometric parameters		**Flow parameters**	
Axial chord/chord	0.59	Mass flow rate	5 [kg/s]
Pitch/chord (mid-span)	0.8	Temperature ratio T_c/T_∞	0.556
Span/chord	0.69	Exit Mach number	0.62

6.1.2 New Shielded Vane Design

The axial distance between the continuous slot at the trailing edge of the combustor and the vanes was reduced for the new vane design. The studies for a new vane design focused on the development of a new cooling system for the vane using an upstream slot, while maintaining the feasibility of the design, manufacture, and assembly. After a series of studies of different combinations of vane setup and cooling systems, the profile of the vane was also altered. The vanes downstream of the combustor wall were extended towards the combustor wall, whereas the remaining vanes were not altered. The pre-existing cooling slot at the trailing edge of the upstream combustor wall was modified and used to cool the vane leading edge, as will be discussed in section 6.1.4. This enabled the removal of the shower head region in the vane leading edge which was no longer required, along with the corresponding internal passage. The vane leading edge thickness could then be reduced. In the proposed design, a flat faced combustor wall trailing edge and a flat faced vane leading edge were positioned adjacent to each other, to enable the minimization of the axial distance between them and accommodate a potential circumferential displacement of the two components during operation. The original and shielded cascades are shown in Figure 6.2.

The computational flow domain is shown in Figure 6.3. The geometry of both leakage cavities was kept the same and the boundary conditions and the coolant to mainstream mass flow rate ratio for both the hub and the casing leakage slots were the same as in the original case. The vane components were shifted axially towards the combustor transition duct so that the distance

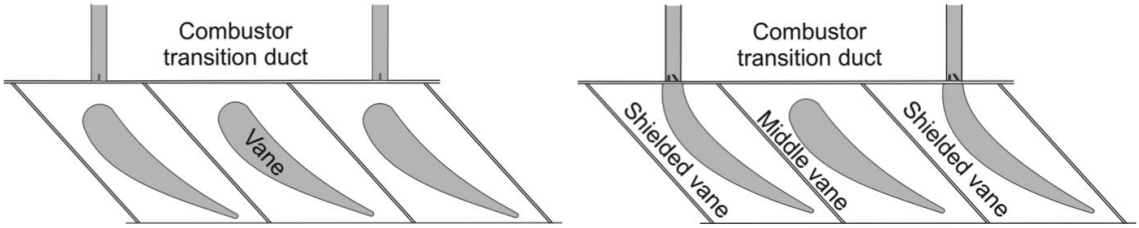

(a) Original cascade (b) Shielded cascade

Figure 6.2: Vane configurations

between the middle vane leading edge and the leakage slot was reduced from 0.2 of the axial chord in the original case to 0.1 of the axial chord.

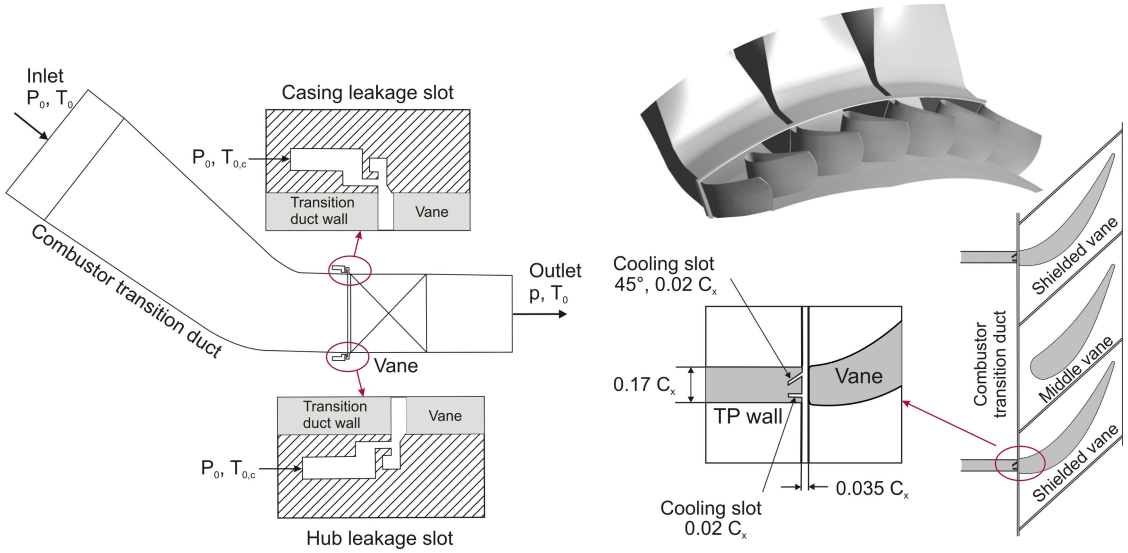

Figure 6.3: Computational domain geometry (duplicated for clarity) with details of the cooling slots for the new shielded vane

In order to apply this concept to an engine, the flow field downstream of the new vane design should be similar to the original, so that the downstream rotor blade row is not affected. The effect of the change of the axial distance between the components on the vane and endwall cooling also needs to be understood and the cooling and leakage slots between the components should be successfully sealed, as in the original design.

6.1.3 Aerodynamic Design and Aerothermal Performance

Due to the shielding of the leading edge, as well as its reduced thickness, the new vane had a smaller wetted area compared to the original vane and therefore a smaller surface to cool. Although the vane thickness at the leading edge region was reduced the vane can still maintain structural integrity and the internal cooling architecture required to cool downstream parts of the vane. The vane profile from 80% to 100% of the axial chord was identical to the original design.

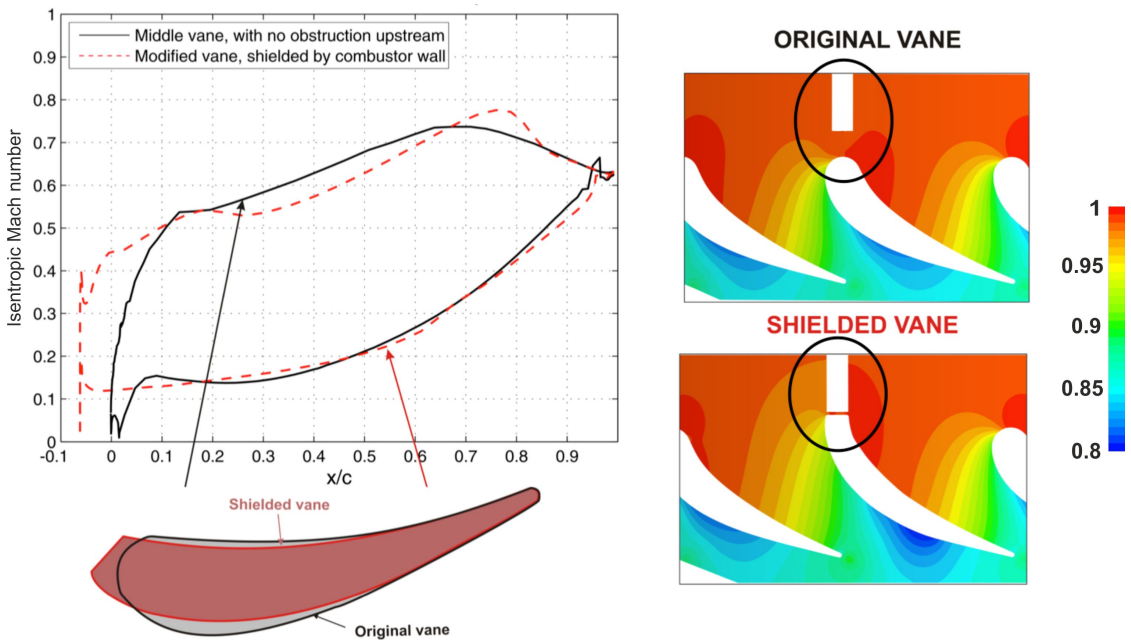

Figure 6.4: Isentropic Mach number and normalized pressure distribution of original vane with no upstream obstruction and new shielded design at 50% span

The vane loading of the shielded design is shown in Figure 6.4 along with that of the original design, in terms of isentropic Mach number distribution at mid-span. The loading of the shielded vane was similar or lower to that of the original vane for the majority of the vane profile. The shielded vane had larger pressure and velocity gradients starting from 75% of the axial chord. This high diffusion could cause flow separation and increased loss if the vane was operating at higher exit Mach number.

The new vane design focused on maintaining a similar profile at the rear of the vane in order to provide the same inlet conditions to the downstream rotor. Mid-span static pressure contours

(relative to the inlet total pressure) in Figure 6.4 showed that the high pressure region in the shielded vane design moved upstream and the combustor transition duct wall was loaded. This resulted in a change in the loading distribution of the shielded vane due to the change in geometry in the leading edge region, as well as a pressure difference across the gap between the transition duct and the vane. The mass-weighted average yaw angles downstream of the original and the new shielded vane were $71°$ and $70.2°$ respectively, showing that adequate turning can be achieved with the new design.

The effect of the new design on the boundary layer development is seen in Figure 6.5. This figure shows the distribution of temperature (non-dimensionalized relative to the inlet value) for the original and shielded vane. The wake of the combustor wall in the original case (on the left hand side of the figure) is directed to the vane suction side and leaves a thin layer of mainstream fluid between the wake and the surface of the vane. On the other hand, in the shielded vane, the wake of the combustor wall is absent, as the boundary layer that develops on the combustor wall stays attached to the vane suction side, forming a thicker boundary layer. The absence of the

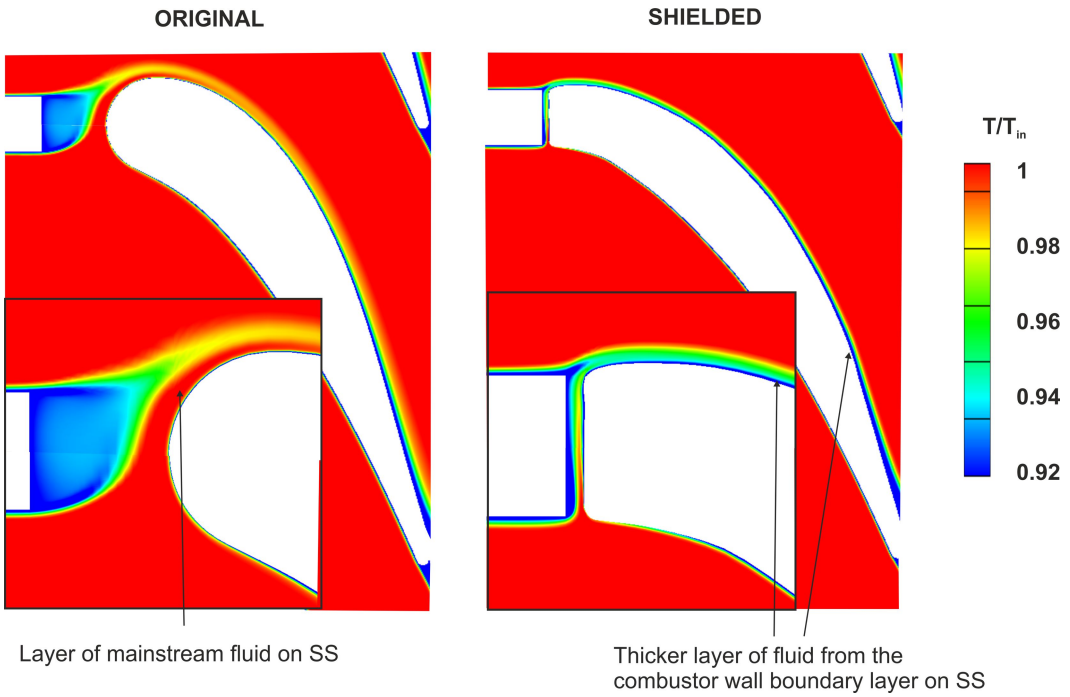

Figure 6.5: Non-dimensional temperature contours for the original and the new shielded vane at 50% span

wake of the combustor wall upstream of the shielded vane results in a lower total pressure loss coefficient. An estimate of the total pressure loss for the two cases showed a difference of 40%. In the new vane the total pressure loss is due to the boundary layer and profile loss only.

The difference in the thermal boundary layer between the two cases naturally affects the heat transfer to the vane surface, as seen in Figure 6.6 which shows the Nusselt number on the suction and pressure side for the original and shielded vane. The Nusselt number on the shielded vane

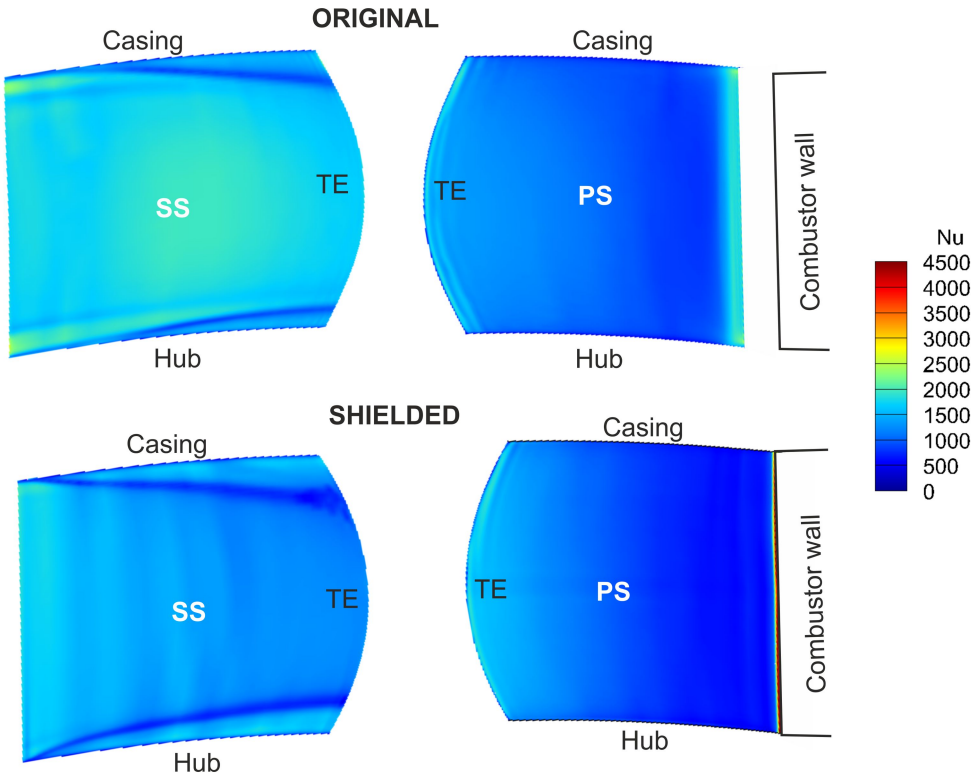

Figure 6.6: Nusselt number on the pressure and the suction side of the original and the new shielded vane

suction side is overall lower compared to the original vane. Near the endwalls, however, this is reversed, with a higher Nusselt number compared to the mid-span. The difference with the original case is due to the difference in the isentropic Mach number, as seen in Figure 6.7. In the shielded vane the isentropic Mach number near the endwall is higher than in the original vane after 70% of the axial chord, leading to higher heat transfer rates to the vane surface. The higher isentropic Mach number on the late suction side of the shielded vane is also observed at mid-span (Figure 6.4); in that region the thick boundary layer of the combustor wall is protecting the vane.

Near the endwall, however, the boundary layer has been lifted off by the passage vortex, and has no protective effect on the vane. The pressure side of the vane is not significantly affected, as the wake of the combustor wall which causes the difference between the two cases is directed to the vane suction side, but is lower for the shielded vane immediately downstream of the combustor wall, due to the absence of a leading edge.

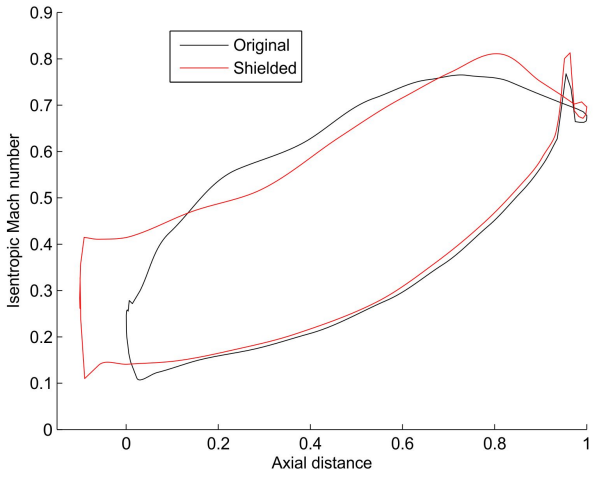

Figure 6.7: Isentropic Mach number distribution on the original and the new shielded vane at 5% span

6.1.4 Cooling Slot Design

One of the main concerns for the new design was whether adequate cooling of the vane leading edge region could be achieved without the use of a showerhead. The change in pressure distribution caused a pressure difference across the gap between the combustor wall and the vane, as seen from the trajectory of the wake and the thermal boundary layer on the right hand side of Figure 6.5. The existing cooling slot on the combustor wall did not provide adequate cooling of both the pressure and the suction side of the vane.

To facilitate distribution of the cooling flow to both vane surfaces a second slot was introduced in a parallel configuration, with one slot close to the vane pressure side and one slot close to the suction side, as shown in Figure 6.8(a). However, this did not stop the hot gas cross-flow from the pressure side to the suction side. The orientation of the pressure side slot was therefore changed

to $45°$ relative to axial, as shown in Figure 6.8(b) (details of the slot geometry are also shown in Figure 6.3). Figures 6.8(a) and 6.8(b) show coolant streamlines coming out of the slots and adiabatic cooling effectiveness contours on the vane surface and suction side. It can clearly be seen that in the first case the coolant from both slots was directed to the suction side of the vane by

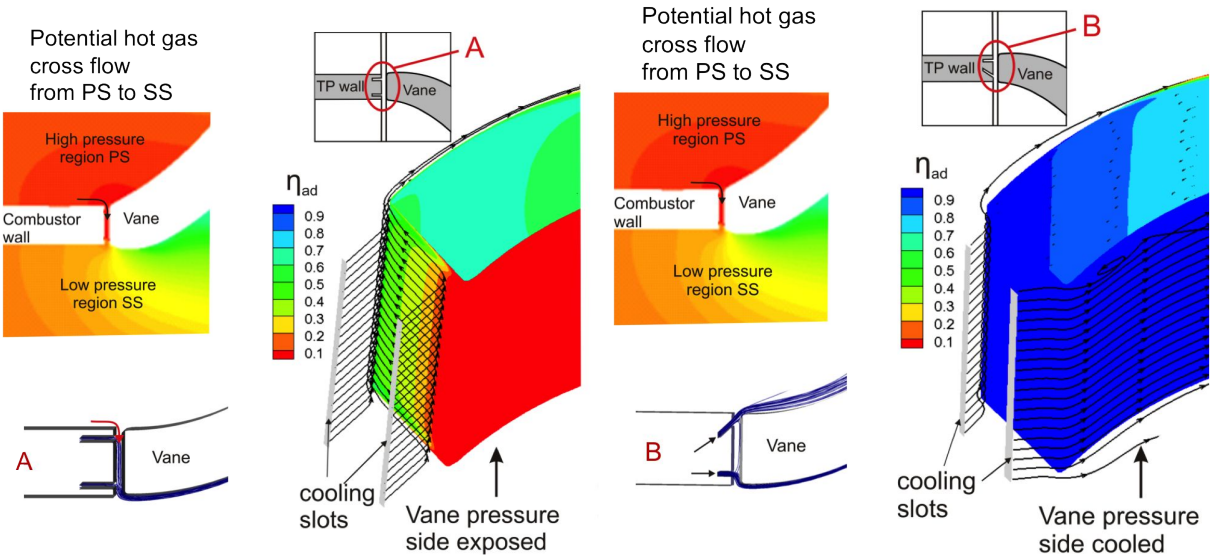

(a) Two parallel slots

(b) Pressure side slot at $45°$

Figure 6.8: Combustor wall cooling slot design

the pressure gradient across the gap, leaving the pressure side unprotected from the hot gas flow. In the second case, the modified slot design enabled the even distribution of coolant flow to both the pressure and the suction side, protecting them from the hot mainstream flow and successfully sealing the gap, as the coolant flow entered the main passage adjacent to the vane surface at both the pressure and the suction side.

6.1.5 Vane Surface Cooling

The use of continuous slots upstream of the vane leading edge enabled uniform distribution of coolant flow to both the pressure and the suction side of the vane. The coolant mass flow rate in the shielded case was at a similar level to the amount of air used for a shower head, 1.3% of the passage inlet flow, and resulted in efficient cooling of the leading edge and the downstream regions of the vane surface through a continuous film of coolant. Figure 6.9 shows the adiabatic

cooling effectiveness on the vane. A cooling effectiveness of at least 0.5 was achieved from the leading edge down to 80% of the axial chord downstream on the suction side and down to 30% of the axial chord downstream on the pressure side. The average cooling effectiveness achieved was 0.363 for the vane pressure side and 0.664 for the vane suction side, with coolant mass flow rates of 0.63% of the passage inlet for the pressure side and 0.68% for the suction side.

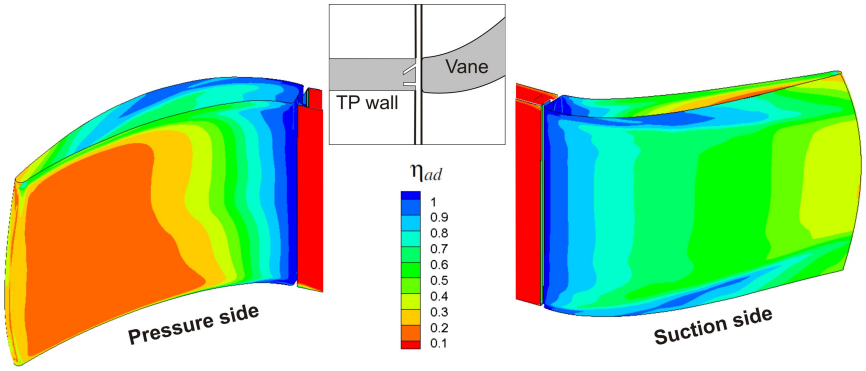

Figure 6.9: Adiabatic film cooling effectiveness on the vane surface, total coolant mass flow rate 1.3% of passage inlet

6.2 Comparison of the Shielded Vane to the Original

The effect of the new design on the aerodynamic flow field and the secondary flow is presented in this section. This is followed by a comparison of the cooling effectiveness on the endwalls between the original and the shielded design to highlight the effect of secondary flow on the endwall flow and cooling.

6.2.1 Aerodynamic Flow Field

As the axial distance between the combustor and the vane was reduced in the new design, the distance between the inter-component slot and the leading edge of the middle vane was halved, as shown in Figure 6.10. The reduction of this distance in studies presented in the literature was seen to move the saddle point very close to the slot, resulting in higher pressure at the exit of the

slot. This could affect secondary flow formation and also cause ingress of hot gas into the cavity and reduce the adiabatic cooling effectiveness on the endwall.

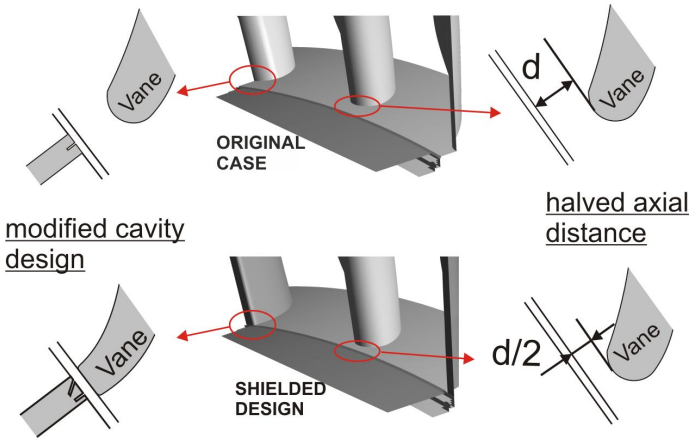

Figure 6.10: Details of original and shielded vane design

In order to assess the severity of this possible effect in the new design, the pressure field at the hub of the shielded vane design was compared to the original case. This is shown in Figure 6.11, where coolant streamlines are also plotted on the hub endwall. In the original case, Figure 6.11(a), there was a small difference in secondary flow formation between the two neighbouring vanes. It can be seen that the saddle point (marked with a white circle in the figure) which characterizes the origin and development of the horseshoe vortex was shifted due to the presence of the combustor wall. The locations of the horseshoe vortices are marked with black dashed lines. Shielding removed the saddle point and hence the horseshoe vortex upstream of every second vane, as shown in Figure 6.11(b). In addition, the saddle point of the middle vane was shifted towards the pressure side due to the vane leading edge being closer to the slot in the shielded case, which affected the pressure distribution upstream of the vane. The smaller pressure gradient across the passage significantly reduced cross-flow at the endwalls, especially in passage B1. As seen in the two figures, the pressure distribution in the lower passage was similar between the two cases, whereas in the top passage the loading of the combustor wall trailing edge resulted in a different pressure gradient and reduced secondary flow in the shielded case compared to the original. The reduction

of the axial distance between the vane and the leakage slot did not affect the flow in that region and there was still coolant flow exiting all the way along the slot.

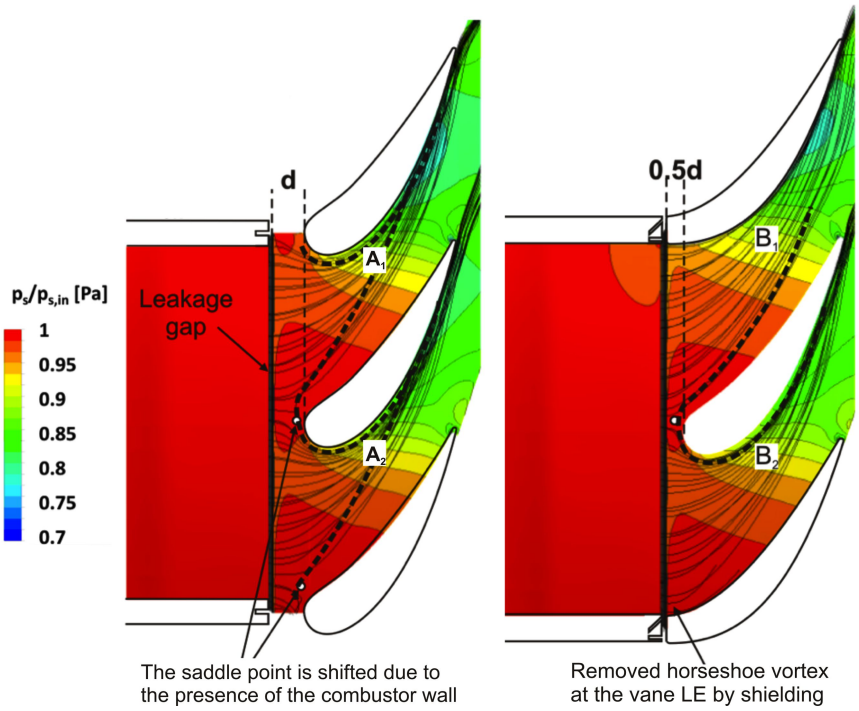

(a) Original case (b) Shielded case

Figure 6.11: Static pressure field, streamlines and secondary flow at hub

6.2.2 Endwall Cooling

When looking at fluid flow away from the surfaces, an equivalent measure of the effectiveness of the cooling process is the normalized temperature θ. Figure 6.12 presents normalized temperature contours in the cavity in four locations, on either side of the leading edge of each of the two neighbouring vanes, for the original and the shielded case. In all locations coolant flow was seen to exit the cavity, reducing the temperature of the flow near the endwall and cooling the endwall surfaces.

In the original case the vane that is downstream of the combustor wall had a very similar pressure field to the one in the centre of the duct, as seen in Figure 6.11(a), resulting in a similar coolant flow distribution at the exit of the slot. The temperature of the flow inside the cavity was higher near the vane suction side on the left hand side of Figure 6.12(a), showing that there is mild

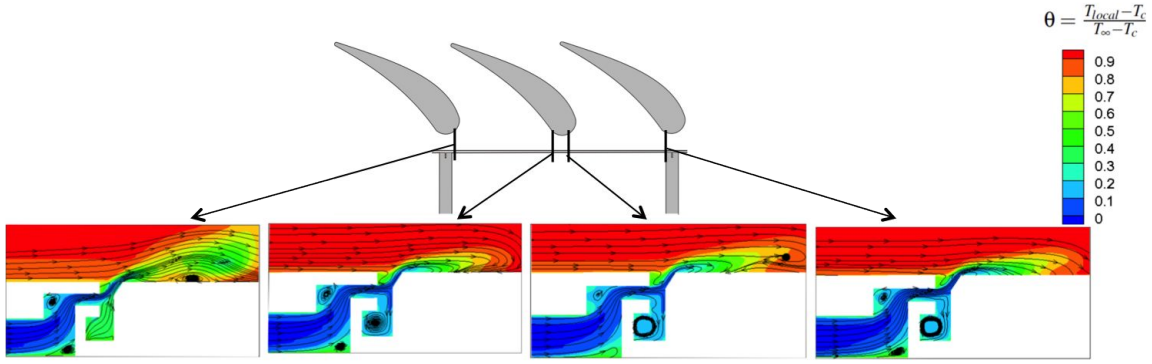

(a) Original case

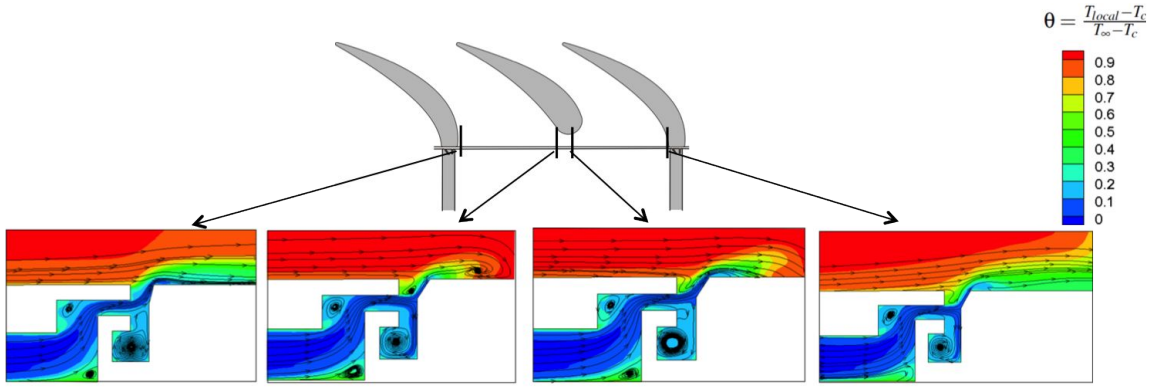

(b) Shielded case

Figure 6.12: Non-dimensional temperature contours and streamlines in leakage cavity

ingress of hot gas into the cavity in the region downstream of the combustor wall trailing edge. Temperature contours and flow streamlines in the same locations are shown for the shielded case in Figure 6.12(b). The region near the middle vane was not affected by the change of axial distance from the slot in the shielded case. In both cases, the coolant flow exiting the cavity remained attached until it reached the saddle point where it got entrained in the horseshoe vortex and swept towards the vane suction side. The regions near the shielded vane pressure and suction side showed significant improvement over the original vane. The temperature inside the cavity was lower, particularly near the shielded vane suction side. In addition, the coolant flow exiting the cavity near the shielded vane pressure and suction side was better attached, resulting in more effective cooling of the surfaces. This was caused by the more favourable pressure gradient between the cavity and the mainstream near the shielded vane leading edge, especially close to the suction side.

The cooling effectiveness from the coolant exiting the leakage slot is shown in Figure 6.13 for the hub endwall. The uniform distribution of coolant observed in the previous figures ensured better coverage of the endwall region. The shielded vane design provided improved cooling of the endwall in the suction side region of the shielded vane compared to the original case, as seen on the left hand side of Figure 6.13. The peak pressure region at the front of the vane was

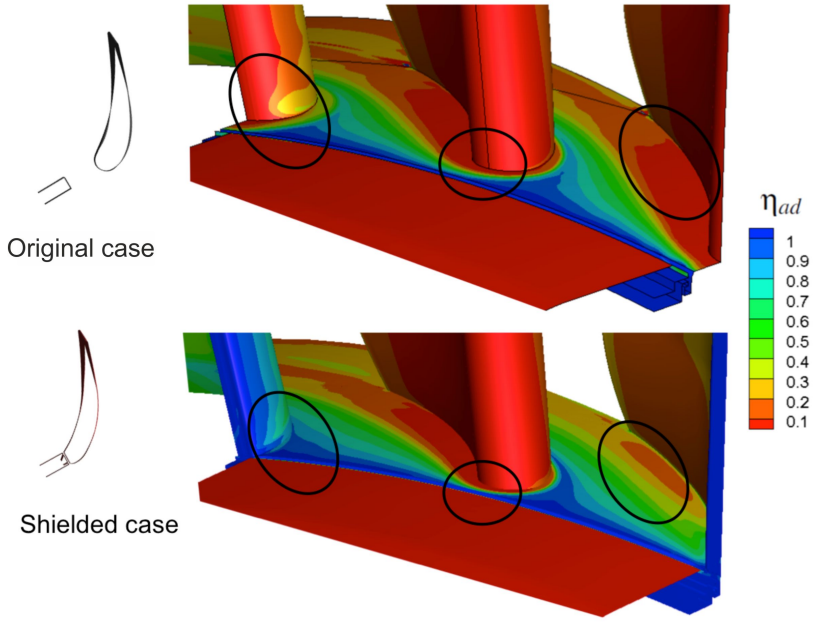

Figure 6.13: Adiabatic cooling effectiveness on the hub endwall for the original and the shielded case

shifted forward relative to the original design, resulting in more coolant flow exiting from the cavity in that location. The uncooled region upstream of the vane leading edge in the original case was removed and the peak heat transfer region on the endwall observed in the experimental studies in Chapter 4 and in the literature was cooled with high adiabatic cooling effectiveness. As expected from the streamline and horseshoe vortex pattern presented in Figure 6.11, the reduction in secondary flow, particularly in the right hand side passage, resulted in a significant increase in adiabatic cooling effectiveness on the hub endwall near the pressure side of the shielded vane. The cooling effectiveness on the endwall near the middle vane leading edge region was not affected by the change of axial distance, as discussed previously. In addition, the reduced pressure gradient in the passage resulted in improved coverage and cooling of the endwall.

Similar results were observed on the casing endwall, Figure 6.14. The region of the endwall near the shielded vane suction side was better cooled than in the original case. The region near the middle vane pressure side, which showed improved cooling in the hub endwall, was marginally better in this case. Significant improvement was observed on the endwall near the shielded vane pressure side.

Table 6.2 shows the coolant mass flow rate relative to the passage inlet mass flow rate and the average cooling effectiveness over the hub and casing endwalls for the original and shielded case. The same total pressure boundary conditions were used in both the original and the shielded case. The mass flow rate of the coolant from the endwall cavities changed due to the change in aerodynamics between the original and shielded case, which altered the driving pressure difference and caused more or less coolant flow to exit from the cavities. In the shielded case more coolant exited the hub cavity than in the original case, whereas the coolant mass flow rate in the casing cavity was lower than in the original case, but still resulted in higher cooling effectiveness. Overall, both endwalls were better cooled in the shielded case, with the same total mass flow rate from the two leakage slots.

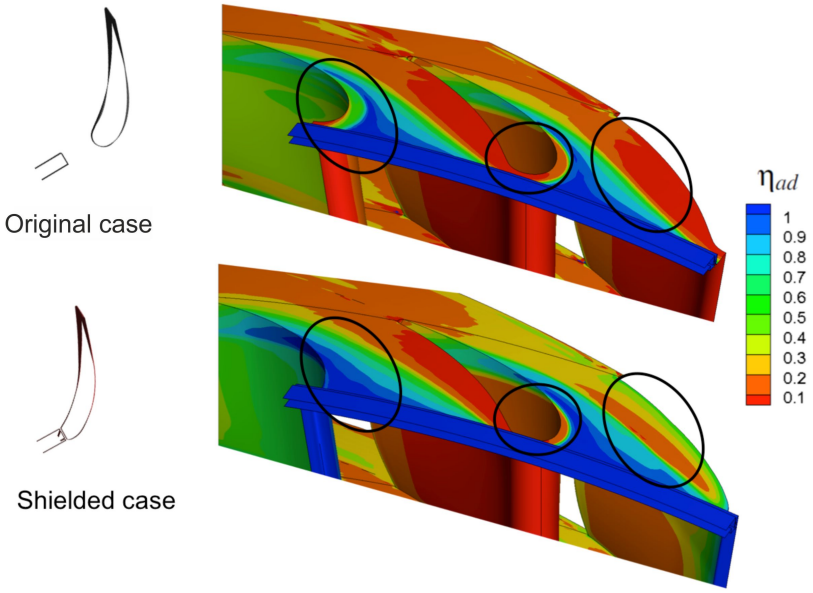

Figure 6.14: Adiabatic cooling effectiveness on the casing endwall for the original and the shielded case

Table 6.2: Endwall slot coolant mass flow rate ratio and average cooling effectiveness on hub and casing endwalls for original and shielded case

	Hub endwall		**Casing endwall**	
	$\frac{\dot{m}_c}{\dot{m}_\infty}$	$\eta_{ad,avg}$	$\frac{\dot{m}_c}{\dot{m}_\infty}$	$\eta_{ad,avg}$
Original	0.76%	0.398	1.02%	0.41
Shielded	1.06%	0.52	0.75%	0.498

6.3 Effect of Engine-Representative Inlet Conditions on the Vane Leading Edge Shielding

In order to determine the robustness of the new concept, the impact of inlet turbulence and swirl on the NGV passage aerodynamics and endwall cooling was investigated; a comparison of the new design to the original case is presented in this section. The effect of engine-representative inlet conditions on the shielded vane geometry is highlighted by contrasting the secondary flow structure developed in the two cases and its effect on endwall cooling. For this study the annular sector used in the previous studies was modified to remove the transition duct and allow for the specification of engine-representative inlet conditions immediately upstream of the vanes. Periodic boundary conditions were set on the sides to model the full annulus. Total pressure boundary conditions were set at the inlet of the duct and the leakage and cooling slots.

6.3.1 Inlet Swirl Profile

The inlet swirl profile used for the numerical studies is shown in Figure 6.15(a). The swirl angle range was $\pm 35°$, as shown in Figure 6.15(a). A uniform inlet turbulence intensity of 15% was used, and the turbulence length scale was $20\,\text{mm}$. The results from numerical studies with inlet swirl and high turbulence were compared against those with high inlet turbulence only to determine the effect of positive and negative inlet swirl.

The computational domain and the definition of swirl orientation used in this study is shown in Figure 6.15. Swirl is positive when having a clockwise rotation when viewed from upstream.

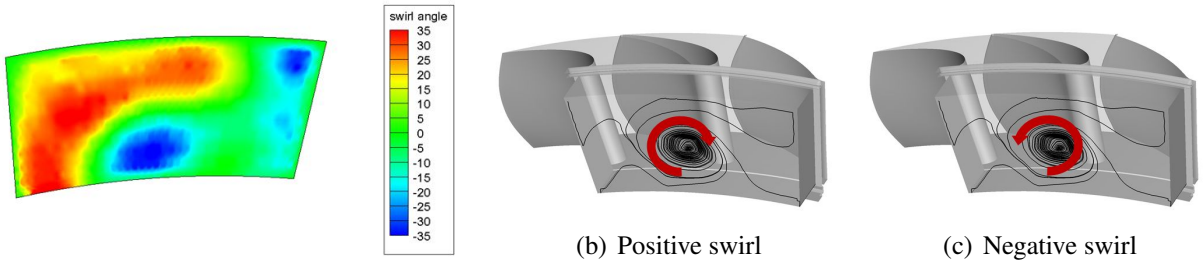

(a) Swirl angle at the inlet

(b) Positive swirl

(c) Negative swirl

Figure 6.15: Swirl profile and computational domain with swirl orientation

6.3.2 Aerodynamic Field

The flow on the endwalls was affected by inlet swirl for both the original and the shielded case. Figures 6.16(a) and 6.16(b) compare streamlines on the hub endwall for the original and shielded cases respectively for no inlet swirl (top), positive (middle), and negative (bottom) swirl.

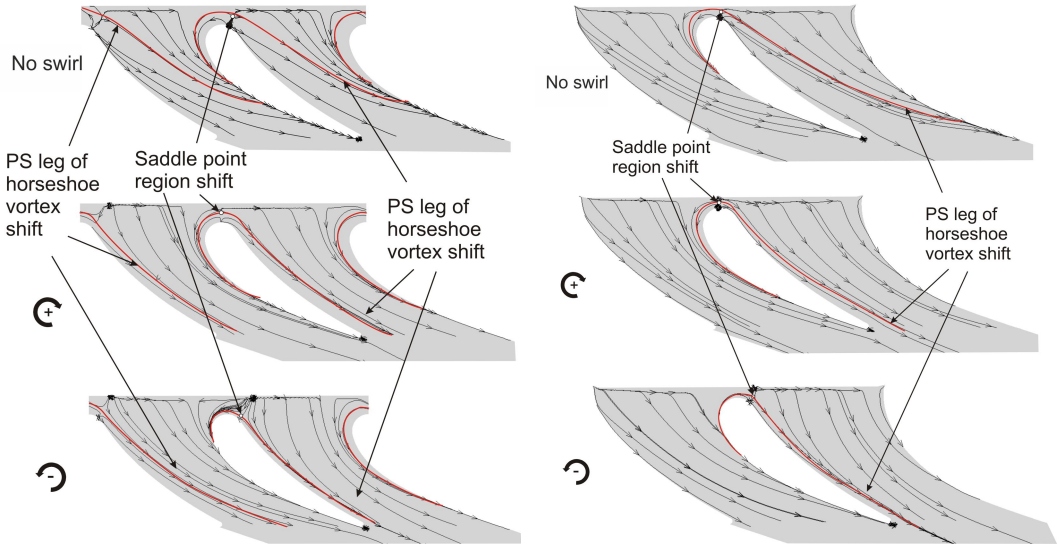

(a) Original case

(b) Shielded case

Figure 6.16: Streamlines on hub endwall for the two cases with and without inlet swirl

For uniform inlet flow without swirl in the original case the horseshoe vortex formation on the middle vane and the vane downstream of the combustor wall was similar. For the shielded

case a horseshoe vortex was only formed upstream of the middle vane stagnation region. The pressure side leg of this horseshoe vortex reached the suction side of the vane downstream of the combustor wall further downstream than in the original case due to the lower cross-passage pressure gradient. This had the benefit of better coverage of the endwalls when coolant from an upstream slot is used. When inlet swirl was introduced, the saddle point of the middle vane was shifted closer to the suction side for positive swirl and further downstream on the pressure side and closer to the vane surface for negative swirl. The pressure side leg of the horseshoe vortex shifted closer to the vane pressure side for positive swirl compared to uniform inlet flow without swirl and even closer for negative swirl.

Streamlines on the casing endwall are shown in Figure 6.17. For uniform inlet flow without swirl the same trends were observed as at the hub endwall. The introduction of inlet swirl reversed the trends, as expected due to the opposite flow angles compared to the hub. The saddle point region of the middle vane shifted further downstream on the pressure side and closer to the vane surface for positive swirl and towards the suction side for negative swirl. The pressure side leg of the horseshoe vortex shifted closer to the vane pressure side for negative swirl compared to uniform inlet flow and even closer for positive swirl.

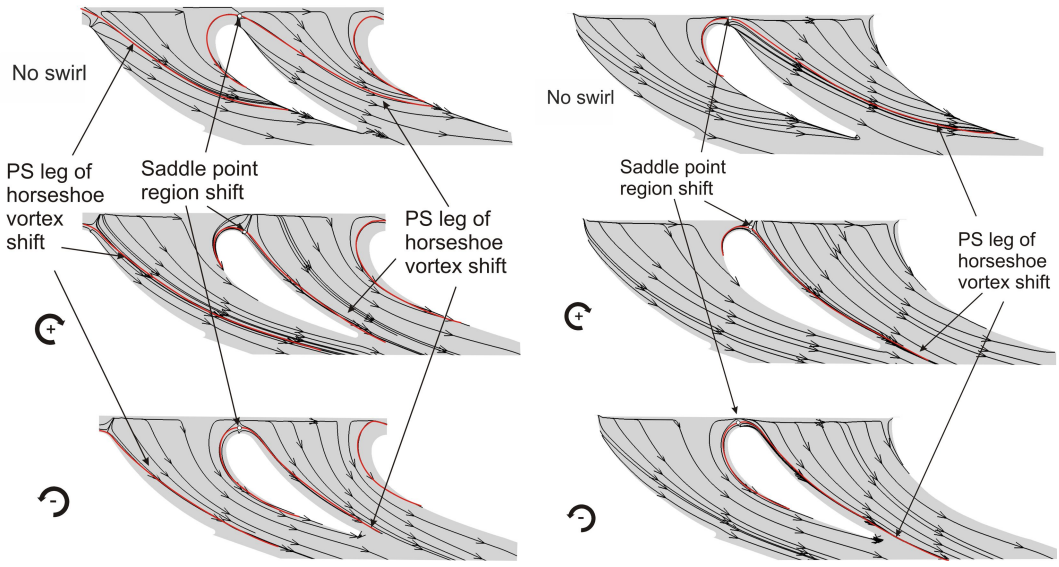

(a) Original case (b) Shielded case

Figure 6.17: Streamlines on casing endwall for the two cases with and without inlet swirl

6.3.3 Thermal Field

The coolant flow exiting from the slots on the hub and casing endwall was inevitably affected by the different aerodynamic field. Figure 6.18 showed non-dimensional temperature isosurfaces of coolant flow exiting from the slots on the endwalls as well as on the combustor wall upstream of the leading edge for the original and shielded cases. High inlet turbulence was introduced for the case without inlet swirl to allow a better comparison, as inlet swirl also augments turbulence levels. Inlet turbulence intensity and length scale boundary conditions were the same for all cases.

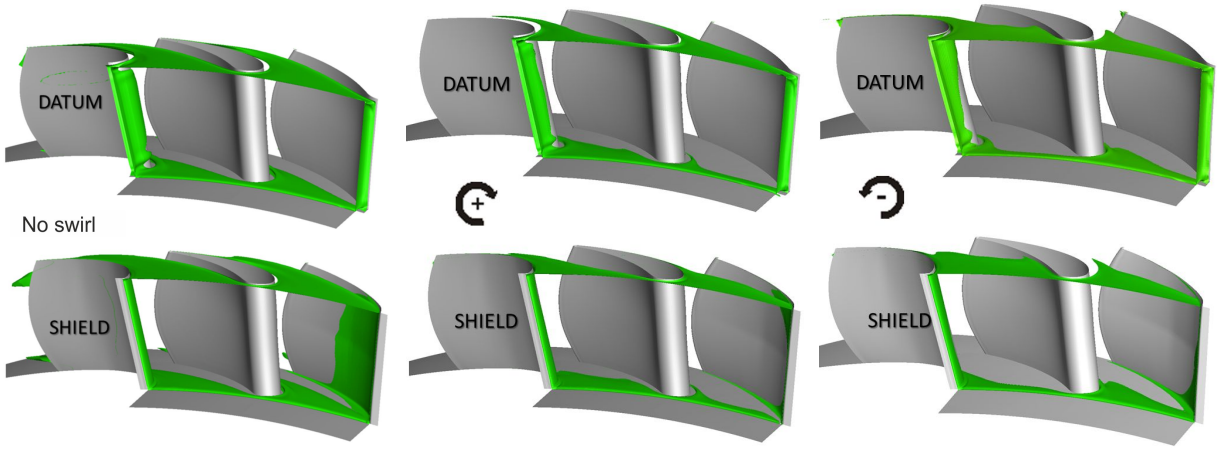

(a) No swirl (b) Positive swirl (c) Negative swirl

Figure 6.18: Non-dimensional temperature isosurfaces for original and shielded case, $\theta = 0.7$, Tu=15%

For no inlet swirl, Figure 6.18(a), the coolant coverage was similar for the left and right hand passages in both cases. In the shielded case both endwalls were better covered due to the reduction of secondary flow; this allowed the coolant film to also protect the endwall near the shielded vane pressure side. The introduction of positive swirl reduced the coolant coverage of the endwalls compared to the no swirl case for both the original and the shielded design, as shown in Figure 6.18(b). In the casing region the coverage was similar in both passages and better coverage was achieved in the shielded case compared to the original. In the hub region positive swirl led to coolant migration towards the left hand side passage. Coolant coverage was also marginally improved in the shielded compared to the original case. Negative swirl led to coolant migration

towards the left hand side passage in the casing region and towards the right hand side passage in the hub region, as shown in Figure 6.18(c). This trend was observed in both the original and the shielded case, with better coverage achieved again in the shielded case. In both cases, with positive and negative swirl, the shielded vane leading edge remained protected from the hot mainstream flow.

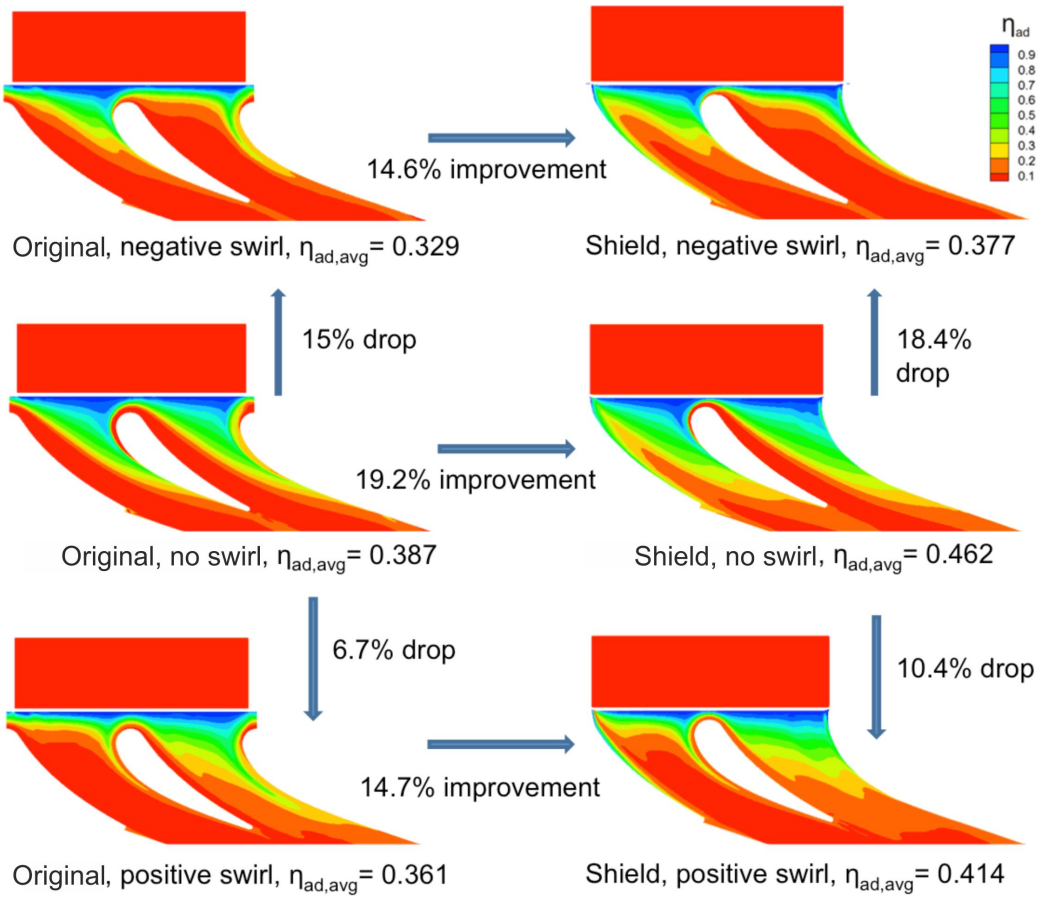

Figure 6.19: Adiabatic cooling effectiveness contours on hub endwall for original and shielded case with negative swirl (top), no swirl (middle), and positive swirl (top), and Tu=15%

In Figures 6.19 and 6.20 adiabatic cooling effectiveness contours on the hub and casing endwalls, respectively, are used as a measure of endwall film coverage to indicate which parts of the coolant film are swept away by swirl and secondary flow. Mass-averaged adiabatic cooling effectiveness on each endwall is used to quantify the improvement in endwall cooling achieved with the shielding concept in all cases.

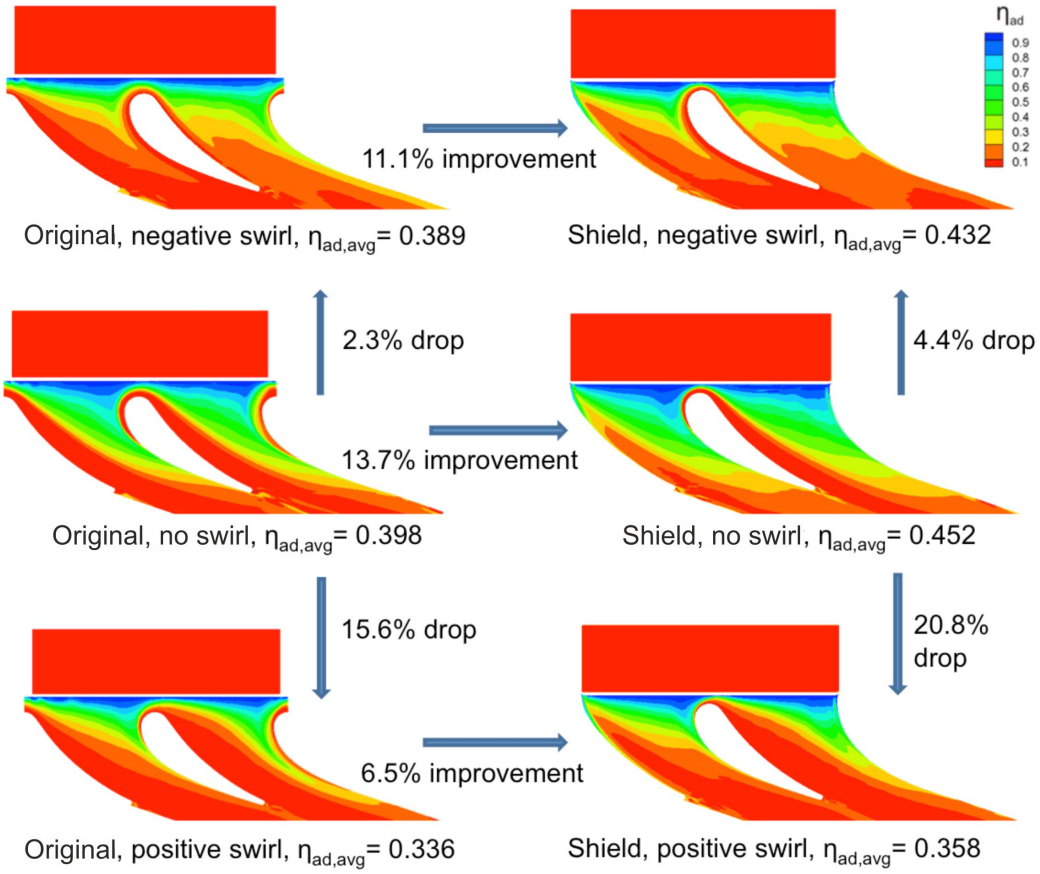

Figure 6.20: Adiabatic cooling effectiveness contours on casing endwall for original and shielded case with negative swirl (top), no swirl (middle), and positive swirl (top), and Tu=15%

On the hub endwall shielding led to a 19.2% improvement in cooling effectiveness compared to the original case for high inlet turbulence. With the addition of swirl, either positive or negative, an improvement of almost 15% was achieved in the shielded design compared to the original. The migration of cooling flow due to inlet swirl led to better coverage of one or the other passage, but both passages were better protected in the shielded case. On the casing endwall the improvement in cooling effectiveness for the shielded design compared to the original was 13.7% for the high turbulence case, 6.5% for positive and 11.1% for negative inlet swirl.

Different swirl orientations can lead to one or the other endwall passage being better protected, as coolant flow gets more or less swept away from the endwall regions near the vane pressure side. The design of the swirler can therefore be optimized in combination with endwall cooling

techniques to suit the operating conditions of the engine and ensure adequate cooling of both endwalls.

Figures 6.21, 6.22, and 6.23 show adiabatic cooling effectiveness contours on the shielded vane pressure and suction side for no inlet swirl, positive, and negative inlet swirl, respectively. In all cases, inlet turbulence intensity was 15%. Positive inlet swirl led to more coolant being swept towards the casing on the pressure side and towards the hub on the suction side. The opposite trend was observed for negative inlet swirl. In all cases, the coolant from the upstream slots was uniformly distributed to the vane pressure and suction sides, forming a continuous film on the vane surface. The vane leading edge was therefore effectively protected in both cases.

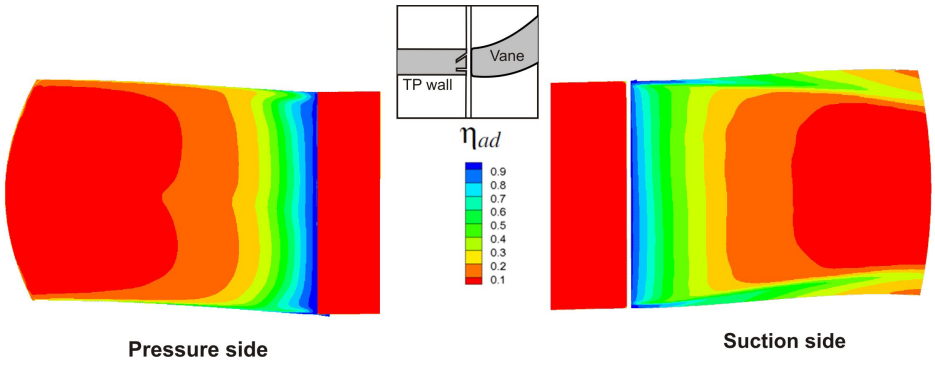

Figure 6.21: Adiabatic cooling effectiveness contours on shielded vane pressure (left) and suction (right) side with no inlet swirl and Tu=15%

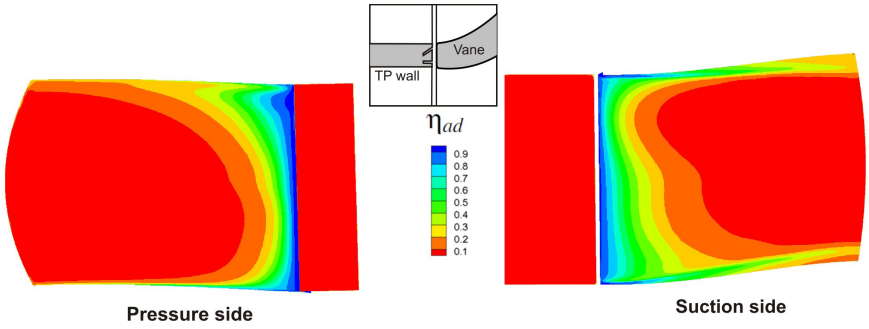

Figure 6.22: Adiabatic cooling effectiveness contours on shielded vane pressure (left) and suction (right) side with positive swirl and Tu=15%

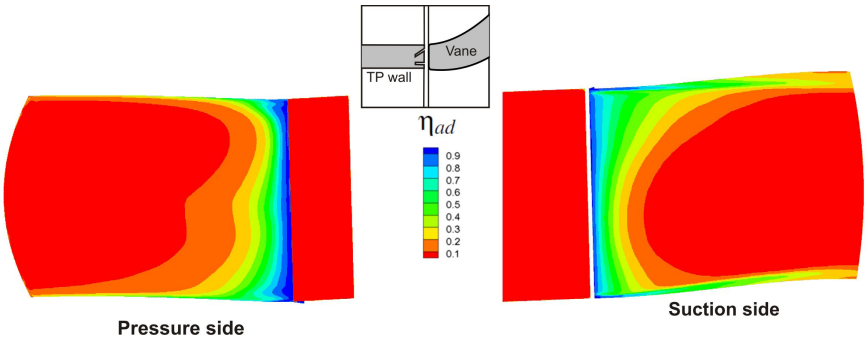

Figure 6.23: Adiabatic cooling effectiveness contours on shielded vane pressure (left) and suction (right) side with negative swirl and Tu=15%

6.4 Conclusions

A novel concept of shielding the nozzle guide vane leading edge using the upstream combustor wall was developed and numerically analysed in this chapter. The vane shielding improved the aerodynamics of the vane by removing the horseshoe vortex and altering the secondary flow. The new vane provided the same turning for the downstream rotor blade row. The new design resulted in significantly lower total pressure loss compared to the original, due to the absence of the wake of the combustor wall upstream of the vane. Furthermore, the thicker, protective boundary layer on the vane suction side resulted in lower heat transfer to the vane surface compared to the original vane. The potential of the concept in effective cooling of the vane was demonstrated successfully. The new design used coolant from two slots at the upstream combustor wall to cool the leading edge. This resulted in a uniform coolant distribution and high cooling effectiveness on the vane surfaces and enabled the removal of the shower head and the corresponding internal cooling passage.

Cooling flow through the hub and casing leakage slots was modelled to ensure that the new design does not have a detrimental effect on the flow in the cavities and the endwall cooling. The change of pressure distribution near the shielded vane with the new design resulted in more coolant exiting the cavity in that region and a more uniform distribution within the passage, leading to improved cooling of the endwalls compared to the original case. The reduced axial distance

between the slot and the vane leading edge was not seen to affect the cooling flow. Overall, effective cooling of the cavity was achieved, with lower temperatures in the shielded case. The cooling effectiveness on the endwall regions within the passage was improved with the vane geometry modification, due to the reduction in strength of the secondary flow and the removal of the horseshoe vortex with the shielded design. The increase in average adiabatic film cooling effectiveness on the endwalls was 25%, with the same total coolant mass flow rate. A successful implementation of the new concept would cool the vane adequately without increasing the coolant requirements, which could have led to increased aerodynamic loss. It would also significantly simplify the vane geometry by removing the shower head features and some of the downstream film cooling holes, while providing a more uniform temperature distribution of the vane surface.

The concept was investigated under engine-representative conditions of high inlet turbulence and swirl. Inlet swirl resulted in a reduction in the strength of secondary flow for both the original and the new design. The saddle point was shifted and the horseshoe vortex formation upstream of the middle vane stagnation region was altered in both cases. High inlet turbulence intensity and swirl did not affect the cooling of the shielded vane leading edge, as coolant was seen to be uniformly distributed to the pressure and the suction side of the vane. The absence of a horseshoe vortex in the shielded case allowed the coolant film to protect the endwall near the shielded vane pressure side, with no inlet swirl, positive, and negative swirl, under high inlet turbulence conditions. The adiabatic cooling effectiveness on the endwalls with the same coolant mass flow rate was also increased under high swirl and high turbulence intensity inlet conditions, with a better performance for negative inlet swirl. The improved cooling effectiveness achieved with the shielded design may permit an increase in turbine entry temperatures, leading to higher overall efficiency and reduced emissions or increased component life under the same operating conditions due to the lower metal temperatures, especially on the vane endwall near the suction side.

Chapter 7
Experimental Investigation of the Vane Leading Edge Shielding Concept

The new shielded vane shielding concept was tested experimentally in the high speed cascade to determine the aerodynamic performance of the new vane and the heat transfer to the vanes and endwalls. For this purpose a model of the new shielded vane was manufactured using stereolithography. The annular vane profile developed through the numerical studies presented in Chapter 6 was smoothed and linearized and scaled to fit in the experimental facility and a fillet was added on the hub and the casing. The new shielded vane replaced vane 2 in the cascade and was also painted black to minimize reflections. A sketch of the new shielded cascade is shown in Figure 7.1(b); the original cascade used in the experimental facility is shown in Figure 7.1(a) for comparison. All vanes were hollow to increase manufacturing accuracy, with a wall thickness of at least 5mm.

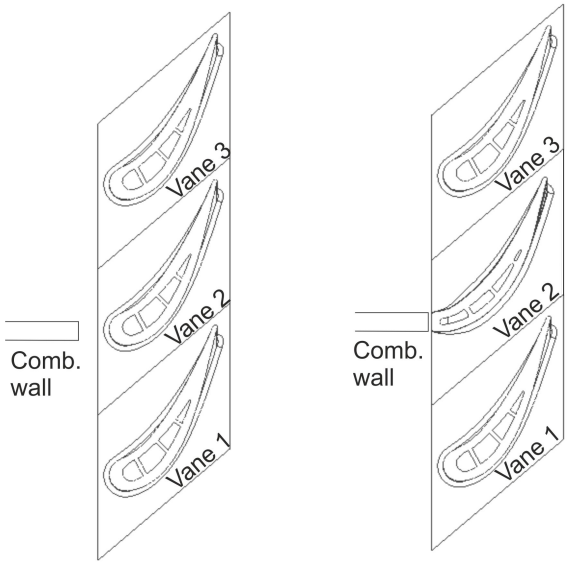

(a) Original cascade (b) Shielded cascade

Figure 7.1: CAD sketch with original and shielded cascade for the experimental facility

7.1 Aerodynamic Field around the Shielded Vane

Periodic flow in the cascade with the shielded vane was achieved with the use of the same sidewalls as in the datum case and the use of both tailboards at 71.5° and verified with a traverse with the five-hole probe downstream of the cascade at 50% span. The total pressure loss coefficient obtained for the shielded vane cascade is shown in Figure 7.2. The total pressure in all passages was the same and so was the loss in the wakes of vanes 1 and 3. The total pressure loss coefficient levels were the same as in the datum case for all passages and for vanes 1 and 3, whereas the shielded vane had lower aerodynamic loss compared to the original and a narrower wake. The maximum total pressure loss coefficient of the original central vane was 15% higher than the adjacent ones, whereas the shielded vane had a maximum total pressure loss coefficient 15% lower than the adjacent vanes. A comparison between the original and shielded vane showed a drop in the maximum total pressure loss coefficient at mid-span of 30%.

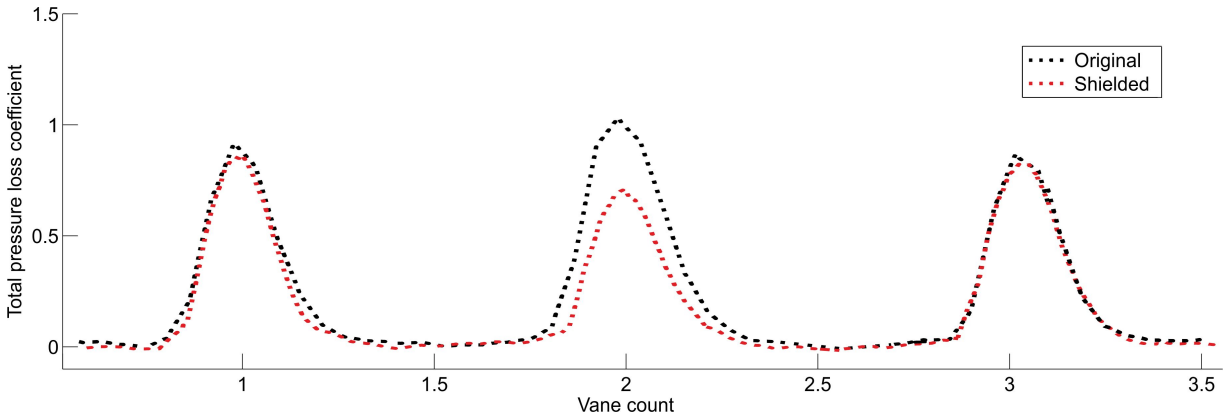

Figure 7.2: Total pressure loss coefficient downstream of the cascade for the new shielded vane compared to the datum case

The wakes of the vanes are also seen in the spatially resolved data obtained with the five-hole probe downstream of the cascade in Figure 7.3. In the original vane cascade the thickness of the wake of the central vane was greater than the neighbouring vanes, as discussed in Chapter 4, and the total pressure loss coefficient was also higher, Figure 7.3(a). In the shielded vane cascade, Figure 7.3(b), the wake of the new vane was significantly narrower than the original. The total

pressure loss was reduced compared to both the original central vane and the neighbouring vanes which do not have the added loss due to the combustor wall.

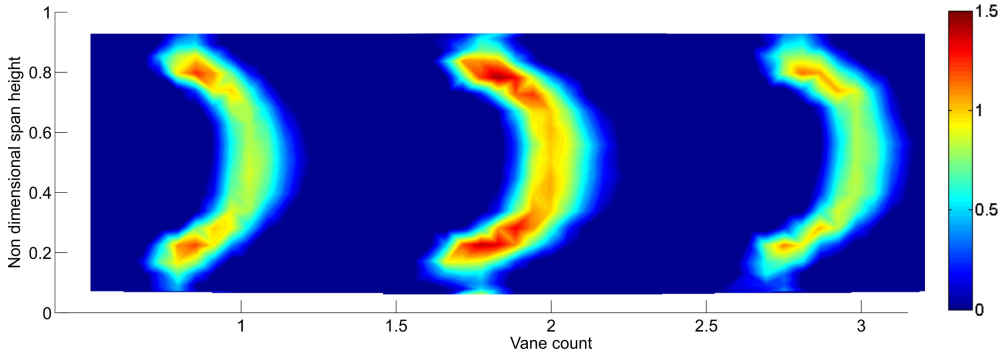

(a) Original vane cascade

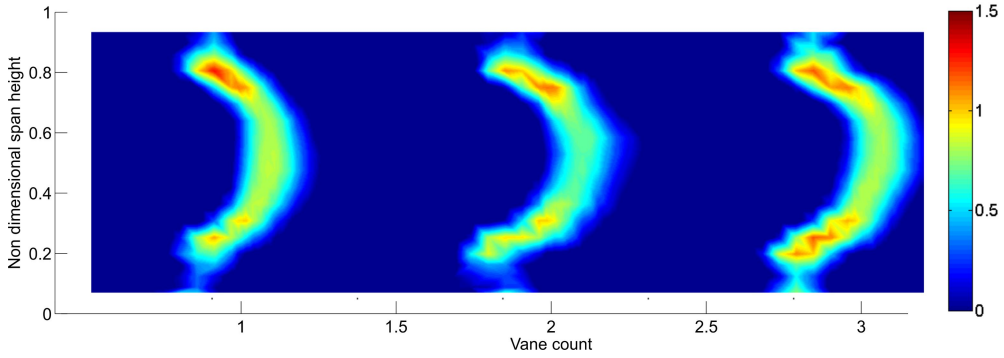

(b) Shielded vane cascade

Figure 7.3: Spatially resolved total pressure loss coefficient downstream of the cascade for low inlet turbulence

Mass-weighted average loss data downstream of the central vane is compared for the original and shielded case in Figure 7.4. The mass-weighted loss coefficient downstream of the new shielded vane was reduced by 49% compared to the original, which corresponds to 9.1% of the outlet dynamic head. The mass-weighted loss coefficient downstream of the two passages of the shielded and adjacent vane was reduced by 32% (loss reduction 4.5% of the outlet dynamic head) relative to the original case. The reduced loss downstream of the shielded vane was due to the smaller wetted area of the new vane and the absence of the wake of the combustor wall, that was seen to increase the total pressure loss coefficient due to its mixing with the vane boundary layer. The reduced loss in the cores at 20% and 80% span was also due to the reduced strength of secondary flow and the removal of the horseshoe vortex on the shielded vane leading edge.

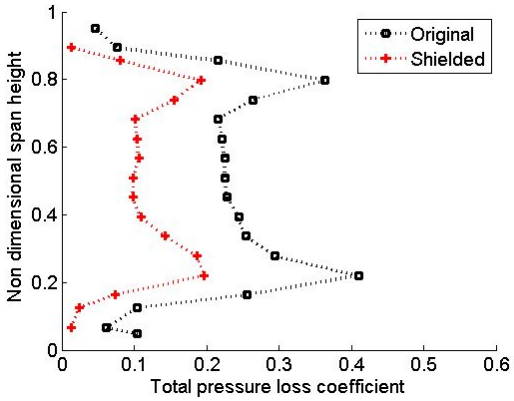

Figure 7.4: Mass-weighted average total pressure loss coefficient for the original and the new shielded vane

The difference in total pressure loss coefficient between the two vanes also extended to the endwall loss, as shown in Figure 7.5 that presents data from the two central passages obtained with a flat Pitot probe downstream of the cascade. The main loss core downstream of the central vane (at the centre of the figure) was significantly reduced for the shielded vane, whereas the loss core downstream of vane 3 (on the right hand side of the figure) was similar in magnitude between the two cases. Furthermore, the loss in the passage between the cores was also reduced, particularly between vanes 1 and 2, due to the reduced cross-passage pressure gradient that weakened secondary flow formation. Loss in the passage between vanes 2 and 3 was similar if not lower for the shielded case compared to the original. The difference between the two passages was therefore significantly smaller in the shielded case.

Due to its different geometry the shielded vane had different loading than the original. The isentropic Mach number distribution obtained at 50% span for the two vanes is shown in Figure 7.6, plotted against the axial chord of the original vane. Data from numerical studies is also shown for comparison. As discussed in Chapter 6, the new vane is longer, extending upstream of the leading edge of the original vane, and has a higher maximum isentropic Mach number on the vane suction side. The exit Mach number of the shielded vane, however, is the same as that of the original vane.

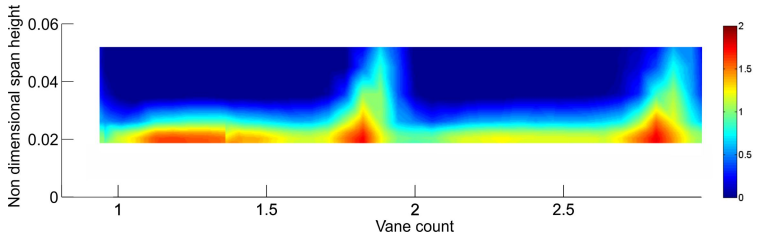

(a) Original case

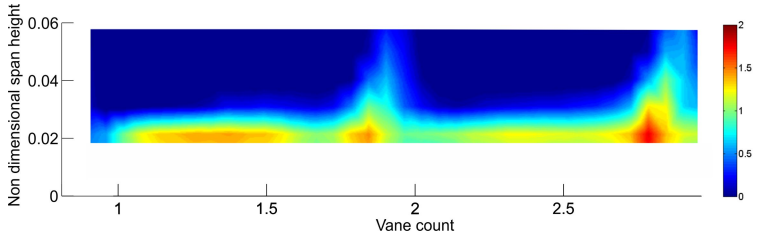

(b) Shielded case

Figure 7.5: Spatially resolved total pressure loss coefficient on the endwall for the original and shielded case, for low inlet turbulence

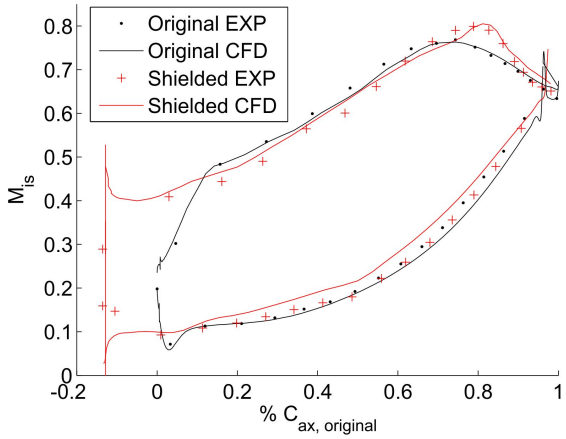

Figure 7.6: Isentropic Mach number distribution on the vane surface for 50% span

The turning of the flow downstream of the shielded vane was maintained; the yaw angle profile was very similar to that of the original vane. The mass-weighted pitchwise average yaw angle for the two vanes is shown in Figure 7.7(a). The underturning near the endwalls was reduced for the shielded vane due to the reduced strength of secondary flow, as discussed in Chapter 6. This was also captured in the spatially resolved distribution of the yaw angle for the original and shielded vane respectively, Figure 7.7(b) and 7.7(c). The distribution of the flow yaw angle at mid-span was similar in the two cases, with marginally higher overturning for the shielded vane.

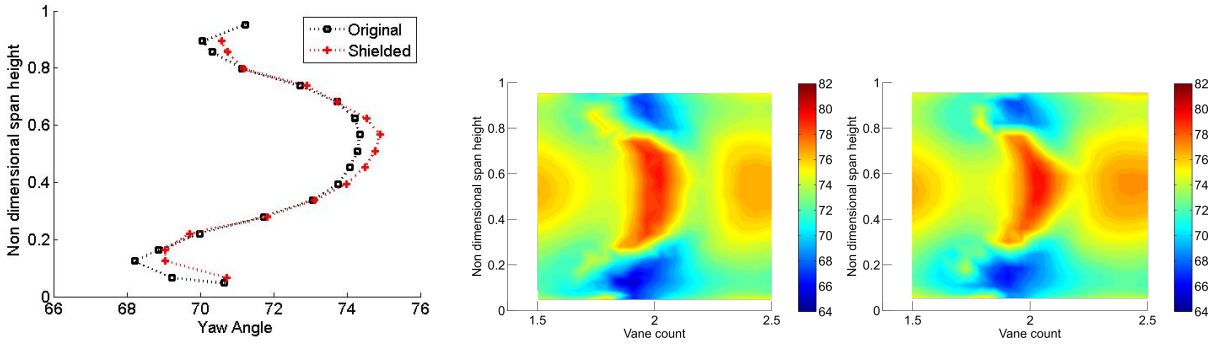

(a) Mass-weighted pitchwise average (b) Original vane (c) Shielded vane

Figure 7.7: Comparison of yaw angle downstream of the original and the new shielded vane

7.2 Thermal Field around the Shielded Vane

The heat transfer field on the shielded vane is presented in this section, using the data obtained through IR thermography on the vanes and endwalls. The data is presented in the form of the dimensionless Nusselt number, based on the axial chord, and is compared to that obtained for the original vane design and presented in Chapter 5.

The effect of the combustor wall was seen on the vane pressure side, Figure 7.8. The peak Nusselt number in the shielded case, Figure 7.8(b) was observed at the start of the shielded vane. On the shielded vane surface, the Nusselt number distribution was uniform and the trends were very similar to those in the datum case, Figure 7.8(a).

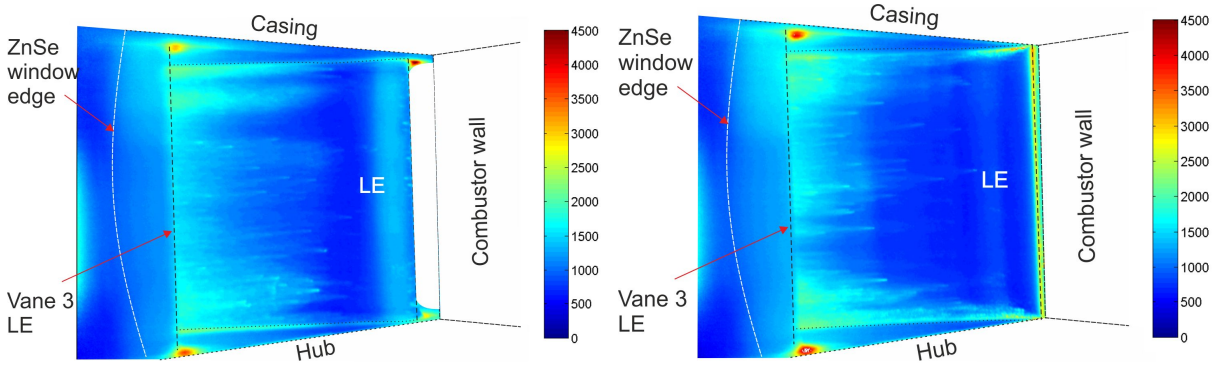

(a) Original vane (b) Shielded vane

Figure 7.8: Nusselt number on the vane pressure side for the original and shielded vane (view 1, Figure 3.25(a))

The main differences between the two vanes were at the start of the vane and near the vane-endwall junction where the Nusselt number locally reached 3000 and 2500 respectively for the shielded vane. The latter were due to the different fillet geometry between the original and the shielded vane seen in Figure 7.9(a). The fillet radius of the shielded vane in the leading edge region was significantly smaller compared to the original vane and increased further downstream. These peaks in heat transfer were confined to a small region that can be cooled from the upstream cooling slots on the combustor wall, as shown in Chapter 6. Further downstream on the vane, the Nusselt number was the same or lower than the original vane for the majority of the axial chord, with an improvement of up to 45%. Regions of higher Nusselt number than the original vane showed an increase of up to 8%, except for the peak Nusselt number regions discussed before, where the difference reached 80%. It should be noted that a plot of the difference between the two cases was not generated for the pressure side view due to the reduced curvature of the shielded vane which results in a much smaller area of the vane viewed by the camera, rendering comparisons using this method misleading for this case. The same applies to the leading edge view and the upstream endwall view.

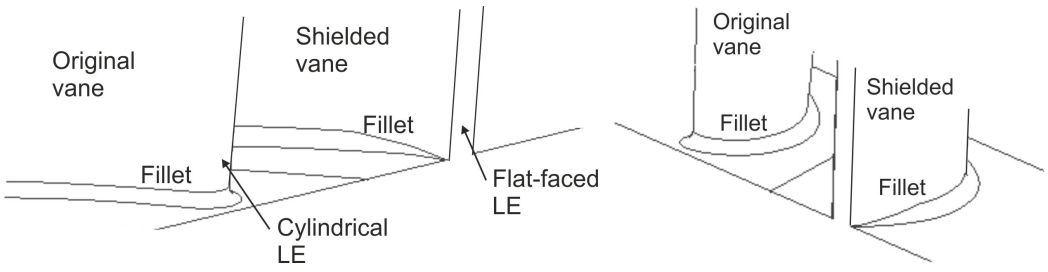

(a) Pressure side (b) Suction side

Figure 7.9: Leading edge fillet for the original and shielded vane

The Nusselt number distribution on the vane leading edge is presented in Figure 7.10. The main difference between the two cases was the uniform Nusselt number distribution on the shielded vane surface. On the leading edge the Nusselt number was higher than the datum case by 1000 (75%), whereas further downstream the values were reduced by 1000 (30%). A high Nusselt number region was observed on the shielded vane leading edge near the hub and a mod-

erate Nusselt number region near the casing. Two peaks in Nusselt number were observed on the hub and casing where the vane meets the endwall due to the difference in the vane leading edge fillet geometry, Figure 7.9(b). Both regions can be cooled from the upstream cooling slots on the combustor wall, as discussed in Chapter 6.

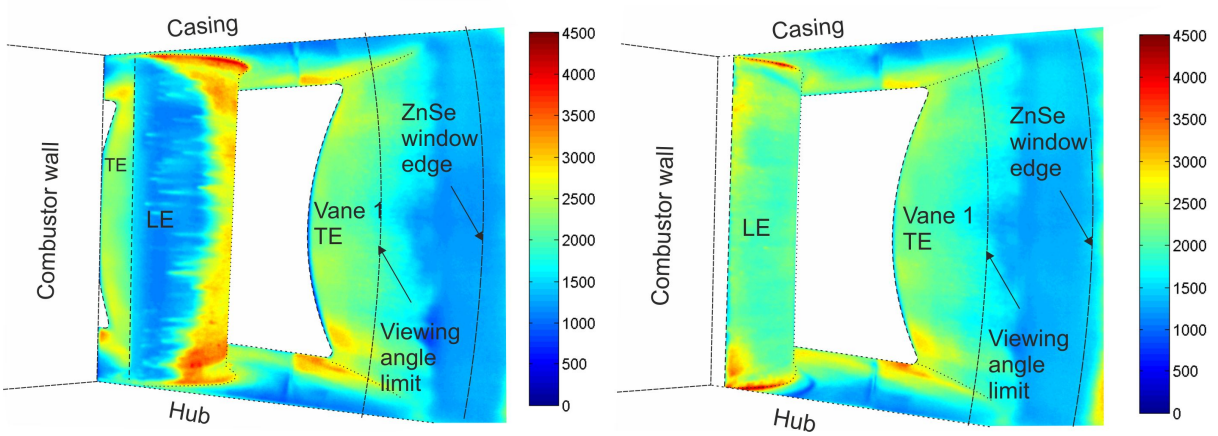

(a) Original vane (b) Shielded vane

Figure 7.10: Nusselt number on the vane leading edge for the original and shielded vane (view 2, Figure 3.25(b))

The heat transfer on the suction side of the vane is shown in Figure 7.11. The Nusselt number on the entire vane surface was lower for the shielded vane compared to the original. This was in agreement with the observations in the numerical studies, Figure 6.6, and was due to the thicker boundary layer on the shielded vane suction side, Figure 6.5. Larger differences were observed in the downstream part of the vane, with a drop of 500 (25%) compared to the original vane, and

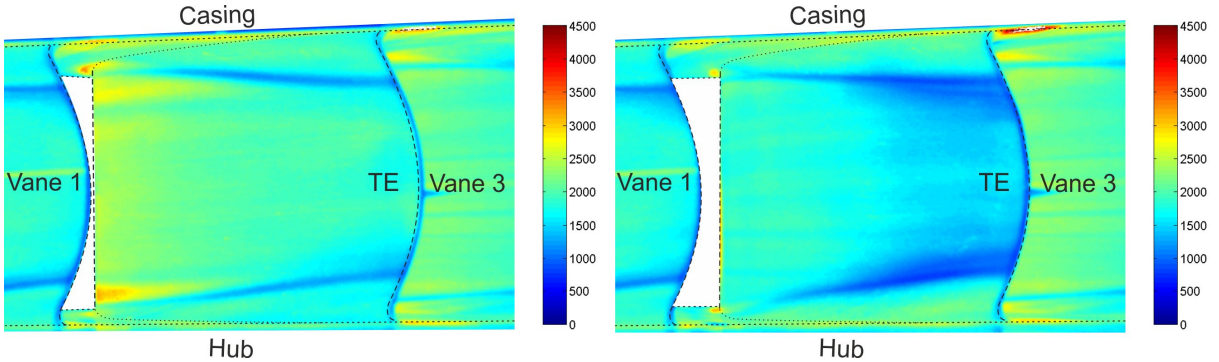

(a) Original vane (b) Shielded vane

Figure 7.11: Nusselt number on the vane suction side for the original and shielded vane (view 3, Figure 3.25(c))

on the sides of the passage vortex trails closer to the mid-span of the vane, where the drop in Nusselt number reached 1000 (40%) near mid-chord. The difference between the Nusselt number of the shielded relative to the original vane, obtained as described in Chapter 5, is shown in Figure 7.12. Two regions of increased Nusselt number on the shielded vane surface were observed between the passage vortex trails and the hub and casing endwalls, where the passage vortex lifts off the boundary layer. This effect is in agreement with the results from the numerical studies in Figure 6.6. In the shielded case the high heat transfer in the region is due to the higher Mach number near the endwall relative to the original case, from 70% axial chord. This was seen at mid-span in the experimental measurements in Figure 7.6 and was also seen to extend to the endwall in the numerical studies presented in Figure 6.7.

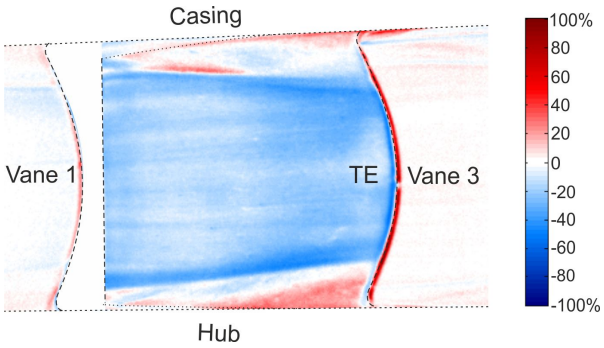

Figure 7.12: Comparison of the Nusselt number on the vane suction side for the shielded vane relative to the original (view 3, Figure 3.25(c))

The heat transfer on the hub endwall, as viewed from upstream, is shown in Figure 7.13. The Nusselt number on the endwall near the vane suction side was lower for the shielded case compared to the original. This was caused by the absence of a horseshoe vortex and the consequent separation line on the endwall near the vane suction side.

A view of the hub endwall from downstream of the cascade is shown in Figure 7.14. The difference in heat transfer in the upstream parts of the endwall noted in the previous figures, especially near the suction side of the central vane, is also seen here. The Nusselt number on the visible part of the endwall was reduced by 500 in the upstream region and increased by 150 at

80% of the axial chord, Figure 7.15. Further downstream on the vane endwall the Nusselt number was the same for the two cases.

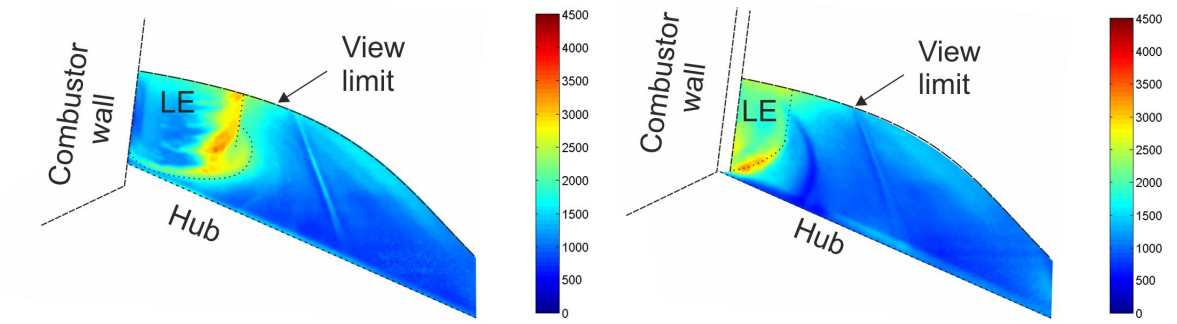

(a) Original vane (b) Shielded vane

Figure 7.13: Nusselt number on the vane endwall viewed from upstream for the original and shielded vane (view 4, Figure 3.25(d))

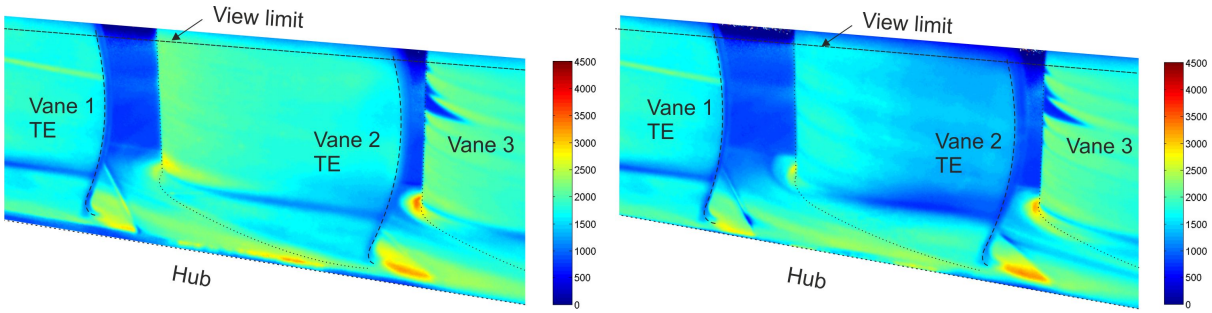

(a) Original vane (b) Shielded vane

Figure 7.14: Nusselt number on the vane endwall viewed from downstream for the original and shielded vane (view 5, Figure 3.25(e))

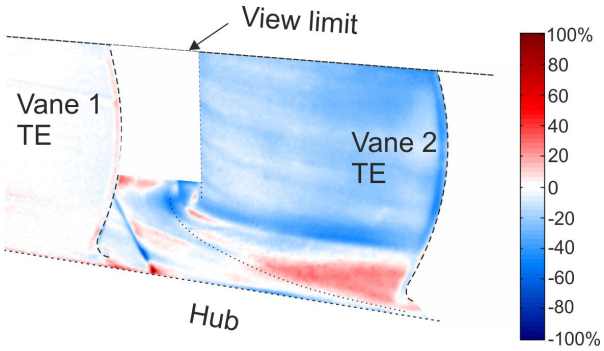

Figure 7.15: Comparison of Nusselt number on the vane endwall viewed from downstream for the shielded vane relative to the original (view 5, Figure 3.25(e))

A better view of the endwall between vanes 2 and 3 is shown in Figure 7.16 and the differences between the measurements are plotted in Figure 7.17. In the shielded case, Figure 7.16(b), the Nusselt number was reduced in the majority of the endwall surface.

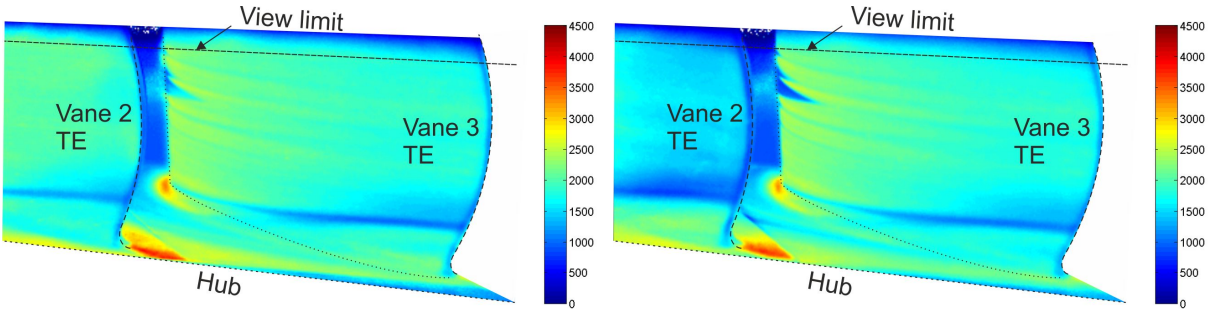

(a) Original vane (b) Shielded vane

Figure 7.16: Nusselt number on the vane endwall between vanes 2 and 3 (view from downstream) for the original and shielded vane

The effect of the new design on the secondary flow was seen on both endwalls. On the endwall between the original vane (vane 1) and the shielded vane suction side, the pressure leg of the horseshoe vortex formed upstream of vane 1 was swept by the cross-passage pressure gradient. As a result, a new boundary layer formed on the endwall downstream of the separation region, increasing the heat transfer to the endwall, to similar levels to the original vanes. However, on the endwall between the shielded vane pressure side and vane 3, the absence of the horseshoe vortex resulted in the endwall being better protected by the incoming boundary layer.

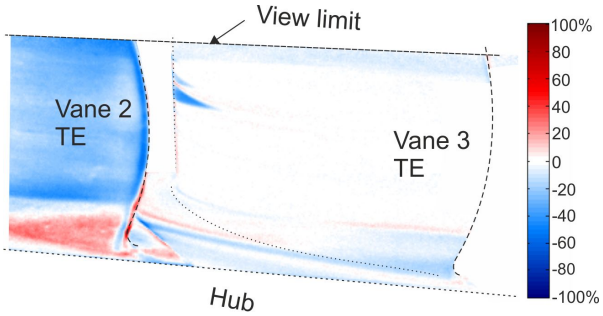

Figure 7.17: Comparison of Nusselt number on the endwall between vanes 2 and 3 (view from downstream) for the shielded vane relative to the original

7.3 Conclusions

The aerothermal performance of the new shielded vane design was analysed in this chapter. The minimization of the axial distance between the combustor and the vane resulted in a significantly smaller wake downstream of the combustor wall trailing edge. Furthermore, the shielding of the vane leading edge resulted in a reduction in secondary flow, as the horseshoe vortex that is formed upstream of every vane was removed for the vane downstream of the combustor wall. The shielded vane therefore showed a significant improvement in aerodynamic performance, with a reduction of the mass-weighted average total pressure loss of 9.1% of the outlet dynamic head compared to the original central vane. The wake downstream of the shielded vane was narrower, the loss cores at 20% and 80% span were smaller, and the loss near the endwall was also reduced. The flow turning downstream of the vane was maintained in the new design, so as to not affect the flow field of the downstream rotor.

The heat transfer to the vanes and endwalls obtained with the use of IR thermography was compared to that of the original vane. The Nusselt number on the vane pressure side was marginally reduced in the new design, and the high Nusselt number at the start of the vane was again on a location that can be covered by the coolant from the combustor wall trailing edge slots, as discussed in Chapter 6. On the suction side, the peak in Nusselt number observed near the leading edge was removed, with maximum values reduced by 30%. The Nusselt number distribution on the shielded vane was uniform with the exception of two high heat transfer regions near the endwalls on the leading edge, which can be again cooled from the upstream coolant slots. Heat transfer on the vane suction side was uniformly lower for the new design, with a drop of 25% compared to the datum case. This was in agreement with the predictions of numerical studies in Chapter 6, a protective effect of the boundary layer on the vane suction side.

The heat transfer on the endwalls was also affected by the alteration in secondary flow formation, with a significant difference noted near the leading edge of the shielded vane on the suction

side. The peak heat transfer in this region was reduced and the endwall can also be cooled from the upstream cooling slots as seen in Chapter 6, as the horseshoe vortex will not sweep away the coolant upstream of the vane leading edge. The endwalls between vanes 1 and 2 and vanes 2 and 3 were both better protected in the new design.

Chapter 8
Shielded Vane Performance under Engine-Representative Inlet Conditions

The experimental studies presented in the previous chapters were carried out under low inlet turbulence conditions. The performance of the vane and the endwalls under engine representative inlet conditions is analysed in this chapter.

8.1 Inlet Turbulence and Swirl Profile

The aerodynamic and thermal field under high inlet turbulence conditions was investigated using the inlet turbulence grid cassette shown in Figure 3.17(a). The estimated streamwise turbulence intensity, calculated using the empirical correlations by Roach (1987), was 13.2% and the integral length scale was 31mm at the vane leading edge. The average total pressure loss coefficient downstream of the grid was 1.1 of the outlet dynamic head and the maximum yaw and pitch angles upstream of the cascade were $\pm 3^{\circ}$.

The performance of the vane under inlet swirl was investigated with the use of the second swirl generator discussed in Chapter 3, with a single pilot swirler for each transition duct. The inlet total pressure loss distribution downstream of the swirl generator is shown in Figure 8.1. The total pressure loss was high in the core of the swirling flow, due to the design of the swirl generator, with values up to 1.4 of the inlet dynamic head. The average total pressure loss upstream of the cascade was 0.8 of the outlet dynamic head. The yaw and pitch angle profile (viewed from downstream) is shown in Figure 8.2, with maximum angles of $\pm 30^{\circ}$. The orientation of the swirl is clockwise viewed from downstream.

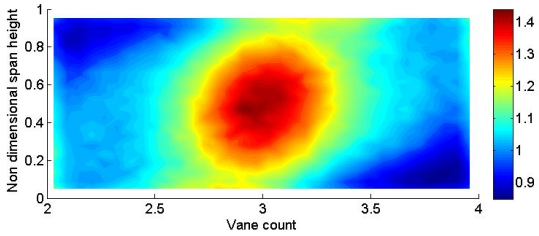

Figure 8.1: Total pressure loss distribution upstream of the cascade with inlet swirl

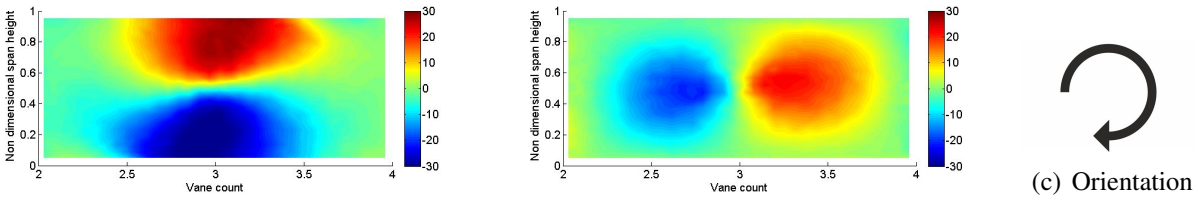

(a) Yaw angle (b) Pitch angle (c) Orientation

Figure 8.2: Swirl profile upstream of the cascade (viewed from downstream)

Downstream of the swirl generator the turbulence intensity was higher than in the low inlet turbulence case. The reference to the inlet swirl case in this chapter refers to this inlet condition of swirl with turbulence. It is noted that more than one parameter is changing between the three different inlet conditions, and changes in the inlet boundary layer between the three cases would also have an effect on the development of secondary flow. The effect of the engine representative inlet conditions on the state of the inlet boundary layer and the total pressure profile is not analysed in this work. The main aim of this chapter is to analyse the performance of the shielded vane under engine-representative inlet conditions, which include high inlet turbulence and inlet swirl as opposed to the inlet condition of low inlet turbulence studied in Chapter 7.

8.2 Aerodynamic Field

Flow periodicity for the high inlet turbulence case was achieved with the same setup of the tail-boards as for the low inlet turbulence case and was verified with a five-hole probe traverse. The total pressure loss coefficient downstream of the cascade is shown in Figure 8.3 for the original and shielded cases for high inlet turbulence. The trends observed were the same as for low inlet

turbulence. The maximum total pressure loss coefficient of the original central vane at mid-span was again higher than the adjacent ones, while the opposite was true for the shielded vane. A comparison between the original and shielded vane for high inlet turbulence showed a drop in the maximum total pressure loss coefficient at mid-span of 35% (compared to 30% for low inlet turbulence).

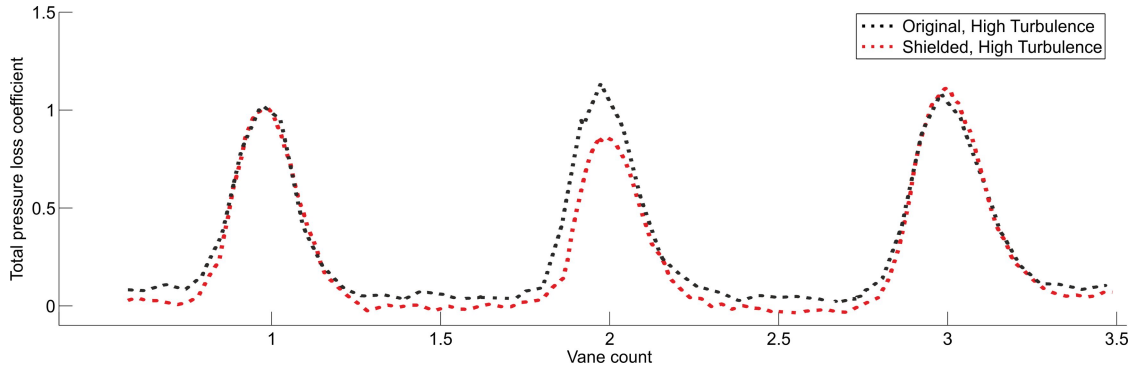

Figure 8.3: Total pressure loss coefficient downstream of the original and shielded cascade at mid-span with high inlet turbulence

Spatially resolved data for the total pressure loss coefficient downstream of the original and shielded vanes (Figure 8.4) agreed with the reduced loss for the shielded vane. In the two figures, where vanes 2 and 3 are shown for both cases, the wake downstream of vane 3 (on the right hand side) was the same for the two cases, in both shape and magnitude. The wake of the original central vane (on the left hand side) was thicker compared to that of the adjacent vane and the pressure loss was higher. The mass-weighted loss for the passage of the central vane was 3% of the outlet dynamic head higher than the adjacent vane. For the shielded case the wake of the shielded vane was thinner and the pressure loss was lower compared to both the original central vane and the adjacent vane that did not have the additional loss due to the upstream combustor wall. The mass-weighted loss for the passage of the shielded vane was 1.7% of the outlet dynamic head lower than the adjacent one.

A comparison of the mass-weighted data for the original and shielded vane, Figure 8.5, showed a similar total pressure loss coefficient profile with an average value that was 20% lower for the shielded vane (loss reduction 6.9% of the outlet dynamic head). The mass-weighted loss

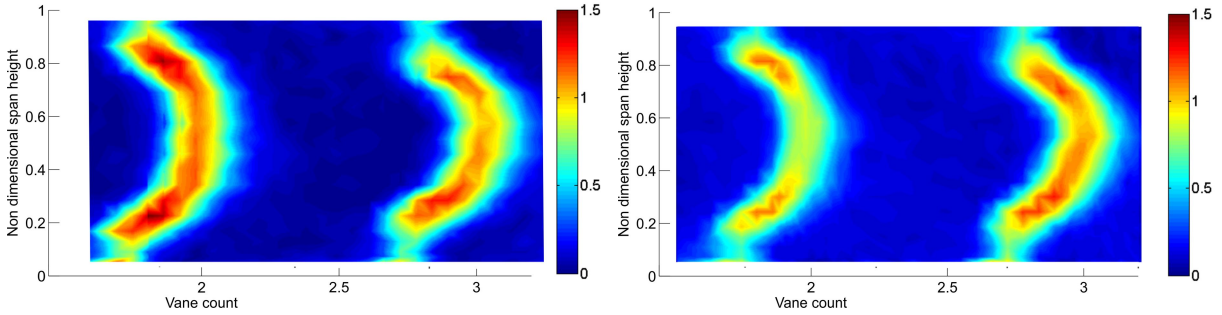

(a) Original cascade (b) Shielded cascade

Figure 8.4: Spatially resolved total pressure loss coefficient for original and shielded cascade with high inlet turbulence

coefficient downstream of the two passages of the central and adjacent vane was reduced by 14% (4.5% of the outlet dynamic head) for the shielded case compared to the original.

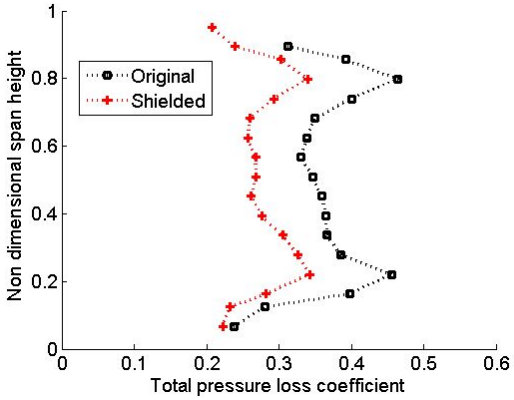

Figure 8.5: Comparison of mass-weighted average total pressure loss coefficient between original and shielded vane with high inlet turbulence

For the investigation of the effect of inlet swirl on the aerodynamic field, flow periodicity was achieved with the same tailboard setup. The total pressure loss coefficient downstream of the cascade is shown in Figure 8.6 for the original and shielded cases for inlet swirl. In this case, the loss downstream of the vanes that were in the core of the swirl (vanes 1 and 3) was diffused, due to both the variation of the inlet total pressure in the radial and circumferential directions, and the rotation of the flow. The central vane was not as affected by the inlet flow conditions as it was downstream of the combustor wall, and therefore its total pressure loss was concentrated in a smaller area. The maximum total pressure loss coefficient for the central vane at mid-span was significantly higher than the adjacent vanes.

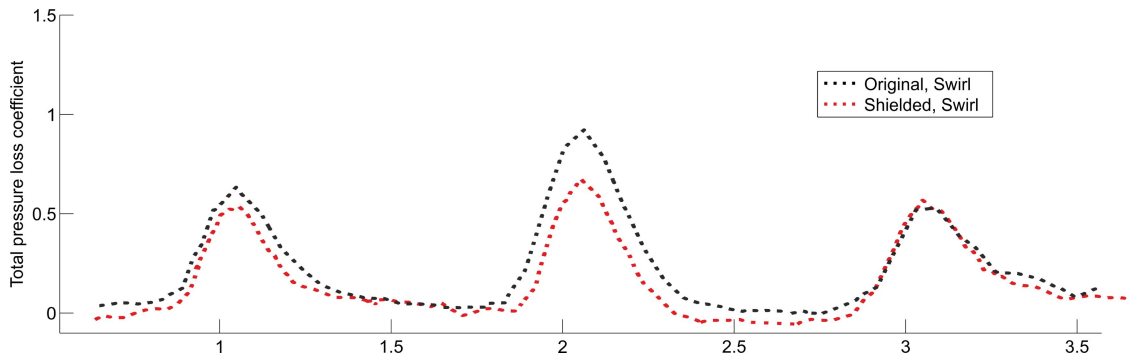

Figure 8.6: Total pressure loss coefficient downstream of the original and the shielded cascade at mid-span with inlet swirl

The same trend was observed for the shielded case, with inlet swirl resulting in higher loss for the central shielded vane compared to the adjacent ones. In this case, the difference in the maximum total pressure loss was not as high, due to the better aerodynamic performance of the shielded vane. The total pressure loss coefficient in the passage between vanes 1 and 2 was also higher compared to the passage between vanes 2 and 3, showing increased diffusion of the total pressure loss downstream of the vanes that were not downstream of the combustor wall compared to the cases without inlet swirl.

A comparison of the spatially resolved data downstream of the original and the shielded vane, shown in Figure 8.7, highlighted the significant difference in the total pressure loss downstream of the vanes. It should be noted that the scale in this figure is different from that in Figure 8.4, in order to better capture the differences between the vanes. Inlet swirl resulted in a reduction in the total pressure loss coefficient in the mid-span region for vanes 1 and 3 that were facing the largest variation in incidence angles across the span. Their wakes were also rotated, due to the clockwise rotation of the inlet flow. A comparison of the mass-weighted loss for the original case showed that the loss in the passage of the central vane was 0.5% of the outlet dynamic head higher than the adjacent one. On the other hand, the passage of the shielded vane had a mass-weighted loss 4.4% of the outlet dynamic head lower than the adjacent passage.

The total pressure loss profile of the central vane was different in shape from both the adjacent vanes, and the central vane without inlet swirl. The total pressure loss was higher in the half of the

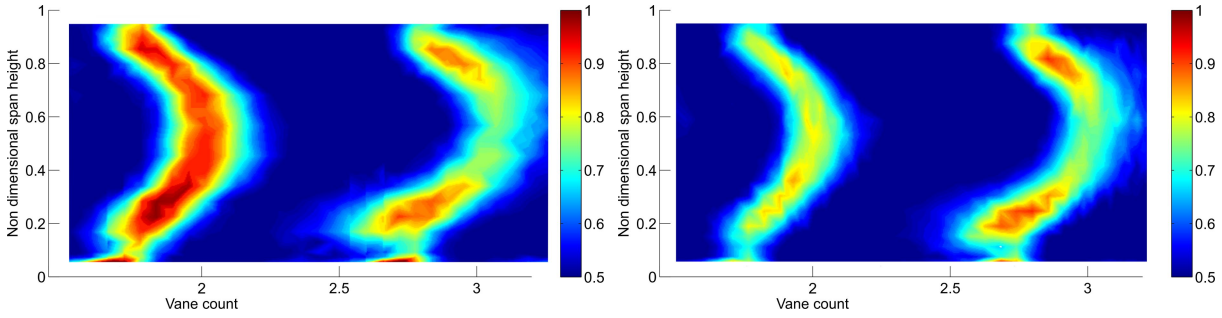

(a) Original vane cascade (b) Shielded vane cascade

Figure 8.7: Spatially resolved total pressure loss coefficient for original and shielded vane with inlet swirl

vane near the hub and lower towards the casing, due to the profile of the swirl. This was observed on both the original and the shielded vane. The static pressure on the early pressure side at the top half of the vane was lower than the bottom half under inlet swirl, resulting in higher acceleration and therefore lower total pressure loss for the top half of the vane. The peaks of the total pressure loss coefficient at 20% and 80% of the vane span were also not observed, a sign that inlet swirl reduced the strength of secondary flow in the central vane. Mass-weighted pitchwise average data for the passages of the original and the shielded vane presented in Figure 8.8 captured this trend. Loss for the shielded vane was significantly lower than both the adjacent vane and the original central vane, and had the same profile as the original vane. The mass-weighted loss coefficient was 24% lower for the shielded vane compared to the original central vane (5.5% of the outlet dynamic head). A comparison of the data for the two passages showed a reduction in the mass-weighted loss coefficient of 14% for the shielded case, which translates to a loss reduction of 3.1% of the outlet dynamic head.

The effect of different inlet conditions on the aerodynamic field for the original vane cascade is summarized in Figure 8.9, which shows the total pressure loss coefficient for the three different cases at mid-span. Inlet turbulence resulted in an increase in the total pressure loss coefficient for the original cascade, with the wakes of all vanes being similar in size. Inlet swirl reduced the maximum total pressure loss coefficient for all vanes at mid-span, with a greater reduction for vanes 1 and 3. The width of the wake of the central vane was affected the least, whereas the wakes

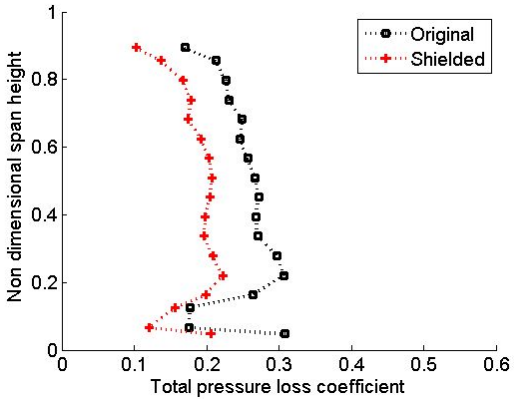

Figure 8.8: Comparison of mass-weighted average total pressure loss coefficient between original and shielded vane with inlet swirl

of vanes 1 and 3 were seen to diffuse more, due to them being aligned with the core of the swirl, as discussed before.

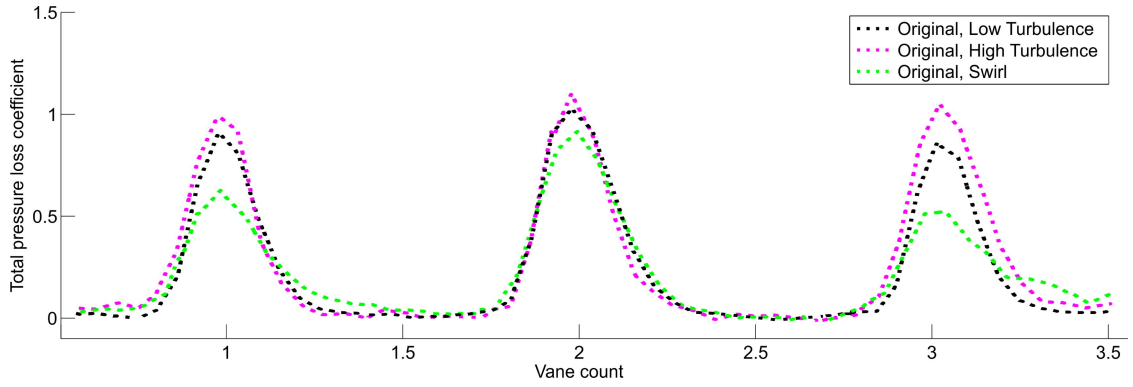

Figure 8.9: Total pressure loss coefficient downstream of the original cascade with different inlet conditions

The same trends were observed in the shielded case, Figure 8.10. The increase of inlet turbulence resulted in an increase of the total pressure loss coefficient for all vanes. A narrower wake with a lower total pressure loss coefficient was observed downstream of the shielded vane. Under inlet swirl the total pressure loss for vanes 1 and 3 is diffused as in the original case. The maximum total pressure loss coefficient for the central vane is similar to that with low inlet turbulence. The reduced loss of the central vane in the case with inlet swirl was largely due to the reduced strength of secondary flow, an effect predicted by the numerical studies and discussed in Chapter 6, which was not as pronounced for the shielded case where secondary flow was already reduced.

The mass-weighted average loss distribution along the span highlighted the improved aerodynamic performance of the shielded vane. For ease of comparison, the low and high turbulence

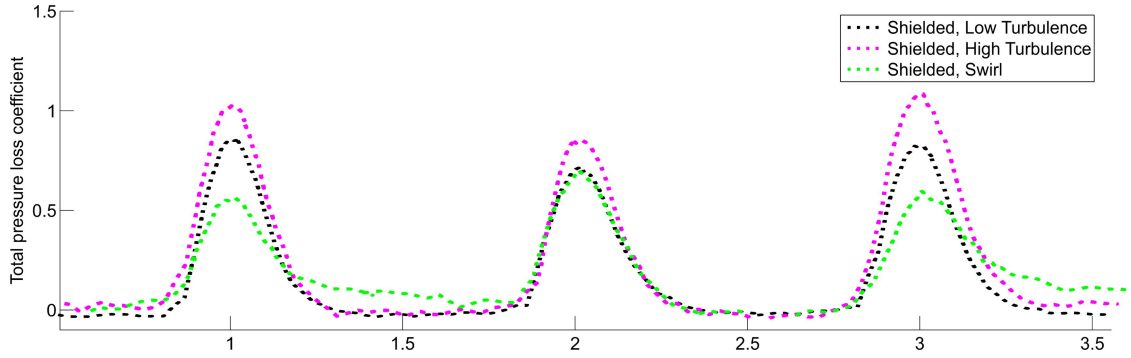

Figure 8.10: Total pressure loss coefficient downstream of the shielded cascade with different inlet conditions

cases are plotted in Figure 8.11(a) and the high turbulence and swirl cases in Figure 8.11(b). An increase in inlet turbulence resulted in an increase in loss downstream of the vane, while the wake profile and average loss distribution were maintained, Figure 8.11(a). The loss of the shielded vane was significantly smaller than the original for both low and high inlet turbulence. Furthermore, the loss cores at 20% and 80% span were weaker for the shielded vane. The difference in loss away from the endwall was significantly higher compared to the loss near the endwall, which was not expected to vary as much between the different cases. The increase in the mass-weighted average loss for the high inlet turbulence compared to the low inlet turbulence case was 15.4% of the outlet dynamic head for the original vane and 17.6% of the outlet dynamic head for the shielded vane.

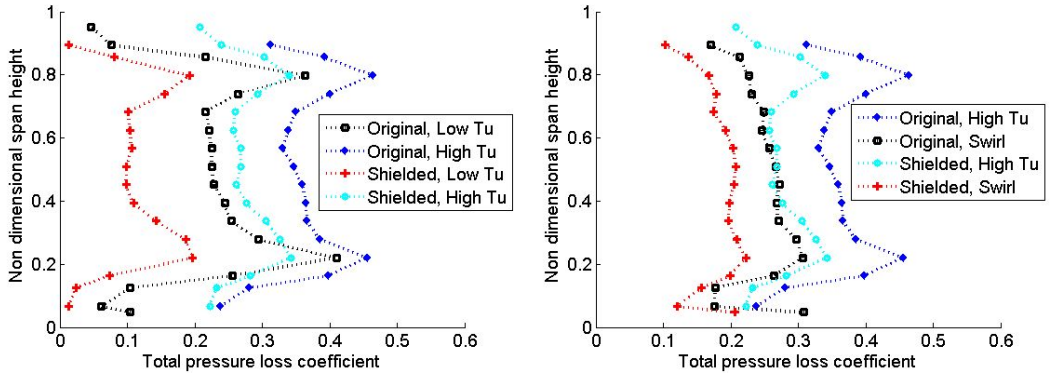

(a) Inlet turbulence intensity

(b) High turbulence and swirl

Figure 8.11: Mass-weighted pitchwise average total pressure loss coefficient downstream of the original and the shielded vane with different inlet conditions

Swirl reduced secondary flow and therefore the higher loss associated with the passage vortex at 20% and 80% span. The spanwise profiles for each inlet condition were similar for the original and shielded vane and the mass-weighted average loss for inlet swirl compared to high inlet turbulence was 11.2% of the outlet dynamic head lower for the original vane and 9.8% of the outlet dynamic head lower for the shielded vane. Inlet swirl showed a significant improvement in total pressure loss over the high inlet turbulence case for both cases. The mass-weighted average values of the total pressure loss coefficient for all cases are summarized in Table 8.1.

Table 8.1: Mass-weighted average total pressure loss coefficient for original and shielded case for different inlet conditions

	Low turbulence	High turbulence	Swirl
Original	0.186	0.34	0.228
Shielded	0.095	0.271	0.173

The total pressure loss coefficient near the endwalls, as obtained with the flat Pitot probe, is shown for all cases in Figure 8.12. In the original vane cascade, Figure 8.12(a), two loss cores appeared downstream of the vanes and a separated region of high loss was observed in the first passage, between 1 and 1.5 vane count. The loss in this passage was higher compared to the adjacent one, between vanes 2 and 3. With the increase of inlet turbulence, Figure 8.12(c), the loss cores increased in size and magnitude, and the aforementioned region of high loss joined the loss core of vane 2. Inlet swirl, Figure 8.12(e), resulted in smaller high loss regions between the vanes compared to both the low and the high turbulence cases, as well as smaller loss cores, due to the reduced strength of secondary flow.

For the shielded vane, the difference between the two passages was significantly smaller. The increase of inlet turbulence, Figure 8.12(d), resulted in a small increase in the size and magnitude of the loss cores, and caused the higher loss region in the passage to move closer to the loss core of the vane, as in the original vane cascade. Inlet swirl also had a similar effect in the shielded as in the original vane cascade, with a small reduction of the total pressure loss in all regions,

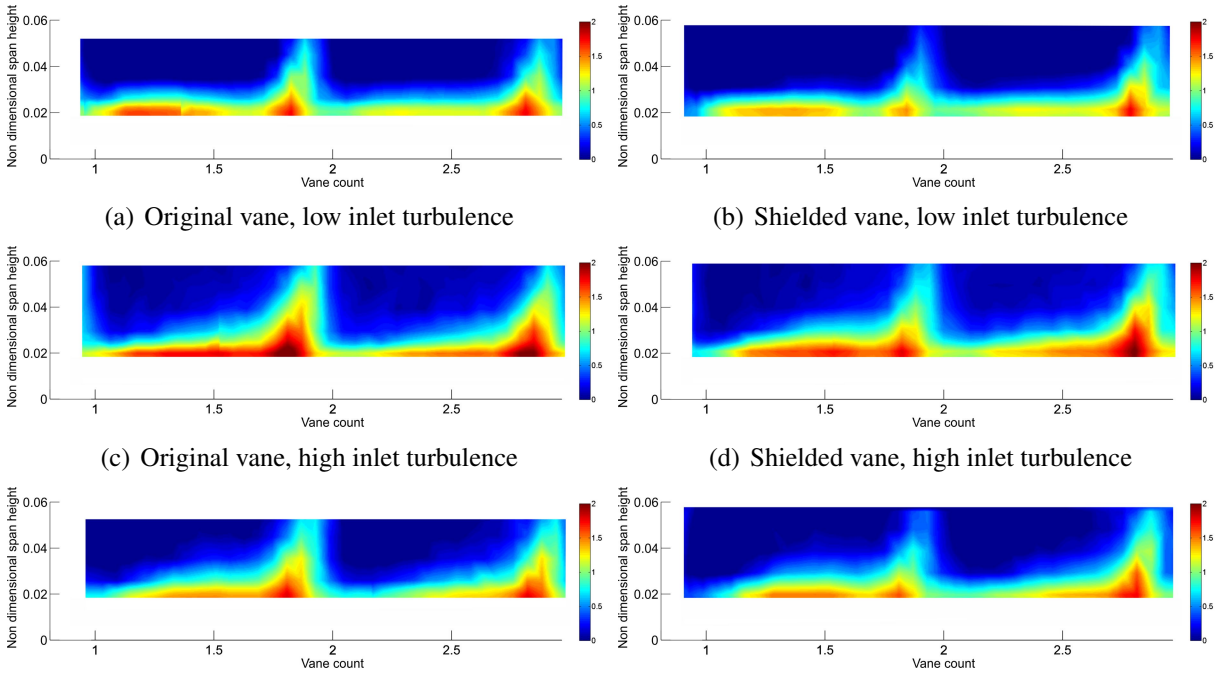

(a) Original vane, low inlet turbulence

(b) Shielded vane, low inlet turbulence

(c) Original vane, high inlet turbulence

(d) Shielded vane, high inlet turbulence

(e) Original vane, inlet swirl

(f) Shielded vane, inlet swirl

Figure 8.12: Spatially resolved total pressure loss coefficient on the endwall for original and shielded cascade with different inlet conditions

Figure 8.12(f). Overall, total pressure loss on the endwall was significantly lower for the shielded vane for all inlet conditions.

The inlet conditions to the cascade affected the pressure distribution around the vanes. A comparison of the isentropic Mach number distribution on the shielded vane surface for different inlet conditions is shown in Figure 8.13 for 50% span. The loading of the vane was affected in the front part of the vane, with variations of the isentropic Mach number on the pressure side of the shielded vane. The increase of inlet turbulence resulted in lower isentropic Mach numbers on the vane surface and higher static pressure until 60% of the axial chord of the vane. Inlet swirl had a similar effect, with even lower isentropic Mach numbers compared to the high inlet turbulence case, particularly until 40% of the axial chord.

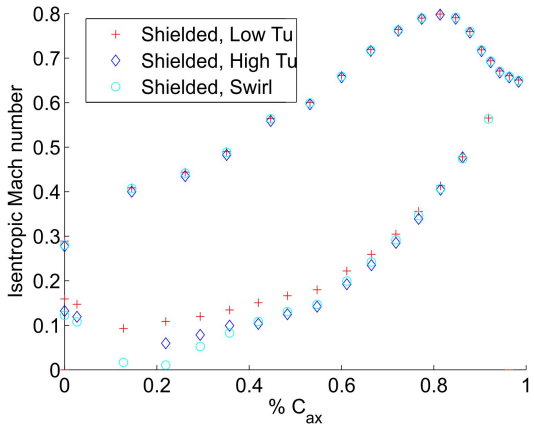

Figure 8.13: Isentropic Mach number on the shielded vane at mid-span with different inlet conditions

A comparison of the mass-weighted pitchwise average yaw angle distribution for the different inlet conditions, Figure 8.14, showed that the turning of the flow at the exit of the cascade was not significantly altered with the new design. For low inlet turbulence, as discussed in Chapter 7, the shielded vane showed less underturning near the endwall. The same effect was observed for high inlet turbulence, which was only found to affect the flow at mid-span and reduce overturning. Inlet swirl increased underturning at the hub for both the original and the shielded vane and also resulted in higher overturning at mid-span compared to the other cases.

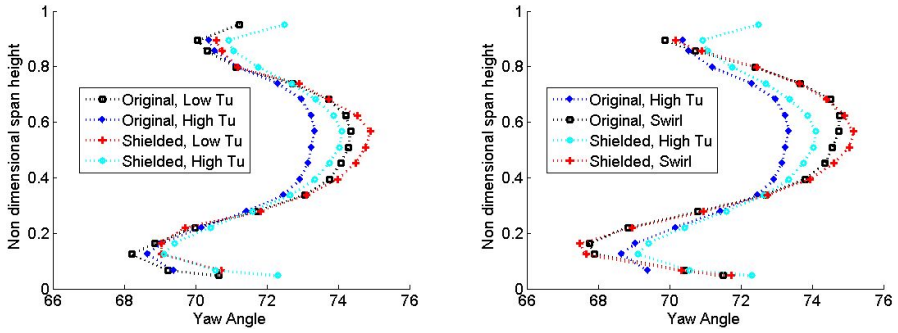

(a) Inlet turbulence intensity (b) Turbulence and swirl

Figure 8.14: Comparison of mass-weighted pitchwise average yaw angle for original and shielded vane with different inlet conditions

The reduction of the strength of secondary flow for inlet swirl was captured in the spatially resolved pitch angle distribution downstream of the cascade, Figure 8.15. The pairs of highly positive and highly negative pitch angle at the hub and casing downstream of the central vane

that were well defined for the original and shielded case for high inlet turbulence (Figures 8.15(a) and 8.15(b)), were reduced in both size and magnitude for inlet swirl. A comparison in the horizontal direction between the two vanes for the same inlet conditions showed a marginal reduction in the strength of the vortices for the shielded case for the inlet swirl, Figure 8.15(d), where the maximum and minimum pitch angles were also lower.

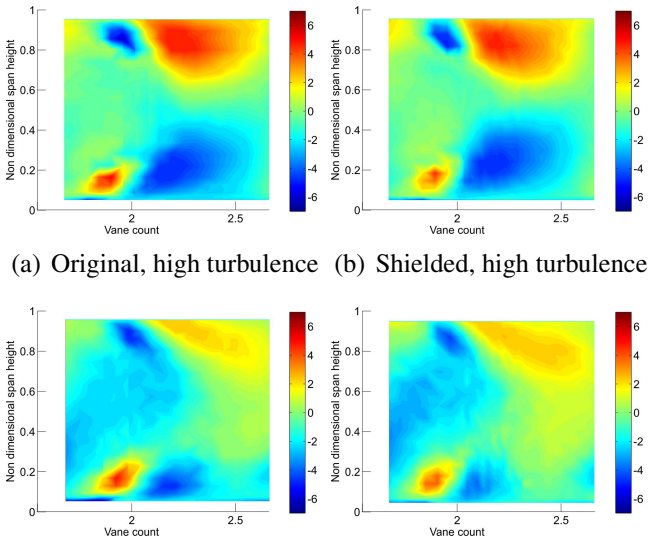

(a) Original, high turbulence (b) Shielded, high turbulence

(c) Original, swirl (d) Shielded, swirl

Figure 8.15: Spatially resolved pitch angle distribution for the three vanes with different inlet conditions

8.3 Thermal Field

The effect of engine-representative inlet conditions on the thermal performance of the original and the shielded vane is analysed in this section with the use of data obtained through IR thermography on the vanes and endwalls, presented in the dimensionless form of Nusselt number.

Figure 8.16 shows the heat transfer distribution on the vane pressure side for the two vanes and the three different inlet conditions of low and high inlet turbulence and inlet swirl. The increase of inlet turbulence intensity resulted in an overall increase in Nusselt number on the vane surface for the original central vane. This effect was more pronounced on the early pressure side of the vane; the drop in Nusselt number that was observed after the first 5% of the axial chord on the original

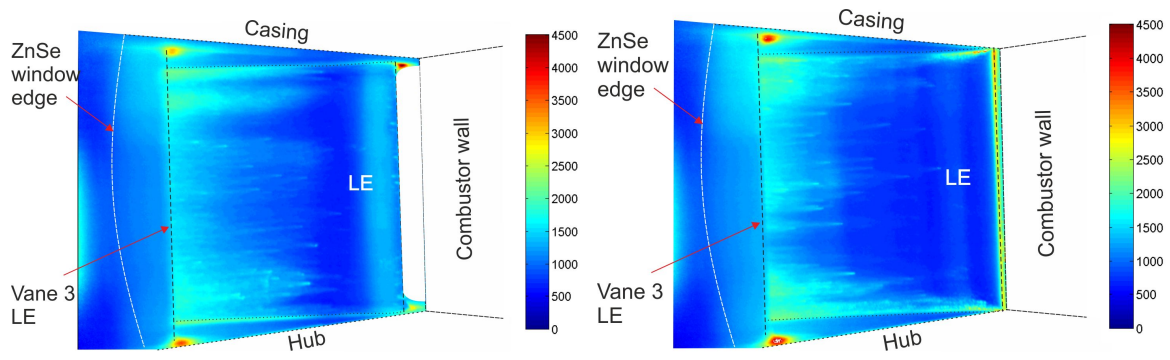

(a) Original vane, low inlet turbulence

(b) Shielded vane, low inlet turbulence

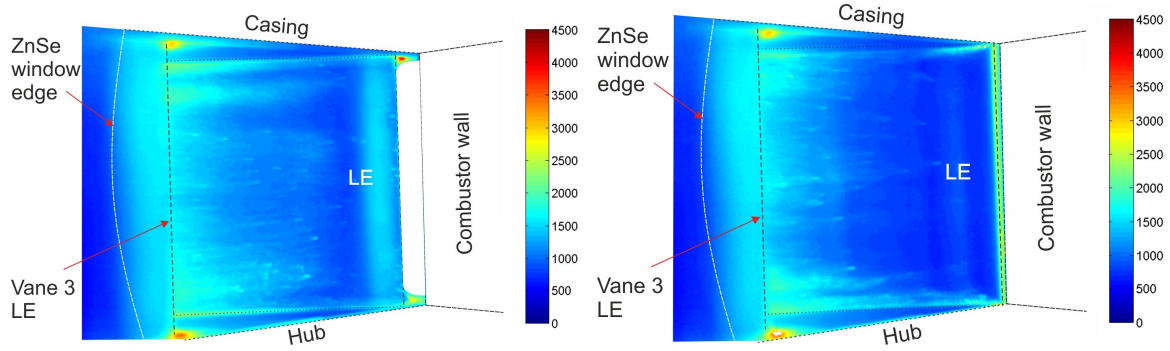

(c) Original vane, high inlet turbulence

(d) Shielded vane, high inlet turbulence

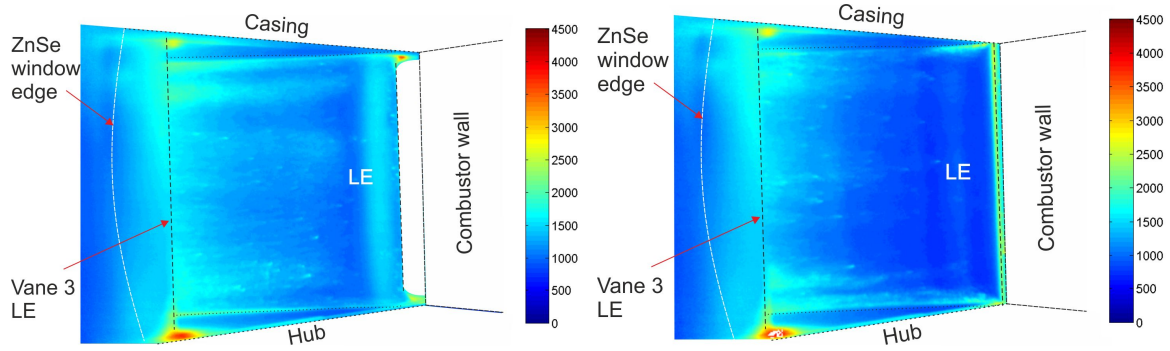

(e) Original vane, inlet swirl

(f) Shielded vane, inlet swirl

Figure 8.16: Nusselt number on the vane pressure side for the original and shielded vane with different inlet conditions (view 1, Figure 3.25(a))

vane became smaller for higher inlet turbulence. This agreed with the drop of the isentropic Mach number on the vane surface, which resulted in increased heat transfer in the region. Heat transfer levels were similar further downstream on the vane surface. The vane leading edge also showed higher Nusselt numbers for higher inlet turbulence.

Inlet swirl also had an effect on the Nusselt number; the maximum levels near the vane leading edge were the same as for the high inlet turbulence case. The decrease in Nusselt number further downstream on the vane surface was noticeably smaller, with values up to 25% higher than the

high inlet turbulence case and 70% higher than the low turbulence case. On the shielded vane surface the increase of inlet turbulence resulted in an increase in Nusselt number away from the endwalls by up to 20%. Inlet swirl increased Nusselt number further, by up to 30% compared to the low turbulence intensity case.

A comparison of the original and the shielded vane for all inlet conditions showed the better performance of the latter for all cases, with Nusselt numbers being significantly lower on the entire vane surface.

Figure 8.17 shows the heat transfer distribution on the vane leading edge for the different cases. Inlet turbulence resulted in an overall increase in Nusselt number on the vane leading edge and on the late pressure side of vane 1 for the original vane. For the shielded case, a similar effect to the original case was observed on vane 1, as expected, whereas the Nusselt number on the leading edge of the shielded vane was not affected. In contrast to the original case, where a new boundary layer formed on the central vane making the vane more susceptible to the characteristics of the flow, the boundary layer on the shielded vane was a continuation of the boundary layer formed on the sides of the combustor transition ducts and therefore not affected by the flow characteristics. Inlet swirl resulted in a more uniform Nusselt number distribution on the central vane, with an increase in the leading edge and a reduction of the magnitude of the peak observed in the datum case. The shielded vane was again not particularly affected by inlet swirl. On the late pressure side of vane 1, inlet swirl resulted in higher Nusselt number in the bottom half of the vane, near the hub, and lower Nusselt number in the top half, a result of the orientation of the swirl. This effect was observed in both the original and the shielded vane, as expected.

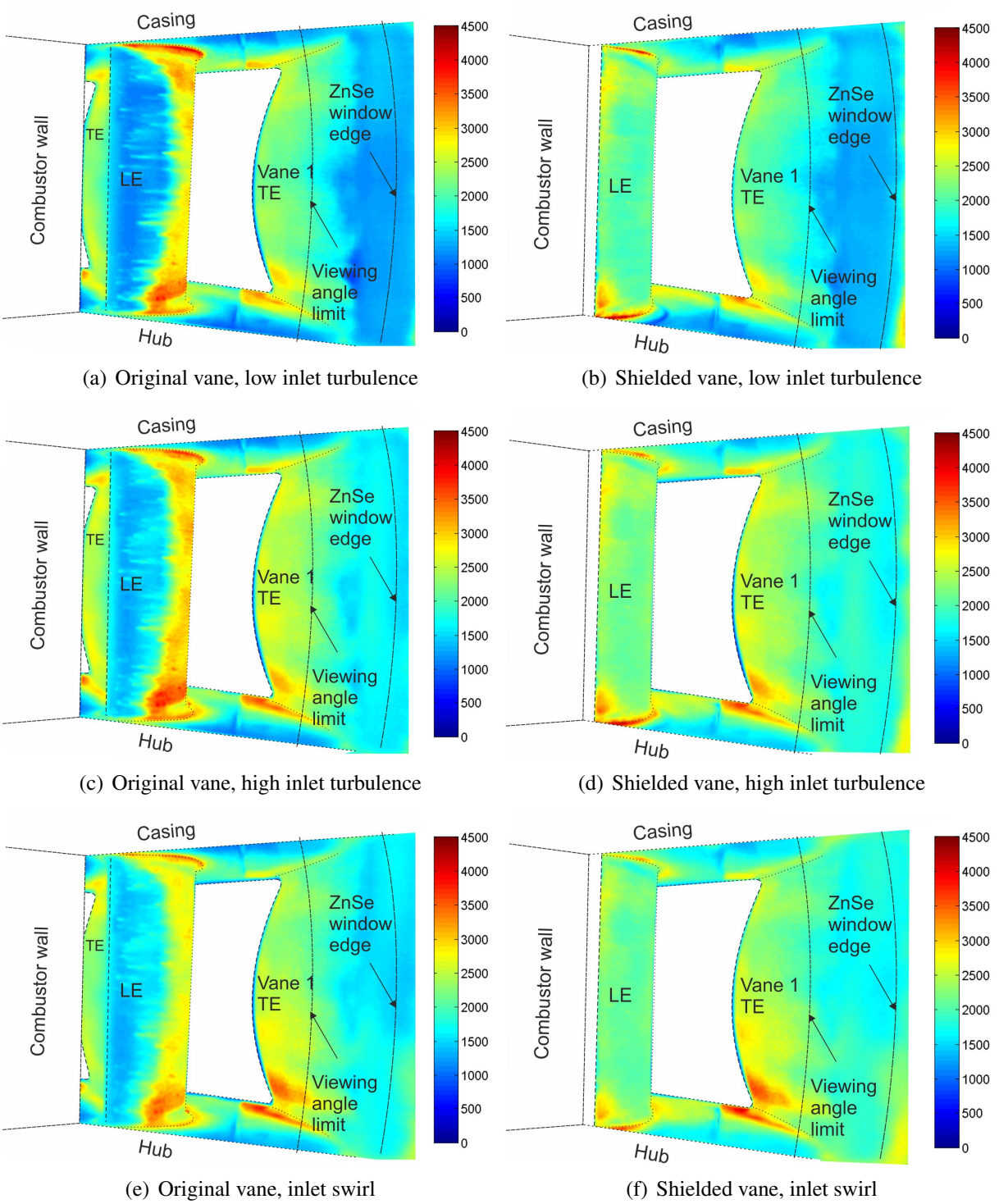

(a) Original vane, low inlet turbulence

(b) Shielded vane, low inlet turbulence

(c) Original vane, high inlet turbulence

(d) Shielded vane, high inlet turbulence

(e) Original vane, inlet swirl

(f) Shielded vane, inlet swirl

Figure 8.17: Nusselt number on the vane leading edge for the original and shielded vane with different inlet conditions (view 2, Figure 3.25(b))

Figure 8.18 compares the heat transfer distribution on the vane suction side for the six cases. The increase of inlet turbulence intensity augmented the Nusselt number on the entire vane surface, in accordance with findings in the literature discussed in section 2.3.1. The maximum values

near the vane mid-chord increased by approximately 15%; the increase in the downstream regions of the vane was $10-15\%$. The trails of the passage vortex on the vane surface were more confined to the endwall region compared to the low inlet turbulence case. The Nusselt number in the region of the passage vortex trails was increased by $20-30\%$ for the higher inlet turbulence case.

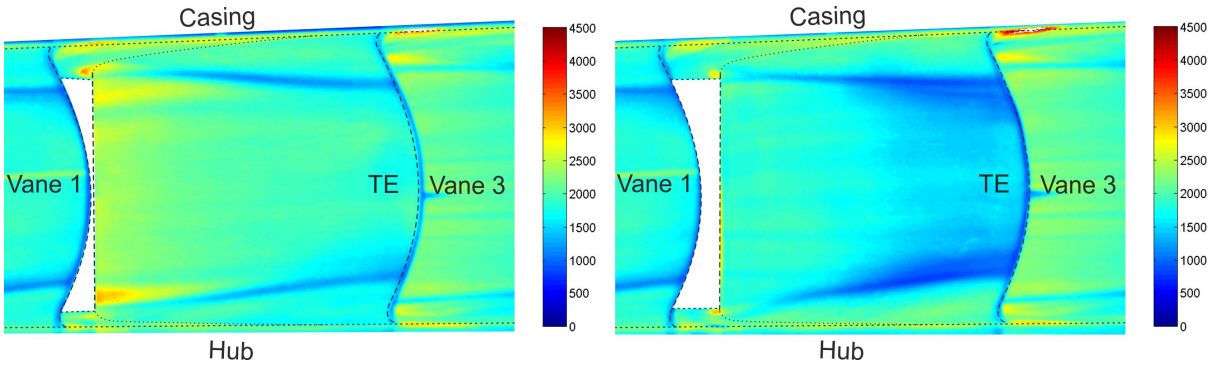

(a) Original vane, low inlet turbulence

(b) Shielded vane, low inlet turbulence

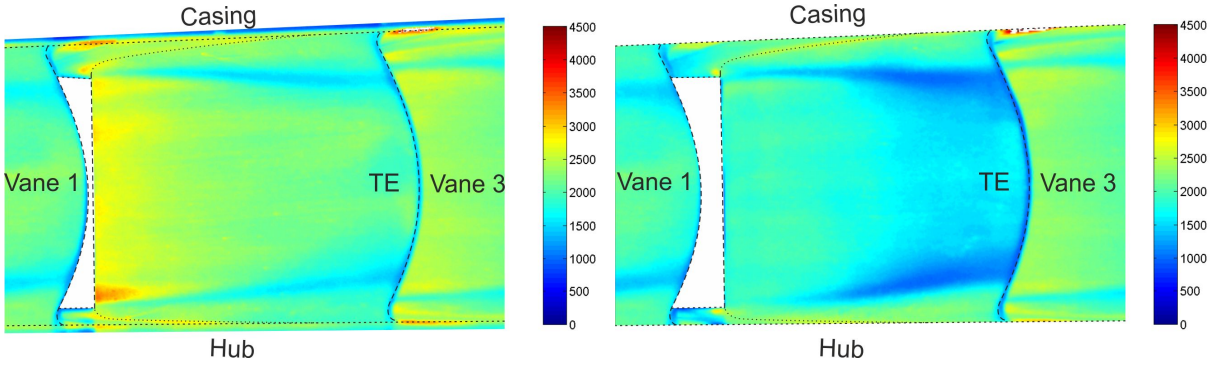

(c) Original vane, high inlet turbulence

(d) Shielded vane, high inlet turbulence

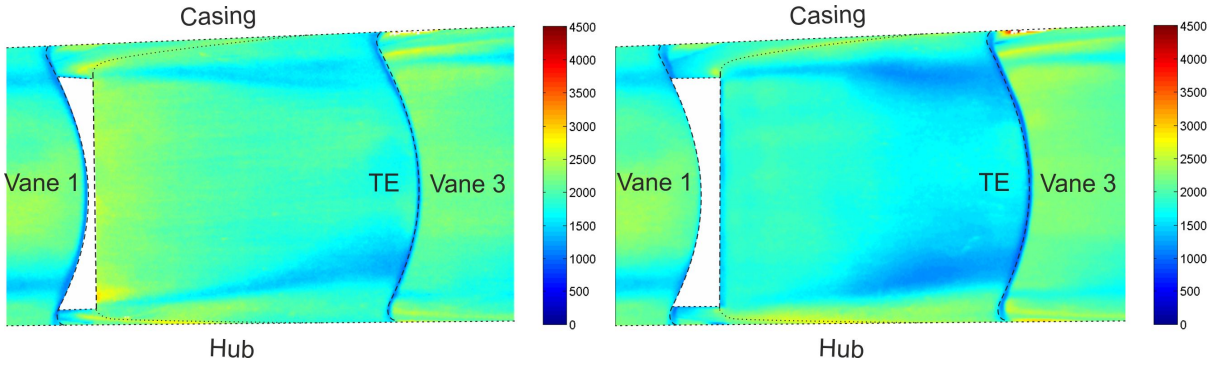

(e) Original vane, inlet swirl

(f) Shielded vane, inlet swirl

Figure 8.18: Nusselt number on the vane suction side for the original and shielded vane with different inlet conditions (view 3, Figure 3.25(c))

Inlet swirl had a different effect on the heat transfer to the vane. The maximum Nusselt number near the vane leading edge was similar to the datum case with low inlet turbulence and the levels

on the vane surface were marginally reduced from $20 - 80\%$ span. The main difference compared to the low inlet turbulence case was around the trails of the passage vortex. These were now more asymmetric due to the rotation of the inlet flow, they were not as well defined, and had a higher Nusselt number compared to the datum case. The trail near the casing was closer to the endwall, whereas the trail near the hub was not particularly affected. The heat transfer in the region of the passage vortex trails for this case was between that observed in the low and in the high inlet turbulence cases.

Similar trends were observed on the shielded vane surface. The increase in inlet turbulence resulted in an overall increase in Nusselt number on the vane, which was smaller compared to the datum case. The trajectory of the passage vortex on the vane surface was again altered, with the vortices more confined to the endwall region, as seen in the numerical studies in Chapter 6, and with a small increase in Nusselt number. The heat transfer levels near the endwalls in the region including the trails of the passage vortex were higher. Inlet swirl resulted in further movement of the trails of the passage vortex, with the trail near the hub moving away from the endwall and the trail near the casing being more confined to the endwall compared to both the low and the high inlet turbulence case. Heat transfer to the vane surface was increased from $40 - 80\%$ span, particularly in the downstream region of the vane suction side.

The heat transfer on the vane endwall was compared for the two geometries and the three different inlet conditions in Figure 8.19, which showed the Nusselt number on the endwall in the vane leading edge region, as viewed from upstream of the cascade. The effect of inlet turbulence and swirl on the vane leading edge was in agreement with the trends observed in Figure 8.17. The increase of inlet turbulence, Figure 8.19(c), resulted in an increase in Nusselt number on the vane endwall compared to the datum case, particularly in the region close to the vane leading edge fillet, where the Nusselt number was increased by up to 700 (40%).

The introduction of inlet swirl reduced the peak Nusselt number on both the vane leading edge and the endwall relative to the high inlet turbulence case and marginally increased heat transfer

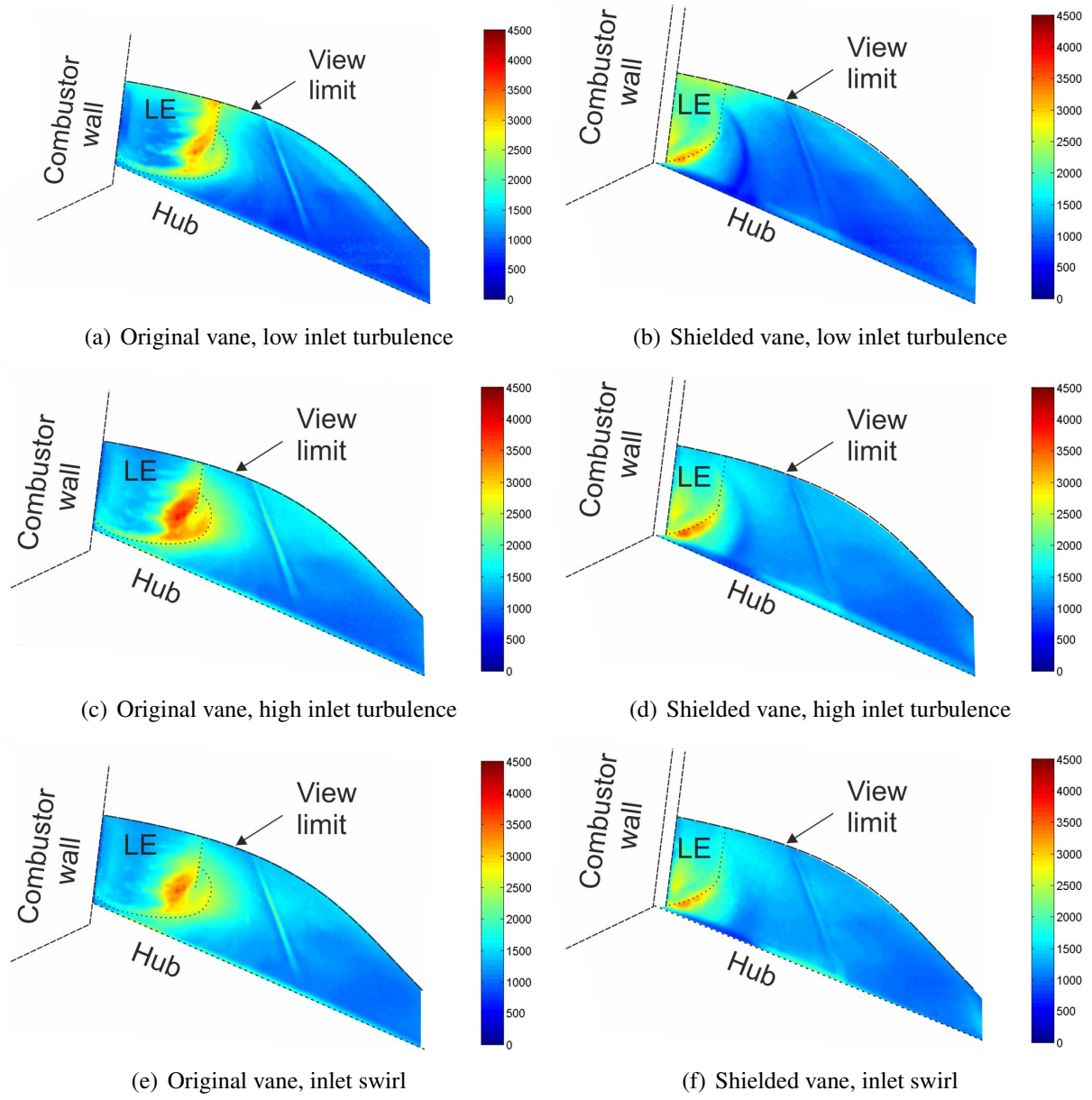

(a) Original vane, low inlet turbulence

(b) Shielded vane, low inlet turbulence

(c) Original vane, high inlet turbulence

(d) Shielded vane, high inlet turbulence

(e) Original vane, inlet swirl

(f) Shielded vane, inlet swirl

Figure 8.19: Nusselt number on the vane endwall viewed from upstream for the original and shielded vane with different inlet conditions (view 4, Figure 3.25(d))

to the endwall away from the high Nusselt region. The increase in Nusselt number for inlet swirl relative to the datum case with low inlet turbulence was 600 (35%).

The same trends were observed in the shielded case, with an increase in heat transfer to the endwall for both the high inlet turbulence and the inlet swirl case. The increase in Nusselt number was highest near the leading edge fillet, and was 300 (20%) for both the high inlet turbulence and the inlet swirl case relative to the low inlet turbulence case. The local increase in the low Nusselt

number trail observed mainly in the low and high inlet turbulence cases for the shielded vane was up to 50% for the high inlet turbulence and up to 90% for the inlet swirl, both relative to the low inlet turbulence case.

Figure 8.20 shows the heat transfer on the hub endwall as viewed from downstream of the cascade for the two vane geometries and the different inlet conditions. The increase in Nusselt number with the increase in inlet turbulence intensity on the vane suction side was in agreement with what was seen in Figure 8.18. The effect on the vane endwall was an increase in Nusselt number of up to 700 from the low inlet turbulence case near the leading edge of the central vane

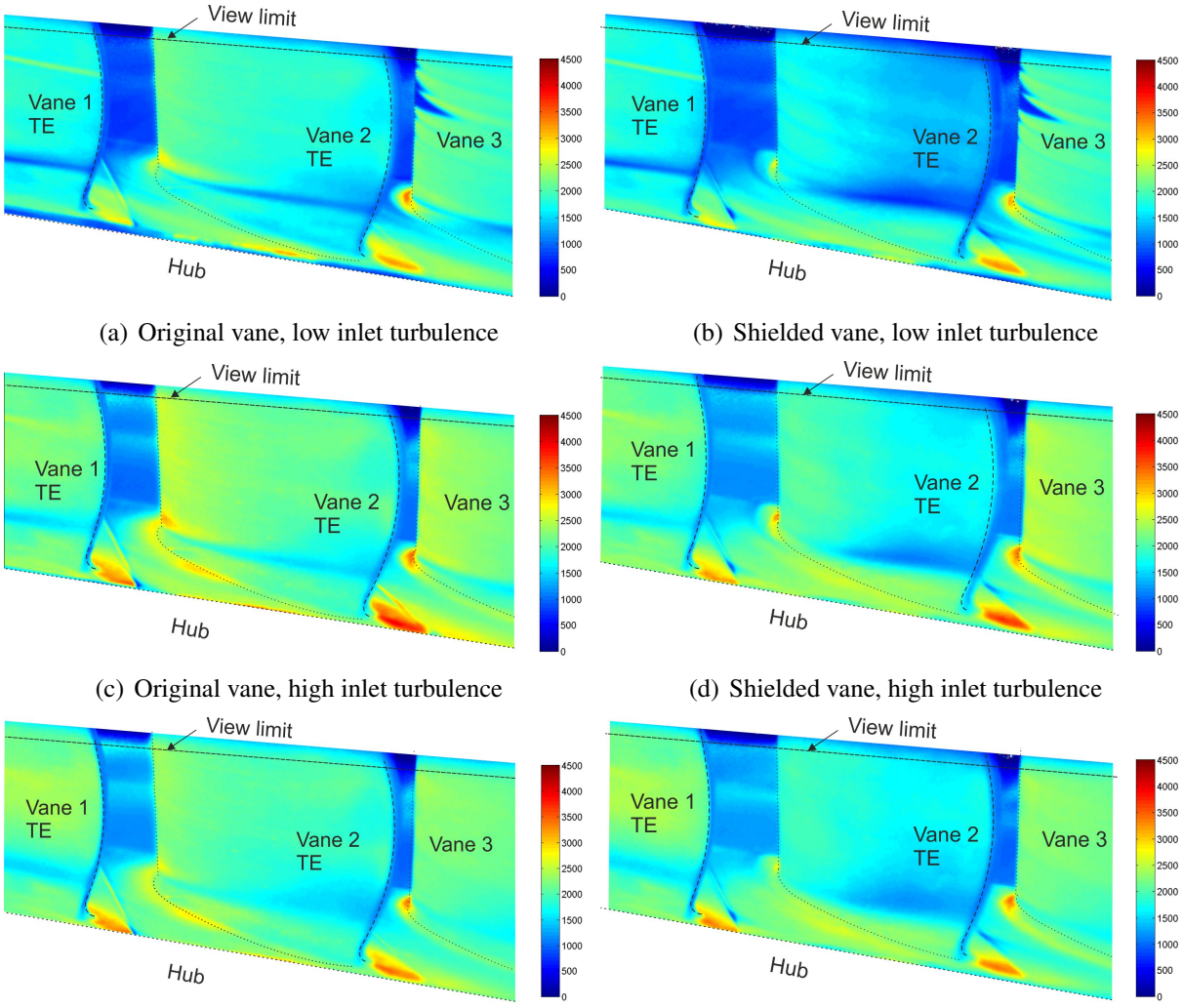

(a) Original vane, low inlet turbulence

(b) Shielded vane, low inlet turbulence

(c) Original vane, high inlet turbulence

(d) Shielded vane, high inlet turbulence

(e) Original vane, inlet swirl

(f) Shielded vane, inlet swirl

Figure 8.20: Nusselt number on the vane endwall viewed from downstream for the original and shielded vane with different inlet conditions (view 5, Figure 3.25(e))

as well as near the trailing edge of vane 1. There was also a region in the endwall close to the suction side of the central vane in the downstream region where the Nusselt number was the same for both cases. Inlet swirl had a similar effect, with a smaller increase in Nusselt number, of 600, near the leading edge of the central vane and the trailing edge of vane 1, in agreement with the differences observed from upstream of the cascade, Figure 8.19. Similar trends were observed in the shielded case, with an increase in Nusselt number for both the high inlet turbulence intensity and the inlet swirl in comparison to the low turbulence intensity case.

8.4 Comparison of Heat Transfer between the Two Vane Designs

The differences in heat transfer between the original and the new vane geometry for the different inlet conditions are presented in this section. The data obtained from the heat transfer measurements and presented in section 8.3 is plotted in terms of difference between the two cascades for the same inlet conditions.

Figure 8.21 shows the difference between the two vanes for low and high inlet turbulence, as well as inlet swirl on the vane suction side. The lower Nusselt number for the shielded vane observed in the low inlet turbulence case was also observed for the other inlet conditions. The increase of inlet turbulence intensity resulted in a similar pattern for the difference in Nusselt number with a significant reduction on the majority of the vane surface. The increase in the Nusselt number near the endwalls was smaller for the higher inlet turbulence case, again due to the more confined secondary flow. For inlet swirl the shielded vane again had lower Nusselt number on the majority of the vane surface, with a smaller drop compared to the other cases, of 400. The increased Nusselt number region was even more confined to the hub endwall in this case and the region on the casing endwall was also smaller than in the low inlet turbulence case. The improved thermal performance of the shielded vane was maintained under both high

inlet turbulence and inlet swirl. A direct comparison of the original and the shielded vane for the

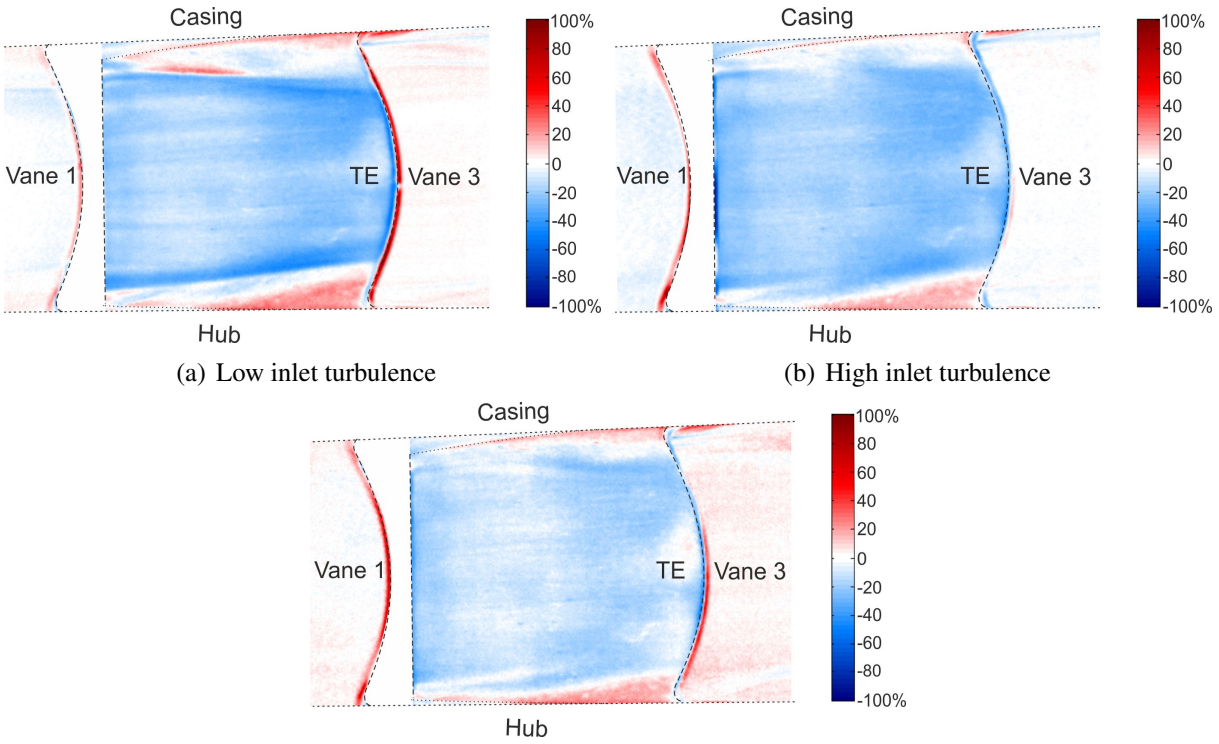

(a) Low inlet turbulence

(b) High inlet turbulence

(c) Inlet swirl

Figure 8.21: Comparison of the Nusselt number on the vane suction side between the original and shielded vane with different inlet conditions (view 3, Figure 3.25(c))

different inlet conditions showed a reduction in heat transfer levels by up to 25% for high inlet turbulence and $10 - 15\%$ for inlet swirl.

Data for the vane leading edge and the hub endwall from the upstream view has been omitted, due to the very different profile and curvature in that region that does not allow direct comparisons in this way. The heat transfer on the hub endwall viewed from downstream of the cascade is compared in Figure 8.22 for all inlet conditions. For the low inlet turbulence case the Nusselt number on the vane endwall was lower for the shielded case. The increase of inlet turbulence did not affect this trend, with lower Nusselt number in the shielded case for the majority of the endwall. An exception to this was the patch near the vane leading edge at mid-pitch and the patch near the vane trailing edge at mid-pitch, which were thought to be caused by a small misalignment between the two components.

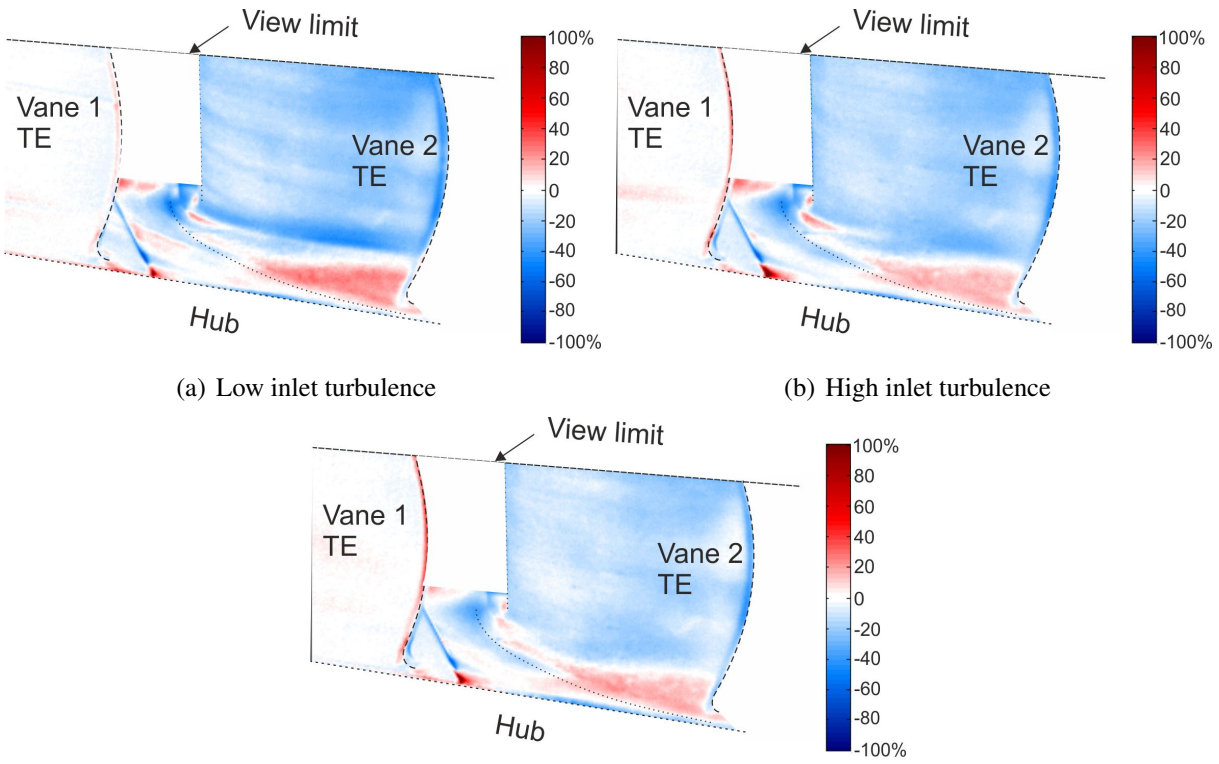

(a) Low inlet turbulence

(b) High inlet turbulence

(c) Inlet swirl

Figure 8.22: Comparison of the Nusselt number on the vane endwall viewed from downstream between the original and shielded vane with different inlet conditions (view 5, Figure 3.25(e))

8.5 Conclusions

The performance of the new shielded vane design was analysed under engine-representative inlet conditions. Flow periodicity and total pressure loss downstream of the cascade were assessed with a traverse with the five hole probe and the heat transfer on the vanes and endwalls was measured using IR thermography.

The better performance of the new design was demonstrated under both high inlet turbulence and inlet swirl with turbulence. The wake of the new vane was narrower than the original for all inlet conditions, and the total pressure loss was lower. The higher aerodynamic efficiency of the new design was maintained under high inlet turbulence conditions, with the new vane demonstrating a reduction in the mass-weighted average total pressure loss of 6.9% of the outlet dynamic head compared to the original vane. The improvement in aerodynamic performance of

the new vane over the original under inlet swirl was 5.5% of the outlet dynamic head in terms of the mass-weighted average total pressure loss.

The increase of inlet turbulence resulted in a higher total pressure loss coefficient compared to the low inlet turbulence case. The average total pressure loss for the high inlet turbulence intensity was increased by 15.4% and 17.6% of the outlet dynamic head for the original and shielded vane respectively relative to the low inlet turbulence cases. The loss cores in the spatially resolved data and the peaks in the mass-weighted average data observed at 20% and 80% span for the cases with low and high inlet turbulence were removed with the introduction of inlet swirl. The average total pressure loss under inlet swirl compared to the high inlet turbulence intensity was 11.2% of the outlet dynamic head lower for the original and 9.8% of the outlet dynamic head lower for the shielded vane.

Closer to the endwalls the increase of inlet turbulence intensity resulted in an increase in total pressure loss, whereas the introduction of inlet swirl resulted in a reduction in total pressure loss on the endwall between the vanes, due to the reduced secondary flow strength. The same trends were observed in the shielded case, with the total pressure loss near the endwalls being lower than in the original case for all inlet conditions. In addition, the smaller loss core downstream of the shielded vane that was observed under low inlet turbulence conditions was maintained under both high inlet turbulence and inlet swirl.

The loading of the vane was also affected by the inlet conditions, with the isentropic Mach number at mid-span on the pressure side of the shielded vane being lower with the increase in inlet turbulence intensity and dropping further with the introduction of inlet swirl. This was a result of the lower total pressure in these cases in comparison to the low inlet turbulence case. In all cases the turning of the flow downstream of the shielded vane was maintained, so as to minimize any effects on the performance of the downstream rotor and facilitate the application of the new design. The reduced strength of secondary flow for inlet swirl was also captured in the

spatially resolved pitch angle distribution, where the size of the vortex cores and the maximum angles were significantly lower compared to the high inlet turbulence case.

The increase of inlet turbulence intensity resulted in an increase in Nusselt number on the vane surface for the original case. The regions most affected were the vane leading edge and the endwall near the vane leading edge on the suction side and near the vane trailing edge on the pressure side. The average increase in Nusselt number for the high inlet turbulence case was up to 15% on the vane pressure side (locally reaching 35% in the low Nusselt region downstream of the leading edge) and $10 - 15\%$ on the suction side. The Nusselt number on the early pressure side was not significantly affected due to the lower isentropic Mach number on the vane surface. The passage vortex trails on the suction side were more confined to the endwall region and the increase in Nusselt number in that region ranged from 20% to 30%. On the hub endwall the maximum increase in Nusselt number, noted on the leading edge of the central vane and on the trailing edge of vane 1, was 40%.

Inlet swirl resulted in a more uniform heat transfer distribution on the vane leading edge, with a lower peak in Nusselt number compared to both the low and the high inlet turbulence case. The increase in Nusselt number on the vane pressure side was higher than for the inlet turbulence case, up to 15% on the vane surface, and locally reaching 70% in the low Nusselt number region. The Nusselt number on the majority of the vane suction side was reduced by 5% compared to the low inlet turbulence case and increased by up to 15% near the hub. The casing passage vortex trail was more confined to the endwall, whereas the hub passage vortex trail was diffused further away from the endwall. The heat transfer levels on the hub endwall were between those observed in the low and the high inlet turbulence cases, with an increase in Nusselt number of up to 30% relative to the low inlet turbulence case near the vane leading edge fillet and a higher increase further away from the vane. The increase in Nusselt number near the trailing edge of vane 1 was 20%.

The effect of engine-representative conditions on the shielded vane was less pronounced than on the original vane. The change in Nusselt number on the early suction side with the increase

of inlet turbulence and the introduction of inlet swirl was negligible, as the boundary layer on the vane surface was a continuation of the one formed on the combustor transition duct wall and was less affected by the small changes in the flow characteristics. The heat transfer on the late suction side was higher for both the high inlet turbulence and the inlet swirl compared to the low inlet turbulence, with the Nusselt number increasing by up to 7% and up to 15% respectively. The Nusselt number on the vane pressure side was increased by up to 20% (25% for inlet swirl) in the centre of the vane and reduced by up to 15% (10% for inlet swirl) near the endwalls. Inlet turbulence and inlet swirl increased the Nusselt number on the vane endwall near the trailing edge by up to 25%.

The improved thermal performance of the shielded vane in comparison to the original was demonstrated under both high inlet turbulence and inlet swirl with turbulence. The reduction in Nusselt on the shielded vane for high inlet turbulence ranged from 50% on the early pressure side and $25 - 30\%$ further downstream, 25% on the vane suction side, and by 55% on the endwall near the vane leading edge. The local increase in Nusselt number on the hub endwall in the vane leading edge region was 25%.

For inlet swirl the reduction in Nusselt number for the shielded vane in comparison to the original reached $10 - 15\%$ on the vane suction side, 50% on the early pressure side and $25 - 30\%$ further downstream, and 45% on the hub endwall near the vane leading edge. The local increase in Nusselt number on the hub endwall in the vane leading edge region was 30% and 5% in the vane trailing edge region.

Overall the Nusselt number was mostly lower for the shielded case compared to the original for all inlet conditions. Furthermore, the regions with higher Nusselt number than the original case were mostly regions that can be cooled with the new design for the vane and endwall cooling discussed in the numerical studies in Chapter 6.

Summary and Conclusions

Summary

Combustors and turbines are traditionally designed and optimized separately, but as the need for more compact designs arises and the components are getting closer together the interactions between them cannot be disregarded. The high temperature, highly turbulent, swirling flow at the exit of the combustor has a significant effect on the aerothermal field and the cooling of the downstream vanes and endwalls, with an impact on the life and overall performance of the engine. Computational studies need a good baseline validation platform, whereas experimental studies are typically carried out in low speed conditions and non-representative Reynolds numbers and cannot provide accurate measurements of heat transfer.

The goal of this thesis was to investigate the interactions between the combustor and the nozzle guide vane of a gas turbine with can combustors. The main aims and objectives of this work have been met and were presented in this thesis:

A high speed experimental facility was built that provides the experimental flexibility of a low speed cascade for high speed studies. The Mach number was matched to the engine and the Reynolds number was half, significantly higher than in other studies carried out, enabling the study of the aerodynamic field, secondary flow, and heat transfer under engine-representative operating conditions. The effect of the combustor wall and vane clocking was investigated experimentally. The modelling methodology was then used for the numerical investigation of new vane designs and concepts. A novel concept of using the combustor wall trailing edge to shield the vane leading edge was presented and the design was analysed and compared to the datum configuration, giving promising results for the cooling of the vane and endwalls and the reduction of aerodynamic loss. The validity of the shielding and cooling concept was numerically investigated under

engine-representative inlet conditions. The new vane design was tested in the experimental facility, demonstrating its improved performance over the original vane. The improved performance of the shielded vane was also demonstrated under engine-representative inlet conditions.

The results obtained and presented in this thesis highlighted the capabilities of the facility. The experimental and numerical methods used in this work were suitable for the purpose of this study which was to compare the effect of the different geometric setups on the vane aerothermal performance and analyse the improvements achieved with the new vane design, enhancing the physical understanding behind the phenomena observed.

The main results and conclusions of this work have been discussed in the individual chapters and are summarized in the following section.

Conclusions

Effect of Combustor Wall

The combustor wall increased the aerodynamic loss downstream of the central vane due to the mixing of its wake with the boundary layer on the vane. The increase in the average total pressure loss coefficient relative to the adjacent vane passage was 9.2% of the outlet dynamic head. However, the presence of the wall and the alteration of the pressure field changed the shape of the horseshoe vortex around the leading edge of the vane, making the pressure side leg stronger and the suction side leg larger with lower vorticity at the core. A secondary, counter-rotating vortex appeared as the flow approaching the vane from the pressure side near the endwalls rolled up between the combustor wall and the horseshoe vortex on the vane leading edge. This had two main effects on the heat transfer to the vane: high Nusselt number trails at 6% and 94% span and a significant reduction in the peak heat transfer on the endwall near the early suction side by 23%, from 3500 on vane 3 to 2700 on the central vane. This peak heat transfer region has been reported

to cause extensive damage to the vanes, and its reduction significantly increases component life. The presence of the combustor wall also reduced the heat transfer in the stagnation region.

Effect of Vane Clocking

The investigation of clocking of the combustor wall towards the vane pressure and suction side (by 10% pitch) had some interesting effects on the aerodynamic and heat transfer field. The total pressure loss increased by 0.2% of the outlet dynamic head for pressure side clocking and by 1.1% for suction side clocking. The effect of the combustor wall on the loss profile was more pronounced for clocking towards the suction side, where the loss around the mid-span region of the vane was higher than in the datum case. The wake of the combustor wall, directed towards the vane suction side, mixed with the boundary layer after mid-chord, in a high Mach number region, resulting in a thicker wake with higher pressure loss. The shape of the vortices in the leading edge region changed with the change of the relative position of the wall and the vane and the secondary vortex observed in the datum case was not seen for 10% PS clocking.

The thermal field was also affected by the vane clocking. Clocking towards the pressure side resulted in higher heat transfer in the leading edge region and on the vane pressure side at 20% of C_{ax}, whereas the Nusselt number on the vane suction side was reduced. On the other hand, clocking towards the suction side did not have a strong effect on the Nusselt number on the vane leading edge, and resulted in a small reduction on the vane pressure side and a small increase on the suction side. The latter was due to the reduction of the protective effect of the wake of the combustor wall which was further away from the vane surface. The effect of clocking on the suction side heat transfer was reversed close to the endwalls, where the wake of the combustor wall had no effect and the heat transfer was dictated by whether the vane was less or more exposed to the hot mainstream flow. The Nusselt number was therefore marginally lower than the datum for 10% PS clocking and marginally higher for 10% PS clocking. The Nusselt number in the peak heat transfer region on the vane endwall, which is of highest interest, was significantly higher for

both cases compared to the datum, with Nusselt number levels closer to those observed on the adjacent vanes, as the combustor wall and the horseshoe vortex had no protective effect in these cases.

Leading Edge Shielding Concept

The investigation of a new concept for the combustor-turbine interface led to the development of a shielded vane design with slot cooling from the upstream combustor wall. The numerical investigation of this design showed that the total pressure loss was reduced by 40% compared to the original vane, due to the absence of the wake of the combustor wall which reduced mixing loss and the smaller wetted surface of the new vane, which reduced profile loss. The heat transfer to the vane was also reduced, particularly on the suction side which was protected by the boundary layer of the combustor wall.

Shielded Vane Cooling

The slot cooling concept was shown to provide adequate cooling to the vane using less air than a typical showerhead. It is noted that the amount of cooling air used for a turbine nozzle guide vane is not as crucial as for subsequent stages, since it does not have a thermodynamic penalty on the cycle; the only penalty is aerodynamic loss. The main benefit of the concept lies in the more uniform temperature distribution on the vane. This was achieved because the new design removed the horseshoe vortex upstream of the vane leading edge, as the distance between the combustor wall and the vane was minimized. The reduced strength of secondary flow then allowed improved coverage of the vane and endwalls from upstream continuous slots. The cooling effectiveness on the hub and casing endwalls was 25% higher than in the original case, using an engine-representative total coolant mass flow rate for the two endwalls. The main improvement on the endwall was near the vane pressure side, where the reduced secondary flow allowed better coverage of the endwall, assisted by the efficient cooling of the vane all the way to the hub and casing endwall. The second area of significant improvement was near the vane suction side in the leading edge region, where

the removal of the horseshoe vortex allowed the cooling of the area downstream of the vortex in the peak heat transfer region on the endwall that was previously uncooled due to the flow being entrained in the vortex and separating from the endwall.

Robustness of Cooling Concept

The investigation of the effect of engine-representative flow at the inlet on the performance of the shielded vane showed that the vane leading edge can be protected under both high inlet turbulence and inlet swirl. The cooling effectiveness on the endwalls was also better for the shielded case, with an improvement over the original case of 19% for high inlet turbulence and 14% for inlet swirl for the hub endwall. The increase in average cooling effectiveness on the casing endwall was 13% for high inlet turbulence, 11% for negative, and 6% for positive inlet swirl. Inlet swirl was also seen to reduce the average cooling effectiveness and the coolant coverage of the vane and endwalls compared to the high inlet turbulence case.

Shielded Vane Performance

The average total pressure loss coefficient downstream of the new shielded vane was reduced by 9.1% of the outlet dynamic head compared to the original vane and was similar to the loss of the adjacent vanes which did not have the added loss of the wake of the combustor wall. The flow turning downstream of the vane was similar to the original, minimizing disruptions to the downstream rotor. The removal of the horseshoe vortex and the vane leading edge resulted in lower heat transfer to the early pressure and suction side of the vane. The effect was more pronounced on the suction side, where the shielded vane had a uniform Nusselt number, removing the peak in the transition region. The peak heat transfer on the endwall near the vane was also removed.

Performance for Inlet Turbulence Case

The high turbulence inlet condition had a significant effect on the aerodynamic performance of the vane. The mass-weighted average total pressure loss coefficient was higher than that with low

inlet turbulence, with average values that were 15.4% of the outlet dynamic head higher for the original vane. The total pressure loss downstream of the shielded vane was affected to a similar extent, with an increase in the average total pressure loss of 17.6% of the outlet dynamic head. The turning of the flow downstream of the cascade was also affected by the increase in inlet turbulence with a drop in the maximum yaw angle of 1° in the region from $30 - 70\%$ span.

The increase of inlet turbulence resulted in an increase in Nusselt number on the vane and the endwalls. On the vane pressure side, this ranged from 50% in the low Nusselt region on the vane surface to a smaller increase of 10% on the early pressure side, as well as downstream of the low Nusselt region. On the leading edge the increase in Nusselt number due to inlet turbulence was 30% and further downstream on the suction side a nearly uniform increase in Nusselt number was observed, by 15%. On the endwall the Nusselt number was increased by 50% and the peak heat transfer near the vane leading edge was increased by 22% (600). The same applied to the shielded vane, with smaller changes in Nusselt number between the low and high inlet turbulence cases.

Performance for Inlet Swirl Case

The main effect of the swirl (with turbulence) inlet condition on the aerodynamic performance was the significant reduction in secondary flow. The total pressure loss coefficient downstream of the cascade did not exhibit the same loss cores at 80 and 20% span. The total pressure loss for inlet swirl was increased in comparison to the low inlet turbulence case but was significantly lower than with high inlet turbulence. The average loss compared to the high inlet turbulence case was 11.2% and 9.8% of the outlet dynamic head lower for the original and shielded vane respectively. The yaw angle in the mid-span region was similar to that with low inlet turbulence. The effect of inlet swirl was also seen in the pitch angle distribution, where the strength of the vortices was smaller, as seen by the lower minimum and maximum angles near the hub and casing.

The introduction of inlet swirl (with turbulence) increased heat transfer to the vane surface compared to the low inlet turbulence case, to levels closer to those observed with high inlet turbu-

lence. On the vane pressure side, the increase in Nusselt number was significant on the entire vane surface, and the drop in Nusselt number after 5% of the axial chord became significantly smaller; the Nusselt number was 80% higher than in the low inlet turbulence case. The Nusselt number on the vane surface was marginally higher than for high inlet turbulence. On the vane leading edge, the Nusselt number was increased by 30% and further downstream on the suction side, the Nusselt number was between the levels observed with low and with high inlet turbulence, 10% higher than the low turbulence case. The Nusselt number on the vane endwall was also increased by 50%, as in the high turbulence case, but there was no increase in heat transfer in the region of the peak near the leading edge relative to the datum case. The same trends were observed on the shielded vane, with a smaller increase in heat transfer to the vane surface.

Shielded Vane Performance under Engine-Representative Conditions

The improved aerothermal performance of the new shielded vane compared to the original was demonstrated under engine-representative inlet conditions of high turbulence and swirl. The lower aerodynamic loss of the new vane compared to the original was maintained under high inlet turbulence, where the drop in mass-weighted average total pressure loss was 6.9% of the outlet dynamic head and under inlet swirl with turbulence, where the drop was 5.5% of the outlet dynamic head. The loss on the endwall was also lower for the shielded vane for all inlet conditions. The maximum difference in yaw angle at mid-span was 1°, with higher turning of the flow in the shielded case.

In terms of heat transfer the improved performance of the vane observed for low inlet turbulence was maintained under more engine-representative inlet conditions. The Nusselt number on the pressure side of the shielded vane was significantly smaller for all inlet conditions. The difference between the shielded and the original vane in the higher heat transfer regions on the vane-endwall junctions was reduced for high inlet turbulence and inlet swirl with turbulence and can be cooled from the upstream cooling slots, as shown in the numerical studies. The heat trans-

fer on the vane leading edge was uniform for the shielded vane, reducing the peak observed in the original vane by 1000 for high inlet turbulence and by 700 for inlet swirl with turbulence. Further downstream on the suction side, the same trends were observed as for the low inlet turbulence case, with a significant drop in Nusselt number by approximately 500 for high inlet turbulence and by 300 for inlet swirl with turbulence. The higher heat transfer region near the hub on the late suction side was also reduced for both high inlet turbulence and inlet swirl with turbulence. On the vane endwall the peak heat transfer was moved from the early suction side in the original vane closer to the start of the shielded vane, in a region that can be cooled from the upstream cooling slots. Away from the vane the heat transfer to the endwall was also reduced compared to the original case for all inlet conditions.

Suggestions for Future Work

The design and manufacture of a highly modular facility opens numerous possibilities for experimental studies. The facility has been designed to allow for modifications to the working section to be performed, and has anticipated the installation of a cooling system which was designed and installed at the end of this project. Further experimental studies should therefore move towards the implementation of aerodynamic and heat transfer studies with fully cooled vanes and endwalls. The vanes and endwall cavities have been designed as individual components and fully cooled vanes can easily be manufactured and placed in the cascade. The infrared thermography technique can be used to map the heat transfer on the vanes and compare it to the datum geometry of the uncooled vane. This can allow testing of different vane cooling configurations, varying the number and location of cooling holes, as well as different endwall cooling geometries.

With the addition of cooling to the facility, the cooling concept for the shielded vane should also be validated under engine-representative inlet conditions. The coolant feed system for the upstream slots and the endwalls has already been designed for the shielded case as part of this work. The cooling effectiveness achieved with the new design can then be compared to the cooling

effectiveness of the original vane with the arrays of film cooling holes in the leading edge region. A next step would be the combination of the two vane designs and the inclusion of film cooling holes on the downstream parts of the shielded vane, to provide a fully cooled shielded vane design that will use less coolant and have a more uniform temperature distribution than the original vane. It is noted that in this case coolant from the trailing edge coolant should be included in both vanes. However, since the vane geometry was maintained in the trailing edge region, the change in the absolute value of total pressure loss due to the trailing edge is not expected to be different between the two cases.

The effect of misalignment on the vane cooling should also be experimentally investigated. Small misalignments between the parts can appear during operation, as the gaps that arise from the assembly of the individual components close due to thermal expansion. These are significantly smaller than the different clocking positions studied in this work: they are up to $2 - 3$ mm at full scale and can have a significant effect on the shielded vane heat transfer and cooling.

The detailed experimental measurements have provided a baseline for the validation of computational studies. Further work in the combustor-turbine interaction field should focus on more integrated studies of the combustor and the turbine interface. This can include the development of new cooling patterns for the vane surfaces and endwalls that can later be tested experimentally in the facility. Further investigation of the shielded vane concept can be carried out as well as an experimental investigation of the integrated vane concept proposed in the numerical studies in the literature. In this case, the effect of trailing edge loss should also be addressed.

Concluding Remarks

The main contribution of this thesis lies in the development of a new, improved vane design. The numerical studies that were employed to enhance the physical understanding of the phenomena captured in the experiments for the original vane were used to design a vane where the leading edge was shielded by the upstream combustor wall. This was shown to have a better aerodynamic

performance, as well as lower heat transfer to the vane. The improvement was seen in both the experimental and the numerical studies; the numerical studies were then employed to identify the source of the difference in performance between the two designs.

The reduction of the secondary flow and the removal of the horseshoe vortex upstream of the vane halved the aerodynamic loss. Furthermore, the lack of a detached wake of the combustor wall resulted in a thicker, protective boundary layer on the vane surface that reduced heat transfer levels to the vane, particularly on the suction side. The improved performance of the new vane was maintained under engine-realistic inlet conditions.

A cooling concept for the new vane was proposed in this work and its potential was shown in numerical studies. The system was based on the pressure distribution around the vane cooling slots to ensure uniform distribution of coolant flow. This was shown to provide adequate cooling of the vane leading edge region for engine-realistic inlet conditions in the numerical studies presented in this thesis.

The heat transfer to the new shielded vane was lower due to the minimization of the axial distance between the combustor and the vane and the subsequent alteration of the secondary flow. As a result, the vane leading edge region can be cooled effectively with a more uniform coolant coverage than what is typically achieved with a showerhead. The new concept can simplify the vane design without compromising structural integrity, as the thickness of the vane is maintained downstream of the leading edge region. The endwalls can be cooled with high effectiveness using the amount of air that was used to seal the inter-component gaps. An implementation of the new design can improve the aerodynamic performance of the turbine due to the significant reduction in total pressure loss, provide a more uniform temperature field on the vane, and reduce the peak heat transfer region on the leading edge-endwall junction. The improvement of the temperature field achieved with the new design can increase component and engine life or allow an increase in turbine entry temperatures, leading to higher overall effectiveness and reduced emissions. The

reduction in the vane exit temperature non-uniformity may also have an aerodynamic benefit in the rotor.

This thesis also highlights the need for integrated component studies, as effects that can be detrimental to individual component efficiencies can be utilized to improve the overall performance of the engine.

Bibliography

H. M. Abo El Ella and S. A. Sjolander. An Application of a Low Cost High Contrast Oil Flow Visualization Technique in a Transonic Blow-down Wind Tunnel for the Investigation of Secondary Flows. *21st ISABE Conference, Busan, Korea*, 2013.

A.R. Abu Talib. *Detailed Investigation of the Low-Temperature Analogy of an Aircraft Engine Standard Fire-Test*. PhD thesis, University of Oxford, 2003.

T. Ai, C. Koeneke, H. Arimura, and Y. Hyakutake. Development of an Air Cooled G Class Gas Turbine (The M501GAC). ASME paper no. GT2009-60321, 2009.

F. E. Ames. The Influence of Large-Scale High-Intensity Turbulence on Vane Heat Transfer. *J. Turbomach.*, 119(1):23–30, 1997.

F. E. Ames and M. W. Plesniak. The Influence of Large-Scale, High-Intensity Turbulence on Vane Aerodynamic Losses, Wake Growth, and the Exit Turbulence Parameters. *J. Turbomach.*, 119(2):182–192, 1997.

F. E. Ames, C. Wang, and P. A. Barbot. Measurement and Prediction of the Influence of Catalytic and Dry Low NOx Combustor Turbulence on Vane Surface Heat Transfer. *J. Turbomach.*, 125(2):221–231, 2003.

T. Arts. Film Cooling: What Did we Learn from our Measurements? *Annals New York Academy of Sciences*, 934:126134, 2001.

I. Aslanidou, B. Rosic, V. Kanjirakkad, and S. Uchida. Leading Edge Shielding Concept in Gas Turbines with Can Combustors. *J. Turbomach.*, 135(2)(2):021019, March 2013.

S. Baldauf, A. Schulz, and S. Wittig. High-Resolution Measurements of Local Effectiveness From Discrete Hole Film Cooling. *J. Turbomach.*, 123(4):758–765, 2001.

M. D. Barringer, K. A. Thole, and M. D. Polanka. Effects of Combustor Exit Profiles on Vane Aerodynamic Loading and Heat Transfer in a High Pressure Turbine. *J. Turbomach.*, 131(2): 021008, 2009a.

M. D. Barringer, K. A. Thole, and M. D. Polanka. An Experimental Study of Combustor Exit Profile Shapes on Endwall Heat Transfer in High Pressure Turbine Vanes. *J. Turbomach.*, 131(2):021009, 2009b.

M.D. Barringer, K.A. Thole, M.D. Polanka, J.P. Clark, and P.J. Koch. Migration of Combustor Exit Profiles Through High Pressure Turbine Vanes. *J. Turbomach.*, 131(2):021010, 2009c.

A. M. Basol, R. Kai, A. I. Kalfas, and R. S. Abhari. Integrated Combustor Turbine Design for Improved Aerothermal Performance: Effect of Dilution Air Control. *J. Eng. Gas Turbines Power*, 134(9):091501, 2012.

T. Behr, A. I. Kalfas, and R. S. Abhari. A probabilistic uncertainty evaluation method for turbomachinery probe measurements. *The XVIII Symposium on Measuring Techniques in Turbomachinery, Thessaloniki, Greece*, 2006.

M. W. Benner, S. A. Sjolander, and S. H. Moustapha. The Influence of Leading-Edge Geometry on Secondary Losses in a Turbine Cascade at the Design Incidence. *J. Turbomach.*, 126(2): 277–287, 2004.

M. F. Blair. Experimental Study of Heat Transfer and Film Cooling on Large-Scale Turbine Endwalls. *J. Heat Transfer*, 96(4):524–529, 1974.

M. F. Blair. Influence of Free-Stream Turbulence on Turbulent Boundary Layer Heat Transfer and Mean Profile Development, Part IExperimental Data. *J. Heat Transfer*, 105(1):33–40, 1983.

M. F. Blair. Experimental Study of Heat Transfer in a Large-Scale Turbine Rotor Passage. *J. Turbomach.*, 116(1):1–13, 1994.

D. G. Bogard and K. A. Thole. Gas Turbine Film Cooling. *J. Propul. Power*, 22(2):249–270, 2006.

R. S. Bunker. A Review of Shaped Hole Turbine Film-Cooling Technology. *J. Heat Transfer*, 127(4):441–453, 2005.

R. S. Bunker. Gas Turbine Heat Transfer: Ten Remaining Hot Gas Path Challenges. *J. Turbomach.*, 129(2):193–201, 2007.

T. L. Butler, O. P. Sharma, H. D. Joshlyn, and R. P. Dring. Redistribution of an Inlet Temperature Distortion in an Axial Flow Turbine Stage. *J. Propul. Power*, 5(1):64–71, 1989.

N. D. Cardwell, N. Sundaram, and K. A. Thole. Effect of Midpassage Gap, Endwall Misalignment, and Roughness on Endwall Film-Cooling. *J. Turbomach.*, 128(1):62–70, 2006.

N. D. Cardwell, N. Sundaram, and K. A. Thole. The Effects of Varying the Combustor-Turbine Gap. *J. Turbomach.*, 129(4):756–764, October 2007.

H. W. Coleman and W.G. Steele. *Experimentation, Validation, and Uncertainty Analysis for Engineers*. John Wiley and sons, 3rd edition, 2009.

F. Coletti, A. Armellini, T. Arts, and C. Scholtes. Aerothermal Investigation of a Rib-Roughened Trailing Edge Channel With Crossing JetsPart II: Heat Transfer Analysis. *J. Turbomach.*, 133(3):031024, 2011.

D. Corriveau and S. A. Sjolander. Influence of Loading Distribution on the Performance of Transonic High Pressure Turbine Blades. *J. Turbomach.*, 126(2):288–296, 2004.

L. C. Daniels and D. L. Schultz. Heat Transfer Rate to Blade Profiles - Theory and Measurement in Transient Facilities. *VKI Lecture Series, Vol 1& 2*, 1982.

W. N. Dawes. A Comparison of Zero and One Equation Turbulence Modelling for Turbomachinery Calculations. *35th ASME International Gas Turbine Conference, Brussels, Belgium*, 1990.

J. D. Denton. Loss Mechanisms in Turbomachines. *J. Turbomach.*, 115(4):621–656, 1993.

J. D. Denton and G. Pullan. A Numerical Investigation Into the Sources of Endwall Loss in Axial Flow Turbines. ASME paper no. GT2012-69173, 2012.

S. L. Dixon. *Fluid Mechanics and Thermodynamics of Turbomachinery*. Elsevier-Butterworth-Heinemann, 2005.

J. E. Doorly and M. L. G. Oldfield. The Theory of Advanced Multi-layer Thin Film Heat Transfer Gauges. *Int. J. Heat Mass Transfer.*, 30(6):1159–1168, 1987.

D. J. Dorney, K. L. Gundy-Burlet, and D. L. Sondak. A Survey of Hot Streak Experiments and Simulations. *International Journal of Turbo and Jet Engines*, 16(1):1–15, 1999.

M. G. Dunn, H. L. Martin, and M. J. Stanek. Heat-Flux and Pressure Measurements and Comparison With Prediction for a Low-Aspect-Ratio Turbine Stage. *J. Turbomach.*, 108(1):108–115, 1986.

S. V. Ekkad, S. Ou, and R. B. Rivir. A Transient Infrared Thermography Method for Simultaneous Film Cooling Effectiveness and Heat Transfer Coefficient Measurements from a Single Test. *J. Turbomach.*, 126(4):597–603, 2004.

A. D. Fitt, C. J. P. Forth, B. A. Robertson, and T. V. Jones. Temperature Ratio Effects in Compressible Turbulent Boundary Layers. *Int. J. Heat Mass Transfer*, 29(1):159–164, 1986.

L. Fottner. *Advanced Methods for Cascade Testing AGARDograph AG328*, chapter 2.1: Simulating Cascade Flow Parameters, pages 3–7. C. Hirsch ed., NATO AGARD, 1993a.

L. Fottner. *Advanced Methods for Cascade Testing AGARDograph AG328*, chapter 2.2: Subsonic Cascades (Compressors, Turbines), pages 12–22. C. Hirsch ed., NATO AGARD, 1993b.

S. Friedrichs. *Turbine Heat Transfer*, pages 219–254. Cambridge Turbomachinery Course, 2012.

S. Friedrichs, H. P. Hodson, and W. N. Dawes. Distribution of Film-Cooling Effectiveness on a Turbine Endwall Measured Using the Ammonia and Diazo Technique. *J. Turbomach.*, 118(4): 613–621, 1996.

S. Friedrichs, H. P. Hodson, and W. N. Dawes. Aerodynamic Aspects of Endwall Film-Cooling. *J. Turbomach.*, 119(4):786–793, 1997.

S. Friedrichs, H. P. Hodson, and W. N. Dawes. The Design of an Improved Endwall Film-Cooling Configuration. *J. Turbomach.*, 121(4):772–780, 1999.

D. R. H. Gillespie. *Intricate Internal Cooling Systems for Gas Turbine Blading*. PhD thesis, University of Oxford, 1996.

D. R. H. Gillespie, S. T. Kohler, Z. Wang, and P. T. Ireland. Full Surface Local Heat Transfer Coefficient Measurements in a Model of an Integrally Cast Impingement Cooling Geometry. *J. Turbomach.*, 120(1):92–99, 1998.

S. G. Goebel, N. Abuaf, J. A. Lovett, and C.-P. Lee. Measurements of Combustor Velocity and Turbulence Profiles. ASME paper no. 93-GT-228, 1993.

R. J. Goldstein and H. H. Cho. A Review of Mass Transfer Measurements Using Napthalene Sublimation. *Experimental Thermal and Fluid Science*, 10(4):416–434, 1995.

R. J. Goldstein and R. A. Spores. Turbulent Transport on the Endwall in the Region Between Adjacent Turbine Blades. *J. Heat Transfer*, 110(4a):862–869, 1988.

R. J. Goldstein, K. Y. Lau, and C. C. Leung. Velocity and Turbulence Measurements in Combustion Systems. *Exp. Fluids*, 1:93–99, 1983.

R.J. Goldstein, H.P. Wang, and M.Y. Jabbari. The Influence of Secondary Flows near the Endwall and Boundary Layer Disturbance on Convective Transport from a Turbine Blade. *J. Turbomach.*, 117(4):657–665, 1995.

R. A. Graziani, M. F. Blair, J. R. Taylor, and R. E. Mayle. Experimental Study of Endwall and Airfoil Surface Heat Transfer in a Large Scale Turbine Blade Cascade. *J Eng. Gas Turbines Power*, 102(2):257–267, 1980.

M. Gritsch, A. Schulz, and S. Wittig. Adiabatic Wall Effectiveness Measurements of Film-Cooling Holes With Expanded Exits. *J. Turbomach.*, 120(3):549–556, 1998.

S. Hada and K. A. Thole. Computational Study of a Midpassage Gap and Upstream Slot on Vane Endwall Film-Cooling. *J. Turbomach.*, 133(1):011024, 2011.

J. C. Han. Fundamental Gas Turbine Heat Transfer. *J. Thermal Sci. Eng. Appl.*, 5(2):021007, 2013.

J. C. Han and L. M. Wright. *The Gas Turbine Handbook*, chapter Enhanced Internal Cooling of Turbine Blades and Vanes, page 321352. U.S. DOE, National Energy Technology Laboratory, Morgantown, WV, 2006.

J. C. Han, S. Dutta, and S. V. Ekkad. *Gas Turbine Heat Transfer and Cooling Technology*. Taylor and Francis (New York), 2nd edition, 2013.

S. P. Harasgama, C. D. Burton, and K. S. Chana. Measurements and Computations of External Heat Transfer and Film Cooling in Turbines. *Defence Research Agency Technical Memorandum P 1223, also Proceedings of the X International Symposium on Air Breathing Engines (ISABE)*, 1992.

S. Harrison. Secondary Loss Generation in a Linear Cascade of High Turning Turbine Blades. *J. Turbomach.*, 112(4):618–624, 1990.

F. Haselbach and H. P. Schiffer. Aerothermal Investigations on Turbine Endwalls and Blades. ASME paper no. GT2004-53078, 2004.

K. S. Hermanson and K. A. Thole. Effect of Inlet Conditions on Endwall Secondary Flows. *J. Propul. Power*, 16(2):286–296, 2000.

K. S. Hermanson and K. A. Thole. Effect of Nonuniform Inlet Conditions on Endwall Secondary Flows. *J. Turbomach.*, 124(4):623–631, 2002.

H. P. Hodson and R. J. Miller. *Experimental Methods for Aerothermal Research*, pages 713–799. Cambridge Turbomachinery Course, 2012.

J. H. Horlock, D. Watson, and T. V. Jones. Limitations on Gas Turbine Performance Imposed by Large Turbine Cooling Flows. *J. Eng. Gas Turbines Power*, 123(3):487–494, 2001.

Y. Huang and V. Yang. Dynamics and Stability of Lean-Premixed Swirl-Stabilized Combustion. *Prog. Energy Combustion Sci.*, 35(4):293–364, 2009.

P. T. Ireland and T. V. Jones. Liquid Crystal Measurements of Heat Transfer and Surface Shear Stress. *Meas. Sci. Technol.*, 11(7):969–986, 2000.

P.T. Ireland, A.J. Neely, D.R.H. Gillespie, and A.J. Robertson. Turbulent Heat Transfer Measurements Using Liquid Crystals. *Int. J. Heat Fluid Flow*, 20(4):355–367, 1999.

E. Ito, I. Okada, K. Tsukagoshi, A. Muyama, and J. Masada. Development of Key Technologies for the Next Generation Gas Turbine. ASME paper no. GT2010-23233, 2010.

S. Jacobi. Influence of Lean Premixed Combustor Geometry on the First Turbine Vanes Aerothermal Performance. Master's thesis, Swiss Federal Institute of Technology (ETH) Zurich, 2013.

P. Jenny, C. Lenherr, R. S. Abhari, and A. Kalfas. Effect of Hot Streak Migration on Unsteady Blade Row Interaction in an Axial Turbine. *J. Turbomach.*, 134(5):051020, 2012.

D. B. M. Jouini, S. A. Sjolander, and S. H. Moustapha. Aerodynamic Performance of a Transonic Turbine Cascade at Off-Design Conditions. *J. Turbomach.*, 123(3):510–518, 2001.

M. B. Kang, A. Kohli, and K. A. Thole. Heat Transfer and Flowfield Measurements in the Leading Edge Region of a Stator Vane Endwall. *J. Turbomach.*, 121(3):558–568, 1999.

B. Khanal, L. He, J. Northall, and P. Adami. Analysis of Radial Migration of Hot-Streak in Swirling Flow Through High-Pressure Turbine Stage. *J. Turbomach.*, 135(4):041005, 2013.

S. J. Kline and F. A. McClintock. Describing Uncertainties in Single-Sample Experiments. *Journal of Mechanical Engineering*, pages 3–8, January 1953.

D. G. Knost and K. A. Thole. Computational Predictions of Endwall Film-Cooling for a First Stage Vane. ASME paper no. GT2003-38252, 2003.

F. Kost and M. Nicklas. Film-Cooled Turbine Endwall in a Transonic Flow Field: Part IAerodynamic Measurements. *J. Turbomach.*, 123(4):709–719, 2001.

P. Kupferschmied, P. Koppel, W. Gizzi, C. Roduner, and G. Gyarmathy. Time-Resolved Flow Measurements with Fast-Response Aerodynamic Probes in Turbomachines. *Meas. Sci. Technol.*, 11:1036–1054, 2000.

B. Lakshminarayana. Fluid Dynamics and Heat Transfer of Turbomachinery. *John Wiley and Sons, Inc.*, 1996.

L. S. Langston. Crossflows in a Turbine Cascade Passage. *J Eng. Gas Turbines Power*, 102(4): 866–874, 1980.

L. S. Langston. Secondary Flows in Axial Turbines - A Review. *Annals of the New York Academy of Sciences*, 934:11–26, 2001.

L. S. Langston, M. L. Nice, and R. M. Hooper. Three Dimensional Flow within a Turbine Cascade Passage. *J. Eng. Gas Turbines Power*, 99(1):21–28, 1977.

A. H. Lefebvre. *Gas Turbine Combustion*. CRC Press, 3rd edition, 2010.

C. Liess. Experimental Investigation of Film Cooling With Ejection From a Row of Holes for the Application to Gas Turbine Blades. *J. Eng. Gas Turbines Power*, 97(1):21–27, 1975.

J. P. Longley. *Introduction to 3-D Flows in Turbomachinery*, pages 79–116. Cambridge Turbomachinery Course, 2012.

S. Luque. *A Fully Integrated Approach to Gas Turbine Cooling System Research*. PhD thesis, University of Oxford, 2012.

S. Luque, V. Kanjirakkad, I. Aslanidou, R. Lubbock, B. Rosic, and S. Uchida. A New Experimental Facility to Investigate Combustor-Turbine Interactions in Gas Turbines with Multiple Can Combustors. *J. Eng. Gas Turbines Power*, 137(5):051503, 2015.

S. P. Lynch and K. A. Thole. The Effect of Combustor-Turbine Interface Gap Leakage on the Endwall Heat Transfer for a Nozzle Guide Vane. *J. Turbomach.*, 130(4):041019, 2008.

S. P. Lynch and K. A. Thole. The Effect of the Combustor-Turbine Slot and Midpassage Gap on Vane Endwall Heat Transfer. *J. Turbomach.*, 133(4):041002, 2011.

S. P. Lynch, K. A. Thole, A. Kohli, C. Lehane, and T. Praisner. Endwall Heat Transfer for a Turbine Blade With an Upstream Cavity and Rim Seal Leakage. ASME paper no. GT2013-94942, 2013a.

S. P. Lynch, K. A. Thole, A. Kohli, C. Lehane, and T. Praisner. Aerodynamic Loss for a Turbine Blade With Endwall Leakage Features and Contouring. ASME paper no. GT2013-94943, 2013b.

M. Mansour, N. Chokani, A. I. Kalfas, and R. S. Abhari. Time-Resolved Entropy Measurements Using a Fast Response Entropy Probe. *Meas. Sci. Technol.*, 19:115401, 2008.

C. M. Mazzoni, C. Klostermeier, and B. Rosic. Influence of Large Wake Disturbances Shed From the Combustor Wall on the Leading Edge Film Cooling. *J. Eng. Gas Turbines Power*, 136(8): 081503, 2014.

Meech Static Eliminators Ltd. *Vortex tube product brochure*.

A. B. Mehendale and J. C. Han. Influence of High Mainstream Turbulence on Leading Edge Film Cooling Heat Transfer. *J. Turbomach.*, 114(4):707–715, 1992.

R. J. Miller and J. D. Denton. *Loss Mechanisms in Turbomachines*, pages 79–116. Cambridge Turbomachinery Course, 2012.

Mitsubishi Heavy Industries Ltd. J-series gas turbine product brochure. 2013. URL `http://www.mhi.co.jp/en/products/pdf/H480-48GT28E1-B-0.pdf`.

R. J. Moffat. Describing the Uncertainties in Experimental Results. *Experimental Thermal and Fluid Science*, 1(1):3–17, 1988.

S. Nasir, J. S. Carullo, W. Ng, K. A. Thole, H. Wu, L. J. Zhang, and H. K. Moon. Effects of Large Scale High Freestream Turbulence and Exit Reynolds Number on Turbine Vane Heat Transfer in a Transonic Cascade. *J. Turbomach.*, 131(2)(2):021021, 2009.

M. Nicklas. Film-Cooled Turbine Endwall in a Transonic Flow Field: Part IIHeat Transfer and Film-Cooling Effectiveness. *J. Turbomach.*, 123(4):720–729, 2001.

D. O. O'Dowd. *Aero-Thermal Performance of Transonic High-Pressure Turbine Blade Tips*. PhD thesis, University of Oxford, 2010.

D. O. O'Dowd, Q. Zhang, I. Usandizaga, L. He, and P. M. Ligrani. Transonic Turbine Blade Tip Aero-Thermal Performance With Different Tip Gaps: Part IITip Aerodynamic Loss. ASME paper no. GT2010-22780, 2010.

D. O. O'Dowd, Q. Zhang, L. He, P. M. Ligrani, and S. Friedrichs. Comparison of Heat Transfer Measurement Techniques on a Transonic Turbine Blade Tip. *J. Turbomach.*, 133(2):021028, 2011.

M. L. G. Oldfield. Impulse Response Processing of Transient Heat Transfer Gauge Signals. *Journal of Turbomachinery*, 130:021023, 2008.

J. Ong and R. J. Miller. Hot Streak and Vane Coolant Migration in a Downstream Rotor. *J. Turbomach.*, 134(5):051002, 2012.

J. Ong, R. J. Miller, and J. D. Denton. The Prediction of Hot Streak Migration in a High Pressure Turbine. *Proc. IMechE, J. Power and Energy*, 224 (1):119–128, 2010.

A. Perdichizzi. Mach Number Effects on Secondary Flow Development Downstream of a Turbine Cascade. *J. Turbomach.*, 112(4):643–651, 1990.

A. Pfau, J. Schlienger, A.I. Kalfas, and R.S Abhari. Virtual four sensor fast response aerodynamic probe (frap). *16th Symposium on Measuring Techniques in Transonic and Supersonic Flow in Cascades and Turbomachines, Cambridge, UK*, 2002.

T. Povey, K. S. Chana, T. V. Jones, and J. Hurrion. The Effect of Hot-Streaks on HP Vane Surface and Endwall Heat Transfer: An Experimental and Numerical Study. *J. Turbomach.*, 129(1): 32–43, January 2007.

T. J. Praisner and C. R. Smith. The Dynamics of the Horseshoe Vortex and Associated Endwall Heat TransferPart I: Temporal Behavior. *J. Turbomach.*, 128:747–754, 2006a.

T. J. Praisner and C. R. Smith. The Dynamics of the Horseshoe Vortex and Associated Endwall Heat TransferPart II: Time-Mean Results. *J. Turbomach.*, 128:755–762, 2006b.

T. J. Praisner, C. V. Seal, L. Takmaz, and C. R. Smith. Spatial-Temporal Turbulent Flow-Field and Heat Transfer Behavior in End-Wall Junctions. *Int. J. Heat Fluid Flow*, 18:142–151, 1997.

I. Qureshi, A. Beretta, and T. Povey. Effect of Simulated Combustor Temperature Nonuniformity on HP Vane and End Wall Heat Transfer: An Experimental and Computational Investigation. *J. Eng. Gas Turbines Power*, 133(3):031901, 2010.

I. Qureshi, A. Beretta, K. Chana, and T. Povey. Effect of Aggressive Inlet Swirl on Heat Transfer and Aerodynamics in an Unshrouded Transonic HP Turbine. *J. Turbomach.*, 134(6):061023, 2012a.

I. Qureshi, A. D. Smith, and T. Povey. HP Vane Aerodynamics and Heat Transfer in the Presence of Aggressive Inlet Swirl. *J. Turbomach.*, 135(2):021040, 2012b. ASME paper GT2011-46037.

R. W. Radomsky and K. A. Thole. Detailed Boundary Layer Measurements on a Turbine Stator Vane at Elevated Freestream Turbulence Levels. *J. Turbomach.*, 124:107–118, 2002.

M. M. Rai and R. P. Dring. Navier-Stokes Analyses of the Redistribution of Inlet Temperature Distortions in a Turbine. *J. Propul. Power*, 6(3):276–282, 1990.

P. E. Roach. The Generation of Nearly Isotropic Turbulence by Means of Grids. *Int. J. Heat Fluid Flow*, 8(2):82–92, June 1987.

R. J. Roback and R. P. Dring. Hot Streaks and Phantom Cooling in a Turbine Rotor Passage: Part 1Separate Effects. *J. Turbomach.*, 115(4):657–666, 1993.

B. Rosic and C. Klostermeier. Interaction of Combustor Wall and First Vane Leading Edge Film Cooling in an Industrial Gas Turbine. *14th International Conference on Fluid Flow Technologies (CMFF '09), Budapest, Hungary*, Sept 2009.

B. Rosic, J. D. Denton, J. H. Horlock, and S. Uchida. Integrated Combustor and Vane Concept in Industrial Gas Turbines. *J. Turbomach.*, 134(3):031005, 2011.

H. Schlichting. *Boundary Layer Theory*. Mc Graw-Hill, 1968.

D. L. Schultz and T. V. Jones. Heat-Transfer Measurements in Short-Duration Hypersonic Facilities. *AGARDograph 165, Advisory Group for Aerospace Research & Development, Neuilly-sur-Seine, France*, 1973.

O. P. Sharma and T. L. Butler. Predictions of Endwall Losses and Secondary Flows in Axial Flow Turbine Cascades. *J. Turbomach.*, 109(2):229–236, 1987.

C. H. Sieverding. Recent Progress in the Understanding of Basic Aspects of Secondary Flows in Turbine Blade Passages. *J. Eng. Gas Turbines Power*, 107(2):248–257, 1985.

C. H. Sieverding. *Advanced Methods for Cascade Testing AGARDograph AG328*, chapter 1.5: Types of Cascade Tunnels, pages 7–9. C. Hirsch ed., NATO AGARD, 1993.

K. A. Thole. *The Gas Turbine Handbook*, chapter 4.2.3 Airfoil Endwall Heat Transfer, pages 353–362. National Energy Technology Laboratory, US Department of Energy, 2006.

K. A. Thole, A. K. Sinha, D. G. Bogard, and M. E. Crawford. Mean Temperature Measurements of Jets with a Crossflow for Gas Turbine Film Cooling Application. *Rotating Machinery - Transport Phenomena*, Edited by J. H. Kim and W. J. Yang, Hemisphere, New York, 1992.

A. Thrift, K. Thole, and S. Hada. Impact of the Combustor-Turbine Interface Slot Orientation on the Durability of a Nozzle Guide Vane Endwall. *J. Turbomach.*, 135(4):041019, 2013.

A. A. Thrift, K. A. Thole, and S. Hada. Effects of an Axisymmetric Contoured Endwall on a Nozzle Guide Vane: Adiabatic Effectiveness Measurements. *J. Turbomach.*, 133(4):041007, 2011a.

A. A. Thrift, K. A. Thole, and S. Hada. Effects of an Axisymmetric Contoured Endwall on a Nozzle Guide Vane: Convective Heat Transfer Measurements. *J. Turbomach.*, 133(4):041008, 2011b.

A. A. Thrift, K. A. Thole, and S. Hada. Effects of Orientation and Position of the Combustor-Turbine Interface on the Cooling of a Vane Endwall. *J. Turbomach.*, 134(6):061019, 2012.

M. D. Turrell, P. J. Stopford, K. J. Syed, and E. Buchanan. CFD Simulation of the Flow Within and Downstream of a High-Swirl Lean Premixed Gas Turbine Combustor. ASME Paper no. GT2004-53112, 2004.

G. J. Van Fossen, R. J. Simoneau, and C. Y. Ching. The Influence of Turbulence Parameters, Reynolds Number, and Body Shape on Stagnation Region Heat Transfer. *J. Heat Transfer*, 117(3):597–603, 1995.

P. P. Walsh and P. Fletcher. *Gas Turbine Performance*. Blackwell Science, 2004.

H. P. Wang, S. J. Olson, R. J. Goldstein, and E. R. G. Eckert. Flow Visualization in a Linear Turbine Cascade of High Performance Turbine Blades. *J. Turbomach.*, 119(1):1–8, 1997.

A. P. Weiss and L. Fottner. The Influence of Load Distribution on Secondary Flow in Straight Turbine Cascades. *J. Turbomach.*, 117(1):133–141, 1995.

Andrew P. S. Wheeler, Nicholas R. Atkins, and Li He. Turbine Blade Tip Heat Transfer in Low Speed and High Speed Flows. *J. Turbomach.*, 133:041025, 2011.

S. H. Wiers and T. H. Fransson. Experimental Investigation of the Periodicity in a Sector of an Annular Turbine Cascade. *15th Bi-Annular Symposium on Measuring Techniques in Transonic and Supersonic Flow in Cascades and Turbomachines, Firenze, Italy*, 2000.

L. Zhang, M. Baltz, M. Padupatty, and M. Fox. Turbine Nozzle Film Cooling Study Using the Pressure Sensitive Paint (PSP) Technique. ASME Paper no. 99-GT-196, 1999.

Q. Zhang, D. Sandberg, and P. M. Ligrani. Mach Number and Freestream Turbulence Effects on Turbine Vane Aerodynamic Losses. *J. Propul. Power*, 21(6):988–996, 2005.

Appendix

At the final stages of this project, a cooling system was designed for the experimental facility to provide cold air at lower than ambient temperature to cool the vanes and the endwalls. The air is cooled with the use of vortex tubes, a schematic of which is shown in Figure 8.23. Compressed air enters the spinning chamber of the tube tangentially, forcing the air to rotate at very high speed, forming a vortex and a pressure gradient which results in fast, high energy air migrating to the outer edge of the tube and slower, low energy air remaining at the core. A conical nozzle at one end of the tube allows the hot, high energy air at the outer radius of the vortex tube to exhaust, whereas the cold air at the core of the vortex is forced out of the other end of the tube. A valve is used to adjust the amount of air that is bled through the hot end, therefore controlling the mass flow rate and temperature of the air that exits from the cold end. A vortex tube can provide a temperature drop of up to $50°$C (Meech Static Eliminators Ltd.), depending on the percentage of mass flow that is exhausted from the hot end.

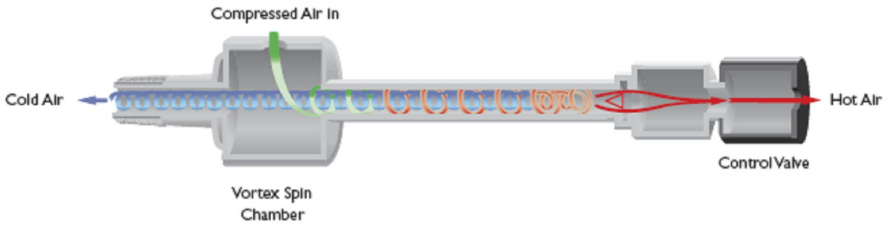

Figure 8.23: Schematic of vortex tube, Meech Static Eliminators Ltd.

The cooling system is designed to provide cooling for two endwalls and three vanes. A number of vortex tubes are therefore required, in a parallel setup, to provide the required coolant mass flow rate at an adequate temperature. This is achieved using four vortex tubes from *Exair Corporation*, with a capacity of $150\,\text{ft}^3$/min each (approximately 85 g/s), that can operate with a supply pressure of up to 250 psi $(17.2$ bar$)$. The mass flow rate through the vortex tubes is linked to the temperature drop provided and can be adjusted via the exhaust nozzle. The combined capacity of the tubes

at 70% cold fraction (70% of the air exhausted through the cold end), will cover the coolant requirements of 230 g/s. The system requires a running time of several minutes to allow all parts of the supply system to the vanes and endwalls to be cooled down and the system to achieve thermal equilibrium before an experiment can be performed.

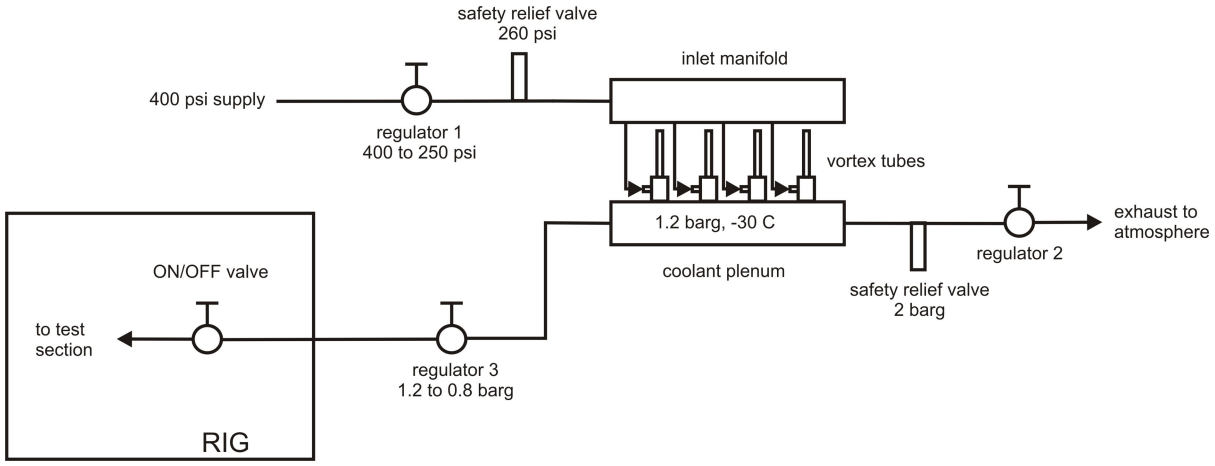

Figure 8.24: Schematic of the cooling system for the experimental facility

A schematic of the cooling system, designed to a capacity of 300 g/s, is shown in Figure 8.24. The coolant is supplied from a high pressure line (400 psi, 27.6 bar), to allow the vortex tubes to provide maximum refrigeration. The system comprises an inlet flow regulator from *Auld Valves Ltd.* (HP regulator) to drop the pressure to 250 psi $(17.2$ bar) before the inlet manifold that allows the distribution of the supply air to the four vortex tubes. The cold air from the vortex tubes is supplied to a plenum and a surplus valve from *Auld Valves Ltd.* maintains the pressure in the plenum (upstream of the valve) at 1.2 barg. A second regulator from *Auld Valves Ltd.* (LP regulator) is used to lower the pressure on the supply line to the experimental facility to the design value of 0.8 barg. Finally, a handle valve is installed on the supply line to the experimental facility. All components downstream of the vortex tubes are insulated to minimize heat gain from the atmosphere.

Before an experimental run, the cooling supply is disconnected and the surplus valve maintains the pressure in the coolant plenum at 1.2 barg. The vortex tubes are operated until the system reaches equilibrium. During an experimental run, the cooling supply is connected, allowing cold

air to flow to the facility. The design of this system provides the flexibility to maintain the same coolant pressure and temperature for runs with different mass flow rates, as the surplus valve will not allow the pressure to build up in the coolant plenum, exhausting any extra mass flow supplied by the vortex tubes that is not required for the cooling of the test section. The coolant-to-mainstream pressure ratio can be varied through the adjustment of the LP regulator and the temperature ratio through the adjustment of the vortex tubes. Finally, as this is a high pressure system designed to comply with EU requirements, two safety relief valves are installed on the system to exhaust the high pressure air in the system in the case of failure of the regulators.

The vanes are designed with small plena on the hub and casing, to which coolant is supplied through showerheads to ensure a uniform distribution of the air. The coolant is then supplied to the internal passages which are maintained the same as in the engine.

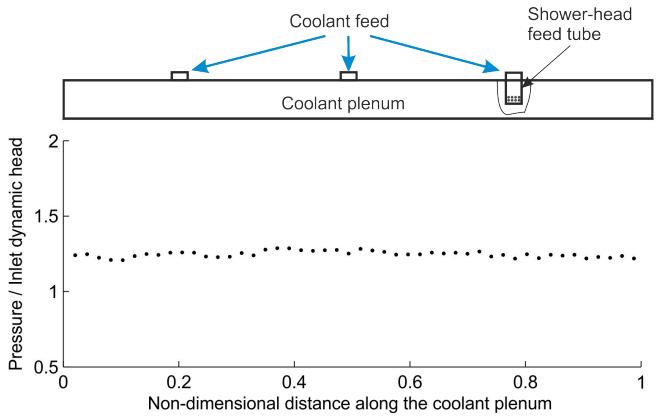

Figure 8.25: Pressure distribution at the exit of the continuous cooling slot

The coolant to the hub and casing plena for endwall cooling is supplied from three locations in each plenum, again with the use of showerheads to ensure a uniform distribution of the air. A number of small vortex tubes from *Meech Static Eliminators Ltd.* with a maximum capacity of $35\,\mathrm{ft}^3$/min (21 g/s) were used for initial tests of the capabilities of the setup. One of these vortex tubes was connected to a plenum with 48 pressure tappings along the continuous coolant slot to assess the uniformity of the coolant pressure during a test. The size and geometry of the plenum was the same as those designed for the cascade, covering four vane passages in the pitchwise direction. A sketch of the coolant plenum and the pressure distribution at the exit of the slot

relative to the inlet dynamic head are shown in Figure 8.25. This figure presents a cut through the coolant plenum across the circumferential direction, with three feed locations for the coolant on the top of the plenum, where showerhead feed tubes are fit. The cooling air exits the plenum from the bottom through the continuous slot.